

REPORT DOCUMENTATION PAGE				Form Approved OMB No. 0704-0188	
Public reporting burden for this collection of information is estimated to average 1 hour per response, including the time for reviewing instructions, searching existing data sources, gathering and maintaining the data needed, and completing and reviewing the collection of information. Send comments regarding this burden estimate or any other aspect of this collection of information, including suggestions for reducing the burden, to Department of Defense, Washington Headquarters Services, Directorate for Information Operations and Reports (0704-0188), 1215 Jefferson Davis Highway, Suite 1204, Arlington, VA 22202-4302. Respondents should be aware that notwithstanding any other provision of law, no person shall be subject to any penalty for failing to comply with a collection of information if it does not display a currently valid OMB control number. PLEASE DO NOT RETURN YOUR FORM TO THE ABOVE ADDRESS.					
1. REPORT DATE (DD-MM-YYYY) 13-12-2007		2. REPORT TYPE Final Report		3. DATES COVERED (From – To) 01-Dec-04 - 01-Dec-07	
4. TITLE AND SUBTITLE Physics and Chemistry of Microwave Laser-induced Discharge in Gas Flows and Plasma Jets			5a. CONTRACT NUMBER ISTC Registration No: 3058		
			5b. GRANT NUMBER		
			5c. PROGRAM ELEMENT NUMBER		
6. AUTHOR(S) Dr. Yuri Fedorovich Kolesnichenko			5d. PROJECT NUMBER		
			5d. TASK NUMBER		
			5e. WORK UNIT NUMBER		
7. PERFORMING ORGANIZATION NAME(S) AND ADDRESS(ES) Moscow Technical Club (MTC-IVTAN) Izhorskaya str., 13/19 Moscow 127412 Russia				8. PERFORMING ORGANIZATION REPORT NUMBER N/A	
9. SPONSORING/MONITORING AGENCY NAME(S) AND ADDRESS(ES) EOARD Unit 4515 BOX 14 APO AE 09421				10. SPONSOR/MONITOR'S ACRONYM(S)	
				11. SPONSOR/MONITOR'S REPORT NUMBER(S) ISTC 04-7003	
12. DISTRIBUTION/AVAILABILITY STATEMENT Approved for public release; distribution is unlimited.					
13. SUPPLEMENTARY NOTES					
14. ABSTRACT This report results from a contract tasking Moscow Technical Club (MTC-IVTAN) as follows: This basic research project is focused on understanding the fundamental mechanisms by which microwave generated plasmas can be used to influence internal and external supersonic flowfields. The contractor will also evaluate using laser impulses to further control the microwave generated plasmoid position and structure. Plasma jet penetration in a flow and plasmadynamic acceleration of disperse particles and their seeding in supersonic flows will also be investigated. The approach will include kinetic and flowfield modeling coupled with experimentation. The potential payoff is to evaluate the effectiveness of this approach for reducing external aerodynamic drag and providing control of local shock structures and flow conditions.					
15. SUBJECT TERMS EOARD, Aviation Technology, Aerodynamics					
16. SECURITY CLASSIFICATION OF:			17. LIMITATION OF ABSTRACT UL	18. NUMBER OF PAGES 87	19a. NAME OF RESPONSIBLE PERSON SURYA SURAMPUDI
a. REPORT UNCLAS	b. ABSTRACT UNCLAS	c. THIS PAGE UNCLAS			19b. TELEPHONE NUMBER (Include area code) +44 (0)1895 616021

Partner Project 3058p

“Physics and Chemistry of MW Laser-Induced Discharge in Gas Flows and Plasma Jets”

Final Report

**To European Office of Aerospace Research and
Development**

**Period 01.12.2004 – 01.12.2007
(Entire Period of the Project)**

**Project Manager
Dr. Yuri Kolesnichenko**

**Moscow
2007**

Project team

Yu. F. Kolesnichenko	Dr. in Physics and Mathematics, IHT, Project Manager
Yu. I. Anisimov	Dr. in Physics and Mathematics, SPbSU, optic measurements
S. A. Afanas'ev	Engineer, IHT, MW and RF equipment
O. A. Azarova	Dr. in Physics and Mathematics, gas dynamic modeling
V. G. Brovkin	Dr. in Technical Sciences, IHT, MW experiment
A. A. Gorynya	Engineer, ARSRIRE, MW generator
V. I. Ivanov	Engineer, SRIMM, gas dynamic installation
D.V. Khmara	Senior Engineer, kinetic modeling and processing
V. A. Lashkov	Dr. in Technical Sciences, SRIMM, gas dynamic experiment
I.Ch. Mashek	Professor, SPbSU, optic methods
M. I. Rivkin	Dr. in Technical Sciences, ARSRIRE, MW radiation system

Assistance at different stages of investigation by

Dr.'s **S. N. Sergeev** and **V. N. Sukhov**,
Eng.'s **S. A. Varga**, **E. D. Shlifer**, **M. I. Gurevich** and **A. A. Schmitt**,
technical personnel **A. K. Molodov**, **S. S. Epishin** and **T. A. Semenova**,

is greatly acknowledged

CONTENT

List of acronyms and notations.....	6
Introduction.....	8
Section 1. Interaction of MW radiation with Laser spark and plasma stimulators	15
1.1. Introduction.....	15
1.2. Laser-MW experimental complex.....	15
1.3. Breakdown characteristics of stimulated MWD and LS.....	16
1.4. Structural and dynamic characteristics.....	20
1.5. Interaction of MW with decaying laser spark plasma.....	23
1.6. Gasdynamic effects.....	23
1.7. Interaction of MW radiation with UV laser flash.....	25
1.8. Interaction of MW radiation with external plasma channel (HVS)	27
1.9. Investigation of HVS triggering by means of LS.....	30
Conclusions.....	31
References to Section 1.....	32
Section 2. Kinetic modeling of MW interaction with laser-created plasmas.....	33
2.1. Kinetic modeling of MW interaction with decaying laser spark under various ambient pressures (thermal mode).....	34
2.1.1. Modeling of the laser spark decay and determination of transparency time “windows” under various pressures.....	35
2.1.2. Interaction of MW with decaying laser spark.....	38
2.1.3. The influence of LS shape factor on filament origination conditions.....	40
2.2. Kinetic model of MW interaction with ultra-short pulse laser filament (non-equilibrium mode)	40
2.2.1. Results of kinetic modeling.....	40
Figures to Section 2.....	43
Conclusions.....	53
References to Section 2.....	54

Section 3. Numeric modeling of gas dynamic effects arising under interaction of MW discharge channel with AD body.....	55
3.1. Limited length low density channel effect upon supersonic flow past cylindrical body with complicated cavity.....	56
3.1.1. Statement of the problem.....	57
3.1.2. Calculation results.....	58
Conclusions.....	66
References to Section 3.1.....	67
3.2. On details of flow structure during the interaction of an infinite thin rarefied channel of constant density with a shock layer of blunt cylinder.....	68
3.2.1. Statement of the problem.....	68
3.2.2. Calculation results.....	69
Conclusions.....	85
References to Section 3.2.....	85
3.3. Numerical analysis of a thin low density channel effect on supersonic streamlining for $M_\infty = 3$.....	87
3.3.1. Statement of the problem.....	87
3.3.2. Calculation results.....	90
3.3.2.1. Cylinder flow symmetry.....	90
3.3.2.2. Plane flow symmetry.....	94
Conclusions.....	101
References to Section 3.3.....	101
Section 4. Plasmadynamic experiments.....	103
4.1. Experimental investigation of influence of MW discharge on aerodynamic drag of different bodies.....	103
4.1.1. Intensification of gas vortex motion in the shock layer on the body.....	103
4.1.1.1. Models design.....	103
4.1.1.2. Results of experimental research of models with gas injection.....	104
4.1.2. Experimental investigation of drag of sphere with gas injection.....	107

4.1.3. Investigation MW discharge influence on streamlining of a sphere with a spike.....	110
4.2. Development of experimental facility.....	114
4.2.1. Substantiation of necessity of conducting of gasdynamic investigations at higher Mach number.....	115
4.2.2. Improvement of wind tunnel TBS.....	117
4.2.2.1. Working flow with Mach number $M=2$	117
4.2.2.2. Working flow with Mach number $M=3$	118
4.2.3. Building of a new focusing MW system.....	120
4.2.4. Construction of gas heater.....	126
Conclusions.....	129
References to Section 4.....	130
Section 5. Laser-induced MW discharge.....	131
Conclusions.....	147
References to Section 5.....	148
Section 6. Plasmadynamic applications of Magneto-Plasma Compressors.....	150
6.1. Magneto-Plasma Compressor in Vacuum Regime.....	150
6.2. Magneto-Plasma Compressor in Residual Gas-Regime.....	157
6.3. Magneto-Plasma Compressor in High-Pressure Residual Gas regime.....	162
6.4. Miniature Magneto-Plasma compressor in HPRGR.....	176
Conclusions.....	181
References to Section 6.....	182
Summary.....	184
Acknowledgments.....	192

List of acronyms

2-D – two dimensional

AD – aerodynamic

BSW – bow shock wave

CCD – charge coupled device

CW – continuous wave

DR – dissociative recombination

EM – electromagnetic

EOA – electron-optical amplifier

HF – high frequency

HV – high voltage

LV – low voltage

LBD – low-threshold ball discharge

LED - light emitted diode

MW – microwave

MWD – microwave discharge

PC – personal computer

RF – radio-frequency

RT – rotational-translational

SMD – stimulated microwave discharge

SS – supersonic

UV – ultra-violet

Notations

ρ - gas density

v - velocity

ε - specific energy of gas

p – gas pressure

T – gas temperature

T_e – electron temperature

σ - electron conductivity

E – electric field intensity

H – magnetic field strength

λ - wavelength of EM radiation

k – wave number

ω - angular frequency

ω_H – cyclotron frequency

n_e – electron concentration

ν_i - ionization frequency

ν_m – frequency of elastic collisions of electrons with molecules

N – neutral particles concentration

R, D – radius and diameter of AD model

η - interaction efficiency

μ_0 – magnetic permittivity of vacuum

g_m – the statistic weight of emission state m

A_{mn} – the Einstein coefficient for $m \rightarrow n$ transition

λ_{mn} - wavelength of $m \rightarrow n$ transition

C_{A0} - the Alfven velocity

U – voltage

I - current

Introduction

This Report reviews the period of the Project 3058p “Physics and Chemistry of Laser-Induced MW Discharge in Gas Flows and Plasma Jets” implementation. Finding out of conditions for efficient influence of energy injection on aerodynamic characteristics of supersonic body was one of the main objectives of the previous Project 2014p, successfully completed in 2004. In frames of its implementation high efficiency of MW discharge filament interaction with aerodynamic body was obtained. It reached the value about 30 under $M=2.1$ flow conditions at 24mm diameter blunt body. Having spent of about 30mJ to create specific MW plasmoid saved was about 1J in body drag during interaction with it. Moreover, due to the fact that only several percents of the absorbed MW energy were spent on filament creation, the physical efficiency was found to be 1000. Simultaneously rather large scattering of the instant values due to variation in discharge properties was noticed. To avoid these factors and to rise up the efficiency of MW energy utilization, combination of MW and Laser was proposed. Application of laser-stimulated MW breakdown along with elongation of MW channel and rising up the Mach number of supersonic flow should let us sufficiently increase discharge performance and interaction efficiency for all types of supersonic model shape. This is the main objective of the first Task of the current Project.

Creation of gas/plasma flows with high Mach number and high stagnation temperature demands complex aerodynamic installations with high power consumption. Thus, such investigations are practically unavailable for modest abilities of typical scientific laboratory. Nevertheless, there are opportunities for creation of quasi-stationary plasma jets with high flow enthalpy in laboratory conditions. The base for creation of high-enthalpy plasma jets can be quasi-stationary coaxial plasma accelerators (MPC). This type of accelerators generates plasma jets of different gases (H_2 , He, N_2 , Ar) with comparatively high density in compression area (up to 10^{16} - 10^{17} cm^{-3}), temperatures about 3 eV, gas velocity in jets focus up to 70 km/sec for He and 38 km/sec for N_2 . The typical duration of current impulse in this type of accelerators is 100-200mcsec. Thus, one can generate plasma flow and realize non-stationary or quasi-stationary interaction of it with AD bodies or media. Exactly these conditions seem to be favorable for revealing pure plasma effects in flow – body interaction. This is the main objective of the second Task of the Project.

Thus, further basic research efforts for high power microwaves, lasers and plasma jets in super- and hypersonics are to improve the fundamental understanding of the limitations of the beamed energy concept.

The Project is implementing by the two Institutions: Institute of High Temperatures RAS (Moscow) – leading Institute and Scientific Research Institute of Mechanics and Mathematics of St.-Petersburg State University.

New facilities were created for the Project implementation:

- Flexible MW – Laser stand in IHT RAS with wide range of MW parameters control and gas pressure variation, 3 wavelengths of Nd:YAG laser operation in nanosecond generation regime with ability of mutual position of MW – laser beams variation
- Picosecond Nd:YAG laser on 2 wavelengths (St-Petersburg)
- MW – Laser stand in SRIMM based on Ruby laser and microsecond pulse duration MW generator
- Magneto – plasma Compressor in Residual Gas Regime with ability of plasma jet interaction with impulse neutral supersonic jet and flow seeding (St-PSU)

Also during the period of the Project implementation efforts were applied on diagnostic tools improvement.

Main efforts during the first Quarter were concentrated on assembling, tuning and testing of these experimental facilities, as well as diagnostic tools improvement.

The work in the 2nd Quarter was concentrated in the following directions:

- Starting of experiments on the created MW – Laser installation (IHT) for obtaining and investigation of combined MW and Laser discharge under different conditions. Pilot experiments with picosecond Laser.
- Analytic investigation of non-linear stage of MW channel origination and evolution with pointing out of inherent gas dynamic effects (ionization-thermal instability) in cylindrical symmetry
- Preparation of kinetic scheme for gas dynamic numeric modeling of MW filament origination
- Numeric investigation of kinetic processes which accompany ionization-thermal instability in such highly non-uniform object, as MW channel

- Starting of numeric investigation of parametric links for a problem of aerodynamic bodies streamlining by supersonic flow under the influence of energy deposition in cylindrical symmetry and comparison of the obtained results with those for 2D-plane geometry
- Putting into operation and obtaining of basic parameters of MPC stand (St-PSU) and abilities of the experimental complex as a whole.

Numeric investigation of MW filament origination was implementing in collaboration with Prof. Doyle Knight (Rutgers University).

Also the works for modernization of MW generator were carried out on the gas dynamic stand of SRIMM. They were aimed at raising of stability of MW generator operation in a single-mode regime.

The work in the 3rd Quarter was concentrated in the following directions:

- Starting of experiments on the created MW – Laser installation (IHT) for obtaining and investigation of combined MW and Laser discharge under different conditions.
- Estimation of transformation effectiveness of picosecond laser pulse energy in thermal energy, inputted in gas under the normal conditions.
- Kinetic modeling for determination of the levels of MW reduced field and the values of depolarization reduction of external field, which are sufficient for arising of MW filament from decaying plasma of the dotted laser spark during typical times of filament formation of about 1 microsecond.
- Numerical modeling on a basis of Euler equations some delicate effects of a thin limited length low-density channel action on supersonic flow past AD bodies for the case of cylindrical symmetry
- Investigation of dynamic parameters of plasma jet produced by Magneto – plasma Compressor in Residual Gas Regime
- Experiments on wind tunnel of SRIMM at increasing of a lifetime and intensity of a vortex in a shock layer during MW filament interaction with supersonic AD body.
- Code preparation and debugging for numeric investigation of MW filament origination, which is implemented in collaboration with Prof. Doyle Knight (Rutgers University), was continued.

The work in the 4th Quarter was concentrated in the following directions:

- Experiments on the MW – Laser installation (IHT) for obtaining and investigation of combined MW and Laser discharge under different conditions.
- Estimation of transformation effectiveness of picosecond laser pulse energy in thermal energy, inputted in gas under the normal conditions.
- Kinetic modeling for determination of rate constants and heat effect for energy exchange reactions under specific conditions of vibronic states excitation in MW gas discharge
- Numerical modeling on a basis of Euler equations of a thin limited length low-density channel effect upon supersonic flow past cylindrical AD body with complicated cavity
- Experiments on wind tunnel of SRIMM at increasing of a lifetime and intensity of a vortex in a shock layer during MW filament interaction with a special supersonic AD body
- Investigation of dynamic parameters of plasma jet produced by Magneto – plasma Compressor in Residual Gas Regime

The work in the 5th Quarter was concentrated in the following directions:

- Experiments on the MW – Laser installation (IHT) for obtaining and investigation of combined MW and Laser discharge under different conditions were performed and estimation of effectiveness of nanosecond laser pulse energy in UV region input in gas under the conditions of supersonic flow
- Continued were kinetic modeling for evaluation of conditions for MW discharge origination during MW interaction with decaying laser spark, as well as numerical modeling on a basis of Euler equations of a thin limited length low-density channel effect upon supersonic flow past cylindrical AD body with complicated cavity
- Investigation of dynamic parameters of plasma jet produced by Magneto – plasma Compressor in Residual Gas Regime was completed
- Experiments on wind tunnel of SRIMM at increasing of a lifetime and intensity of a vortex in a shock layer during MW filament interaction with supersonic AD body were continued.

The work in the 6th Quarter was concentrated in the following directions:

- Experimental investigation of MW radiation interaction with laser plasma under different conditions in geometry when laser beam in the working chamber was directed along the electric field vector of MW wave
- Kinetic investigation of ambient medium pressure influence on transparency time “windows” for incident MW of decaying LS domain and determination of the minimal necessary MW

power density for launching of ionization avalanche

- Numerical modeling on a basis of Euler equations the behavior of front drag force during an interaction of flat/cylinder shock layer with energy deposition regions of different geometry
- Improvement of gas dynamic channel of wind tunnel and preparation for operation at Mach number 3. Experimental investigation MW discharge influence on streamlining of a sphere with counterflow in airflow with Mach number 2
- Investigations of Magneto – Plasma Compressor generated jets under the high static pressures and development of MPC experimental setup for jet mixing investigation.

The work in the 7th Quarter was concentrated in the following directions:

- Experimental investigations of MW and laser radiation interaction with linear plasma channels/stimulators
- Modernization of laser operation control scheme for optimization of laser radiation parameters on the 4th harmonics ($\lambda \sim 262\text{nm}$) of Nd:YAG laser
- Quantifying plasma parameters under laser beam action, as well as their evolution in space and time to find out the best conditions for MW field imposing. Kinetic investigation of MW pulse interaction with long thin spark created by ultra-short laser pulse
- Numerical modeling on a basis of Euler equations of a thin low-density channel effect on supersonic streamlining AD body with wedge-shaped ledge to investigate flow structure inside the area behind the back surface of the body
- Creating of supersonic flow with Mach number $M=3$ at wind tunnel TBS
- Designing and assembling of new experimental setup for investigation of mixing processes between supersonic neutral flows and hypersonic plasma jets, created by MPC.

The work in the 8th Quarter was concentrated in the following directions:

- Experimental investigations of the 4th harmonics ($\lambda \sim 262\text{nm}$) of Nd:YAG laser radiation interaction with linear plasma channels
- Kinetic investigation for optimization of laser-pulse-controlled MW energy deposition
- Numerical modeling on a basis of Euler equations of a thin low-density channel effect on supersonic streamlining AD body with $M=3$
- Experimental investigation of influence of joint action of MW discharge and gas injection through a spike in airflow with Mach number 2

- Investigation of mixing processes between supersonic neutral flows and hypersonic plasma jets, created by MPC
- Code preparation and debugging for numeric investigation of MW filament origination, which is implemented in collaboration with Prof. Doyle Knight (Rutgers University), was continued.

The work in the 9th Quarter was concentrated in the following directions:

- Experimental investigations of MW interaction with laser radiation on the 4th harmonics ($\lambda \sim 262\text{nm}$) of Nd:YAG laser
- Initiation of MW discharge by means of UV laser radiation and determination of conditions and initiation ranges of MW discharge
- Investigation of different modes of MW discharge initiation – by means of creation of laser spark or by irradiation of initiation area without spark origination
- Optimization by means of kinetic investigation of MW pulse interaction with long thin spark created by ultra-short laser pulse
- Numerical modeling on a basis of Euler equations of a thin infinite low-density channel effect on supersonic streamlining of blunt cylinder to investigate the flow structure inside the separated region in front of the body
- Investigations of mechanisms of jet arising in MPC operated in RGR, measuring of local temperatures and estimation of the value of jet charge efflux in external space

The work in the 10th Quarter was concentrated in the following directions:

- Attaining of MW discharge initiation by a coaxial laser radiation on the second harmonics ($\lambda \sim 532\text{nm}$) of Nd:YAG laser
- Determination of thresholds and initiation domains of MW discharge in dependence a delay between laser and MW pulses
- Investigation of different modes of MW discharge initiation – by means of creation of laser spark or by irradiation of initiation area without spark origination
- Numeric investigation of air pressure influence on transparency time windows for incident MW of elongated LS domain and determination of the minimal needed MW power density for the launch of ionization avalanche

- Numerical modeling on a basis of Euler equations of a thin infinite low-density channel effect on supersonic streamlining of blunt cylinder to investigate the flow structure and its stability inside the separated region in front of the cylinder body
- Designing and investigation of low-dimensional Miniature MPC, its energetic characteristics and parameters of produced jet
- Code debugging and testing for numeric investigation of MW filament origination, which is implemented in collaboration with Prof. Doyle Knight (Rutgers University).

The work in the 11th Quarter was concentrated in the following directions:

- Measurements of threshold characteristics of MW discharge in a wide range of pressures under initiation by differently oriented laser spark or in sparkles regime of laser radiation on the second harmonics ($\lambda \sim 532\text{nm}$) of Nd:YAG laser
- Evaluation of a new kinetic mechanism of medium heating in gas discharge by numeric investigation of influence the transformation of electron energy into medium heating during the row electron-impact excitation of $O(^3P_j)$ levels with their following relaxation in collisions with neutral particles
- Numerical modeling on a basis of Euler equations of a thin infinite low-density channel effect on supersonic streamlining of blunt cylinder to investigate the flow structure and its stability inside the separated region in front of the cylinder body
- Creation of multi-target laser system for plasmadynamic investigations at supersonic wind tunnel
- Engineering development and manufacturing of the new microwave focusing system to increase intensity of the electric field in the area of focus of the system at supersonic wind tunnel for $M=3$ airflow
- Code testing for numeric investigation of MW filament origination, which is implemented in collaboration with Prof. Doyle Knight (Rutgers University).

The work in the 12th Quarter was concentrated in verifying of the most important previously obtained results and providing experiments and computation for interaction of MW discharge with AD body in Mach 3 flow.

The Final Report consists of six Sections. Each paragraph presents both new results, obtained during the 12th Quarter and the most important results obtained during the period of the Project implementation.

Section 1. Interaction of MW radiation with Laser spark and plasma stimulators

1.1. Introduction

The results of experiments [1] have shown high efficiency of MW radiation interaction with Laser spark (LS). Mutual action of two intensive waves of different range results in modification of threshold, structural and dynamic characteristics of the observed phenomena. Let us enumerate consequently those phenomena, which can be detected practically visually. First of all, this is a decrease of thresholds of MW and laser discharges initiation under the atmospheric and reduced air pressure. Then, pronounced amplification of sound effects under the simultaneous action of MW and laser impulses, as well as changing of laser spark color and characteristic initial MW discharge structure. Besides, the stable effect of laser plasma heating by MW radiation is fixed – starting from the stage of laser plasma formation and up to hundreds of microseconds on its decay phase. All the mentioned effects are studied thoroughly during the reported period.

1.2. Laser – MW installation

Laser – MW installation was created in IHT RAS [1] for investigation of high-power MW interaction with laser spark. The scheme of laser radiation transportation in the domain of its interaction with microwaves is shown at Fig.1. From generator IR radiation ($\lambda \sim 1.06$ microns) via rotary mirrors and amplification cascades is entering the crystal frequency converter (DKDP crystal doubler). Then radiation of $\lambda \sim 532$ nm via rotary mirrors, quartz illuminator and focusing length reaches the focal domain of MW radiation. The experiments were carried out in different orientation of focused beams.

In each experimental cycle at its beginning and at the end the level of the incident laser energy was tested means of air breakdown and in the case of deviation of the obtained values by more than 30% the laser was turning off for crystal cooling. Later on some of the cycles were repeated.

The stable formation of the laser spark under the atmospheric pressure is registered starting with the incident energy level exceeding 10 mJ. The energy flux density was estimated to be about $3 \cdot 10^{11}$ W/cm² for energy pulse 10mJ and pulse duration 10 ns. This value is in

agreement with the value of the breakdown field in atmospheric pressure air, which is about 1.3×10^7 V/cm.

Realizing of energy input in the vacuum chamber through the quartz illuminator the ability of creation of laser spark under the reduced air pressure was also tested. Laser spark was stably obtained to ~ 70 -100 Torr under the laser beam energy 130-90 mJ.

MW generator (magnetron) operates at $F=13\text{GHz}$ with pulse duration in the range $\tau \sim 1$ -50 mcs and impulse power up to $P \sim 750$ kW. This allows to realize in the focal region electric field strength of EM wave up to 3 - 3.5 kV/cm. First of all it should be noted that already in the first experimental series laser spark creation has led to initiation of MW discharge.

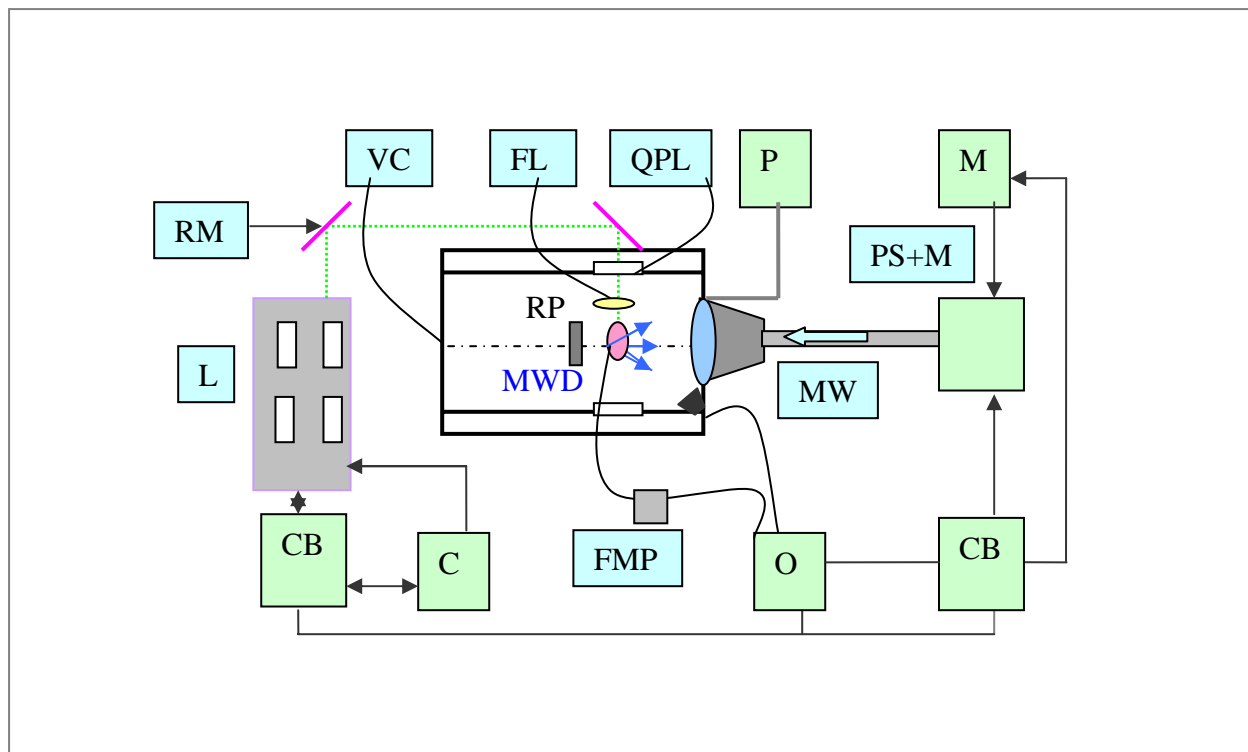


Fig.1 Installation scheme

VC – vacuum chamber, FL – focusing lens, QPL – quartz port-light, P – pump, M – modulator, PS+M – power source, magnetron, MWD – microwave discharge, RP - reflecting plate, RM - reflecting mirrors, L – Nd:YAG laser, CB – control block, C – cooling block, FMP – photo-multiplier, O – oscilloscope

1.3. Breakdown characteristics of stimulated MWD and LS

By means of set mirrors laser spark was produced with orientation along or across the wave vector of MW wave. Measurements of threshold characteristics of MW discharge were

carried out in a wide range of pressures under initiation by differently oriented laser spark or in sparkles regime of laser radiation.

Experimental conditions and methods Let us consider experimental conditions under which threshold characteristics were investigated. Measurements were carried out in the range of air pressure from 10 Torr up to 750 Torr. For MW frequencies (in our case $F=13$ GHz) these pressures refer to the right branch of the Pashen curve, under which electron elastic collision frequency ($\nu \sim 5.3 \cdot 10^9$ P) exceeds (or, sufficiently exceeds) the angular MW radiation frequency ($\omega = 2\pi F$). At that, the diffusive losses of electrons from MW beam are minimal. The lowest pressures under investigation refer to the Pashen curve minimum (when $\omega = \nu$) and under these pressures the most low breakdown fields are fixed. With pressure increase, the level of breakdown field increase proportionally.

All measurements were carried out in impulse regime under the fixed frequency of MW pulses repetition rate (10 Hz) and pulse duration 10 mcs. The area of the optimal interaction was detected by use of thin dielectric plate covered by thermally sensitive dye ($T = 40^\circ$ C). As a result of plate interaction with MW beam the structure of MW field with main maximum of $\sim \lambda/2$ width is visualized. Then, in the central part of this maximum laser radiation is focused by means of focusing lens ($f = 75$ mm). Interaction area does not exceed 5 mm and, as it was shown in experiments, the effectiveness of discharge processes depends greatly of the exactness of MW and laser energy feed of the demanded zone.

The breakdown fact was registered visually and by means of PMT and MW sensor signals, which were displayed on the oscilloscope. Optic fiber was installed near the focus area, MW sensor was installed in the area of divergent part of MW beam. Under the MW discharge occurrence, the level of signal decreases abruptly due to absorption of discharge plasma. Simultaneously, the light signal from MW discharge appears. In this series, laser operated on the second harmonics ($\lambda \sim 532$ nm) with pulse energy $E \sim 60 - 80$ mJ. Lower energy levels (due to losses on the additional mirrors) refer to laser beam orientation along **k** and **E** vectors of MW wave, the higher – along **H** vector. It should be noted that under the entire experiments laser impulse passed ahead of the MW pulse at 10 - 20 mcs. This item was discussed in our previous work [2], where it was shown that such delay is necessary for higher efficiency of MW discharge initiation. This effect is shown for elevated pressures ($P > 200 - 300$ Torr), whereas for reduced pressures such initiation can be obtained practically during the entire period between pulses. The

previous results have shown [2] that the delay time can decrease under the decrease of MW power. Most likely, the MW power increase should lead to increase of initiation period under the elevated pressures.

Experimental results. In the first series laser beam propagated perpendicularly to MW beam and was parallel to vector **H**. Firstly, the thresholds of self-ignited breakdown and extinction were determined. Then laser was switched on and, again, the breakdown threshold was fixed. Under the reduced air pressures ($\sim 10 - 80$ Torr) laser spark was absent. Later on, with pressure increase ($P \geq 80$ Torr) laser spark appeared and initiated MW discharge. Self-ignited discharge in this pressure range can not be realized due to increase of breakdown field levels, which the present magnetron is not able to provide. Experimental results demonstrate decrease of breakdown threshold even under the presence of laser beam (without spark production, Fig.2a). Laser spark origination decreases the threshold of MW discharge origination even in more pronounced way, the fact that is clearly seen under the elevated pressures (Fig.2b).

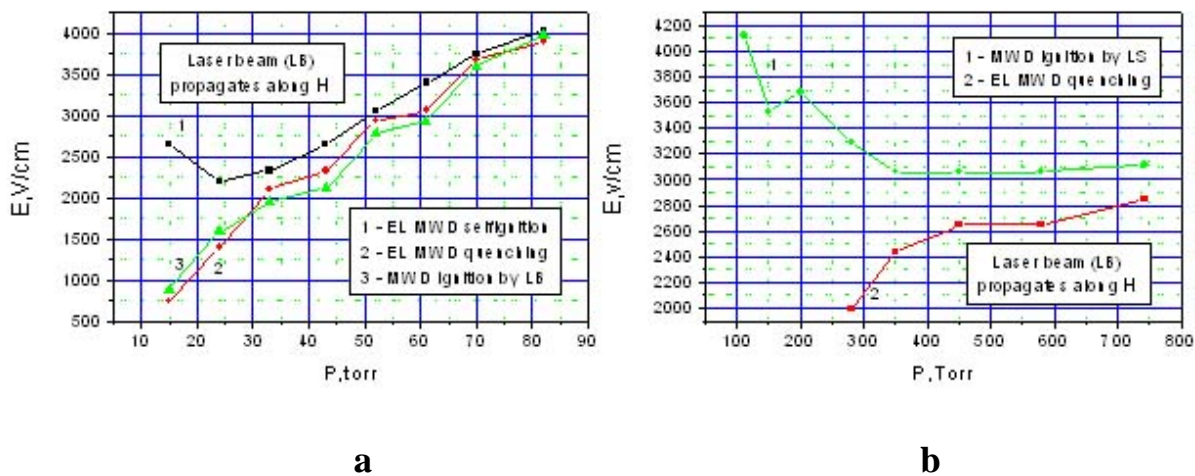


Fig.2. Breakdown characteristics of MW discharge (LB along **H**)

The results of experiments when laser beam propagated along MW beam (parallel to **k**) are presented (Fig.3). Here the procedure of experiment was the same as described above.

As for the first series, the curve of self-breakdown is not shown on the right-hand graph. And finally, below are presented the results for laser beam orientation along vector **E** of MW beam (Fig.4).

The results of experiments demonstrate similarity of breakdown characteristics under the reduced pressures (up to 80 Torr). It should be noticed that such phenomena investigation is

faced to statistical jitter of the measured parameters. In principle, practically linear increase of breakdown field with pressure increase is observed under any mutual orientation of laser and MW beams. In the frames of statistic jitter the values of breakdown MW field are close to each other with variation of interaction geometry. The MW breakdown threshold under the presence of laser beam is visibly less that for self-ignition and in some cases even less that for its extinction. Sufficient decrease of MW breakdown level is observed under the laser spark origination (range $\geq 80 - 100$ Torr). For example, under pressure of 200 Torr the value of breakdown is decreased in 2-3 times, whereas under 500 Torr and higher – at about order of value.

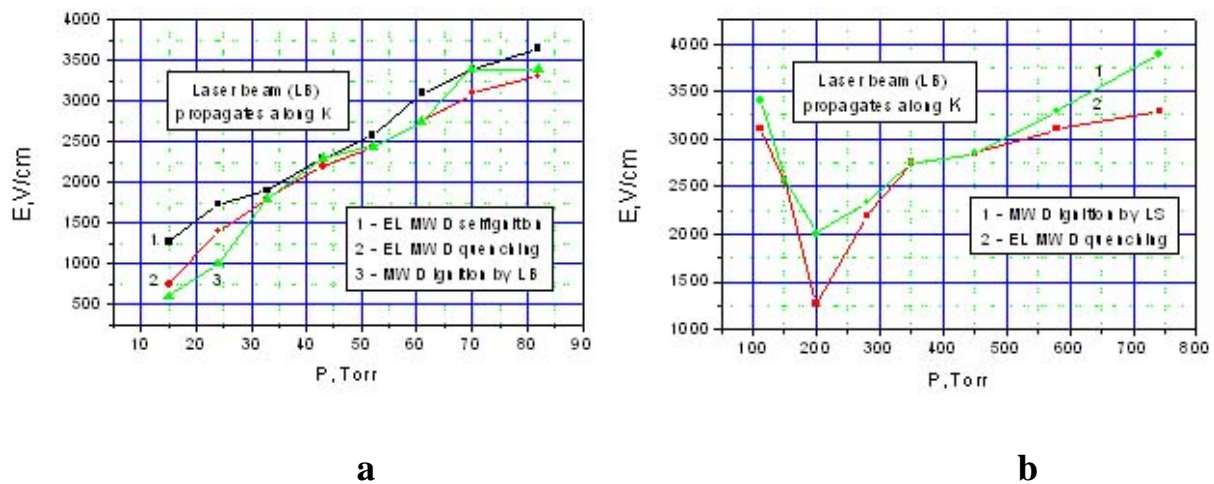


Fig.3. Breakdown characteristics of MW discharge (LB along k)

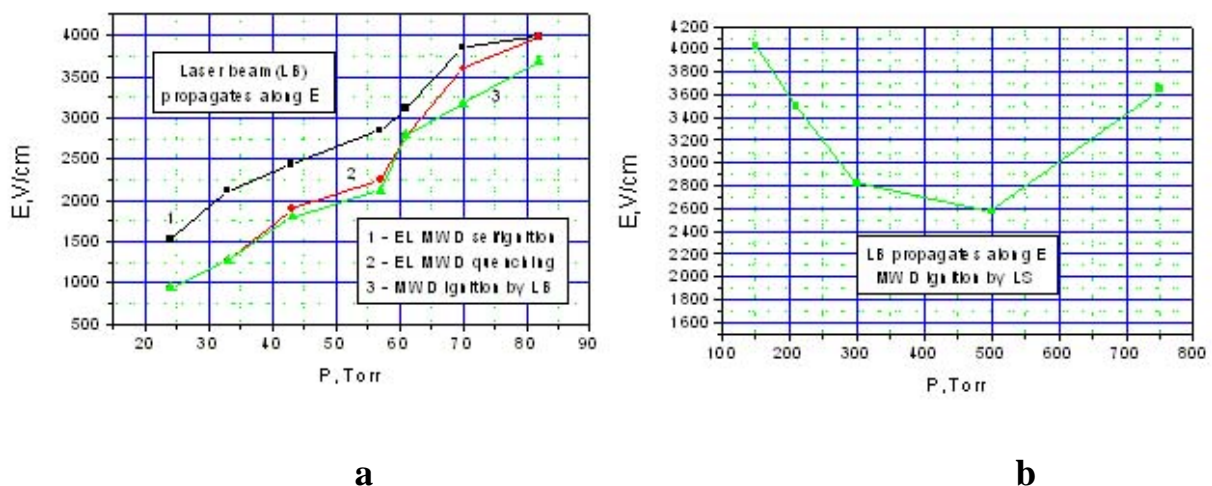


Fig.4. Breakdown characteristics of MW discharge (LB along E)

As it was mentioned above, such experiments are advisably to repeat for obtaining more valuable diapason of parameters jitter.

Special cycle of threshold measurements was carried out under the atmospheric pressure. Both laser and MW field levels were varied. The initial level of MW radiation was chosen close to discharge threshold, then the laser impulse energy was increasing up to MW breakdown origination. After the breakdown the energetic characteristics of MW and laser radiation decreased. Under the lower value of MW field laser energy increased and, again, MW discharge was realized. Such a procedure let us initiate MW discharge under diminishing of MW field intensity, but increasing of laser one. In principle, reverse actions gave a similar result. The decrease of threshold characteristics is well seen at Fig.5 presented below.

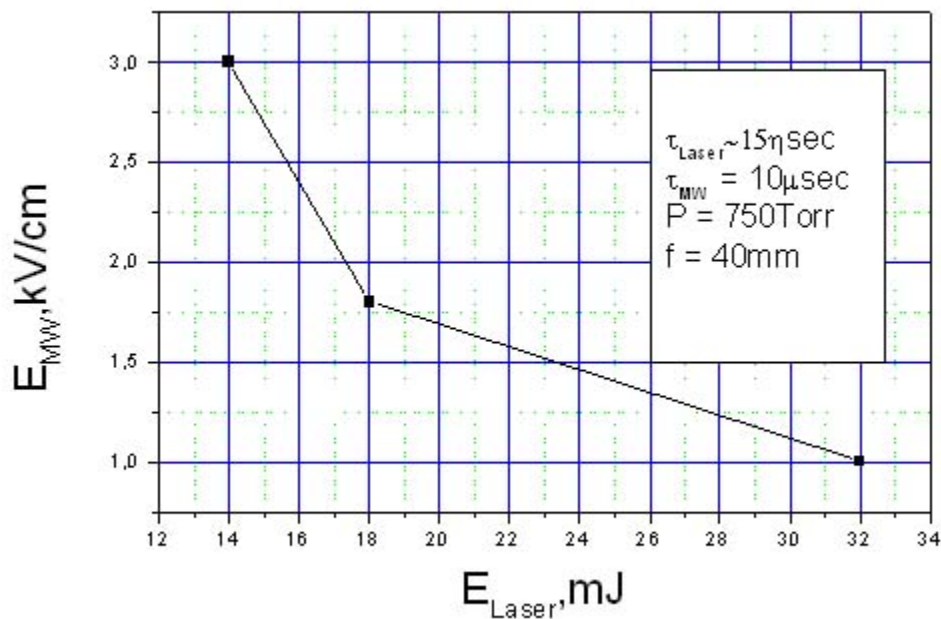


Fig.5. Dependence of breakdown levels of MW discharge over laser energy value

1.4. Structural and dynamic characteristics

In this series of experiments the processes of discharge structure peculiarities under the synchronous and delayed action of laser and MW radiation. We have in view interaction of microwaves with laser plasma in the phases of its creation and decay. In the case when MW pulse

passes ahead the laser one interaction is lacking as under such levels of power MW discharge is not realized.

The scheme of experiments practically was not changed, nearby the focal zone optical fibers were installed. The delays between MW and laser pulses were varied, for structural analysis photo-registration was carried out. Some of peculiarities of discharge structures can be noticed at once. In principle, the dynamics of discharge development from laser spark is similar to that which is observed in the case of ordinary stimulator application. However, the presence of intensive EM (light) wave favours spreading of MW discharge. Moreover, the tendency of MW channels propagation along laser beam is appearing and even curling of these channels around or in the vicinity of laser beam is sometimes observed. It is known that laser sparks generate magnetic fields, the values of which can attain up to 10 – 100 T [3] under the energy flux density $\sim 10^{12} \text{ W/cm}^2$, the level that is most likely attained in our experiments. Probably, MW channels respond on these fields, as they are rather sensitive even on weaker ones. Such swirls characterize the intensity of discharge phenomena. However, this important and interesting phenomenon demands additional exploration.

Below photos of different discharge realizations are presented, obtained in different projections (Fig.6). Let us characterize them and show mentioned above peculiarities. In this series laser spark was produced at the leading edge of MW pulse. The delays in stimulated MW discharge formation under these conditions did not exceed 2 – 5 mcs.

On the first photo only laser spark is presented. The next frame demonstrates the obvious curling of MW channels, propagating from the area of laser spark origination. Further the discharges of sinusoidal and dipole types are well seen. MW discharge can develop both higher or lower and simultaneously in the both sides. The stable initiation of MW discharge was achieved by laser spark passing ahead of MW pulse up to 50 mcs for not so high MW energy flux density (about 10 kW/cm^2) and laser radiation energy about 50 mJ. Thus, for the first time the stable electrodeless MW discharge initiated by laser spark was obtained in experiments both under reduced air pressure (down to several Torr) and at atmospheric one.

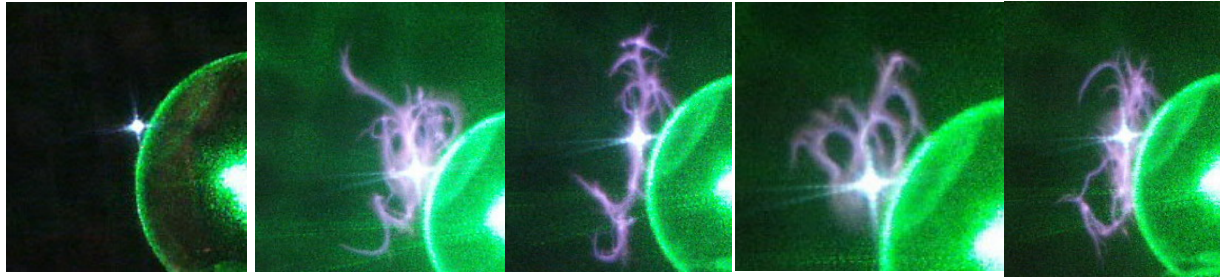


Fig.6. Typical views of MW discharge stimulated by laser spark. Laser beam **along H**-vector.

MW beam – from left to right. pressure 750 Torr, $E_{\text{laser}} \sim 70 \text{ mJ}$, $\tau_{\text{MW}} \sim 10 \text{ mcs}$,
 $S_{\text{MW}} \sim 4 \times 10^4 \text{ W/cm}^2$

In new configuration (laser beam directed **along E**) structural change of discharge is also observed. Under reduced pressures and horizontal laser beam propagation MW discharge had tendency of transversal expansion along light wave [2]. Now discharge structures are elongated in the direction of electric field vector and laser beam. Plasma dipole is formed in the focal region of MW beam, the fact that is well seen at the photos presented below (Fig.7).

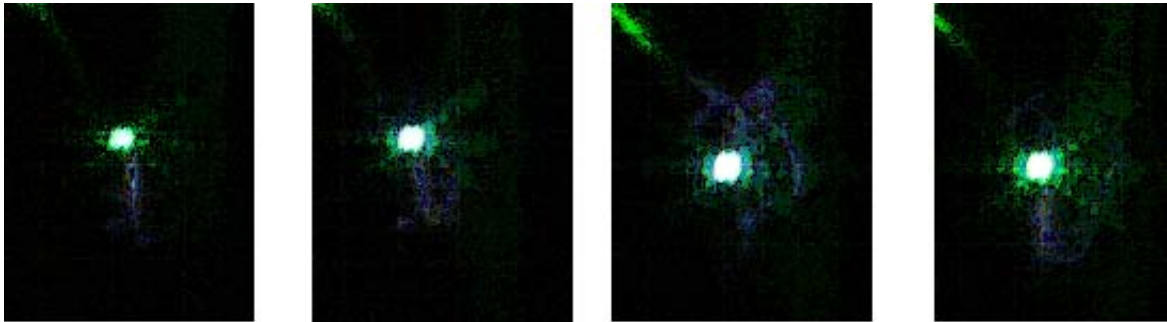


Fig.7. Discharges of atmospheric pressure. First and second: $W \leq 10 \text{ kW/cm}^2$; third and fourth: $W \sim 27 \text{ kW/cm}^2$. Laser beam **along E**-vector (from bottom to up). $t_{\text{del}} = 15 \text{ mcs}$, MW beam – from left to right

With pressure increase the mentioned tendency remains the same. Besides, MW channels are oriented well along laser beam and MW field polarization. It is characteristic that the channel is developing towards propagation of light beam. Interesting peculiarity in discharge formation under the atmospheric pressure is observed. In addition to vertical channels there appear channels of concentric type. Such discharge types are presented at Fig.8.

It should be noted that concentric type channels appear when MW pulse is radiated with $\sim 15 - 20$ mcs delay relative laser one. With increasing of time delay, the discharge takes its ordinary shape.

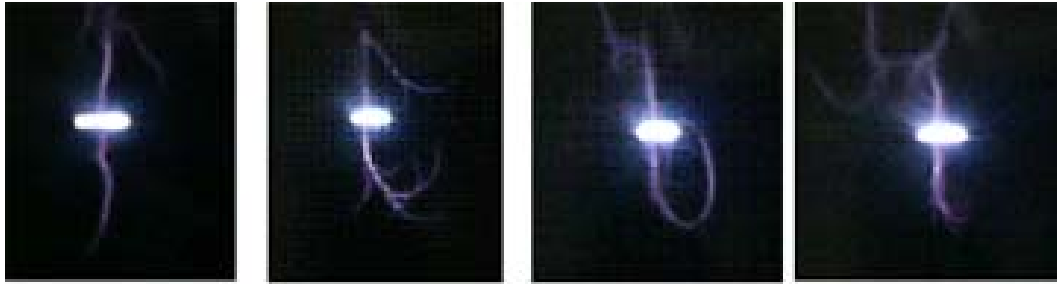


Fig.8. Different types of MW discharge structure at atmospheric pressure. Laser beam along **k**-vector. MW beam – from left to right

In conclusion we can state that in general transversal and axial interaction of laser and MW radiation demonstrates common features, as well as some differences.

1.5. Interaction of MW with decaying laser spark plasma

Exploration of MW discharge creation on the late stages of laser plasma decay demonstrates high efficiency of MW radiation interaction with the residual plasma. Under the low pressures ($P < 70$ Torr) MW discharge can be initiated with time delays reaching values of order of tens milliseconds. In the region of middle pressures ($70 < P < 200$ Torr) such delays are about several milliseconds. And finally, in the interval 300 - 750 Torr MW discharge can be initiated with delays of about hundreds of microseconds. Under the constant level of MW energy the ultimate time of MW pulse delay after which the discharge can be still initiated grows up practically linear with laser pulse energy. Also this ultimate time is growing up with the increase of MW power under the fixed energy of laser pulse, but faster, than linear dependence.

Thus, we can state that in general transversal and axial interaction of laser and MW radiation demonstrates common features, as well as some differences.

1.6. Gasdynamic effects

For registration of the shock-sound effects microphone and pressure sensor were installed in the working chamber. The signals from the devices were displayed on oscilloscope. As the

results of experiments have shown, the variant of combined laser-MW sources application leads to signal sufficient amplification.

The amplitude of a sound signal increases about three times under the combined action of MW and laser radiation. Moreover, this result was obtained in the case when the delay of MW pulse relative laser one did not exceed 30 mcs and laser energy was not less than 50 mJ. The level of MW radiation exceeded 10 kW/cm^2 . The decrease of the both levels abruptly decreased the effect of sound amplification.

Investigation of shock-wave phenomena was also performed by means of pressure sensor Kistler. The sensor was installing at a distance of 7 mm from the discharge zone. The signal registered from the laser spark itself is reproducing rather well, the fact allowing evaluation of the mean shock wave velocity on the delay of signal arriving. The shock wave velocity reaches value $\sim 450 \text{ m/s}$ and signal amplitude does not exceed 400 mV. Signal parameters registered from MW discharge itself have close parameters. In experiment registered were only those realizations in which the contact of MW discharge with sensor was excluded. Radiation of MW pulse with delay 5 – 20 mcs relative laser one, leads, as a rule, to amplification of the amplitude of the signal, coming from MW discharge, up to 30%. Below signals from the Kistler sensor (blue) and photo-multiplier (green) are presented (Fig.9a – only MW, Fig.9 – only laser, Fig.9c – laser + MW).

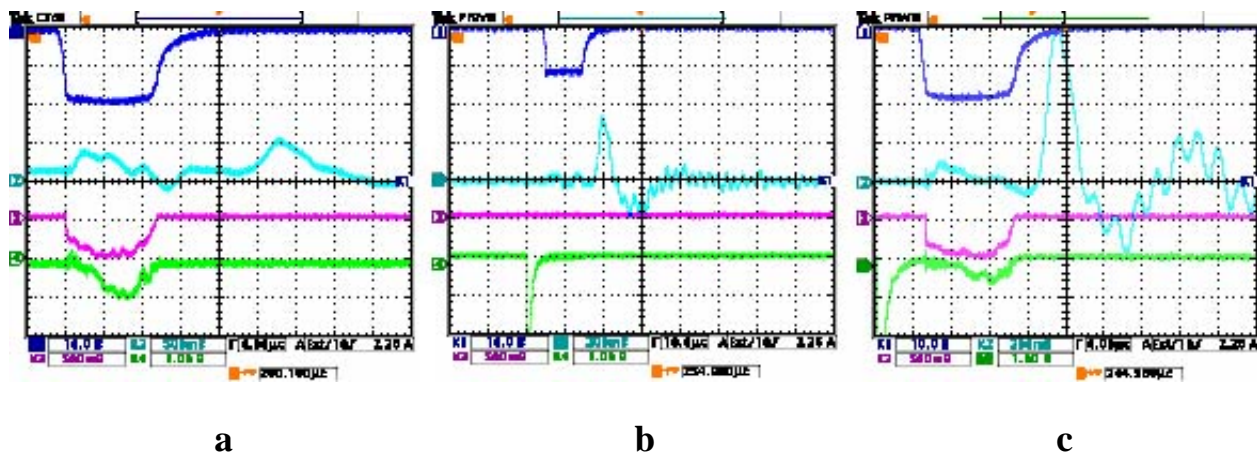


Fig.9. Characteristic signals from pressure sensor ($P = 750 \text{ Torr}$)

The first impulse (Fig.9c) on the lower ray characterizes laser flash origination, the second – MW discharge initiation. On the second ray the pressure impulses with appropriate delays are observed.

So, the results of analysis of MW discharge structures and shock-sound effects registered under the different delays show that the most intensive interaction of MW discharge with laser plasma is observed in the first 5 - 25 mcs. Later on, the conditions for initiation hold out, but energetic interaction is decreasing abruptly. To our opinion, concentric MW channel observed at 10 – 20 mcs, most probably, is developing along the density gradient of the shock wave, propagating away from the laser spark. Its velocity at the distance of 10 mm from energy deposition zone comes to the value about 400 – 500 m/s, the wave having, naturally, the concentric shape. In [4] the shock wave development is optically monitored, its diameter at 20 mcs after laser breakdown being about 18 mm, what practically corresponds to our case. Evidently, the MW channel can not overcome the gasdynamic “wall” in shock wave and propagates along its front. In such a way MW channel visualizes shock wave, created by laser spark.

1.7. Interaction of MW radiation with UV laser flash

UV laser spark obtaining One of the possible ways of creation of plasma region without discharge is application of laser radiation of short wavelength, particularly near ultra-violet. For this purpose modernization of laser operation control scheme was carried out for optimization of laser radiation parameters on the 4th harmonics. At this stage the main task was obtaining of stable laser plasma sphere or spark on the 4th harmonics ($\lambda = 266$ nm). Operation with this harmonics demands permanent adjustment of the optic system, especially in the lack of temperature control of DKDP crystal, which doubles the light beam frequency. Direct measurement of UV energy in the 4th harmonics gave the value about 10 mJ. Thus, the transformation coefficient from the second to the fourth harmonics turned out to be approximately 10%. The obtained energy level let us obtain UV laser flash in air under the atmospheric pressure. The flash development is not accompanied by sound effects, the fact that evidences in favor of greater role of the multi-photon ionization.

Installation of rotatory mirror, the quartz vacuum input and the lens decreases the transformation efficiency to about 5%. Thus, about 3 – 5 mJ are delivered in the MW focal area.

Nevertheless, this level is sufficient to carry out experiments on MW discharge initiation in a wide range of air pressure. Such experiments for determination of MW discharge breakdown

thresholds with and without laser beam action were fulfilled. MW pulse duration was 9 mcs, repetition rate of pulses was 10 Hz. The obtained results are presented at Fig.10.

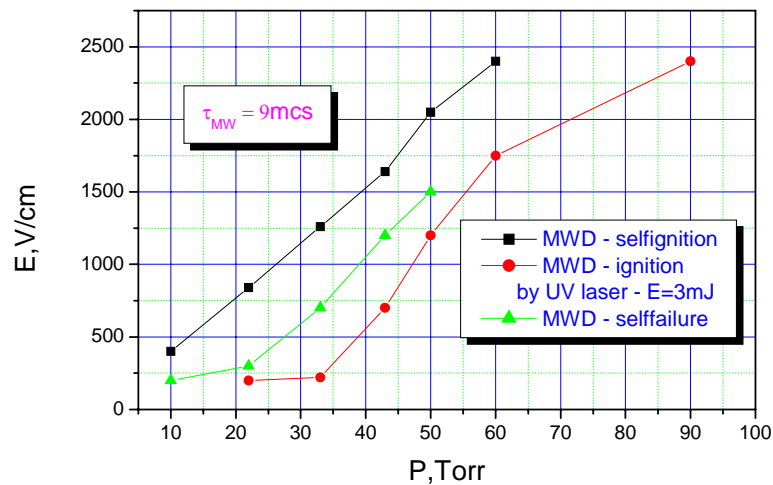


Fig.10. Dependence of air breakdown threshold by MW radiation

The method of breakdown threshold determination consisted in smooth increase of MW field level under the fixed air pressure until the moment of discharge splash origination. The last was registered by means of PMT and visually. At the presented graph the upper curve represents the breakdown threshold of self-ignited electrode less MW discharge in the focal area of vacuum chamber. Then, by slow decreasing of MW field (under the same pressure) the threshold of MW discharge switching off was fixed. These measurements are presented at the middle curve. And, finally, the bottom curve is obtained under the synchronous switching on the laser on the 4th harmonics with MW. In this case sufficient reduction of air MW breakdown threshold is detected. It should be noticed that the value of breakdown threshold was not practically changed when the focal area was illuminated by a mixture of 2nd and 4th harmonic. The total level of laser energy in this case was about 20 mJ. Therefore, MW discharge initiation is caused mainly by the UV component. The presence of laser beam lets obtain MW discharge under the higher pressures. In our case the discharge could be ignited up to 90 Torr. Besides, the laser beam lets create the discharge under the arbitrary delay of MW pulse relative laser one. It means that the discharge is formed under the initiating laser beam irradiation in any moment in diapason 100 ms.

1.8. Interaction of MW radiation with external plasma channel (HVS)

HV spark obtaining and description. The complex MW discharge structure observed on the pictures always consists of simple elements – the separate MW plasma channels. Comparative study of different types of electric discharges, which might be used as a model of the separate MW plasma channel, was undertaken.

For the HV spark creation the pulse magnet energy accumulator (field coil) was applied. The time of spark existence was not more than several microseconds. Energy deposition of this object turned out to be very close to the pulse MW energy and was about several Joules.

Let us briefly describe the spark dynamics. The threshold has two-time stage at rising voltage period on the coil. At first we fix the weak “forerunner” (precursor) - channel ($\tau \sim 0.2 - 0.4$ mcs), which grows from lower zero electrode (earth) on high voltage electrode with velocity about $\sim (2 - 4) \times 10^6$ cm/s. At the second stage the channel propagates from anode to the earth ($\tau \sim 0.4 - 0.8$ mcs) electrode with velocity of order smaller - 10^5 cm/s. The channel lighting level at the second stage is greater on $\sim 30\%$ and its existing time increases in two times. When we placed the magnet near the channel, the existence time of “forerunner” increased up to 2 – 5 mcs and the lighting time of the main channel – up to 10 – 15 mcs. So, the magnet permits to increase the plasma existing time and probably the energy deposition level.

The process in MW and spark discharges are very similar and some discharge properties one may study with using high voltage spark.

Interaction of MWD with external plasma channel. One of the most important tasks of our study is investigation of the MWD initiation possibility by external plasma source. For this purpose the HV spark seems to be suitable and flexible object. One may easily control the direction of the spark channel with respect to wave polarization, transverse to it (or along MW beam propagating direction and so on) for achievement the demanding discharge size or energy deposition in plasma area. We try to define experimentally the approach to this problem.

Already the first experiments [3] with channel oriented along vector E have demonstrated interesting results. The interaction processes demonstrate the MWD structure changing and the channel deflection from its straight propagating line. The channel brightness is decreased at MW field. MWD propagates along and across of the channel. The channels are strongly bending in the supersonic flow and obviously are interacting with microwave.

The experiments had shown the importance of MW pulse-channel moment of interaction. Its trajectory most likely presents the force electric line of convergent wave when interaction takes place at the early channel evolution phase. Moreover, discharge develops along vertical spark – it does not propagate along the radiation axes. On our opinion we've selected the flexible model object - the pulse air spark, which is very similar to the separate MW plasma channel and may be used for its study in some cases.

We've also continued the experiments with horizontal plasma channel oriented along MW beam propagating direction. The electrodes were placed in the focal area in vacuum chamber. Distances between them were about 4cm and experiments were performed at different air pressures.

The main interaction distinctions are also the channel color and transverse size change and MWD movement along the channel. These facts permit us to contend that external plasma channel as a conducting line serves for increasing MWD size from one side and for changing energy deposition at a defined area from another side. Obviously, the quantitative data are very important for such processes understanding.

So, for the first time the effect of very strong interaction of free microwaves with an external longitudinal and cross plasma channel is revealed. This effect may be of importance both for practical use and/or as fundamental trend for further research [5].

Triggering of HV spark by MW pulse. The possibility of triggering of high-voltage spark by MW discharge was investigated in air in the pressure range 200 – 760 Torr. Electrodes were installed along MW radiation axis (chamber axis) at no-breakdown separation distance. One of the electrodes, which was placed in the focal region, also served as MW discharge initiator. The second electrode was displaced at 6 – 3 cm from the first one either in the region of MW beam convergence (in front of focus), or divergence (after the focus). Slender electrodes (1 cm diameter) were oriented perpendicularly to the electric field vector of electromagnetic wave and did not disturb the MW field structure in the focal region.

MW discharged structure changed from sinusoidal to linear and sometimes MW channels are swirling around the main one. The thin (~ 0.5 mm) MW channel smoothly turns into the air spark ($\varnothing \sim 2$ mm). The additional single cross MW channels also appear along the main one. The air spark develops better at the increasing high voltage stage. If the delay of MW pulse relative to maximal (~30 kV) voltage level exceed ~30 mcs the HVS does not evolve.

Below the results obtained under 200 Torr air pressure are presented. In the first series the high-voltage electrode was placed in the MW beam focus, whereas the second (grounded) one – in the convergent beam closer to the radiation source. The characteristic picture of initiated DC spark interaction with MW discharge is presented at photo Fig.11a.

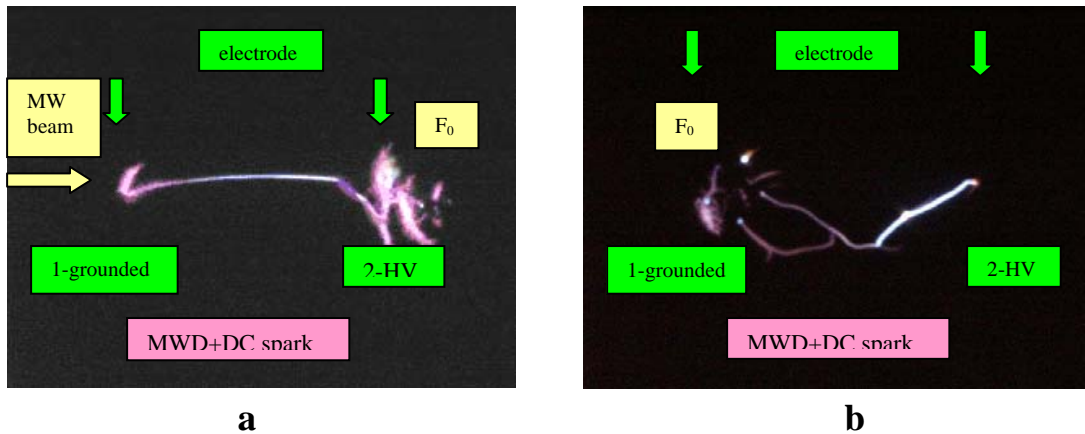


Fig.11. Triggering of high-voltage spark by MW discharge ($P = 200$ Torr)

It is seen that the spark is shorted out from the both ends via MW channels elongated in parallel to beam/DC field axis. These MW channels increase the effective DC channel length for breakdown occurrence. As a rule, thin MW channels smoothly conjunct with DC spark channel, another part of them elongating without shortening up to $l \sim \lambda$ along the DC spark. Transformation of MW channel in DC one takes place continuously, the fact which is well seen from changing of channel coloring from pink (MW) to white-blue (DC spark).

In the next series of experiments the second (grounded) electrode was installed in the region of MW beam divergence (i.e. in the direction away from radiating source). The separation distance between electrodes was kept the same – 6 cm. New peculiarities of MW – DC interaction appeared in this case. In this way MW discharge is consolidated near the high-voltage electrode and weakly interacts with DC spark.

The picture of interaction radically changes when high-voltage was applied on remote electrode, whereas the “focal” one was grounded (Fig.11.b). MW discharge changed its nominal propagation direction – now in the direction of wave vector towards high-voltage electrode. The solitary MW channels became straight and oriented along the DC spark channel, also their branching radically diminished. Typical periodic MW discharge structure is transformed in linear one. Thus, by imposing of an external electric field one can control the process of stimulated MW

discharge formation and even to force it propagate in the opposite direction – away from the MW radiating source.

1.9. Investigation of HVS triggering by means of LS

Experiments were aimed at HV spark triggering by laser spark creation and control of its propagation path. For this, laser spark was created between ring electrodes in the area of DC spark propagation. Laser spark dimensions were 5 mm × 3 mm, electrodes separation was 28 mm and they were placed coaxially with laser beam direction. Laser spark could be obtained at any point between electrodes by means of short-focus lens ($f \sim 4 - 10$ cm).

Experiments have shown that DC channel was triggered stably by laser spark, which originated near high-voltage electrode at a distance up to 12 mm from it. Synchronization between DC voltage supply and laser pulse was attained by change of time delay of laser burst relative high-voltage impulse. We tried to obtain stable DC channel initiation when DC high-voltage amplitude reached 26 – 30 kV. Oscillograms of pre-breakdown regime and joint DC-laser breakdown regime are registered. Photos (from two orthogonal projections) of joint DC-laser breakdown are shown at Fig.12. (left photos).

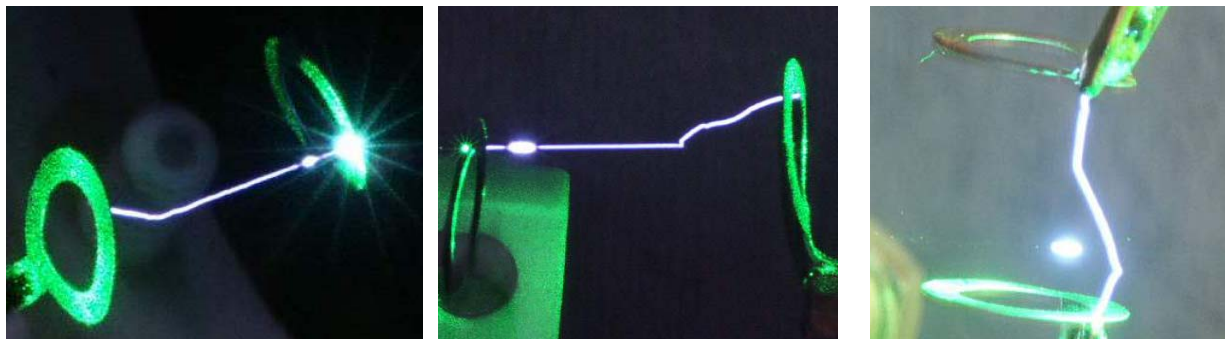


Fig.12.. DC channel triggering and directing by laser spark ($P = 750$ Torr)

It is necessary to mention that under the atmospheric pressure and voltage applied the breakdown between electrodes at 28 mm separation never occurs. Exactly laser spark triggers the span breakdown. The channel of high-voltage breakdown necessarily bridges the electrodes via laser spark domain, propagating in-line up to $2/3$ of separation distance along the laser beam path (Fig.12, left photos).

In the case of transversal electrodes positioning relatively laser beam the initiation occurs unstably and separation distance was diminished in about 2 times. However, DC breakdown and

laser spark are developing as two independent objects and DC channel is bending round the laser spark (Fig.12, right photo).

Thus, orientation of laser beam propagation relative the direction of DC breakdown is an effective factor in DC breakdown triggering in spite of not so evident asymmetry of laser spark dimensions.

Conclusions

So, the main results over the current period are as following:

- For the first time the stable electrodeless MW discharge initiated by laser spark different orientation relatively electric field of MW wave in wide range of air pressure is realized;
- Experiments are carried out under all principle geometries of interaction of MW and laser beams. Laser spark effectively initiates MW discharge, as well as laser beam without spark production;
- The MW breakdown threshold under the presence of laser beam is visibly less that for self-ignition and in some cases even less that for its extinction. Sufficient decrease of MW breakdown level is observed under the laser spark origination;
- In the mode of transversal beams the stable initiation of MW discharge by focused UV laser radiation is obtained. In experiments sufficient decrease of MW discharge initiation threshold was detected in the case of UV laser beam irradiation of the MW focal area;
- MW discharge structures development along the laser beam and across MW beam is revealed (directional effect);
- The ability of igniting of MW discharge during the long period between initiating pulses (up to 100 ms) but under the elevated MW power is fixed;
- It is shown that interaction of MW radiation with laser plasma is most effective under the small delays of MW pulse relative laser one; as a result amplification of pressure and sound from the discharge region is detected;
- For the first time the effect of very strong interaction of free microwaves with an external plasma channel, created by pulse air spark is revealed;
- The ability of HV spark triggering by stimulated MW discharge is shown;
- Experiment has demonstrated efficiency of DC channel initiation and directing by laser spark

References to Section 1

1. Physics and Chemistry of MW Laser-Induced Discharge in Gas Flows and Plasma Jets, 2005, 1st Quarter Report, Partner Project 3058p
2. Ageev V.P., Burdin S.G., Goncharov I.N. et al. "Interaction of powerful laser radiation with solid bodies in gases". Radiotekhnika. (Itogi nauki i tekhniki VINITI). M., 1983, p.143 (in Russian)
3. V.G. Brovkin, S.A. Afanas'ev, D.V. Khmara, and Yu.F. Kolesnichenko. Experimental Investigation of Combined Laser-DC-MW Discharges (AIAA 2006-1459). 44th AIAA Aerospace Sciences Meeting & Exhibit, Reno, NV, 9-12 January, 2006
4. N.Glumac, G.Elliott, and M.Boguszko Temporal and Spatial Evolution of the Thermal Structure of a Laser Spark in Air. 43rd AIAA Aerospace Meeting and Exhibit, AIAA Paper 2005-204.
5. Yu.F. Kolesnichenko, V.G. Brovkin, S.A. Afanas'ev, D.V. Khmara, V.A. Optimization of Laser-Pulse-Controlled MW Energy Deposition. AIAA paper 2007-1228. 45th AIAA Aerospace Sciences Meeting & Exhibit, Reno, NV, 8-11 January, 2007

Section 2. Kinetic modeling of MW interaction with laser-created plasmas

Recent research on microwave energy deposition in air has emphasized its potential for aerodynamic flow control. In particular, microwave plasmoids have been demonstrated experimentally to achieve drag reduction of extraordinary efficiency in supersonic flow past blunt bodies [1, 2]. Perfect gas simulations [3] of the interaction of a thin elongated “density well” (i.e., the thin filament formed within the microwave plasmoid) with a blunt body in supersonic flow have confirmed the principal effect to be thermal. However, a more detailed real gas model is needed for two reasons. First, the timescales for the relaxation of the gas species following the microwave pulse range from the order of the pulse duration ($\tau \sim 1 \mu\text{s}$) to the flow convection time ($\tau \sim 10 \mu\text{s}$). Second, the microwave filament locations are somewhat random. In the meantime the drag reduction efficiency is strongly dependent on the orientation of the filament with respect to the blunt body shock: a filament elongated in the direction of the flow and aligned with the axis of the body yields the largest drag reduction.

Several factors for MW breakdown stimulating at a defined point are effective – elevated number of initial electrons, diminishing of a local neutral gas density, presence of detaching agents like atomic or metastable electronically excited molecular oxygen, for example. Also very effective is local intensification of the applied electric field on some initiator. In principle, all these factors can be realized by laser energy release in a defined spatial domain.

The created laser plasma can be either *thermal* or *non-thermal* depending on the regime of laser beam coupling with a gas. The thermal mechanism is realized during avalanche multiplication of electrons in laser radiation field and leads to thermal plasma in the domain of laser breakdown. The non-thermal mechanism is a result of direct multi-photon ionization. Ultimately the guiding parameter, which defines the resultant plasma characteristics, is laser pulse duration. If laser pulse is long enough (usually of nanosecond scale), then the avalanche mechanism is realized and the applied electric field intensity necessary for the breakdown can be relatively low. Nevertheless, the total energy of such pulse is rather high, as well as energy concentration in breakdown domain, the factors, leading to creation of near-equilibrium plasma with very high temperature and electron concentration/ conductivity. Such plasma is decaying relatively slow – of order of milliseconds and longer. In this case initiating ability of laser spark

can hold out in some time interval and MW field can be applied in wide range of delay relative initiating laser.

For a short pulses (sub-nanosecond) the avalanche mechanism is no longer applicable and only direct multi-photon ionization is coming to the forefront. The shorter the pulse is, the higher radiation intensity is necessary for breakdown, however, the total energy of a pulse can be reduced greatly. This is quite similar to MW breakdown, when rising of field amplitude leads to abrupt shortening of the breakdown pulse duration, so the energy in pulse goes down fast. Besides, the increase of laser field intensity results in appearance of new non-linear effects. For visible and UV range of wavelength this new physics becomes apparent for picosecond and sub-picosecond (femtosecond) pulse duration. One of the most exciting findings of the last 10 years is non-linear effect of filamentation in laser beam of femtosecond duration – “transmission without diffraction” [4,5]. A balance among the beam self-focusing due to the optical Kerr effect, the beam diffraction, and the defocusing effect due to gas ionization can explain this self-guided propagation or filamentation. Under the atmospheric conditions laser pulse in its propagation leaves behind plasma filament of 100 μ m in diameter with electron concentration $\sim 10^{16}\text{cm}^{-3}$. The pulse in UV spectral region with energy budget 0.2mJ can propagate in such regime over meters with energy loss about 40 μ J/m [5]. Evidently, laser beam wavelength is of great importance – the shorter wavelength is, the easier multi-photon ionization takes place. Thus, UV radiation is more effective than visible or IR. The plasma produced by intense laser beam of short pulse duration is cold, non-equilibrium, of moderate conductivity. Such plasma is decaying very fast – of order of nanoseconds or faster. In this case MW pulse should be imposed practically simultaneously with initiating laser one.

This brief survey demonstrates the variety of initial conditions for MW discharge initiation by laser pulse. Thus, it is important to quantify plasma parameters under laser beam action, as well as their evolution in space and time to find out the best conditions for MW field imposing.

2.1. Kinetic modeling of MW interaction with decaying laser spark under various ambient pressures (thermal mode)

The aim of kinetic modeling is in evaluation of conditions for MW discharge origination during MW interaction with decaying laser spark (LS). The conditions are in determination of the time range when residual electron concentration n_e and medium density N make the plasma domain a

transparent one for external MW irradiation (“time window” of transparency). The factors of electron concentration and medium density are a competitive ones during LS decay: from the one hand the LS domain become more and more transparent one when n_e fallings down, on the other hand, medium density N grows due to isobaric collapse of cooling LS domain.

The criterion of the best conditions for MW discharge origination on decaying LS is the minimal necessary MW power density for launching of ionization avalanche is performed under various ambient pressures.

The problem is divided into two successive tasks: the modeling of laser spark decay and modeling of MW interaction with decaying laser spark. At that the final medium composition of decaying LS is an initial one for discharge stage.

2.1.1. Modeling of the laser spark decay and determination of transparency time “windows” under various pressures

Kinetic calculations were performed for 100-750 Tor pressure range for spherical shape of LS. Because of laser plasma is extremely hot it was assumed that initially thermodynamic equilibrium composition of the medium takes place. During spark decay the temperature is changed according the measurements [6, 7] Fig.2.1.1a,b and isobaric compression of the medium occurs according the temperature decreasing.

The temperature of 16000 K, marked in Fig.2.1.1a, was taken as an initial one for atmospheric pressure. It was accepted that during LS decay under other pressures the character (profile) of the temperature change is the same that in Fig.2.1.1a. The measurements of LS domain cooling at various pressures were performed in [7] (Fig.2.1.1b). The measurements show that at high pressures (> 300 Tor) and at decay times > 150 ns the absolute values and the character of temperature decrease are the same (in the limits of 10% experimental uncertainty) for all pressures. On this reason the plasma cooling dynamics was taken as in Fig.2.1.1a - for pressures > 300 Tor, but re-normalized according Fig.2.1.1b - for the pressure 100 Tor. The temperature at 1 mcs decay time (marked in Fig.2.1.1a) was taken as an initial one (“zero time moment”). For pressures > 300 Tor it is 16000 K, for 100 Tor – ≈ 14000 K. The initial composition of the medium was taken as thermodynamic equilibrium one for corresponding initial temperature. The isobaric conditions were accepted for LS domain during decay stage and following MW discharge stage.

For kinetic modeling performing the code described in [8] was used. Kinetic mechanism of discharge in air includes 762 reactions among 43 species (atoms, molecules, ions, excited states).

The results of kinetic calculation of LS decay are shown in Fig.2.1.2-4, where dynamics of charged, neutral and electronically excited particles is presented for the pressures 750 and 100 Tor. As one can see all processes become slower with pressure decreasing.

During the early stage of the spark decay the medium is practically totally ionized with domination of atomic ions. At that, two kinds of reactions determinate the decay of electron concentration:

the three-body reactions of electron-ion recombination



(A = N, O), which reproduce neutral atoms in various excited states.

At the same time electron-ion recombination starts opposite family of associative ionization reactions of electrons and ions NO^+ production:



where N and O the atoms both in the ground and in excited electron state. So, electron concentration decay at early stage is a result of reactions (1) and (2) competition.

During electron concentration decay the significance of reactions (1) decreases. The efficiency of reactions (2) gradually decreases too, owing to both the cooling of the spark and the quenching of excited atoms. Because of realization of reaction (2) with participation of the ground states of N and O atoms has the threshold: of ≈ 2.8 eV, its efficiency rapidly decreases with decreases of the temperature. Other branches of these reactions - with participation of excited atoms - depend on the temperature weakly, but they demand rather high concentration of excited particles in order to be an effective ones.

At intermediate stage of spark decay the main channel of electron losses becomes the reaction of two-body dissociative recombination with molecular ions



$AB^+ = N_2^+, O_2^+, NO^+$ and during the growth of the medium density (as a result of isobaric compression) - the three body reactions



It attracts notice the ion composition of a decaying spark. The ion NO^+ turns out to be absolutely dominative, while the ions of the main air components are absent. The matter is in low ionization threshold of NO^+ formation. On this reason the reactions of NO^+ charge transfer during collisions with neutral particles (N, O, N_2 , O_2) have noticeable energy threshold of 4-5 eV, what hinders for other positive ions formation. At that the complex and cluster ions (N_4^+ , $N_2O_2^+$, O_4^+ , O_4^- and so on), typical for discharge development in “cold” air and dense mediums, are absent.

At the latest stage of spark decay the medium becomes an ordinary air but with some content of NO.

During LS decay the conductivity of plasma domain decreases as $\sigma = n_e(\tau) \times \frac{e^2}{m} \times \frac{v_e}{v_e^2 + \omega^2}$ e, m – the charge and mass of electron, $n_e(\tau)$ – current electron concentration, ω - the circular frequency of MW field ($\omega = 2\pi f$, $f = 13$ GHz), v_e , - the frequency of electron collisions $v_e = \sum_i K_i \times N_i$, where $K_i(T_e)$ is the rate constant of electron-neutral collisions is depended on electron temperature, which equals the gas temperature, N_i is the current particles density, $i = N, O, NO, N_2, O_2$. Rate constants were calculated in Maxwellian approach of electron energy distribution. Thus, conductivity of decaying plasma depends on electron concentration and gas density. The magnitude E_0 of incident MW field suffers depolarization reduction and drops inside the plasma domain to the value of

$$E_{local} = \frac{E_0}{\sqrt{1 + \left(q \times \frac{4\pi\sigma}{\omega} \right)^2}}, \quad (5)$$

q – the factor of polarization reduction (for spherical shape of LS $q = 1/3$). Additional reduction of actual local field is connected with its wave nature, when with the change of particles concentration the relation $\frac{v_e}{\omega}$ changes too, what influences on actual field according multiplier

$\frac{v_e}{\sqrt{v_e^2 + \omega^2}}$. At that both the local field and local density are the variable quantities and exactly

their relation $\left(\frac{E}{N}\right)_{\text{local}}$ determinates all plasma processes with participation of electrons. The

relation $\eta = \frac{(E/N)_{\text{local}}}{E_0/N_0}$ one can determinate as a degree of the LS domain transparency for

incident wave (N_0 – the density of ambient medium). Based on above expressions η is equal to

$$\frac{N_0}{N_{\text{local}}} \times \left[1 + \left(q \times \frac{4\pi\sigma}{\omega} \right)^2 \right]^{-1/2}. \text{ The dependencies of LS domain transparency } (\eta) \text{ during LS decay}$$

are presented in Fig.2.1.5. As it is seen, during decreasing of medium pressure from 750 down to 100 Tor the maximum of transparency increases in five times from about 8 up to 40. At that this maximum shifts towards the later times.

2.1.2. Interaction of MW with decaying laser spark

The modeling of MW interaction with decaying laser spark was performed for the fixed pulse duration of 10 mcs. At that delay times of MW impact on decaying LS were corresponded to maximum of LS transparency for all ambient pressures. Initial medium compositions were varied in dependence on the ambient pressure. The partial contents of the main species for mentioned delays are collected in Table 1. As it is visible from the Table, at low ambient pressure LS domain consists of atoms mainly in spite of comparatively low temperature and large delay times. The reason is in strong deceleration of three-body reactions of atoms recombination into molecules because of low density. At high pressures the medium is a mixture of N_2 and O_2 .

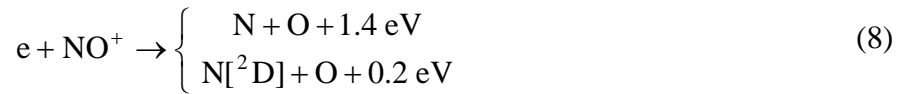
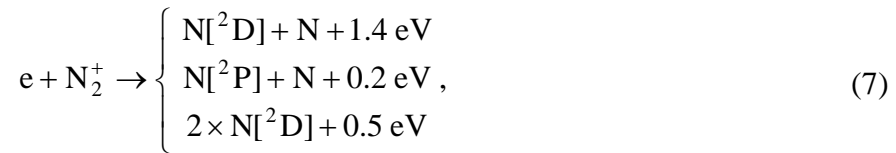
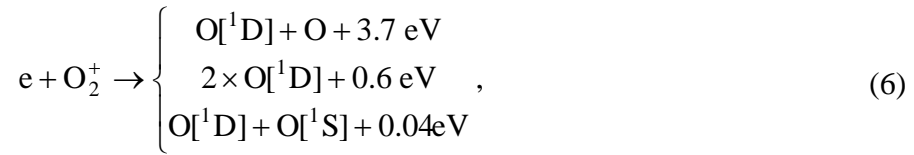
Table 1. Initial conditions and medium composition for various pressures

Pressure, Tor	Density, cm^{-3}	n_e, cm^{-3}	T_g, K	Medium composition, %			
				N^*	O^*	N_2	O_2
100	5.8×10^{17}	2.0×10^{11}	1630	59	26	15	0
300	1.6×10^{18}	6.0×10^{11}	1990	18	34	48	0
500	2.4×10^{18}	8.4×10^{11}	2210	0	36	62	0
750	3.0×10^{18}	1.1×10^{12}	2660	0	34	64	2

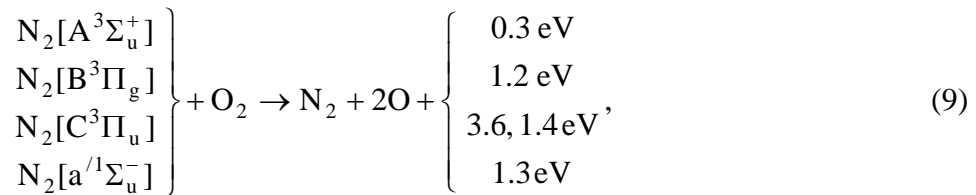
* including electronically excited states

The medium composition (first of all, the relation of O/O₂) influences energy spectra of electrons in plasma and, as a result, the rate constants of electron-neutral collisions (excitation, ionization, dissociation, and attachment) [9]. On this reason field-depended rate constants of electron-neutral reactions were calculated for each medium composition from Table 1 and then were applied for the specific medium.

The kinetic mechanisms of medium heating during MW pulse were in details described in [10]. Such are rotational heating, recombination heating:



and the heating during collisional quenching of excited atoms and molecules (in dependence of medium composition):



The example of n_e and gas temperature dynamics is in Fig.2.1.6. During MW pulse gas temperature grows up to 5000 K. The resumptive data is summarized in Fig.2.1.7, where the dependencies of pressure of maximal transparency, its approach time during LS decay and minimal MW power density needed for ionization avalanche start are given. Comparatively weak dependence of power density at low pressure is a result of the two competing factors:

- 1) the medium is practically an atomic one, which enriches high energy spectra of electrons and thereby accelerates high threshold processes, first of all – ionization;

2) at the same time the relation $\frac{V_e}{\omega}$ at low densities becomes the most unfavorable one ($\ll 1$) and the additional local field reduction takes place, which compensates strong growth of transparency with decreasing of ambient pressure.

2.1.3. The influence of LS shape factor on filament origination conditions

In the context of LS thermal mode consideration the influence of LS shape factor was investigated. Laser spark was assumed as an elongated one. In case of a spherical shape of LS the factor of polarization reduction q is $1/3$, for a stretched along E direction – it is in six times less.

The LS decay features, which forms initial conditions for MW interaction stage was the same that in paragraph 2.1.1. Initial concentrations and temperatures were taken from Table 1.

The dynamics of n_e and gas temperature are in Figs.2.1.8 and 2.1.9. At it is visible power density needed for filament origination during MW interaction with *elongated* laser spark is about hundreds W/cm^2 at the ambient pressure of 100 Torr, and rises to about $10 kW/cm^2$ at 750 Torr.

2.2. Kinetic model of MW interaction with ultra-short pulse laser filament (non-equilibrium mode)

Specific features of such laser spark are: high electron concentration ($\sim 10^{15} cm^{-3}$) at low gas temperature (of order of room one).

The interaction of MW laser spark was considered for air at the pressures $P = 70-750$ Torr under isobaric conditions and incident MW reduced field $E_0/N = 80-120$ Td. The mechanisms of incident field reduction and kinetic mechanism of heating were the same that in paragraphs 2.1.1 and 2.1.2. Initial medium composition was accepted as 78% N_2 , 22% O_2 , $n_e = O_2^+ = 10^{15} cm^{-3}$, gas temperature was 300 K. The polarization factor q for thin long spark was estimated in [11] and comes to ≈ 0.003 .

2.2.1. Results of kinetic modeling

The dynamics of significant particles concentration for medium pressures 750 and 70 Torr during rectangular MW pulse is shown in Fig.2.2.1, 2 correspondingly. At the beginning of the MW pulse partial recombination of electrons takes place. At that, electrons loses at low pressure

is connected with their recombination with simple ions N_2^+ , O_2^+ mainly, while at the high pressure the fast conversion of the simple ions into the complex ones N_4^+ , O_4^+ , $N_2O_2^+$ and others takes place. So, electron recombination happens more rapidly (at low pressure complex ions are presented as a traces because of the ions conversion in a three-body process). Moreover, at the high pressure three-body attachment of electrons to O_2 is visible. The presence of negative ion O_3^- at high pressure is the result of dissociative attachment of electrons to O_2 molecule with following fast conversion $O^- + O_2 + M \rightarrow O_3^- + M$. At low pressure such conversion is strongly slowed and ion O^- is presented in pure form.

The evolution of electron concentration, local reduced field and gas temperature in the paired Figs.2.2.3, 2.2.4 is shown. At the beginning of MW pulse fast heating of the medium happens. At the low pressure the main mechanism of heating is recombination one (6-8) during dissociative recombination (electron concentration remains rather high).

At the high pressures this mechanism at the beginning of the pulse is absent because of fast conversion of molecular ions into complex ones. At that the main mechanism of heating is the collisional quenching of nitrogen triplets and singlet during interactions with molecular oxygen (9). Later, during oxygen dissociation, the mechanism (10) is switch on.

Both in the low and high pressure fast heating leads to temperature growth up to 100-150 K, what entails fast growth of the local reduced field owing to isobaric expansion of plasma domain. The increasing of reduced field launches ionization avalanche and further heating. Under all pressures and at all incident E/N the dynamics of the local reduced field has more or less pronounced peak (Fig.2.3.5), which marks off the beginning of the field depolarization reduction. At later times, reduced field decreases, but the temperature continues growth owing to high concentration of excited and charged particles. At this stage the mechanism of recombination heating “switches on” and at the high pressure, because of the gas temperature is already sufficiently high (about 1000 K) and the complex ions breaks down. The growth of electron concentration decelerates. At this stage the additional channels of ionization – associative and stepped electron impact ionization appears.

The repeated increasing of reduced field under high pressure in spite of high conductivity of medium with a weak growth of electron concentration at the late times marks off the avalanche finish: the rate of medium expansion becomes approximately equals the rate of electrons production in the medium unit of volume. At that the temperature achieves 5000 K and greater.

Fig.2.2.6 in comparison with Fig.2.2.5 shows the common (at all incident E/N and pressures) character of electron concentration connection with the local reduced field. It is notable that at diminution of incident field the initial decreasing of electron concentration even more than more the medium pressure. The reason is in intensification of electron losses during their attachment to O₂: the rate of three-body attachment growth with decreasing of electron temperature.

All the aforesaid are right also for the reasonably larger polarization factors. Fig.2.2.7 demonstrates the same data that in Fig.2.2.3, but for $q = 0.01$ instead 0.003. As it is visible the bigger value of q leads only to deceleration of all processes.

It looks reasonable to accept the position of local reduced field peak in the time scale as a mark of ionization avalanche development. At the high pressures during this time electron concentration increases in about order of value from initial one. The dependencies of avalanche time as a function of pressure for various incident fields are in Fig.2.2.8. As it is seen, at low reduced fields the dependencies are non-monotones ones. Already mentioned influence of three-body attachment becomes apparent in delays of avalanche at high pressures.

One can estimate energy deposition in to plasma, which is needed for avalanche development. Fig.2.2.9 demonstrates dependencies of energy deposition for various pressures and incident fields. With increasing of reduced field the required energy deposition decreases: the higher E/N the higher rate of the fast (direct) ionization. The pressures around atmospheric one give infinite limit of three-body attachment rate (these reactions become a two body ones essentially). On this reason energy deposition weakly depends on the pressure. The increasing of energy deposition at the pressures less than ≈ 200 Torr is conditioned by decreasing of medium density and, as consequence, by increasing of avalanche time. The minimum energy deposition around 250 Torr is a result of optimal competition of the mentioned factors: medium density while it is not very small and tree-body reactions already slowed.

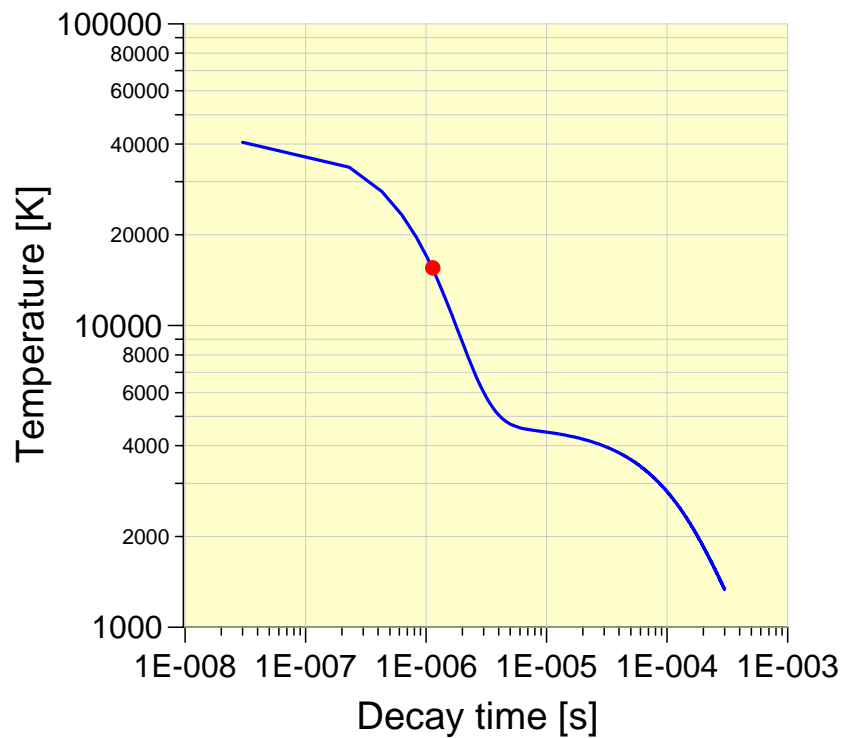


Fig.2.1.1a. Temperature dynamics during laser spark decay at the pressure of 750 Torr

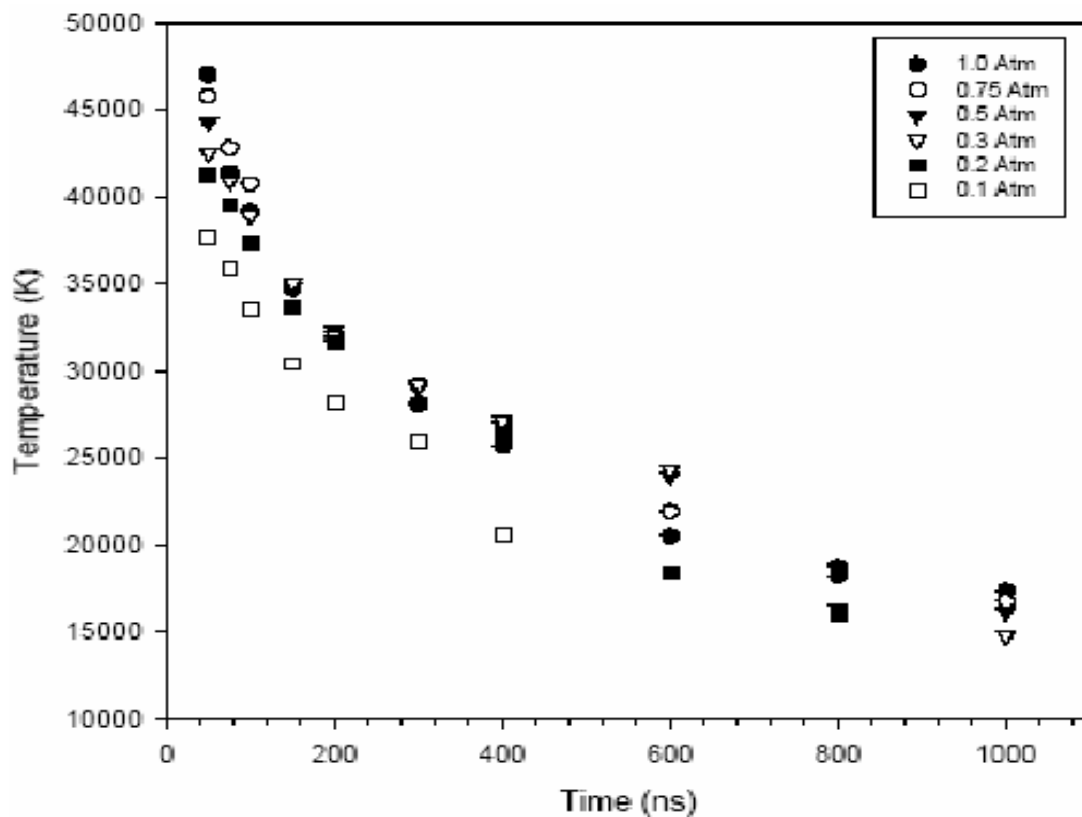


Fig.2.1.1b. Temperature dynamics during laser spark decay at various ambient pressures

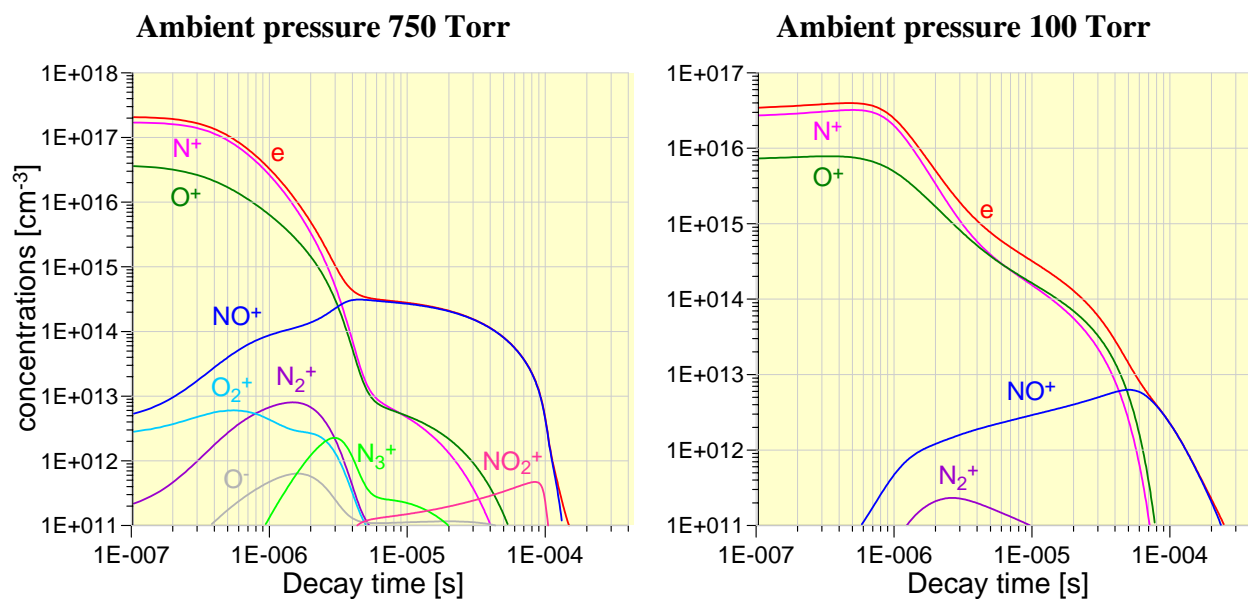


Fig.2.1.2. Dynamics of charged particles during decay of LS

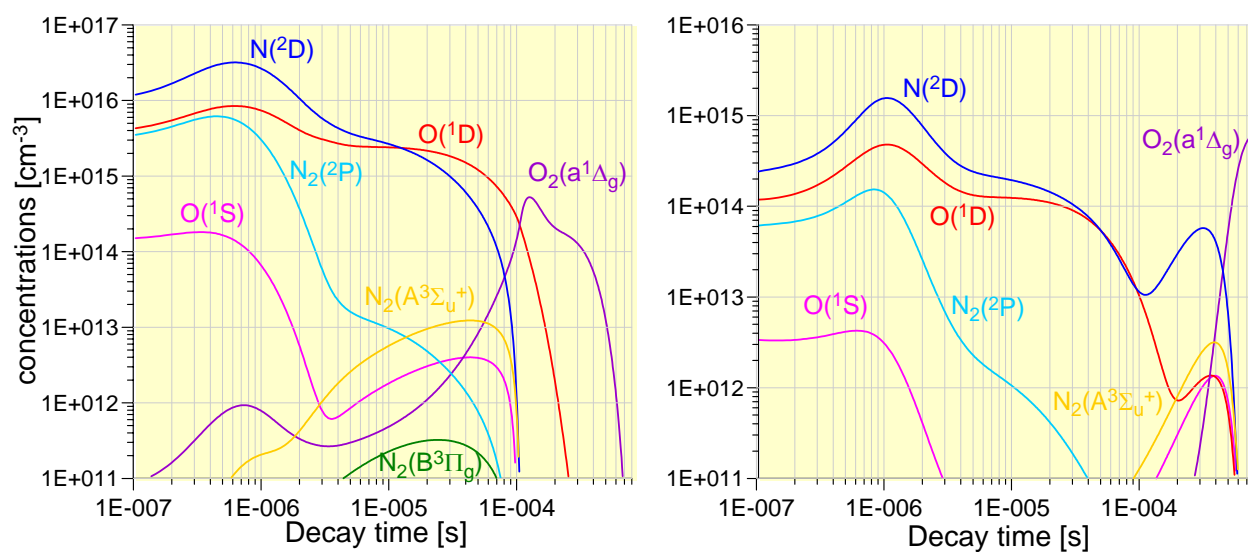


Fig.2.1.3. Dynamics of excited particles during decay of LS

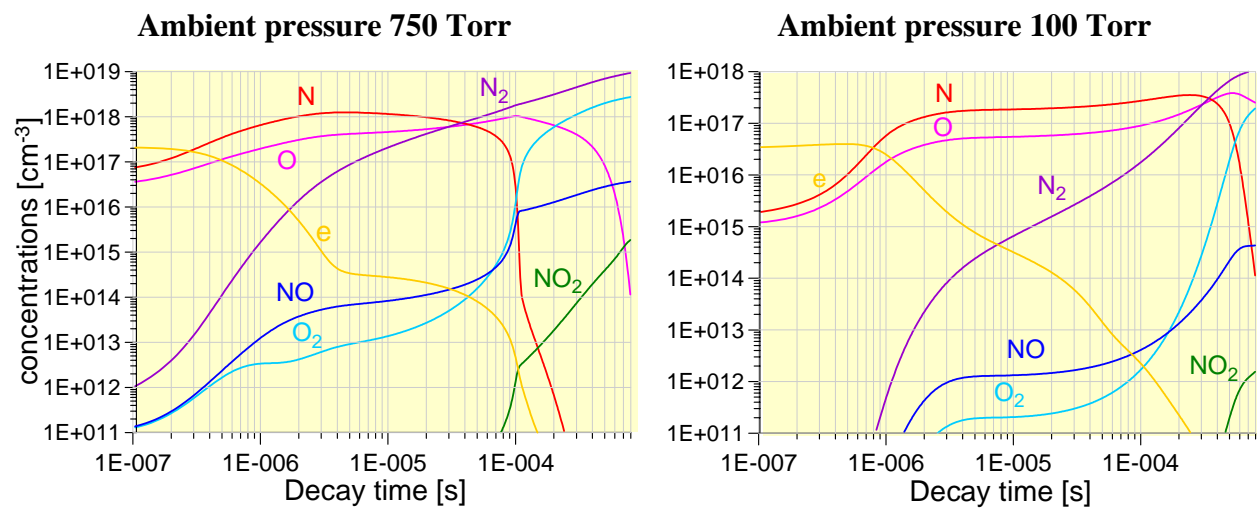
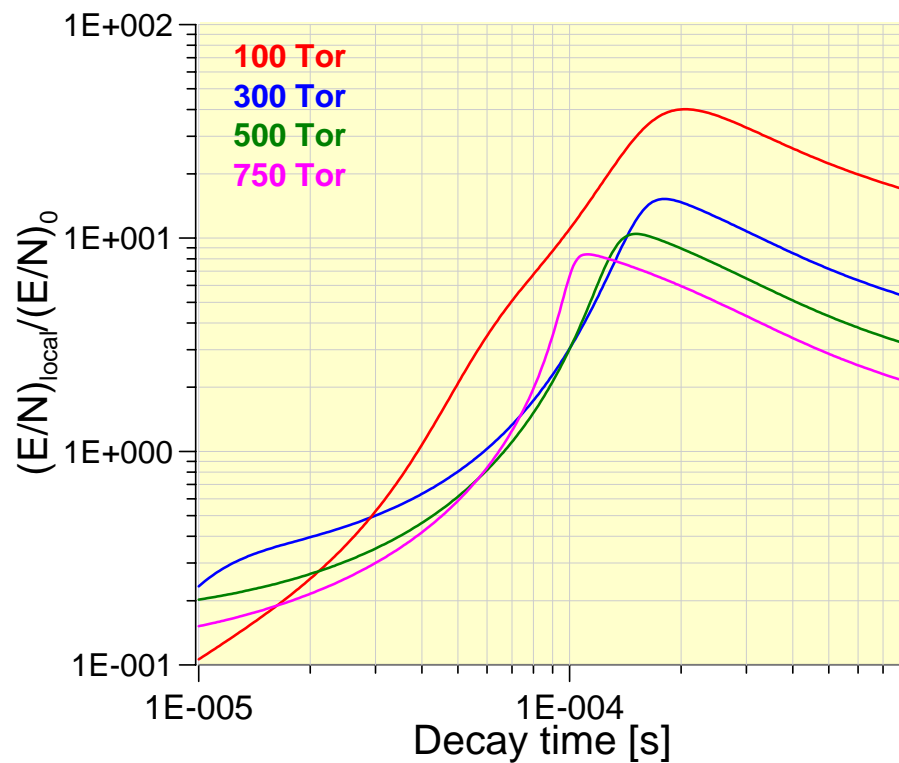


Fig.2.1.4. Dynamics of neutral particles during decay of LS

Fig.2.1.5. LS domain transparency (η) for various pressures

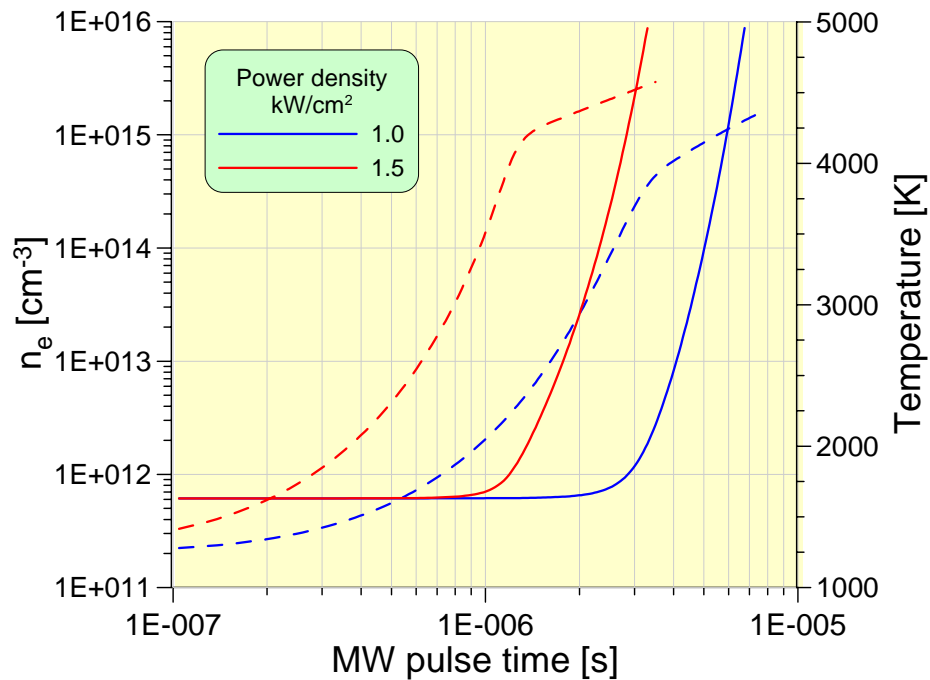


Fig.2.1.6. Dynamics of electron concentration and gas temperature during MW pulse with various power densities under ambient pressure 100 Torr: solid lines – temperature, dashed lines – electron concentration

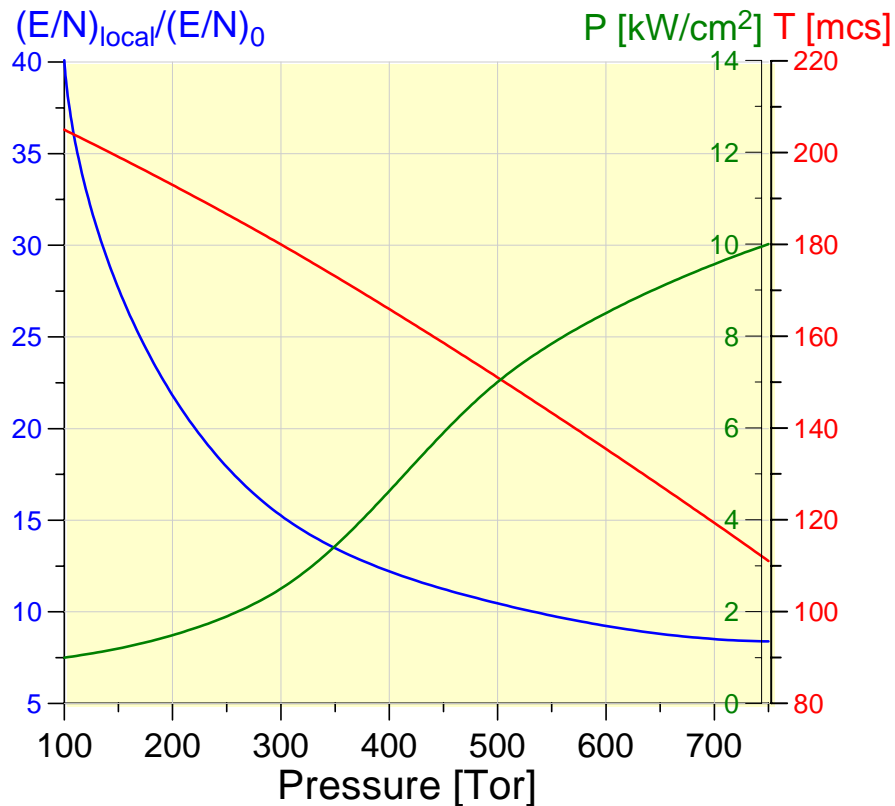


Fig.2.1.7. Maximal transparency of LS, its approach time during LS decay and minimal MW power density necessary for ionization avalanche start

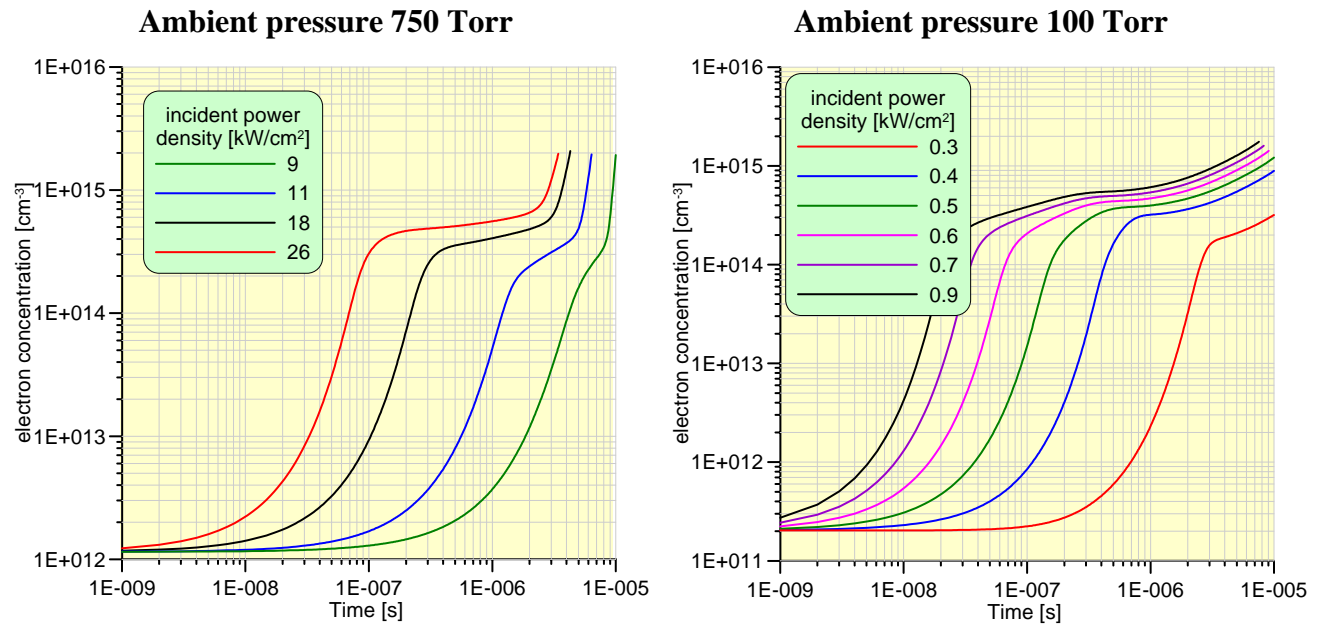


Fig.2.1.8. Dynamics of electron concentration at various incident MW power densities

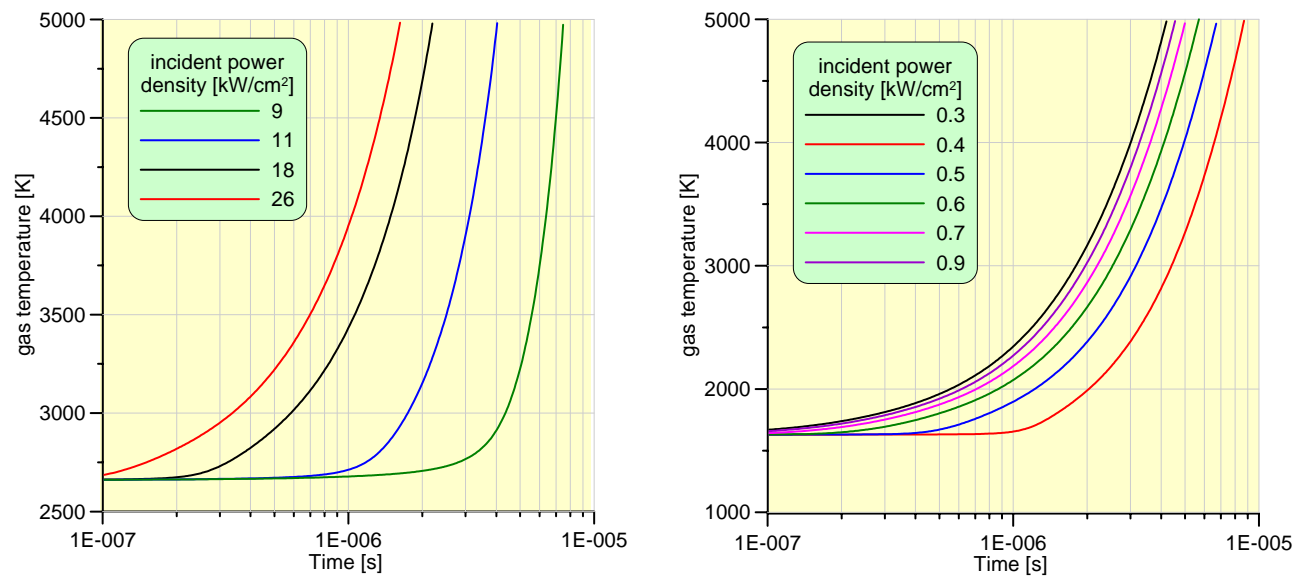


Fig.2.1.9. Dynamics of gas temperature at various incident MW power densities

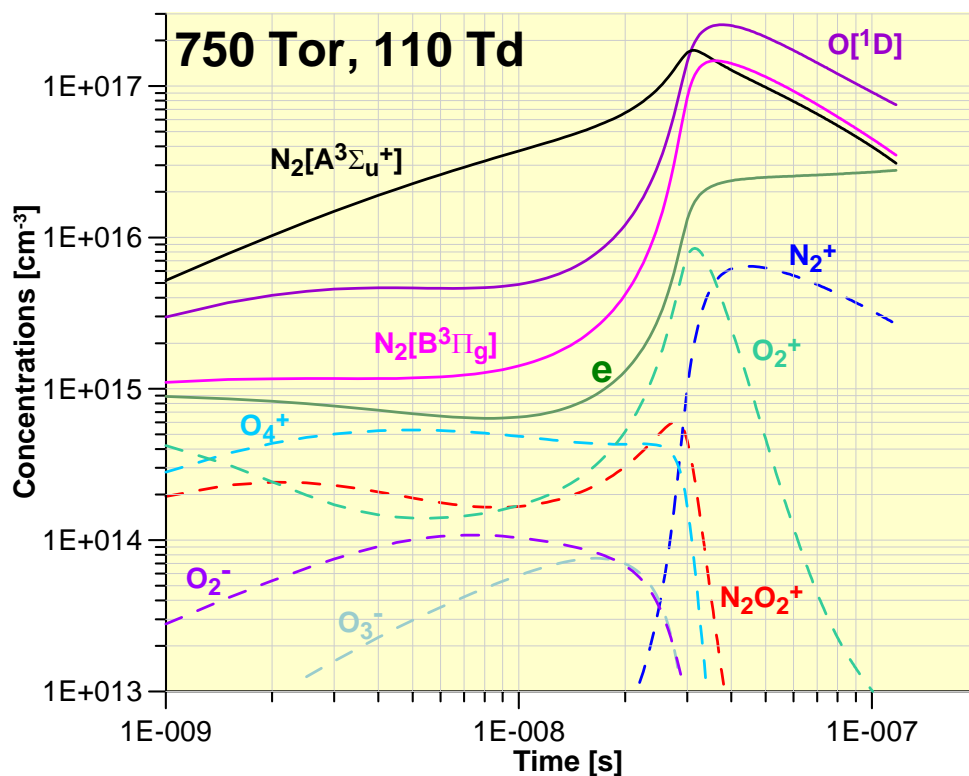


Fig.2.2.1. Dynamics of some excited and charged particles concentrations at $P = 750$ Torr, incident $E/N = 110\text{Td}$

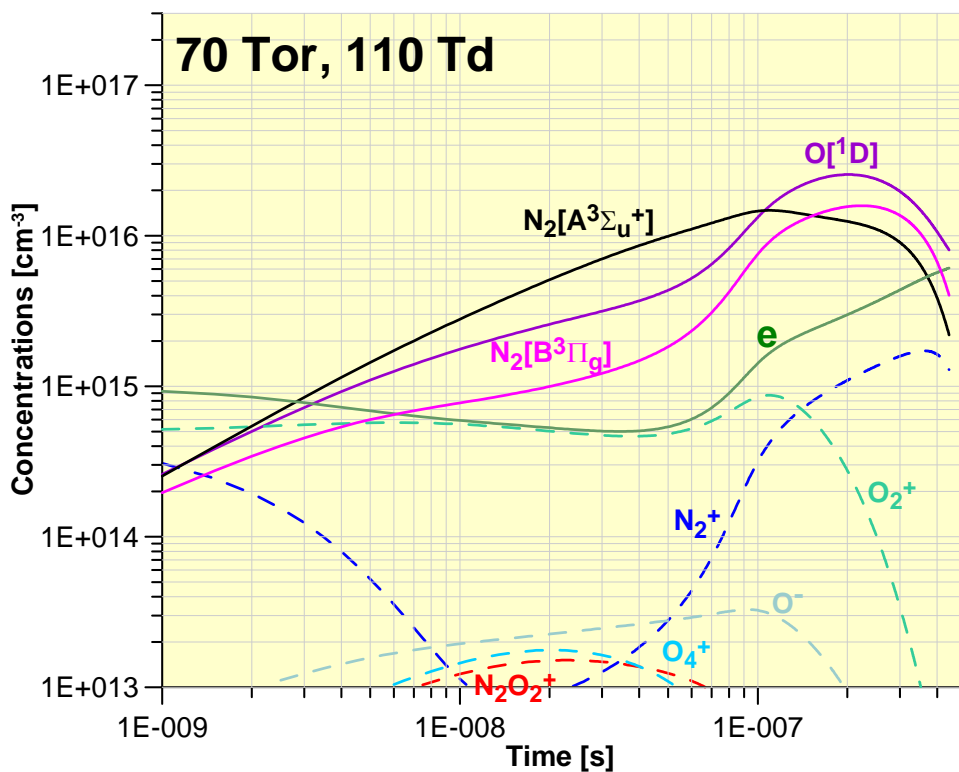


Fig.2.2.2. Dynamics of some excited and charged particles concentrations at $P = 70$ Torr, incident $E/N = 110\text{Td}$

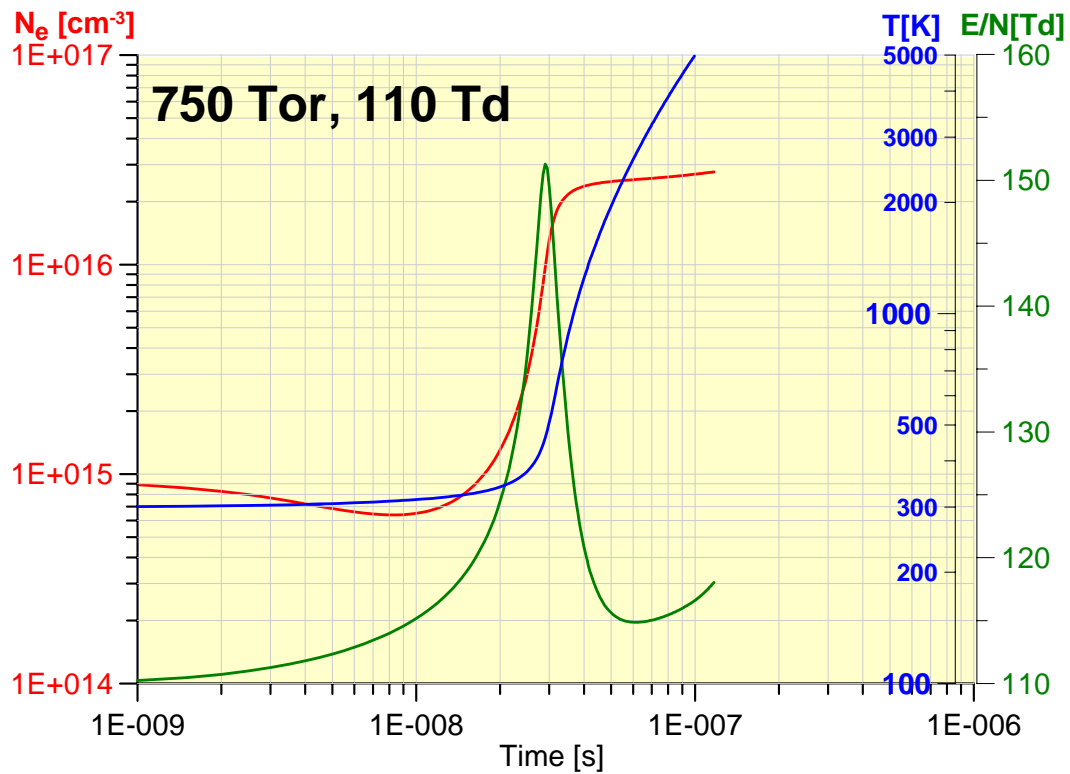


Fig.2.2.3. Dynamics of electron concentration, local reduced field and gas temperature at $P = 750$ Torr, incident $E/N = 110$ Td

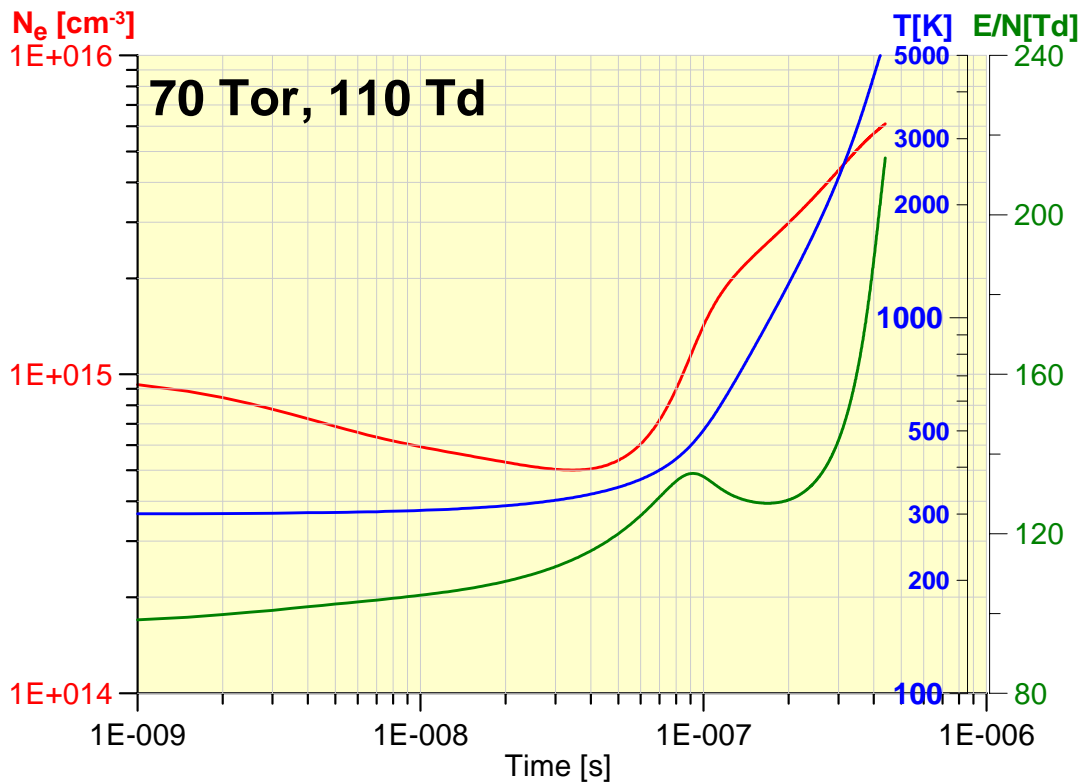


Fig.2.2.4. Dynamics of electron concentration, local reduced field and gas temperature at $P = 70$ Torr, incident $E/N = 110$ Td

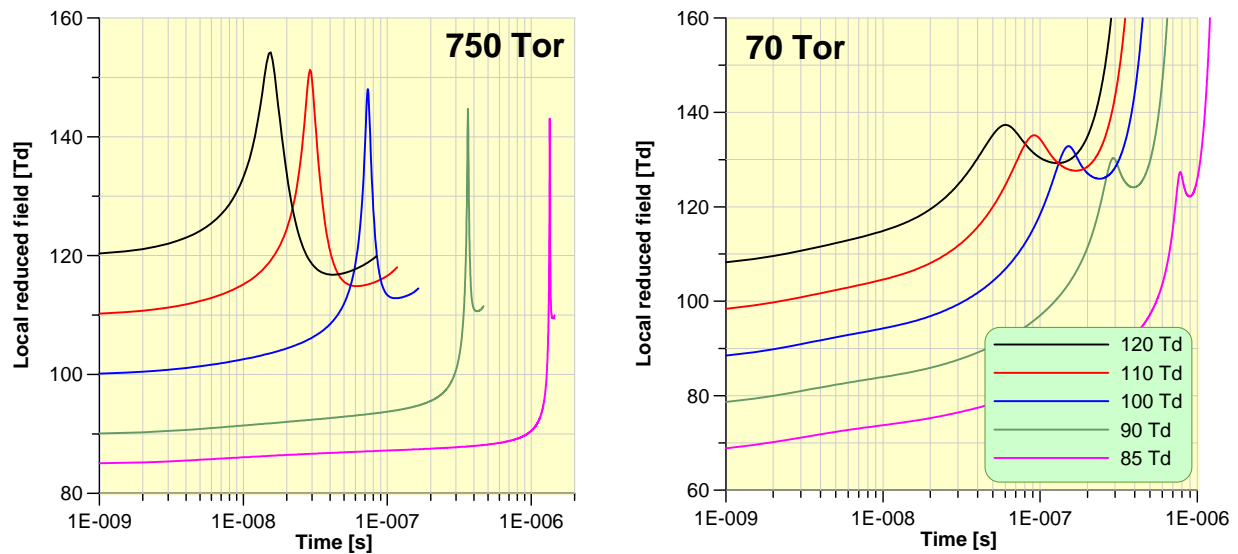


Fig.2.2.5. Dynamics of local reduced field various incident fields under the pressures 750 and 70 Torr

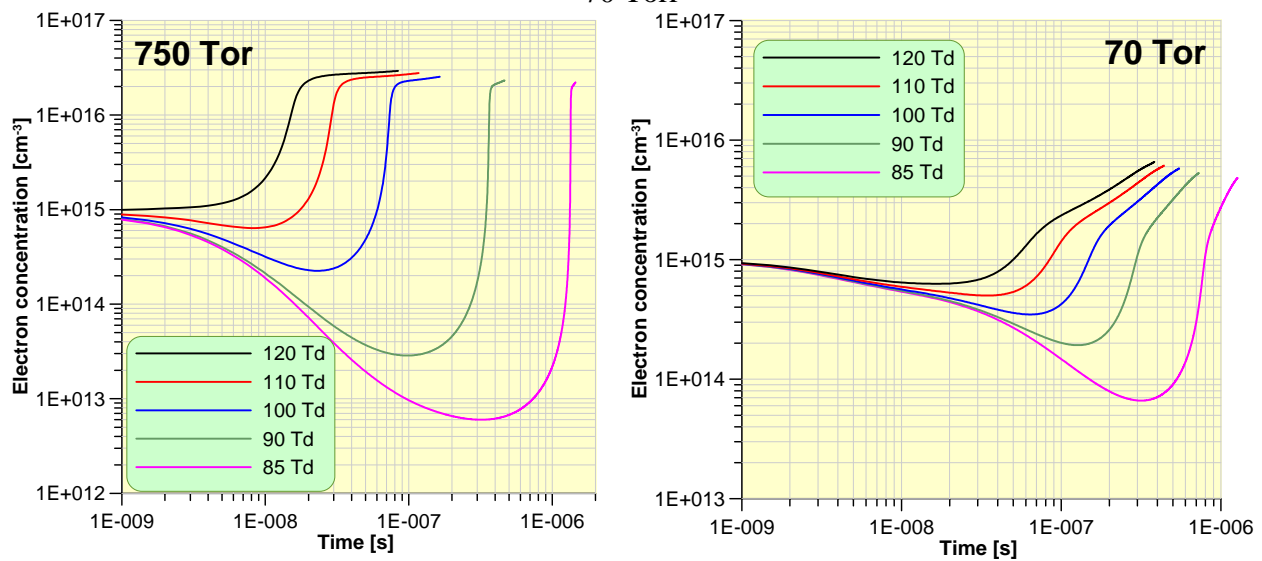


Fig.2.2.6. Dynamics of electron concentration at various incident fields under the pressures 750 and 70 Torr

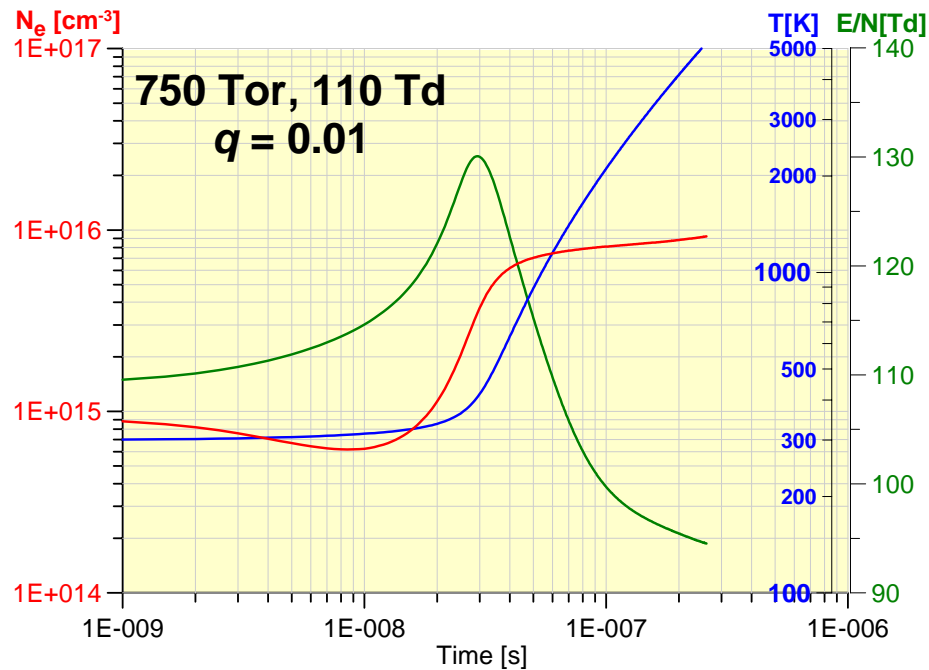


Fig.2.2.7. Dynamics of electron concentration, local reduced field and gas temperature at $P = 750$ Torr, incident $E/N = 110$ Td, polarization factor $q = 0.01$

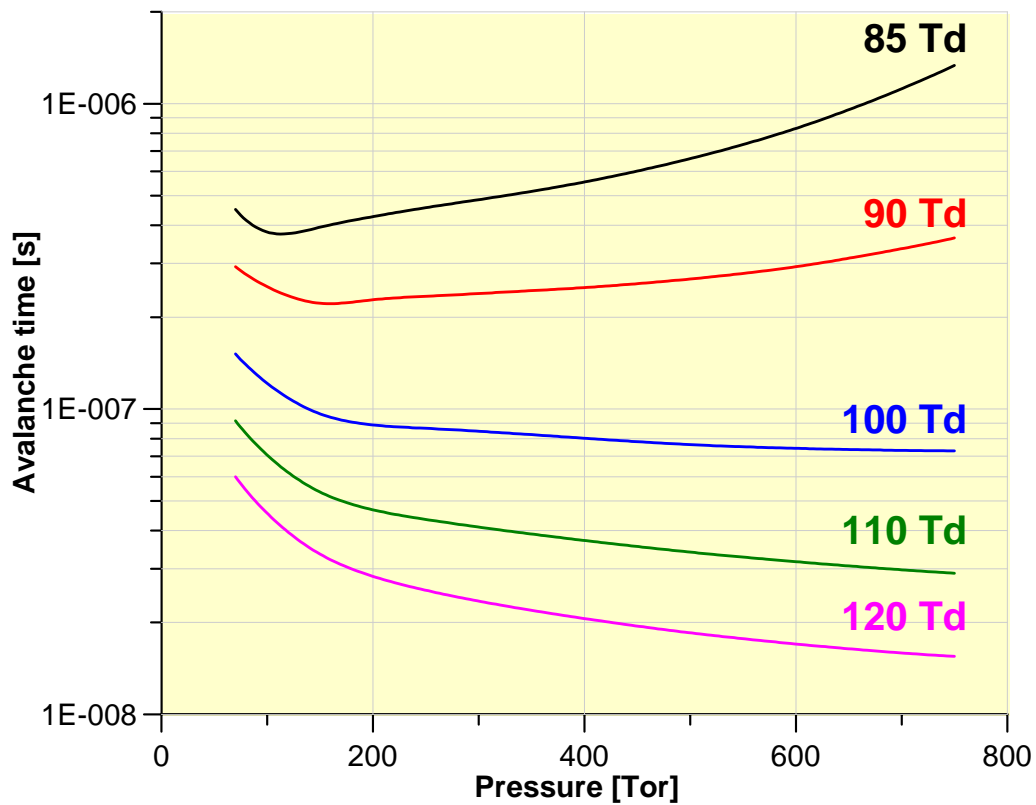


Fig.2.2.8. Avalanche time vs. medium pressure for various incident E/N

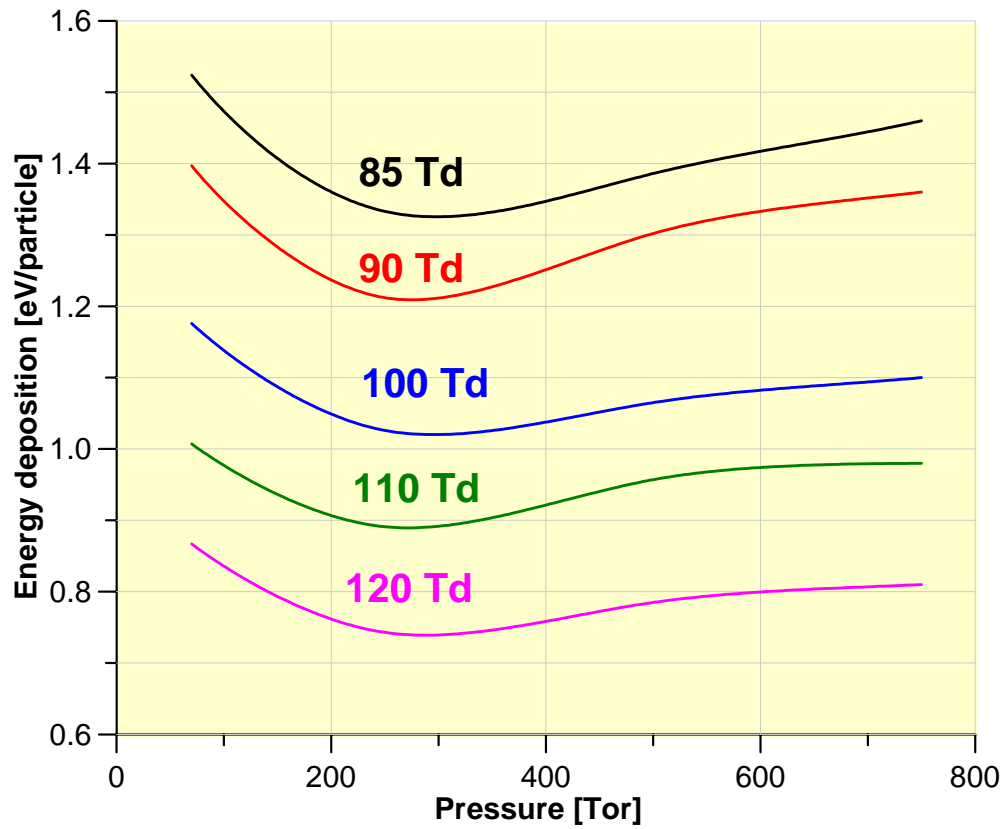


Fig.2.2.9. Dependence of energy deposition at avalanche time for various incident E/N

Conclusions

Kinetic modeling of MW interaction with decaying laser spark under ambient air pressures from 100 Torr to 750 Torr has shown the following distinctive features:

- Laser spark decay kinetics demonstrates relative independence over the pressure in the range 300-750 Torr and has visual deviations from these parameters under the pressure 100 Torr;
- This conclusion is supported by evolution curves of charged, electronically excited and neutral particles, the main electronically excited specie after hundreds of microseconds being $O_2(a^1\Delta_g)$;
- The transparency parameter increases with pressure decrease – about 5 times at 100 Torr in comparison with that for the atmospheric pressure;
- Maximal transparency approach time during LS decay varies from about 200 mcs under 100 Torr down to 110 mcs under the atmospheric pressure;
- Minimal MW power density necessary for ionization avalanche start varies from about 1 kW/cm^2 under 100 Torr up to 10 kW/cm^2 under the atmospheric pressure;
- Laser spark elongated in the direction of electric field of EM wave is somewhat more efficient for initiation of MW discharge than LS of spherical shape.

These results are in reasonable agreement with experiments, nevertheless, further investigations are to be implemented for quantifying the role of laser beam orientation and other factors.

Kinetic investigation of MW pulse interaction with long thin spark created by ultra-short laser pulse has shown that with growth of MW incident field the energy deposition threshold for ionization avalanche start decreases from 1.5 eV/particle at 85 Td down to 0.8 eV/particle at 120 Td. At that, the time of avalanche start decreases from $\sim 1 \mu\text{s}$ down to $\sim 10 \text{ ns}$. Avalanche start is conditioned by gas heating in collisional quenching of excited particles, at later times both quenching and recombination heating support avalanche development. Avalanche process is over when the rate of medium expansion becomes approximately equal to the rate of electrons production in the medium. Temperature growth amounts to $\approx 5000 \text{ K}$ at avalanche end.

References to Section 2

1. Brovkin, V., Kolesnichenko, Y., and Leonov, S. et al., "Study of Microwave Plasma-Body Interaction in Supersonic Flow," AIAA Paper No. 99-3740, 1999.
2. Kolesnichenko, Y., Brovkin, V., Azarova, O., Grudnitsky, V., Lashkov, V., and Mashek, I., "Microwave Energy Deposition for Aerodynamic Application," AIAA Paper No. 2003-0361, 2003.
3. Kolesnichenko, Y., Brovkin, V., Azarova, O., Grudnitsky, V., Lashkov, V., and Mashek, I., "Energy Release Regimes for Drag Reduction in Supersonic Flow," AIAA Paper No. 2002-0353, 2002.
4. Braun A, Korn G, Liu X, Du D, Squier J and Mourou G. Self-channeling of high-peak-power femtosecond laser pulses in air. Opt. Lett. 20 73–5, 1995
5. Couairon and L. Bergé. Light Filaments in Air for Ultraviolet and Infrared Wavelengths. Phys.Rev.Lett. v.88, No.13, pp.135003-1-135003-4 (2002)
6. Glumac N., Elliott G., and Boguszko M., Temporal and Spatial Evolution of the Thermal Structure of a Laser Spark in Air. 43rd AIAA Aerospace Meeting and Exhibit, AIAA Paper 2005-204
7. Glumac N., Elliott G., The Effect of Ambient Pressure on Laser-Induced Plasmas in Air, 44th AIAA Aerospace Meeting and Exhibit, AIAA Paper 2006-399
8. D.V.Khmara, Yu.F.Kolesnichenko Software package for kinetic and spectra emission modeling of gas discharge plasma. Symposium on Thermochemistry and Plasma Processes in Aerodynamics, St. Petersburg, June 2006
9. Partner Project 3058p, "Physics and Chemistry of MW Laser-Induced Discharge in Gas Flows and Plasma Jets", 2nd Quarter Report, p.36
10. Khmara, D., Kolesnichenko, Y., and Knight, D., "Modeling of Microwave Filament Origination," AIAA Paper 2006-0794, 2006.
11. Yu.F.Kolesnichenko, V.G.Brovkin, D.V.Khmara, I.Ch.Mashek, V.A.Lashkov, M.I.Rivkin. Regimes of Laser Plasmas – MW Field Interaction, 44th AIAA Aerospace Meeting and Exhibit, AIAA Paper 2006-0792

Section 3. Numeric modeling of gas dynamic effects arising under interaction of MW discharge channel with AD body

In Section 3 the gas dynamic effect of a thin longitudinal heated low-density channel on supersonic flow around AD bodies of different shapes was considered. This kind of heated channel could be obtained via MW energy injection into a supersonic flow. Situation of an infinite channel is investigated, too. The computed data are in agreement with the experimental ones for the dynamics of the bow shock wave standoff and the stagnation pressure in the experimental investigations of MW energy interaction with supersonic models.

In 3.1 new results on behavior of front drag force and total drag force during an interaction of a thin limited length low-density channel – cylinder shock layer have been obtained. AD body with complicated cavity has been considered. It is established that the presence of the cavity in the cylinder body amplifies the effects of drag force reduction in the process of thin low density channel – shock layer interaction and it is possible the presence of two or three minimums in the front drag force dependence on time. Arising two or three minimums in the dependence of front drag force on time is obtained to connect with eddies generation inside the cylinder shock layer. The special features of flow dynamics for the cases of short and long cavities have been analyzed. The effects established are stronger for smaller values of gas rarefaction in the channel. It is pointed out that there exists the time interval in which the effects established do not practically depend on the radius of the release channel and are defined only by the value of the channel length and the value of gas rarefaction degree in the channel (and the Mach number of oncoming flow).

In 3.2 the results of numerical modeling of an infinite rarefied heated channel of constant density cross-section – cylinder shock layer interaction are presented. Details of flow structure have been analyzed on the most representative grids. Stochastic pulsation flow mode has been observed. Mechanism of pulsations based on relationship between circulation flow and reversal flow is revealed. New flow structure effects concerning generation of contact discontinuities instabilities like Richtmayer-Meshkov instability and shear layer instability have been obtained. Main flow areas forming inside the shock layer has been researched including the flow separation area.

Investigation of details of flow structure for a very thin heated rarefied channel was conducted. The channel radius was equal to one tenth of the body's radius. The vortices

generated via shear layer instabilities were established to be stronger than in the case of less thin channels. Formation of the heated channel inside the shock layer is established. The reversal eddies generated were found to be strong sufficiently for the achievement of turbulent mixing of the hot gas in the formed channel and cold surrounding gas inside the separation area. It is obtained that the turbulent mixing is taken place cyclically in dependence with increasing the amount of the reversal eddies in the separation area. It is shown that in the case of thin channel the small scaled stochastic process dominates with the large scaled flow pulsations.

In 3.3 the results of numerical modeling of a thin low-density heated channel of limited length – shock layer interaction for the Mach number of the oncoming flow $M_\infty=3$ are presented. New flow structure effects for plane and cylinder cases in comparison with the previous results for $M_\infty=1.89$ have been established. Arising additional shock waves and contact discontinuities both in cylinder and plane cases in comparison with the previous results for $M_\infty=1.89$ was established. In cylinder case the peaks generation in the dynamics of the stagnation pressure as the result of Mach reflection of the additional shock wave was characterized. Stagnation pressure growth after its fall down was shown to cause by additional shock wave reflection from the front surface of the body (for the rarefaction degree $\alpha_p=0.2\div 0.3$). Relative bow shock wave coordinate variation is obtained to be greater for longer channels. The possibility of compensation of insufficient channel rarefaction by greater value of the channel length for obtaining the same value of the front drag force has been established.

In 3.4 stochastic pulsation flow mode has been analyzed for the value of the relation a release channel radius to body's radius equal to 0.1 and 0.25. The Mach number of the oncoming flow was equal to 1.89 and 3; the degree of the gas rarefaction in the heated release channel was supplied to be 0.3-0.5. Generation of Richtmayer-Meshkov instability, dynamics of shear layer instability and dynamics of flow defining parameters were investigated. For particular set of the flow parameters a tendency to instability suppressing is shown to take place. These results have been obtained in Rutgers University (USA, New Jersey) in the Laboratory of Computing Design headed by Professor Doyle Knight.

3.1. Limited Length Low Density Channel Effect upon Supersonic Flow past Cylindrical Body with Complicated Cavity

New results on behavior of front drag force and total drag force during an interaction of a thin limited length low-density channel – cylinder shock layer have been obtained. AD body with

steady flow at the time moment t_i and its length was equal to Δl . In these calculations $R_i = 0.05$, $\Delta l = 0.8$, $\alpha_p = 0.5$.

3.1.2. Calculation results

Case I: long cavity. Geometry of the body is presented in Fig. 3.1.1, here $x_1 = 0.5$, $x_2 = 0.6$, $x_3 = 1.2$, $x_4 = 1.5$, $r_1 = 0.08$, $r_2 = 0.16$, $r_3 = 0.2$. As in our previous work [1] in this case the oscillating steady state was shown to establish (Fig. 3.1.2). During the steady state establishing the flow has complicated shock structure and one can see the peaks in the dependences of the stagnation parameters on time connected with numerical representation. The steady state on density establishes more slowly then for the other parameters. It is connected with dynamics of the contact discontinuity arising inside the cavity.

Flow isochors for the interaction process are presented in Fig. 3.1.3. Mechanism of the first eddy generation accompanied by the additional shock waves arising in the area of cylinder shock layer was established in [2] (see Fig. 3.1.3a, 3b). In the presence of the additional shock wave near the entrance part of the cavity there arises the second vortex flow (Fig. 3.1.3c). The second eddy interacts with the front surface and the shock wave normal to the surface is established to generate as the result of the interaction (Fig. 3.1.3c, 3d). In Fig. 3.1.3e it is seen the third eddy generation, later this eddy interacts with the front surface with generating the second shock wave normal to the surface (Fig. 3.1.3f).

The interaction of these three eddies with the body's front surface leads to the presence of three minimums in the front drag force F_s dependence on time (Fig. 3.1.4a). Here

$$F_s = \left(\int_S p ds \right) / S.$$

Note that in the case of blunt cylinder body only one fall down of the front drag force has been established [2]. In Fig. 3.1.4b the dynamics of the total front drag force of all surfaces normal to

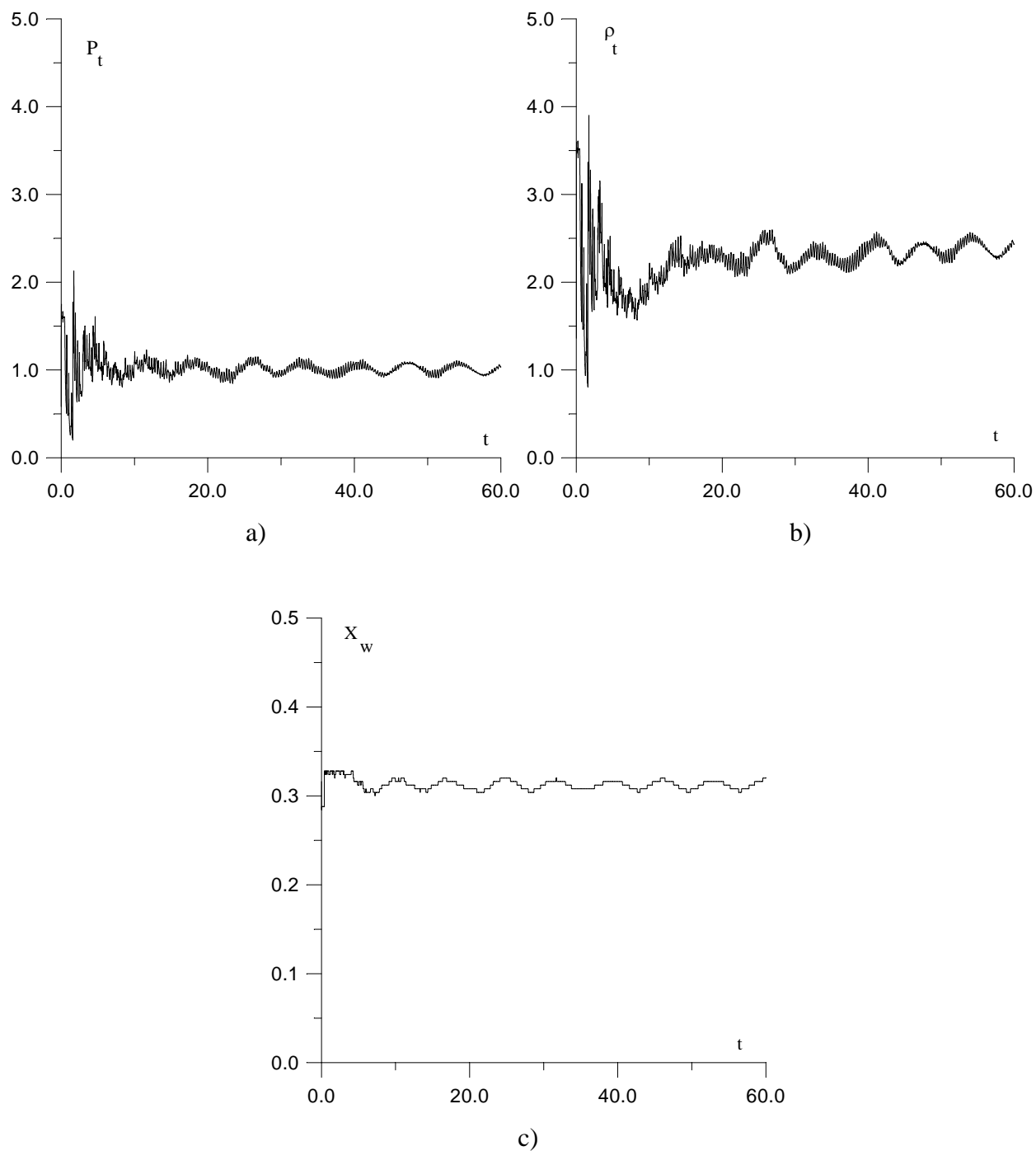


Fig. 3.1.2. Steady state establishing: a) - stagnation pressure dynamics; b) - dynamics of the density in the stagnation point; c) - dynamics of the bow shock wave coordinate

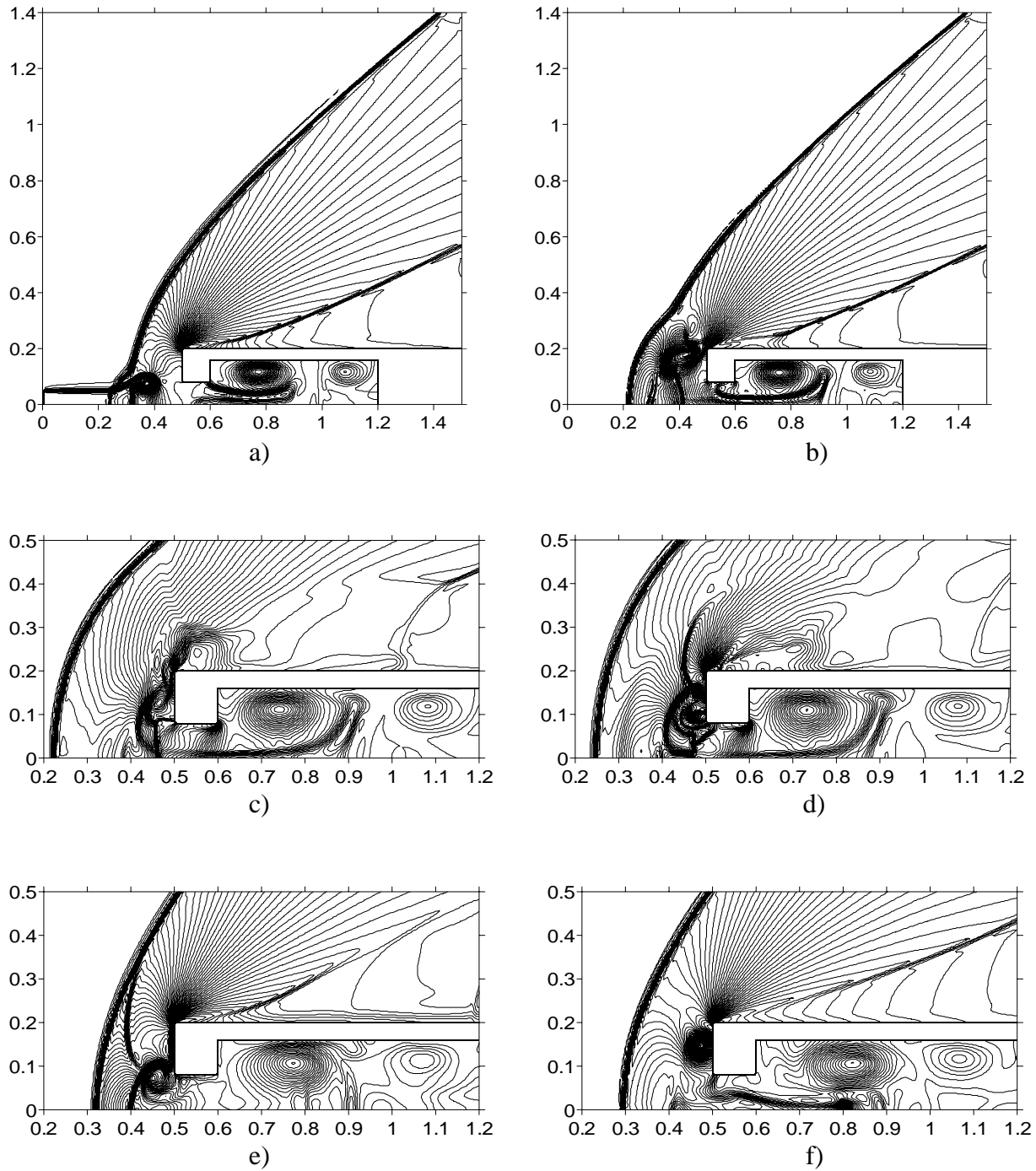
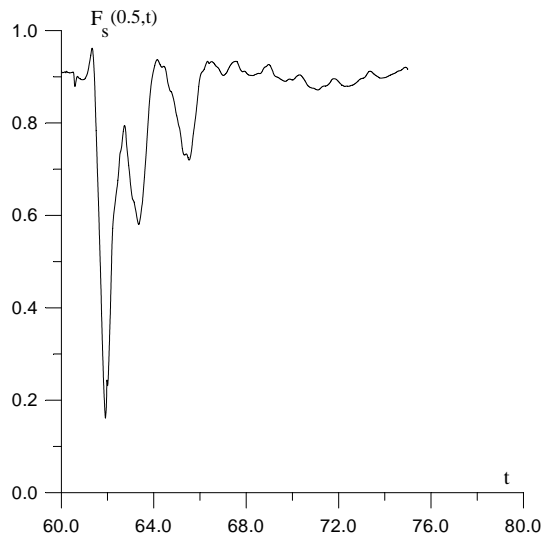
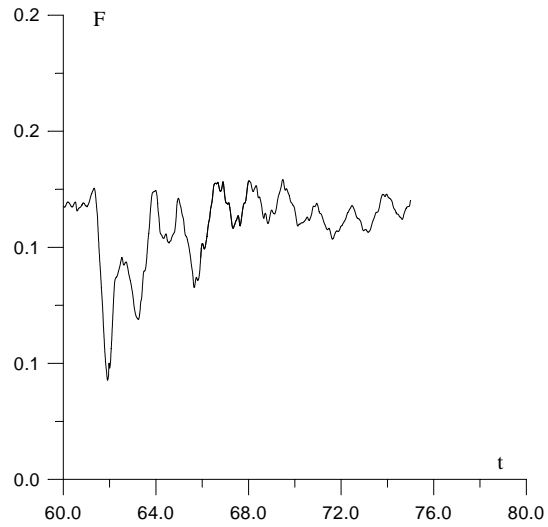


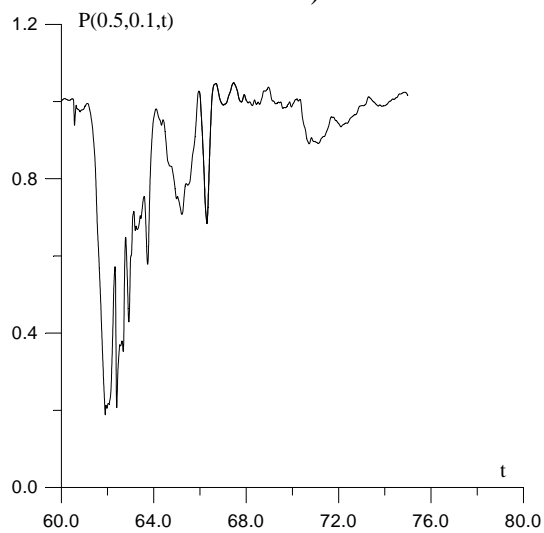
Fig. 3.1.3. Generation of three eddies and two shock waves normal to the front surface during the limited length low-density channel - cylindrical shock layer interaction, a) – $t = 60.8$, b) – $t = 61.6$, c) – $t = 62.1$, d) – $t = 62.3$, e) – $t = 64.0$, f) – $t = 65.5$



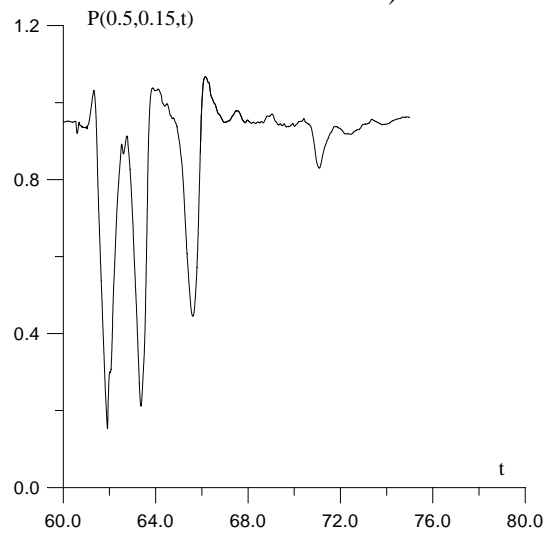
a)



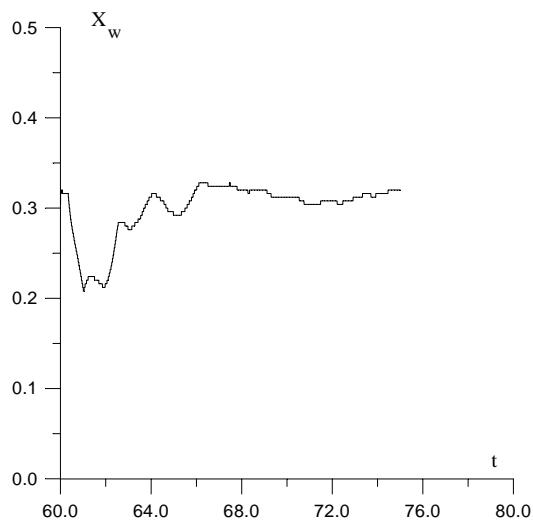
b)



c)



d)



e)

Fig. 3.1.4. Dynamics of the front drag force - a, total drag force - b, pressure in the front surface points - c, d, bow shock coordinate - e. $t_i = 60.8$

the x-axis \mathbf{F} is presented. It is seen that for considered shape of the cavity the effect low-density channel on cylinder shock layer leads to flow instability caused by the new oscillating process taking place inside the cavity. In the calculation the initial steady state didn't establish after the finish of the interaction process. Thus some resonant phenomena are shown to take place in this case.

Next figures show that behavior of the front surface pressure differs a lot for different points (see Fig. 3.1.4c, 4d). It is seen that the pressure dynamics in the point (0.5, 0.15) reflects the considered effect of front drag fall down better than the dynamics in the point (0.5, 0.1). So for experimental registration the optimal location of the pressure sensor is in the point (0.5, 0.15) on the front body surface. Dynamics of bow shock wave coordinate reflects the presence of three eddies in the cylinder shock layer, too (Fig. 3.1.4e).

Mechanism of the second and third minimums arising differs from that for the first minimum generation. The minimums were established to cause by the normal to front body's surface shock waves generation: the shock wave is stronger the fall down is greater. This shock wave was obtained to generate as the result of the eddy - hard wall interaction. The normal shock wave generation for the second eddy - front surface interaction is presented in Fig. 3.1.5.

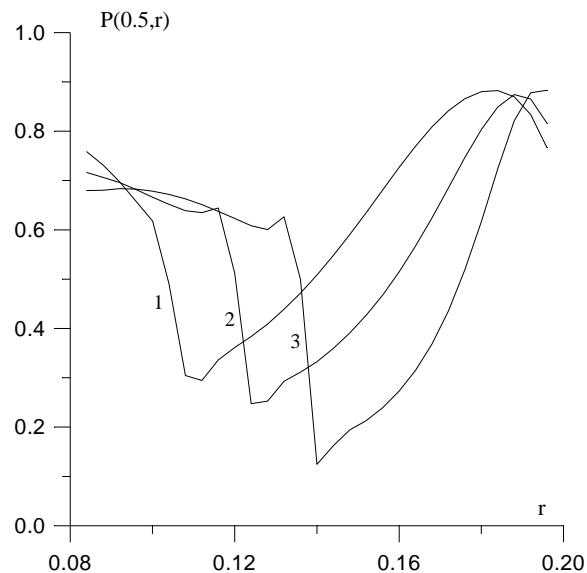


Fig. 3.1.5. Generation of the shock wave normal to front surface, curve 1 – $t = 63.0$,
curve 2 – $t = 63.2$, curve 3 – $t = 63.4$

As it has been mentioned the steady state for the supersonic streamlining the cylinder with the complicated cavity for considered parameters is periodical one. The time period is approximately equal to 7.2. The question is if the phenomenon depends on the time moment of the release action beginning t_i or not. In Fig. 3.1.6 the results for the time moment t_i greater by the value of one half of the time period are presented. It is seen only two minimums in the dynamics of the front drag force and total drag force (Fig. 3.1.6a, 6b).

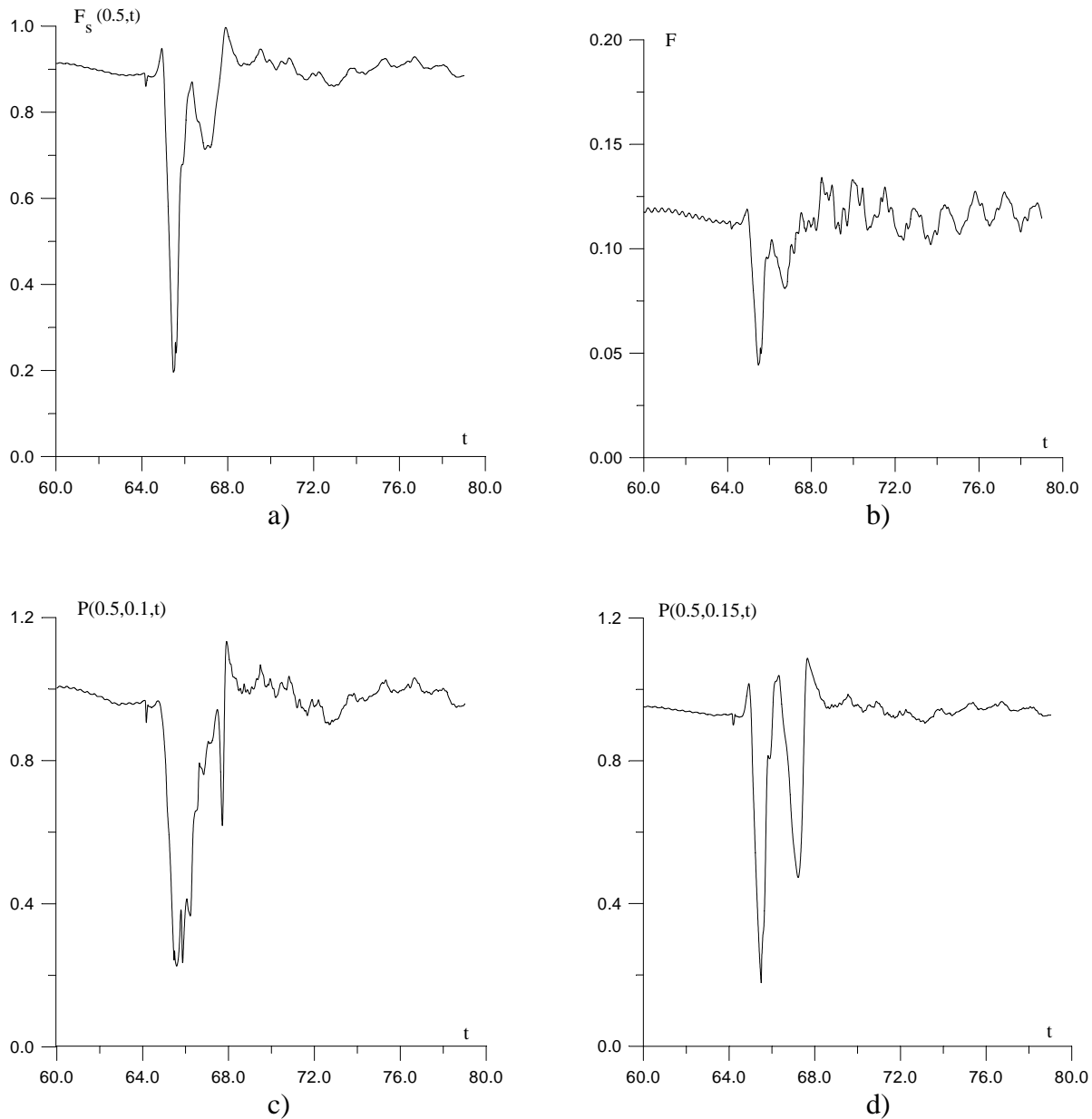


Fig. 3.1.6. Dynamics of the front drag force – a, total drag force – b, pressure in the front surface points – c, d. $t_i = 63.6$

The most clearly the presence of these two minimums is reflected in the pressure behavior in the point (0.5, 0.15) on the front body's surface (Fig. 3.1.6d). Thus for considered cavity geometry the drag forces behavior depends on the time moment of the release action beginning t_i .

Case II: short cavity. Geometry of the body is presented in Fig. 3.1.1, $x_1=0.5$, $x_2=0.6$, $x_3=0.84$, $x_4=1.2$, $r_1=0.08$, $r_2=0.16$, $r_3=0.2$. In this case the process is less dramatic in whole. The oscillating steady state was shown to establish, too. The results are close to those for $x_3=0.9$ (see [1]). The time period is smaller for the shorter cavity (Fig. 3.1.7). Steady state establishing time is smaller than in the previous case.

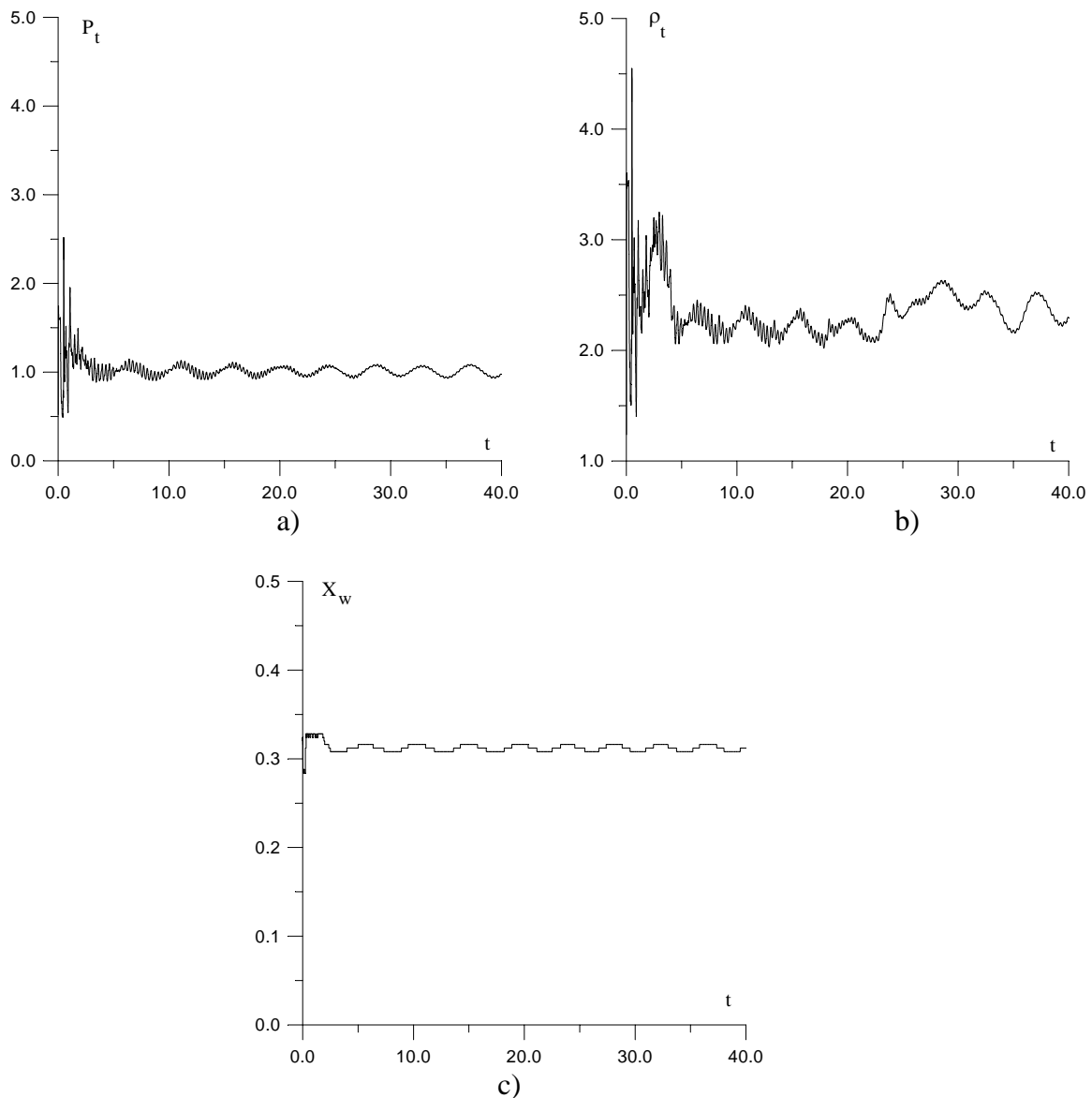
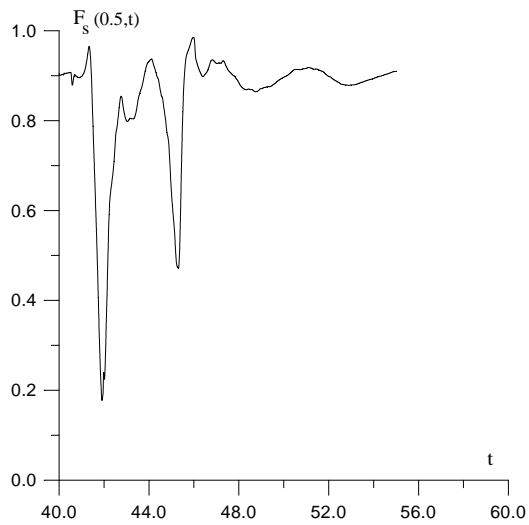
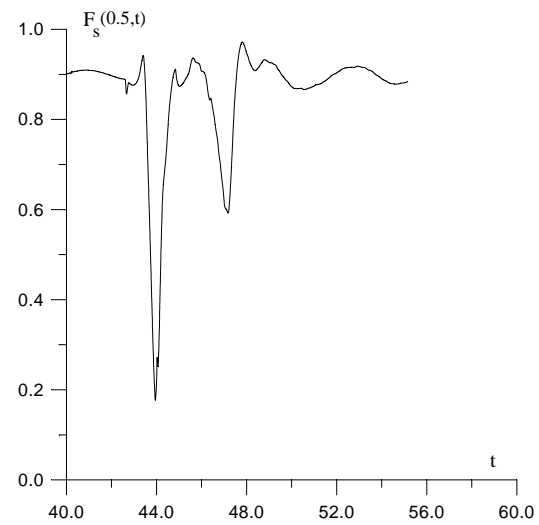


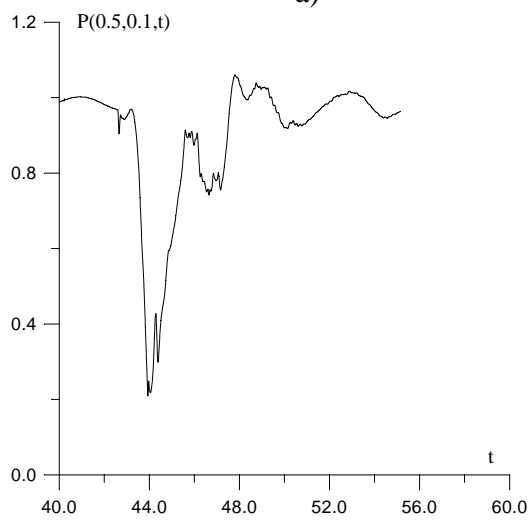
Fig. 3.1.7. Steady state establishing: a) - stagnation pressure dynamics; b) - dynamics of the density in the stagnation point; c) - dynamics of the bow shock wave coordinate.



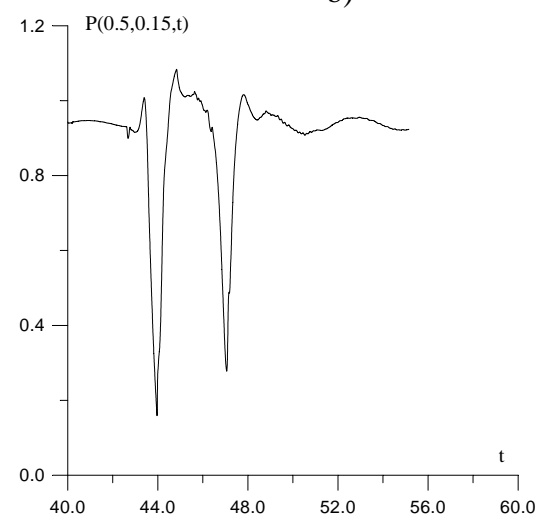
a)



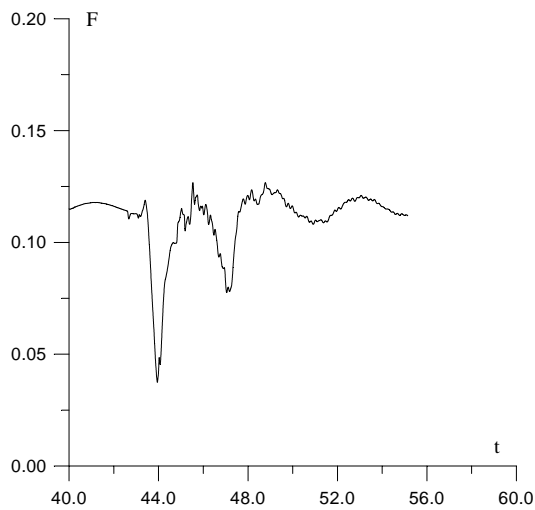
b)



c)



d)



e)

Fig. 3.1.8. Dynamics of the front drag force, $t_i = 40.1$ – a, front drag force, $t_i = 42.1$ – b, pressure in the front surface points – c, d, total drag force – e

The results do not practically depend on the time moment t_i . In Fig. 3.1.8a, 8b the values of t_i differ by the value of one half of the time period (equal to 2.1). Two minimums are seen in the pressure dynamics in the both considered points on the front surface, but the picture is more clear in the point (0.5, 0.15) (Fig. 3.1.8c, 8d). Total drag force dynamics defines by the front drag force behavior (Fig. 3.1.8e). In this case of the cavity geometry the flow instability doesn't arise after finish of the interaction process and the flow goes over into initial unperturbed steady state.

Conclusions

The conclusions on the calculation analyses are:

- presence of the cavity in the cylinder body amplifies the effects of drag force reduction in the process of thin low density channel – shock layer interaction and the presence of two or three minimums in the front drag force dependence on time is possible;
- presence of two or three minimums in the front drag force dependence on time is connected with the effect of two or three eddies generated inside the shock layer;
- mechanism of the first eddy generation was established earlier (see [2, 3]).
- mechanism of the second and third eddies generation is not clear yet; the drag force minimums generation is connected with the shock waves normal to the front surface arising as the result of the eddy – front surface interaction;
- for longer cavities the effect of low-density channel on cylinder shock layer leads to flow instability caused by the new oscillating process establishing;
- for shorter cavities the flow instability doesn't arise after finish of the interaction process and the flow goes over into initial unperturbed steady state;
- for longer cavities the process depends on the value of the time moment of the release action beginning t_i ;
- for shorter cavities the process doesn't practically depend on the value of t_i ;
- the effects established are stronger for smaller values of α_p ;
- there exists the time interval in which the effects established do not practically depend on the radius of channel R_i and are defined only by the value of the channel length Δl and the value of gas rarefaction in the channel α_p .

The last two conclusions follow from our previous results [2,3].

References to Section 3.1

1. Physics and Chemistry of MW Laser-Induced Discharge in Gas Flows and Plasma Jets, 2005, Annual Report, Partner Project 3058p
2. O.A. Azarova, V.G. Grudnitsky, Yu. F. Kolesnichenko. Some Gas Dynamic Aspects of Flow Control by MW Energy Deposition // Proc. of the 6th Int. Workshop on Magnetoplasma Aerodynamics, Moscow, May 24-27. 2005. V.1. P. 152-163.
3. Yu. F. Kolesnichenko, O.A. Azarova, V.G. Brovkin et al. Microwave Energy Release Regimes for Drag Reduction in Supersonic Flows // 40th AIAA Aerospace Meeting and Exhibit, Paper AIAA-2002-0353. P.1-13.

Section 3.2. On details of flow structure during the interaction of an infinite thin rarefied channel of constant density with a shock layer of blunt cylinder

The results of numerical modeling on a basis of Euler equations of an infinite rarefied channel of constant density cross-section - cylinder shock layer interaction are presented. Stochastic pulsation flow mode has been observed. Mechanism of pulsations based on relationship between circulation flow and reversal flow is revealed. New flow structure effects concerning generation of contact boundaries instabilities like Richtmayer-Meshkov instability have been obtained. Main flow areas forming inside shock layer has been researched including the flow separation area. An analysis of defining parameters of the interaction process has been conducted.

3.2.1. Statement of the problem

The statement of the problem is analogical to [1-5]. Numerical modeling is based on the Euler equations in the divergence form for ideal gas. The non-dimensional variables are used. The unit of length measure is $l_n = 10^{-2}$ m the time and velocity units of measure are, respectively, $t_n = 1.6 \times 10^{-5}$ s and $u_n = 6.27 \times 10^2$ m/s. Initial flow parameters corresponded to the normal conditions were $\rho_0 = 1$, $p_0 = 0.2$, $u_0 = 1$, $v_0 = 0$, Mach number of oncoming flow was 1.89. On the entrance boundary the parameters of oncoming flow were used. The boundary conditions had a sense of reflection on the x-axis and on the body's boundaries, and of absence of the reflection on the exit boundaries.

An energy release regarding as an infinite rarefied channel is assumed to arise instantly in the steady flow in front of the bow shock wave at the time moment t_i . The energy release was modeled via the entrance boundary conditions ($x=0$) as an infinite channel of low density ρ_i , $\rho_i = \alpha_p \rho_0$ for $0 \leq r \leq R$, where R is the channel radius, ρ_0 is the density in undisturbed flow, α_p - the degree of gas rarefaction in the channel. Other parameters were equal to those of undisturbed flow. In these calculations $R = 0.05$, $\alpha_p = 0.5$, $t_i = 13.01$.

We used two-dimensional analog of the difference scheme [6]. The scheme is conservative and has the second order of approximation in space and in time. The boundary conditions were expressed via flux functions and included to the calculations without breaking

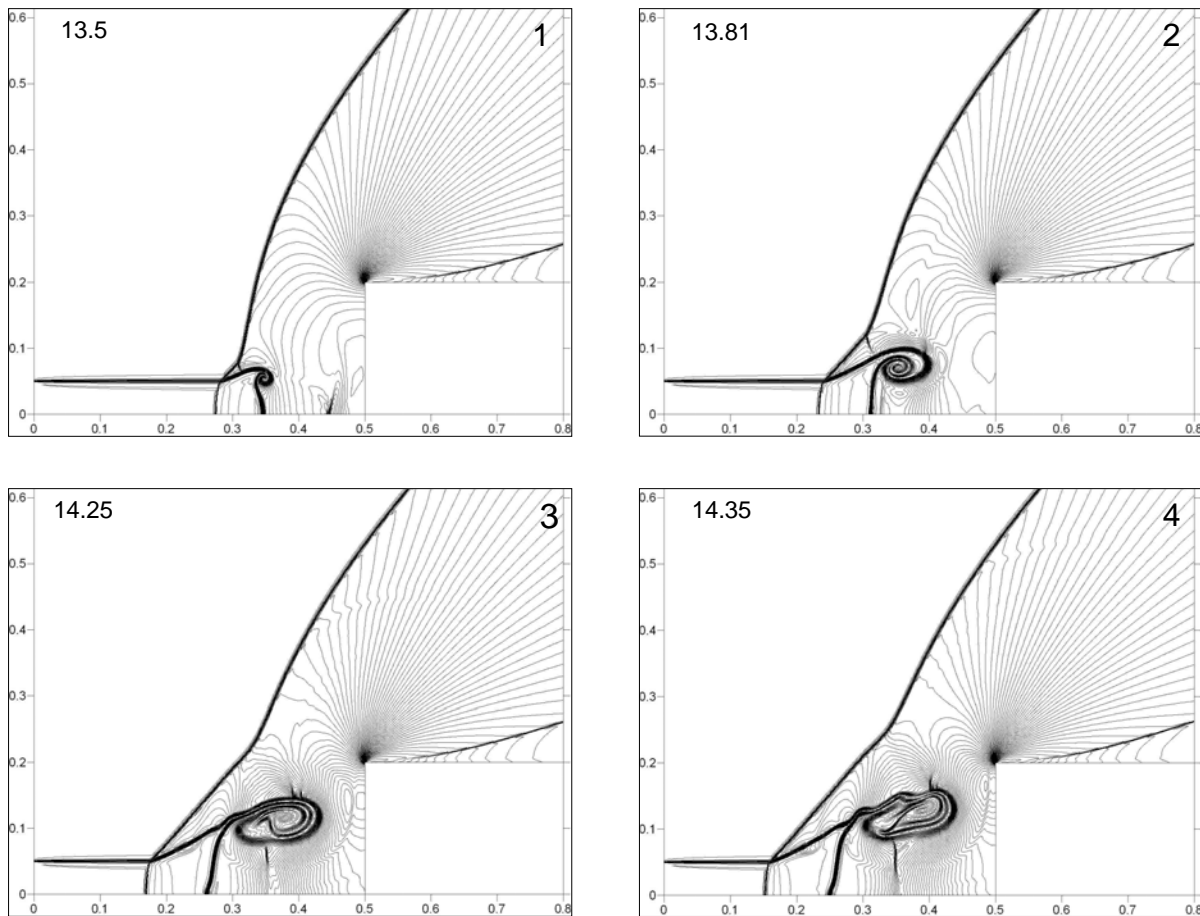


Fig. 3.2.1. Stage I, frames 1-4. Generation of Richtmayer-Meshkov instability

the conservation laws in the calculation area. The orthogonal grid (1600×1600) and the space steps values equal to 0.0005 were used. Numerical facilities turned out to be sufficient for the contact discontinuity instabilities generating representation.

3.2.2. Calculation results

Stage I. Generation and distortion of Richtmayer-Meshkov instability; generation of contact surface instabilities initiated by triple point configuration effect

Blunt cylinder AD body is considered; radius of the body r_b is equal to 0.2. In these calculations the shape of the channel cross-section on the radius is close to step-like data and the

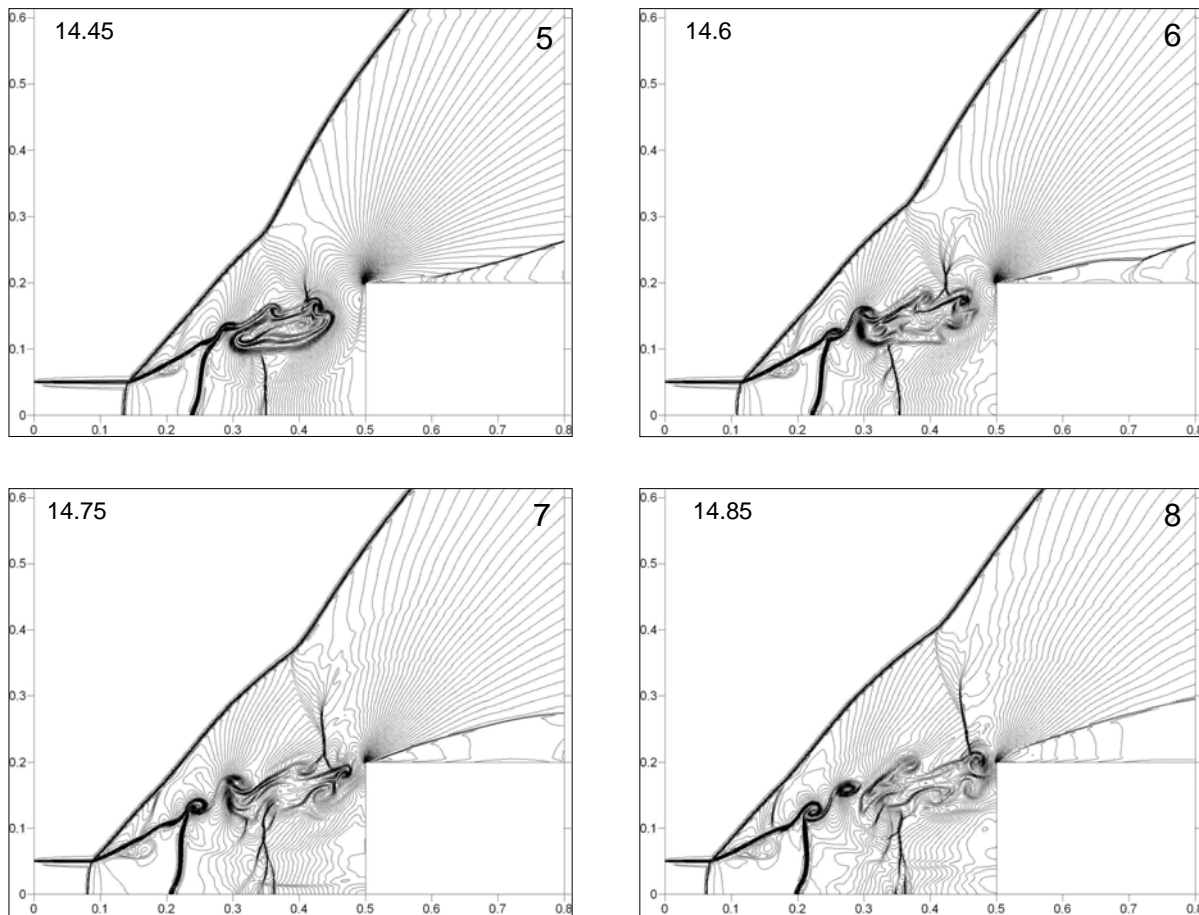


Fig. 3.2.2. Stage I, frames 5-8. Distortion of contact boundaries rolling

numerical spreading of the contact discontinuity is minimized. Thus the energy release is assumed to be an infinite cylinder of constant density. Flow isochors for the first stage of the process of interaction of the channel of low density with the shock layer are presented in Fig. 3.2.1, 2. The values of time moments are defined in the upper left corner of the slides. The beginning of the interaction process is connected with the bow shock wave motion from the body and generation of contact discontinuity instability like Richtmayer-Meshcov instability. The reason of the instability generation is the impulse effect of the bow shock wave upon the contact discontinuities (horizontal and vertical) representing the boundaries of the rarefied channel. Note that the instabilities generate for both contact discontinuities which are rolling together. It is seen the triple configuration generating in the point of the bow shock wave fracture. In these calculations more than 10 weak triple configurations were registered. (Fig. 3.2.1, frames 1, 2).

The phenomenon of conic shock area generation as the result of bow shock front fracture during the interaction with the channel is so-called precursor generation [7]. The boundaries are rolling and it is accompanied by acoustic wave emission and a series of additional shock waves generating above the structure of rolled boundaries and one shock wave down of it (Fig. 3.2.1, frames 3, 4). In the inhomogeneous medium rolled contact discontinuities are affected by the velocity variation, and as the result two smaller eddies generation is observed (Fig. 3.2.1, frame 4, Fig. 3.2.2, frame 5). This instability has a shift character, later it relaxes and disappears. Then the structure of rolled boundaries is distorted with weak shock waves emission down of it. The shock waves above it are converged and interact with the shock wave resulting from the acoustic wave reflection from the front surface of the body.

Heated area bounded by two contact discontinuities inside the shock layer begins to transform and new boundary instability generation is seen near the upper boundary of this area (Fig. 3.2.2, frames 6-8). New boundary instability generation is presented in large scale in Fig. 3.2.3. This instability is initiated by triple point configuration - contact discontinuity interaction. Note, that there is the point of maximum value of the flow temperature in the vortex flow near the contact discontinuity.

Thus, the stage of the process presented in Fig. 3.2.1, 2 may be characterized as the stage of bow shock wave standoff from its undisturbed position to the left from the body, generation, living and distortion of the structure of rolled contact discontinuities, and another kind of instability generation.

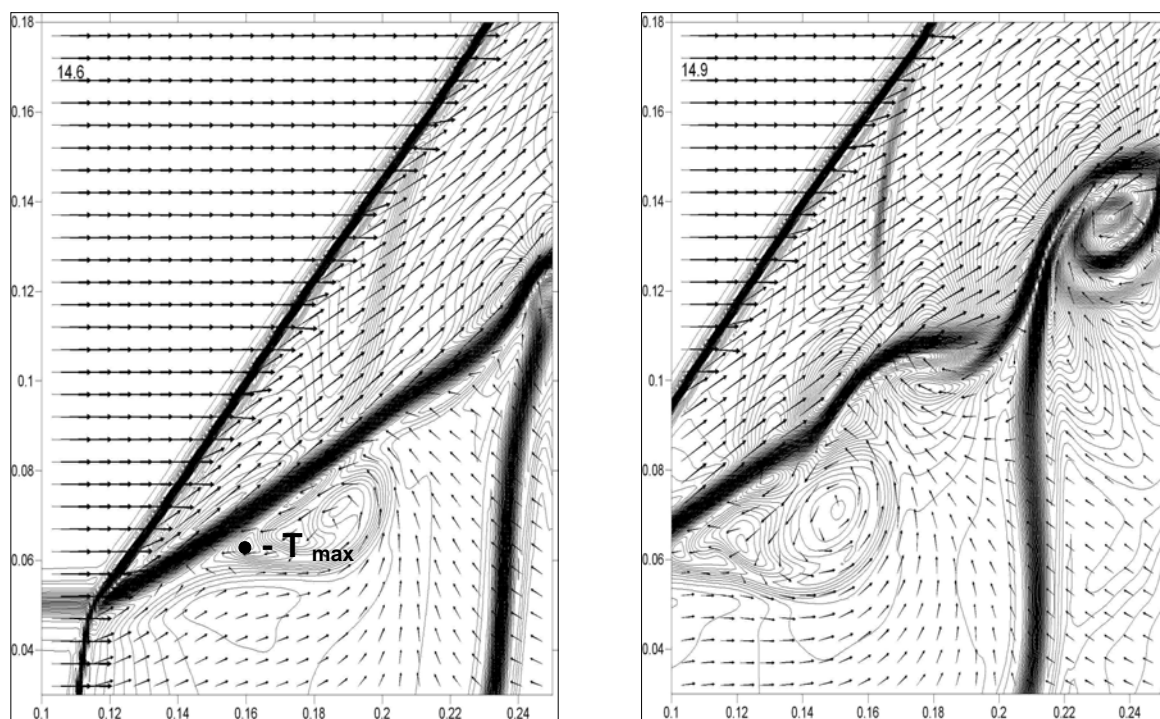


Fig. 3.2.3. Stage I. Generation of contact boundary instabilities initiated by triple point configurations effect.

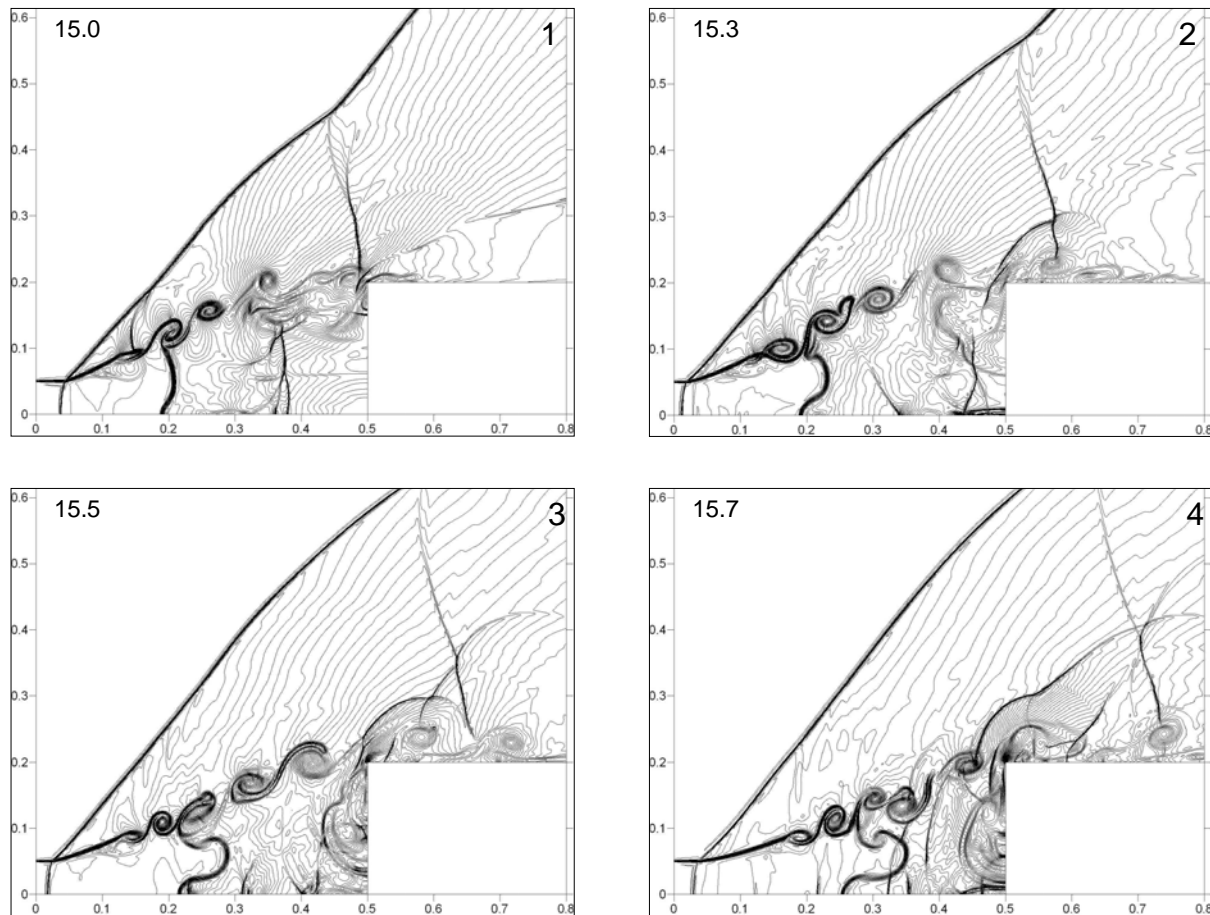


Fig. 3.2.4. Stage II, frames 1-4. Deformation of heated area and stochastic eddies generation as the result of instability of contact discontinuity

Stage II. Deformation of heated area and stochastic eddies generation as the result of instability of contact discontinuity

The second stage of the process is connected with oscillations of the bow shock, irregular contact discontinuities instabilities generation and heated area deformation (Fig. 3.2.4, 5). At the end of the first stage the vortex structure generated from the rolled contact boundaries enriches the body decreasing the pressure on it and as the result some time later the bow shock is broken. The pressure near the body continues to fall down causing return motion of the bow shock wave (Fig. 3.2.4, frames 1-3). At the same time the heated area changes its shape and new rolling boundary structures arise and move to the body. Near the front surface of the body the reversal circulation flow is forming ($t = 15.4$) and later it stops the boundary of the heated area ($t = 16.8$).

Then the bow shock is stopped, too, and its velocity changes the sign. Thus the reversal circulation flow becomes the reason of the bow shock pulsing. This mechanism is partially described in [7] where two first bow shock wave front oscillations have been observed.

Eddies consisting of the rolled boundaries generate stochastically, move towards upper corner of the body and interact with the body causing weak shock waves series towards the bow wave and a series of shock waves (and simple compression waves) normal to the front body's

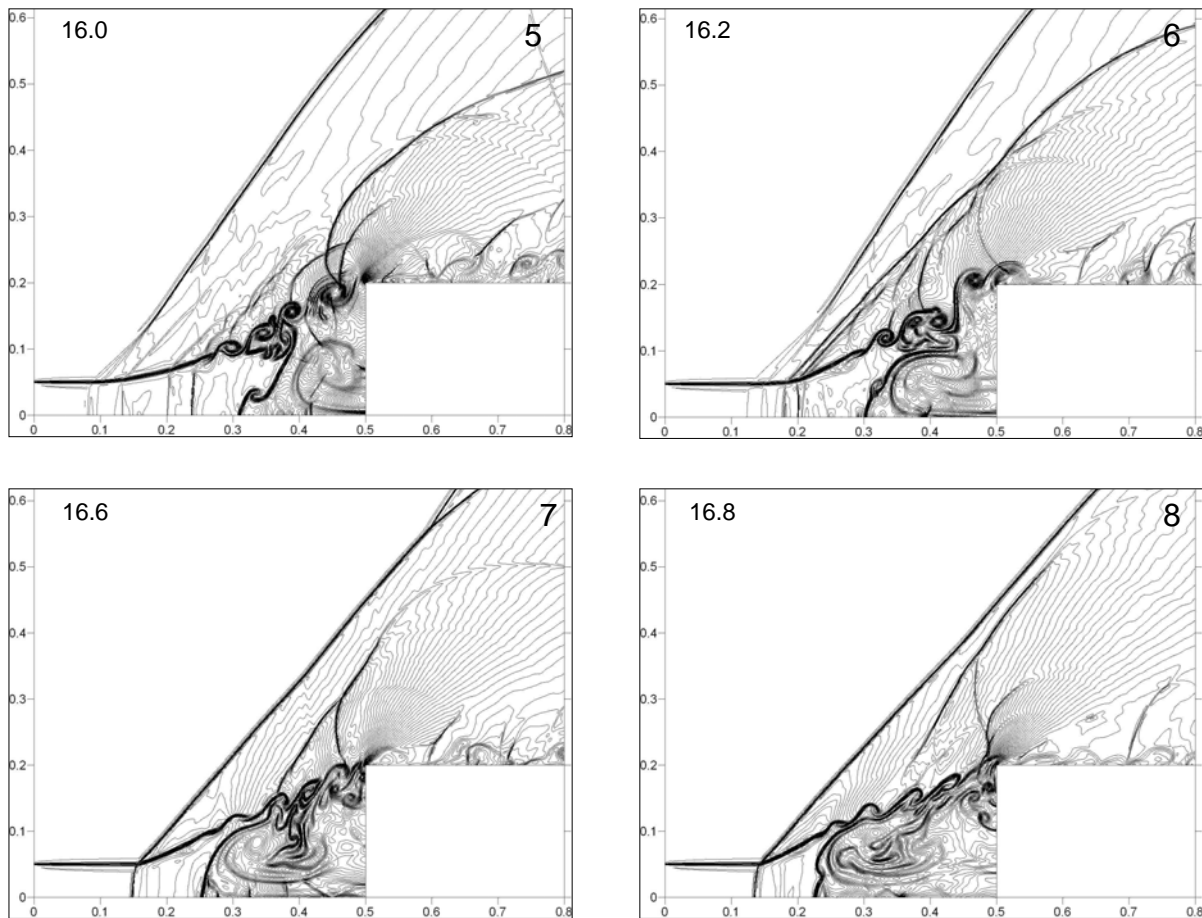


Fig. 3.2.5. Stage II, frames 5-8. Deformation of heated area and stochastic eddies generation as the result of instability of contact discontinuity

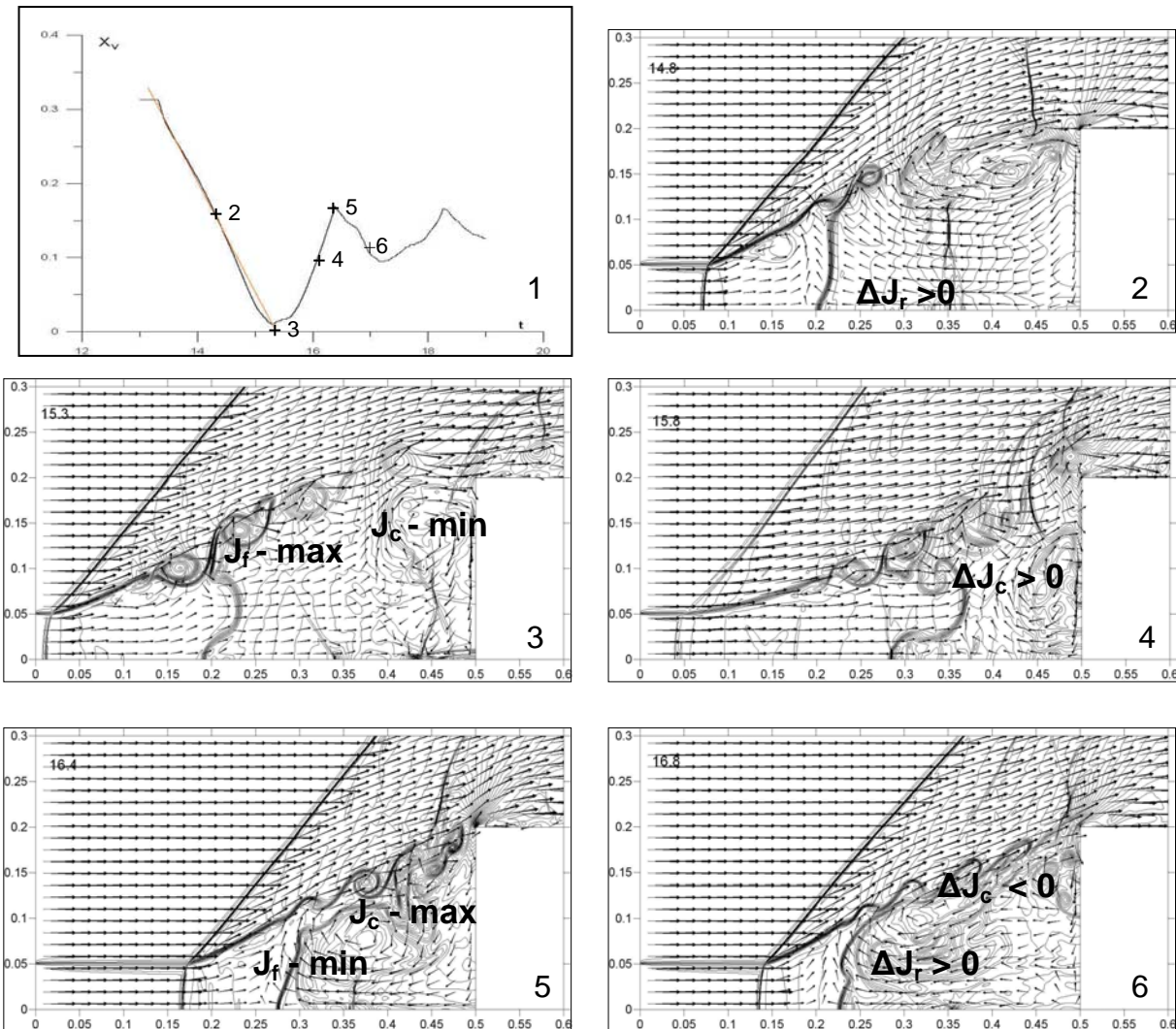


Fig. 3.2.6. Stages I and II. Mechanism of bow shock wave standoff and first pulsation

surface (Fig. 3.2.4, frames 3, 4, Fig. 3.2.5, frames 5, 6). Cumulating of these shock waves on the symmetry axis is a reason of stagnation pressure peaks arising and its pulsation accordingly with regard to compression waves [8]. Stochastic eddies generate the flow separation area of turbulent-like fluctuations joined to the body's surface. At the end of this stage the bow shock front becomes close to flat and eddies are holding out into the line (Fig. 3.2.5, frames 7, 8).

Stages I and II. Mechanism of standoff and first pulsation of the bow shock wave

Consider the mechanism of standoff and first pulsation of bow shock wave via the velocity fields in terms of flows formation in the shock layer at the first and second stages of the

process (Fig. 3.2.6). This mechanism is established to connect with the relationship between circulation and reversal flows and the flow from the heated area arising. The bow shock wave moves from the body. It's velocity on the x-axis is defined with the precision of 0.1% to the theoretical one defined as the solution of the Riemann problem, $D = -0.159$ [8] (Fig. 3.2.6, red line on frame 1). At the end of the first stage the vortex structure generated from the rolled contact boundaries reaches the body. It is seen the reversal flow J_r down of the vortex structure. When the flow from the heated area J_f reached the body the pressure on its surface is decreased (Fig. 3.2.6, frames 2, 3). As the result some time later the bow shock is broken. The pressure near the body continues to fall down causing reverse motion of the bow shock wave. Near the body the circulation flow J_c is generated and increases (Fig. 3.2.6, frames 4, 5). When the circulation

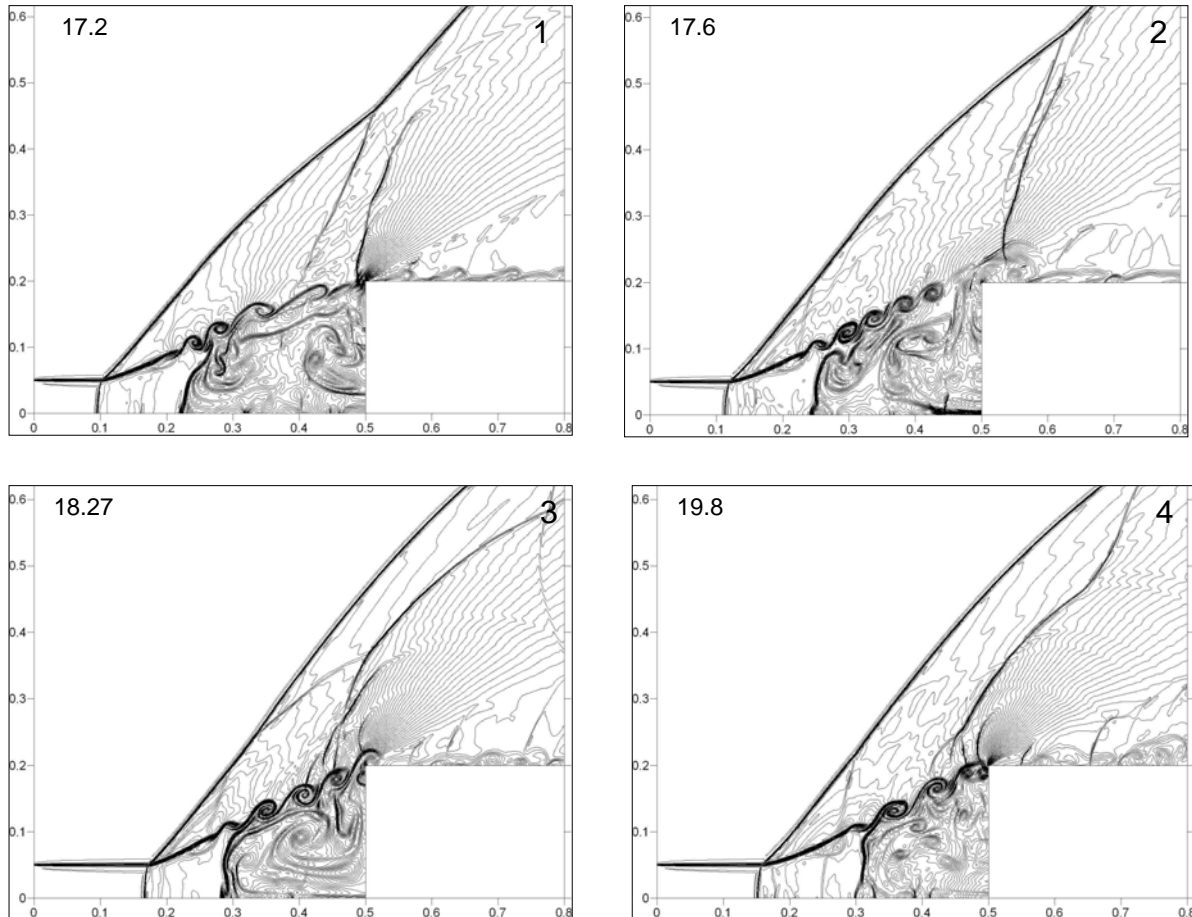


Fig. 3.2.7. Stage III, frames 1-4. The generated eddies are holding out into the line

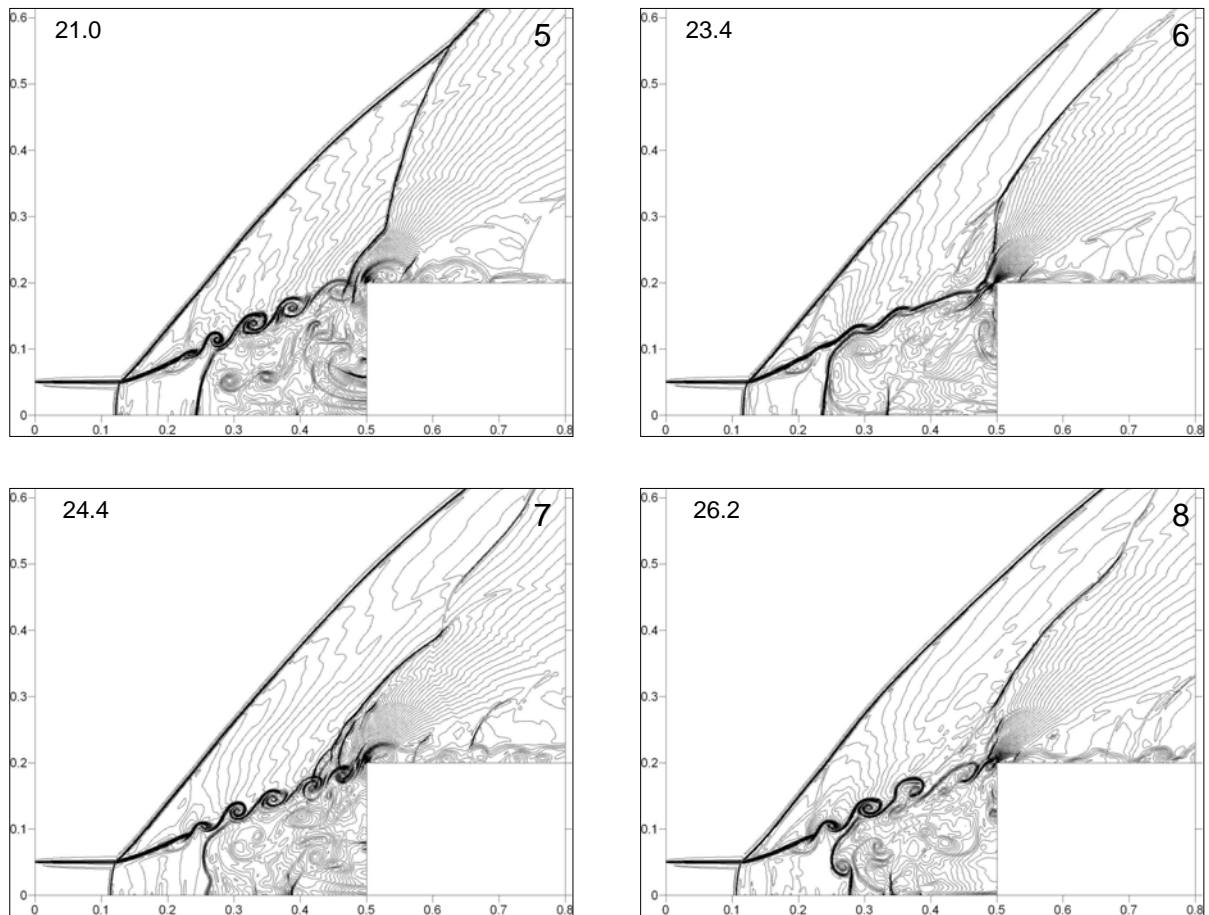


Fig. 3.2.8. Stage III, frames 5-8. Main flow areas formation

flow is maximal the contact boundary is stopped and locks the flow J_f . The pressure on the front surface of the body equalizes. In the down part of the separation area the reversal flow J_r is forming causing return motion of the bow shock wave (Fig. 3.2.6, frames 5, 6).

Stage III. Main flow areas formation

At the final stage researched in these calculations the formation of the main flow areas of the considered pulsation process is completed (Fig. 3.2.7, 8). At this stage all the flow elements described for the second stage are taken place, but heated flow domain deformation are less strong, the eddies generated are holding out into the line. Maximum observed amount of eddies in the line was equal to six. The normal shock cumulating is seen, too (Fig. 3.2.7, frames 1-3).

Above the upper body's surface density and pressure are reduced. In this area weak shock waves arise and blow away from the calculation area (Fig. 3.2.7, frame 4). The turbulent area becomes

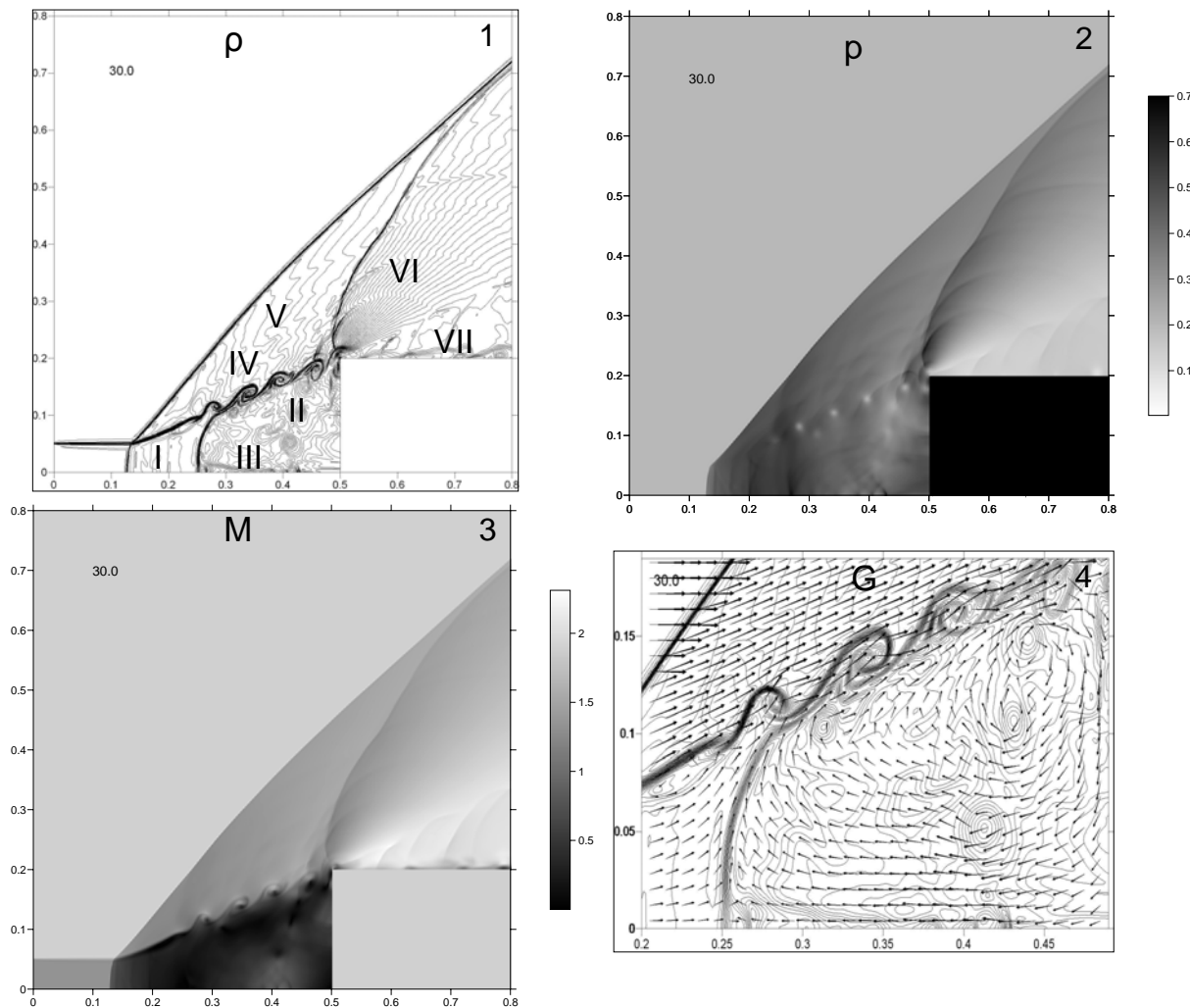


Fig. 3.2.9. Fields of main characteristics of pulsating flow

more homogeneous. At some time moment the contact boundaries don't twist but soon they begin to twist again (Fig. 3.2.8, frames 5-8).

Up to time moment $t=30.0$ the main flow areas inside shock layer are formed (Fig. 3.2.9, frame 1). In Fig. 3.2.9 the fields of pressure (frame 2), local Mach number (frame 3) and flow velocity (frame 4) are presented for this time moment, too.

Thus, these flow areas are:

I - the area of heated flow, bounded by two contact discontinuities, this area is subsonic;

II - the flow separation area of turbulent-like pulsations joined to the body, this area is weak subsonic, too;

III - the reversal circulation flow area situated inside the first two areas;

IV - the area in which the contact boundaries are rolling – the area of instability generation;

V - the triangle area of increased density and pressure bounded by the flat bow shock front, the line of eddies, and curved shock wave with the beginning near the body's corner;

VI - the area of rarefaction wave with the center in the body's corner;

VII - the triangle area of reduced density and pressure joined to upper body's surface in which weak shock waves arise and blow away from the calculation area.

Our calculations on less representative grids suggest that the flow in the shock layer will consist of the areas established and for $t > 30.0$. The considered process is irregular, but the elements of ordering are expressed in the constant existence of the flow areas observed.

Separate vortices centers trajectories consideration: two different types of vortex behavior

Consider the separate vortex center trajectory $L(X_v, Y_v)$, defining in parametrical form by the relations:

$$\frac{dX_v}{dt} = u_v, \frac{dY_v}{dt} = v_v,$$

where X_v , Y_v , u_v , v_v – the values of coordinates and velocity projections of the vortex center for the bow shock coordinate dynamics presented in Fig. 3.2.10. The results showed that there are

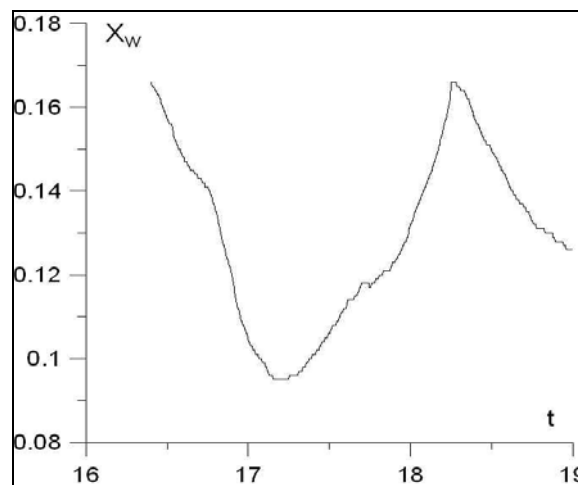


Fig. 3.2.10. Dynamics of bow shock coordinate in the time interval considered for trajectories researched

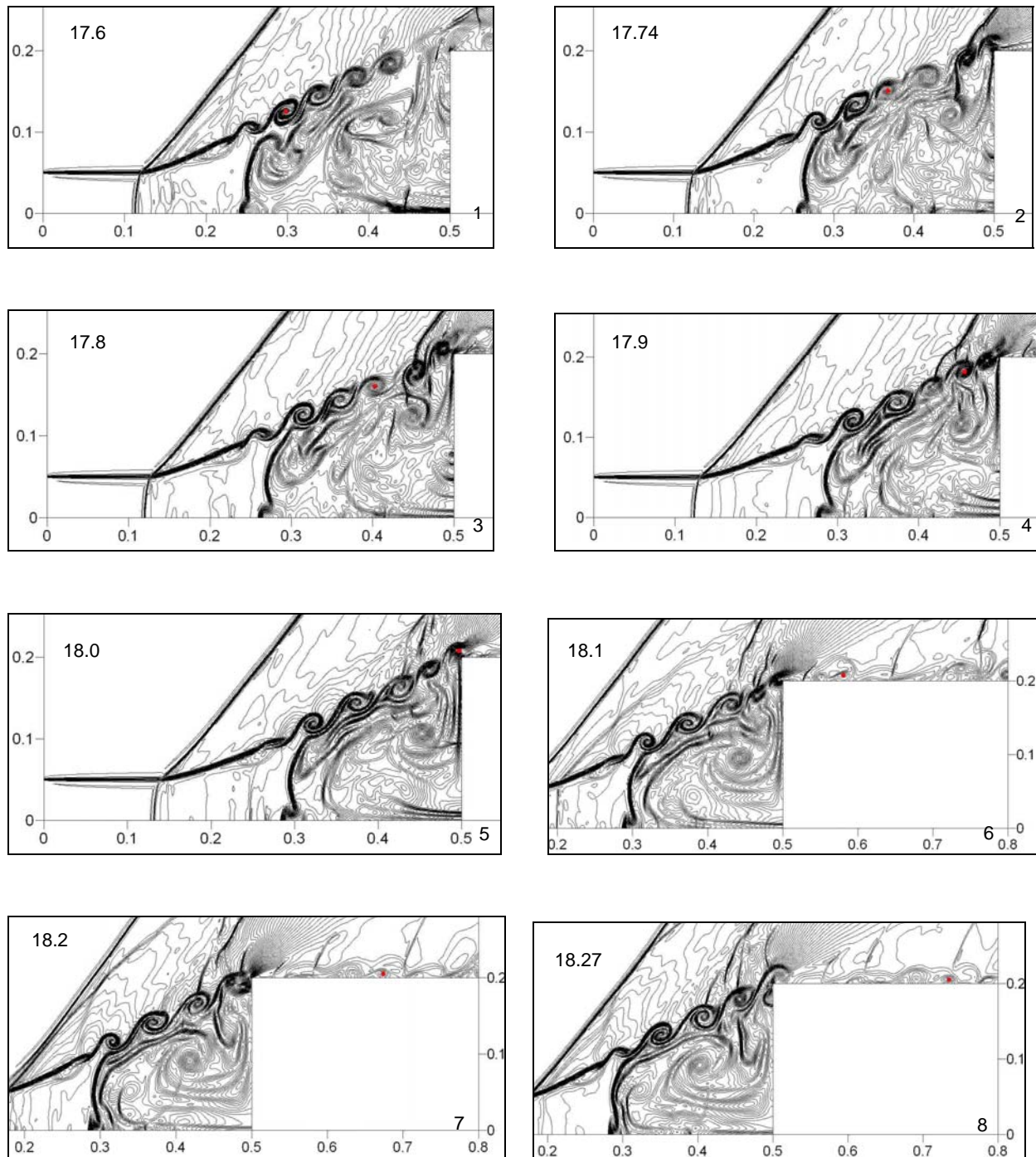


Fig. 3.2.11. Motion of the labeled vortex leaving the calculation area

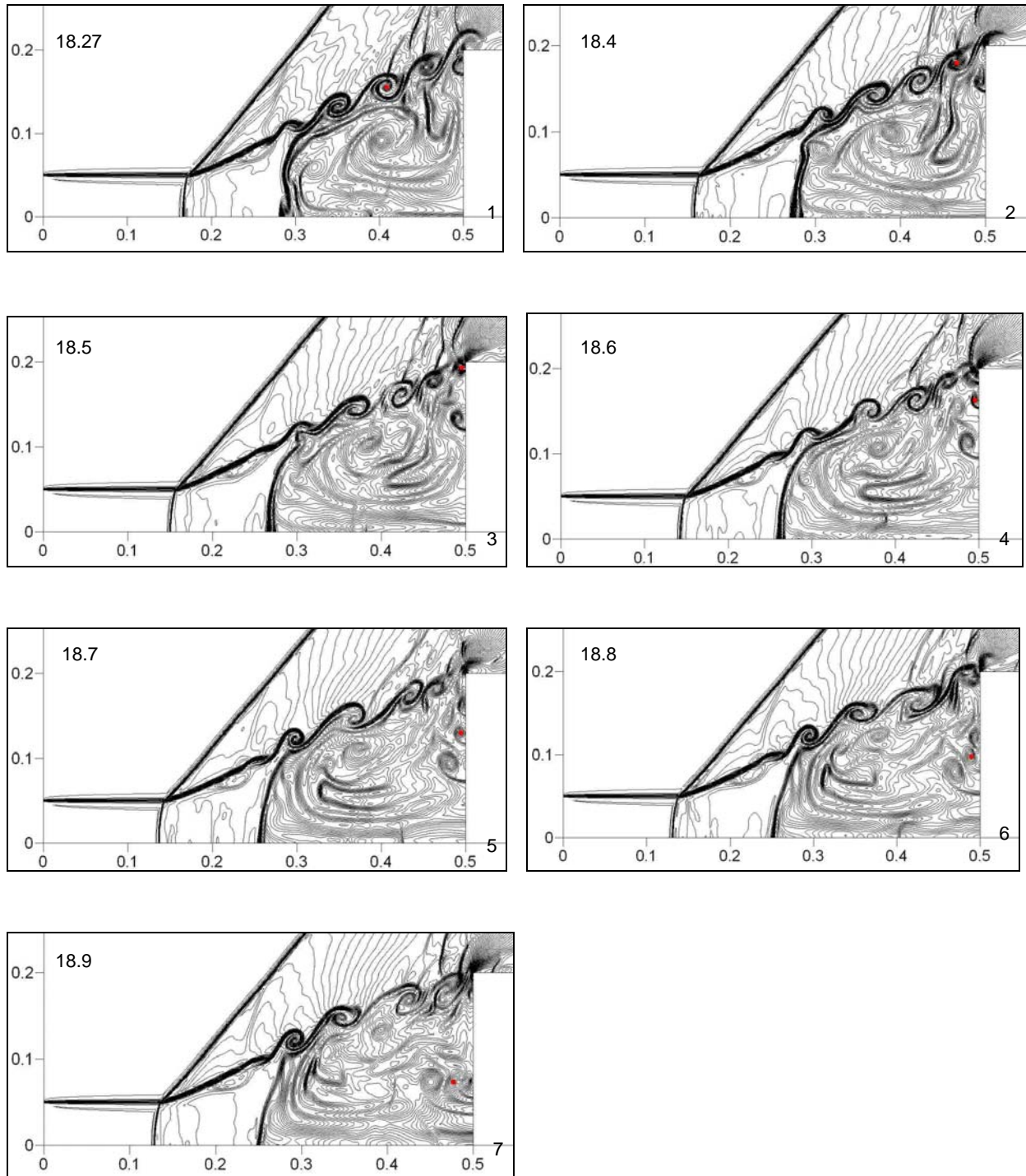


Fig. 3.2.12. Motion of the labeled vortex returning to flow separation area

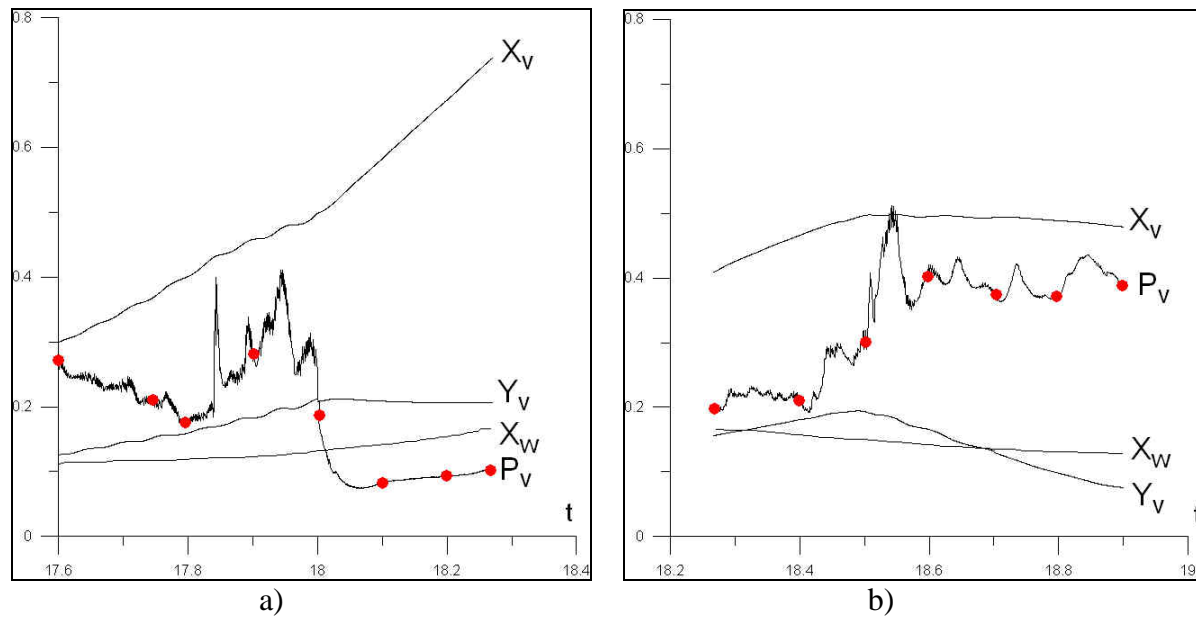


Fig. 3.2.13. History in time of vortex center coordinates X_v , Y_v , pressure in the vortex center P_v , and the bow shock coordinate X_w : a) - the case of the vortex leaving the calculation area; b) - the case of the vortex returning to flow separation area

possible two types of the vortex center dynamics. In one case when the flow from the heated area J_f is taken place the vortex is blown away along the body from the calculation area (Fig. 3.2.11). At the frames the center of considered vortex is defined by red point. In the second case when the flow from the heated area is locked by the contact discontinuity the vortices return to the separation area producing turbulent-like medium non-homogeneities (Fig. 3.2.12). Dynamics of vortex center coordinates X_v , Y_v and pressure value in the vortex center P_v for this two different types of vortex behavior is presented in Fig. 3.2.13. The red points correspond to the values of time moments for Fig. 3.2.11, 12.

Mechanism of heated area boundary pulsations

Mechanism of heated area boundary pulsations is analogical to described above mechanism of the bow shock position pulsations and is connected with relationship between circulation flow J_c and reversal flow J_r (Fig. 3.2.14). When the coordinate of the vertical contact boundary X_o is minimal the circulation flow J_c is generated and reversal flow J_r is maximal

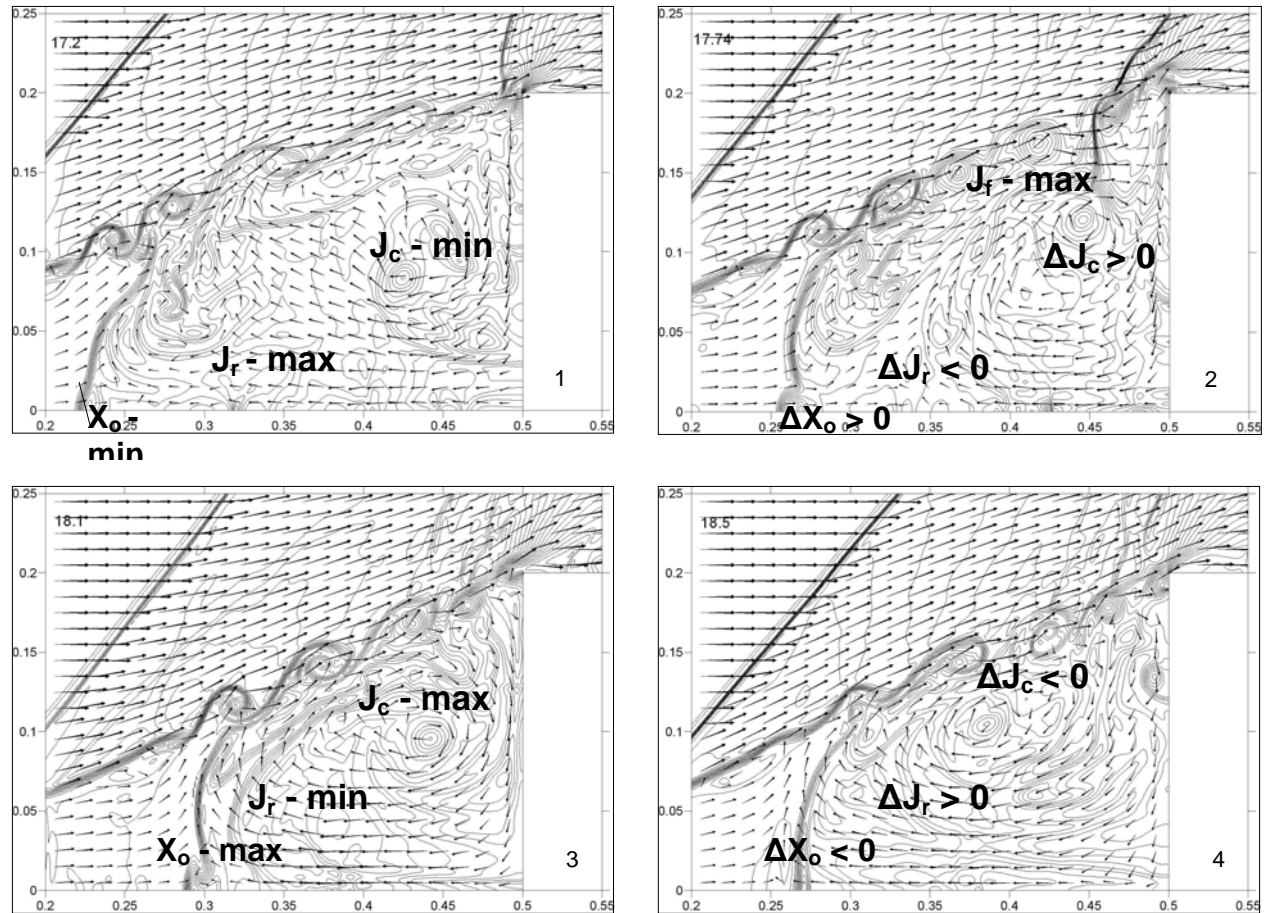


Fig. 3.2.14. Stages III. Mechanism of pulsation of heated area boundary based on relationship between circulation flow J_c and reversal flow J_r

(Fig. 3.2.14, frame 1). Then circulation flow J_c increases, reversal flow J_r decreases and the flow from the heated area J_f is taken place. The boundary of heated area is blown off by this flow (Fig. 3.2.14, frame 2). When the circulation flow J_c becomes maximal the contact discontinuity is stopped and locks the flow J_f (Fig. 3.2.14, frame 3). The reversal flow is being stronger and the contact discontinuity begins to move from the body with this flow (Fig. 3.2.14, frame 4). Then the process is repeated.

Dynamics of the determinant flow parameters

Time history of determinant flow parameters is presented in Fig. 3.2.15. These parameters are: the front drag force (divided to 2π) F ,

$$F = \int_0^{r_b} p r dr ,$$

(frame 1); stagnation pressure (frame 2); bow shock wave coordinate on the x-axis (frames 2, 3); heated area coordinate on the x-axis and x-coordinate of the maximal value of the flow temperature (frame 4). For the comparison our results [4] for less representative numerical technique are presented by red dotted line. In the stagnation pressure dynamics the peaks caused by the cumulating described above have been registered. The values of the attitudes of the peaks are not defined correctly both theoretically and numerically, numerical peaks may rich 10-30%. It is seen that the dynamics of all the pulsating flow parameters are in mutual connection with some shift in time.

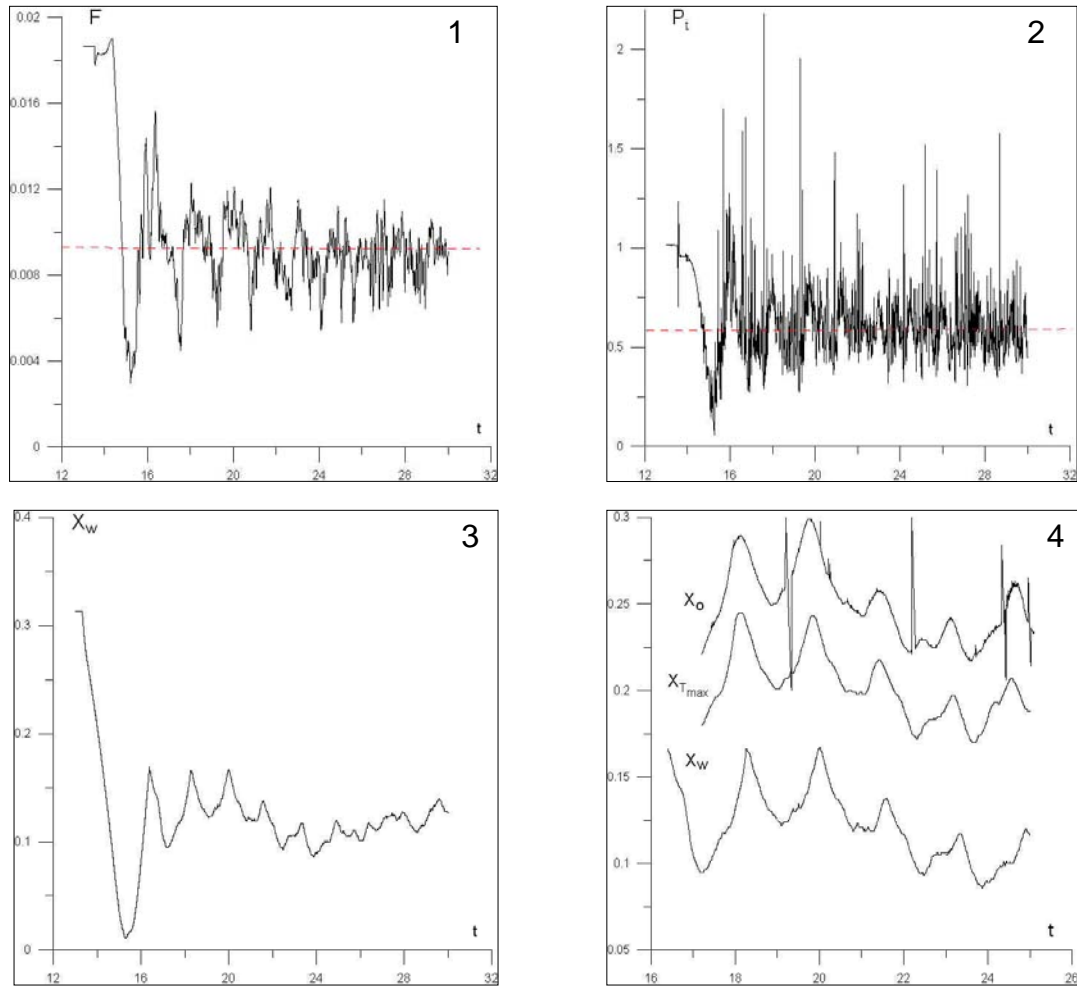


Fig. 3.2.15. History in time of the determinant flow parameters

Conclusions

Investigation of details of flow structure during the interaction of an infinite rarefied channel with cylinder shock layer is implemented:

- stochastic pulsation flow mode is established;
- main flow areas formation inside the shock layer including the flow separation region are investigated;
- new flow structure effects concerning generation of contact boundaries instabilities like Richtmayer-Meshkov instability are obtained;
- mechanism of pulsation based on relationship between circulation flow and reversal flow is revealed;
- flow dynamics parameters are characterized.

References to Section 3.2

1. O.A.Azarova, V.G.Grudnitsky, Yu.F.Kolesnichenko. Some Gas Dynamic Aspects of Flow Control by MW Energy Deposition // Proc. of the 6th Int. Workshop on Magnetoplasma Aerodynamics, Moscow, May 24-27. 2005. V.1. p.152-163.
2. Yu.F.Kolesnichenko, V.G.Brovkin, O.A.Azarova, V.G.Grudnitsky et al. Microwave Energy Release Regimes for Drag Reduction in Supersonic Flows // 40th AIAA Aerospace Meeting and Exhibit, Paper AIAA-2002-0353, p.1-13.
3. O.A.Azarova, V.G.Grudnitsky, Yu.F.Kolesnichenko. Numerical Analysis of a Thin Low Density Channel Effect on Supersonic Flow past Bodies with Wedge-Shaped Ledges // Mathematical Modeling. 2005. V.18. №10. P.104-112.
4. O.A.Azarova, V.G.Grudnitsky, Yu.F.Kolesnichenko. Stationary Streamlining Bodies by Supersonic Flow with an Infinite Thin Low Density Channel // Mathematical Modeling. 2006. T.18. №1. C.79-87.
5. Yu.F.Kolesnichenko, O.A.Azarova, V.G.Brovkin, D.V.Khmara et al. Basics in Beamed MW Energy Deposition for Flow/Flight Control // 42nd AIAA Aerospace Meeting and Exhibit, Paper AIAA-2004-0669, p.1-14.

6. V.G.Grudnitsky, Yu.A.Prohorchuk. One Approach to Constructing Difference Schemes with Arbitrary Order of Approximation of Differential Equations in Partial Derivatives // Dokl. AN SSSR, 1977, v. 234, №6, p.1249-1252.
7. V.I.Artem'ev, V.I.Bergel'son, I.V.Nemchinov, T.I.Orlova, V.A.Smirnov, V.M.Hazins. Variance of the Regime of Supersonic Streamlining an Obstacle via Arising the Thin Channel of Low Density // Mechanics of Liquids and Gases, 1989, №5, p. 146-151.
8. Partner Project 2014p. "Physics and Chemistry of MW Discharge in Gas Flows". 7th Quarter Report, January 2003, p.27.

3.3. Numerical analysis of a thin low density channel effect on supersonic streamlining for $M_\infty = 3$

The results of numerical modeling on a basis of Euler equations of a thin low-density channel – shock layer interaction for the Mach number of the oncoming airflow $M_\infty=3$ are presented. New flow structure effects concerning generation and dynamics of shock waves and contact discontinuities have been obtained. Dynamics of front drag force, stagnation parameters and bow shock wave coordinate has been researched. Comparison with the previous results for $M_\infty=1.89$ has been conducted.

3.3.1. Statement of the problem

The statement of the problem is analogical to [1-3, 5-7]. Numerical modeling is based on the Euler equations in the divergence form for ideal gas. Initial flow parameters corresponded to the normal conditions; the Mach number of oncoming flow was 3. On the entrance boundary the parameters of oncoming flow were used. The boundary conditions had a sense of reflection on the x-axis and on the body's boundaries, and of absence of the reflection on the exit boundaries.

An energy release was modeled via the entrance boundary conditions as the longitudinal channel of low density ρ_i , $\rho_i=\alpha_p\rho_0$ for $0\leq r\leq R$ and $x=0$, where R is the channel width, ρ_0 is the density in undisturbed flow, α_p - the degree of gas rarefaction in the channel. Other parameters were equal to those of undisturbed flow. The energy release is assumed to arise in the steady flow at the time moment t_i and its length was equal to Δl . In these calculations $R=0.05$.

The method employed is the original two-dimensional analog of the difference scheme [8] based on the approach of increasing difference scheme order of approximation on a minimal stencil [9]. The scheme is conservative and has the second order of approximation in space and in time. The boundary conditions were expressed via flux functions and included to the calculations without breaking the conservation laws in the calculation area.

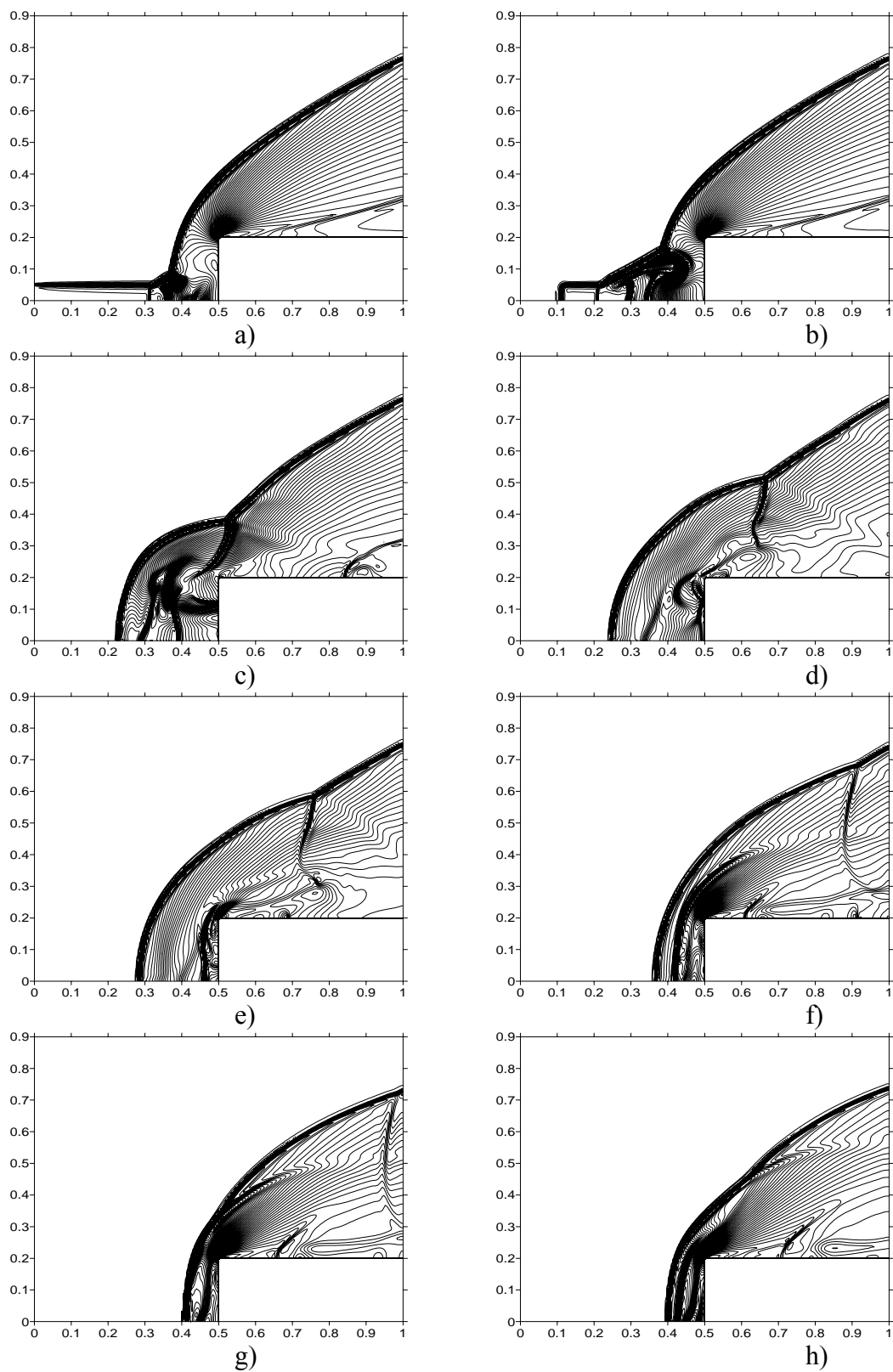


Fig.3.3.1. Density field dynamics during the interaction of low-density channel and cylinder shock layer; a) - $t=10.35$, b) - $t=10.58$, c) - $t=11.06$, d) - $t=11.25$, e) - $t=11.37$, f) - $t=11.54$, g) - $t=11.62$, h) - $t=11.70$

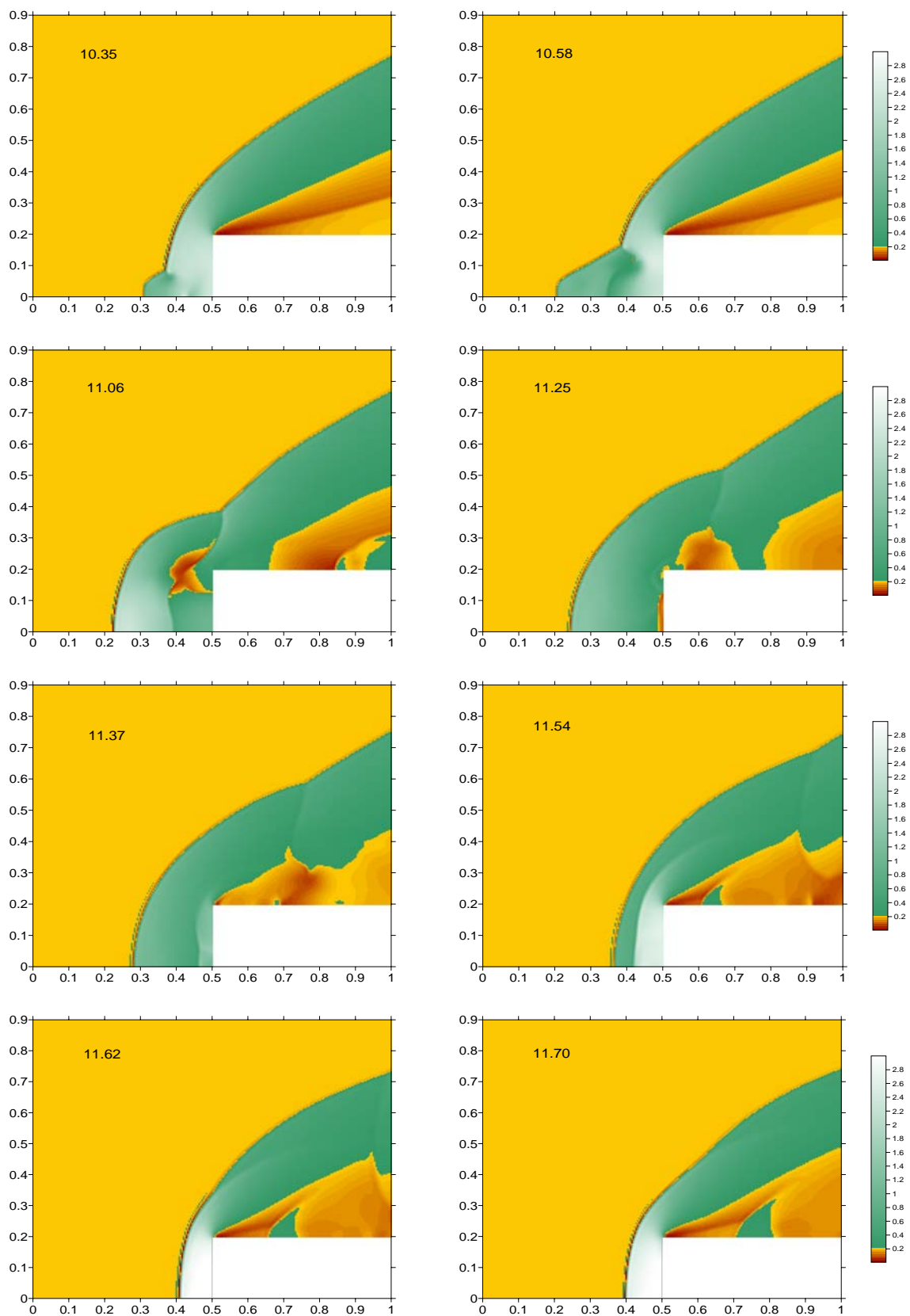


Fig.3.3.2. Pressure field dynamics during the interaction of low-density channel and cylinder shock layer

3.3.2. Calculation results

3.3.2.1. Cylinder flow symmetry. Blunt cylinder AD body is considered. In these calculations the radius of the body r_b is equal to 0.2. Flow isochors for the process of interaction of the longitudinal channel of low density with the shock layer are presented in Fig.3.3.1. Here $\alpha_p=0.3$, $\Delta l=0.8$, $t_i=10.01$. The according slides of the pressure field are presented in Fig.3.3.2. The values of time moments are indicated in the left upper corner of the slides. The base features of the process for $M_\infty=1.89$ [2,3,5,6] have been obtained, too: vortex flow generation (Fig.3.3.1a, 1b), additional shock wave generation (Fig.3.3.1b, 1c), temporary moving of the bow shock wave from its undisturbed steady position (Fig.3.3.1a-1e), weak shock wave generation near the above bodies boundary (Fig.3.3.1f), reflection of the additional shock wave from the front bodies surface (Fig.3.3.1d), and subsequent its confluence with the bow shock wave (Fig.3.3.1g). Additional shock wave is generated as the result of the interaction of the vortex flow with the axis of symmetry at the beginning stage of the interaction (Fig.3.3.1b). The vortex flow moves towards the body. As the result of eddy - front surface interaction another shock wave normal to the surface is established to appear. Analogical shock waves have been obtained earlier in the calculations of cavity streamlining by supersonic flow containing rarefaction channel [10]. In the bow shock flex point the new shock wave arises (Fig.3.3.1c). Additional shock wave moves to the front surface and reflects from it (Fig.3.3.1d). In the dependence upon the value of the channel length both two types of the reflection were established to be possible [1]. Here the regular reflection takes place. In the case of Mach reflection (with generation of triple configuration) the normal to the front body's surface shock wave cumulating on the axis was established to lead to the peaks arising in the dynamics of the stagnation parameters [1]. The reflected primary shock wave moves towards the bow shock wave and converges with it (Fig.3.3.1e-1g). In these calculations the confluence is accompanied by the generation of strong contact discontinuity moving towards the body and for some time interval this contact discontinuity is moving inside the shock layer (Fig.3.3.1h).

Dynamics of the stagnation pressure is presented in Fig.3.3.3a ($\alpha_p=0.3$, $\Delta l=0.8$). Note, that in these calculations $M_\infty=3$. In the opposite to the previous results the stagnation pressure increase is connected with the pressure growth behind the reflected additional shock wave. The dynamics for $M_\infty=1.89$ and $\alpha_p=0.4$, $\Delta l=0.8$ [2] is presented in Fig.3.3.3b. For comparison the stagnation pressure dynamics for the same parameters ($\alpha_p=0.4$, $\Delta l=0.8$) is presented in Fig.3.3.3c.

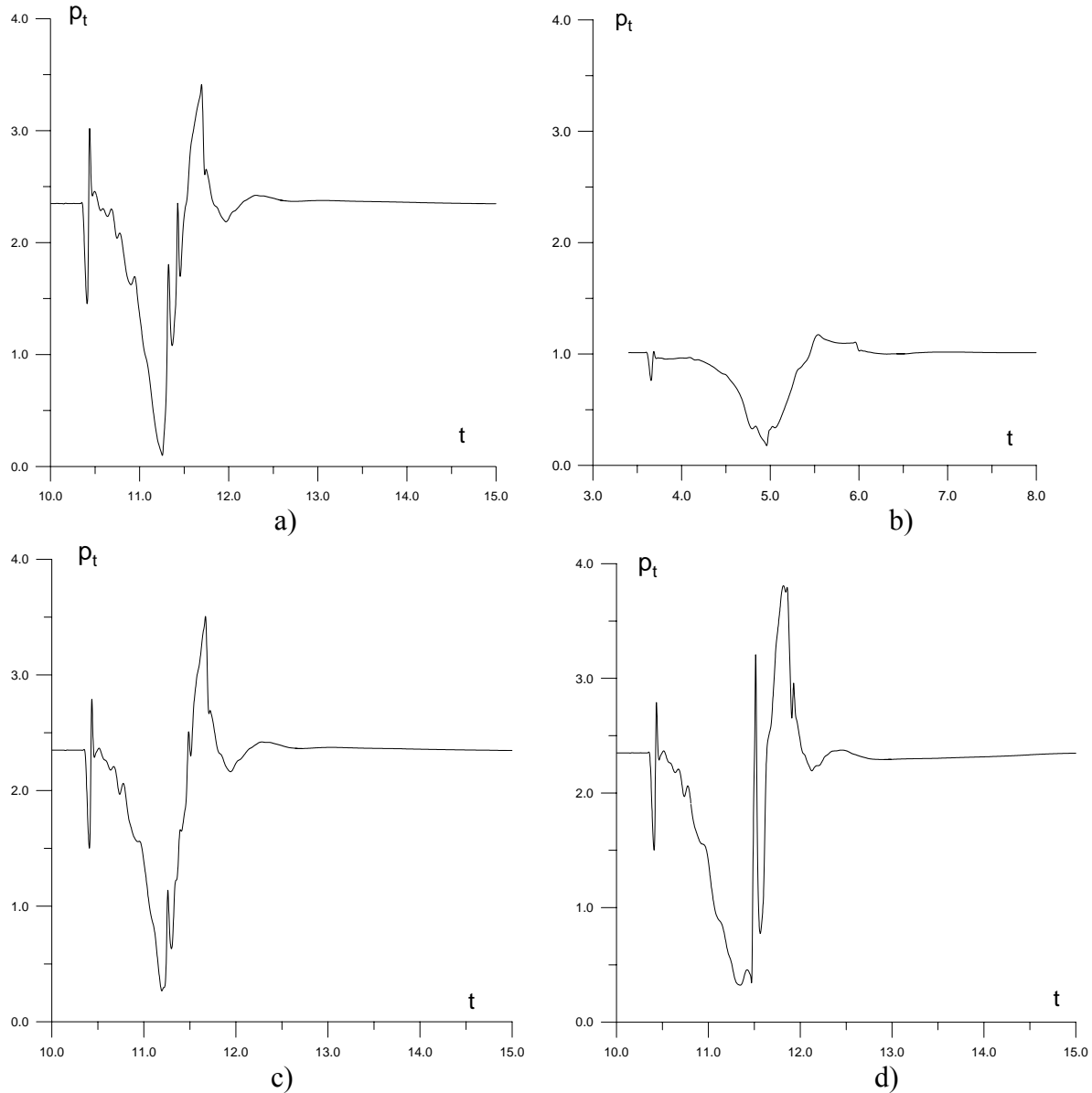


Fig.3.3.3. Dynamics of the stagnation pressure, cylinder flow symmetry; a) $\alpha_p=0.3, \Delta l=0.8$; b) results [1] for $M_\infty=1.89, \alpha_p=0.4, \Delta l=0.8$; c) $\alpha_p=0.4, \Delta l=0.8$; d) $\alpha_p=0.4, \Delta l=1.27$

It is seen that the pressure fall down is greater in these calculations. Stagnation pressure dynamics for more longitudinal channel ($\alpha_p=0.4, \Delta l=1.27$) is presented in Fig.3.3.3d. Here the normal to the front body's surface shock wave cumulating on the axis of symmetry is shown to take place.

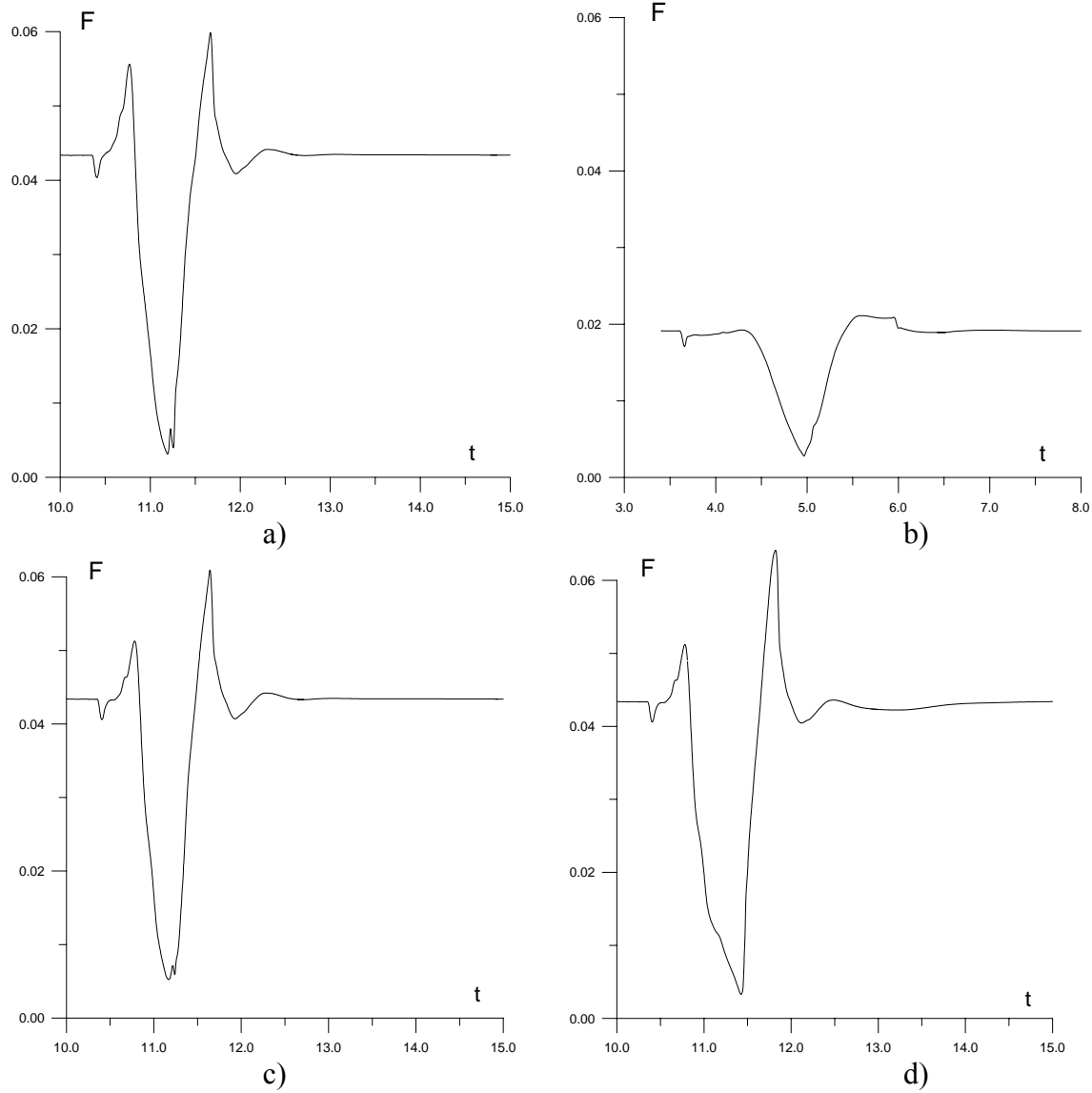


Fig.3.3.4. Dynamics of the front drag force, cylinder flow symmetry; a) $\alpha_p=0.3$, $\Delta l=0.8$, b) results [1] for $M_\infty=1.89$, $\alpha_p=0.4$, $\Delta l=0.8$; c) $\alpha_p=0.4$, $\Delta l=0.8$; d) $\alpha_p=0.4$, $\Delta l=1.27$.

Dynamics of the front drag force (divided to 2π) F and bow shock wave coordinate is presented in Fig.3.3.4, 5. Here

$$F = \int_0^{r_b} p \times r \times dr.$$

The parameters are the same as in Fig.3.3.3.

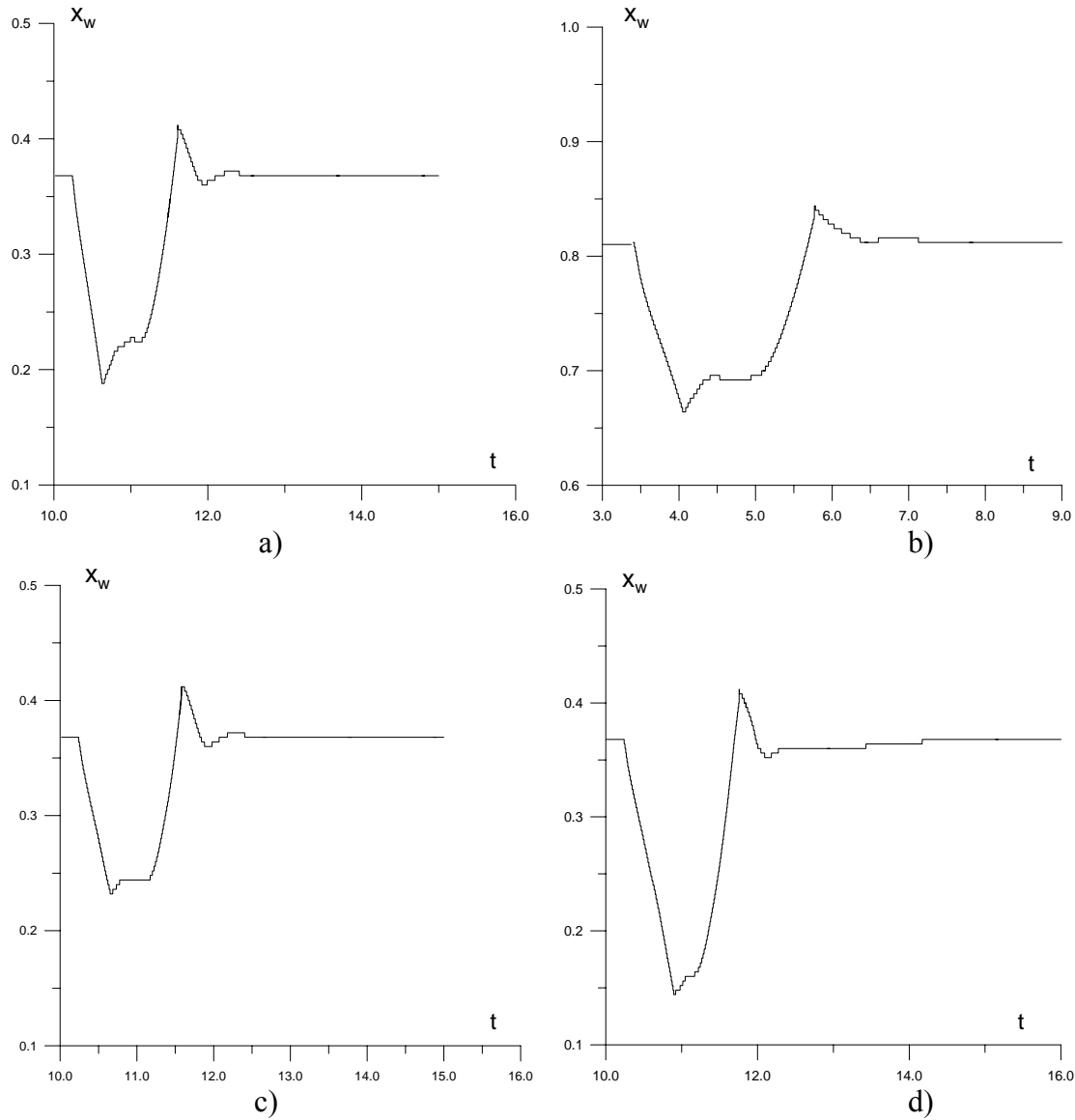


Fig.3.3.5. Dynamics of the bow shock wave coordinate, cylinder flow symmetry; a) $\alpha_p=0.3$, $\Delta l=0.8$, b) results [1] for $M_\infty=1.89$, $\alpha_p=0.4$, $\Delta l=0.8$; c) $\alpha_p=0.4$, $\Delta l=0.8$; d) $\alpha_p=0.4$, $\Delta l=1.27$.

In Table1 the relative changing of the considered parameters Δf is presented,

$$\Delta f = \frac{f_s - f_{\min}}{f_s},$$

f_s is the value of considered parameter for steady flow for p_t and F , x_s – difference between the bodies coordinate and the bow shock wave steady flow coordinate. For the bow shock wave

coordinate the absolute values of the velocity of its variation at the beginning stage V are presented, too.

Table 1. Results for $M_\infty=3$ (cylinder case).

Parameters Functions	$\alpha_p=0.3, \Delta l=0.8$	$M_\infty=1.89, \alpha_p=0.4, \Delta l=0.8$	$\alpha_p=0.4, \Delta l=0.8$	$\alpha_p=0.4, \Delta l=1.27$
Δp_t	0.958	0.825	0.886	0.862
ΔF	0.927	0.853	0.879	0.925
Δx_w	1.36	0.79	1.03	1.70
V	0.47	0.23	0.33	0.34

It is seen that stagnation pressure relative fall down is greater for greater M_∞ and smaller α_p . The same conclusions are follows from the Table 1 for the values of relative fall down of the front drag force, bow shock wave coordinate and the velocity of its variation (see 1-3 columns). Comparison of 3 and 4 columns shows that superposition of the stagnation pressure fall down and cumulating phenomenon decreases Δp_t . However in these calculations it has no effect on ΔF . It is possible to be connected with insufficient precision in drag force numerical representation. Δx_w is greater for longer channels. The reason of it is that the bow shock wave moves for longer time inside the rarefied channel with the same velocity (see the values of V in columns 3 and 4). Note that the value of the velocity at the beginning stage of the interaction process is defined by the decision of the Riemann problem and depends on the value of gas rarefaction degree in channel (and the Mach number of incoming flow) [7]. Note, that it is possible to compensate insufficient channel rarefaction by greater value of the channel length for obtaining the same value of the front drag force (see the values in columns 1 and 4).

3.3.2.2. Plane flow symmetry. Blunt rectangular AD body with the width value y_b equal to 0.2 is considered. Flow isochors for the process of interaction of the longitudinal channel of low density with the shock layer are presented in Fig.3.3.6. Here $\alpha_p=0.2, \Delta l=1.27, t_1=10.01$. In the opposite to the previous results for $M_\infty=1.89$ in these calculations (for $M_\infty=3$) it occurred to obtain generation of the additional shock waves inherent to cylinder flow. It is connected with the shorter distance

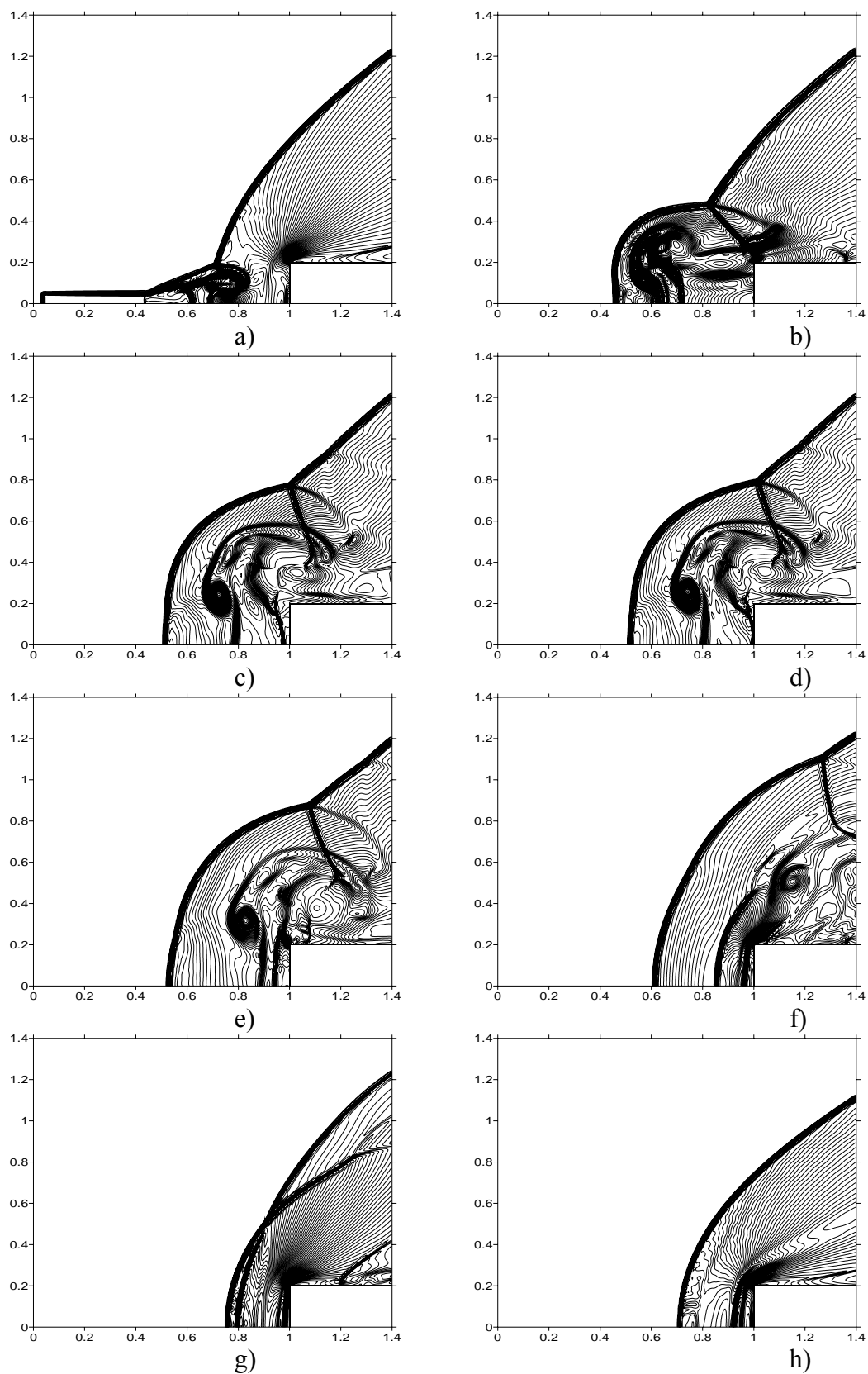


Fig.3.3.6. Density field dynamics during the interaction of low-density channel and plane shock layer; a) - $t=14.85$, b) - $t=15.52$, c) - $t=15.88$, d) - $t=15.91$, e) - $t=16.02$, f) - $t=16.34$, g) - $t=16.77$, h) - $t=17.50$

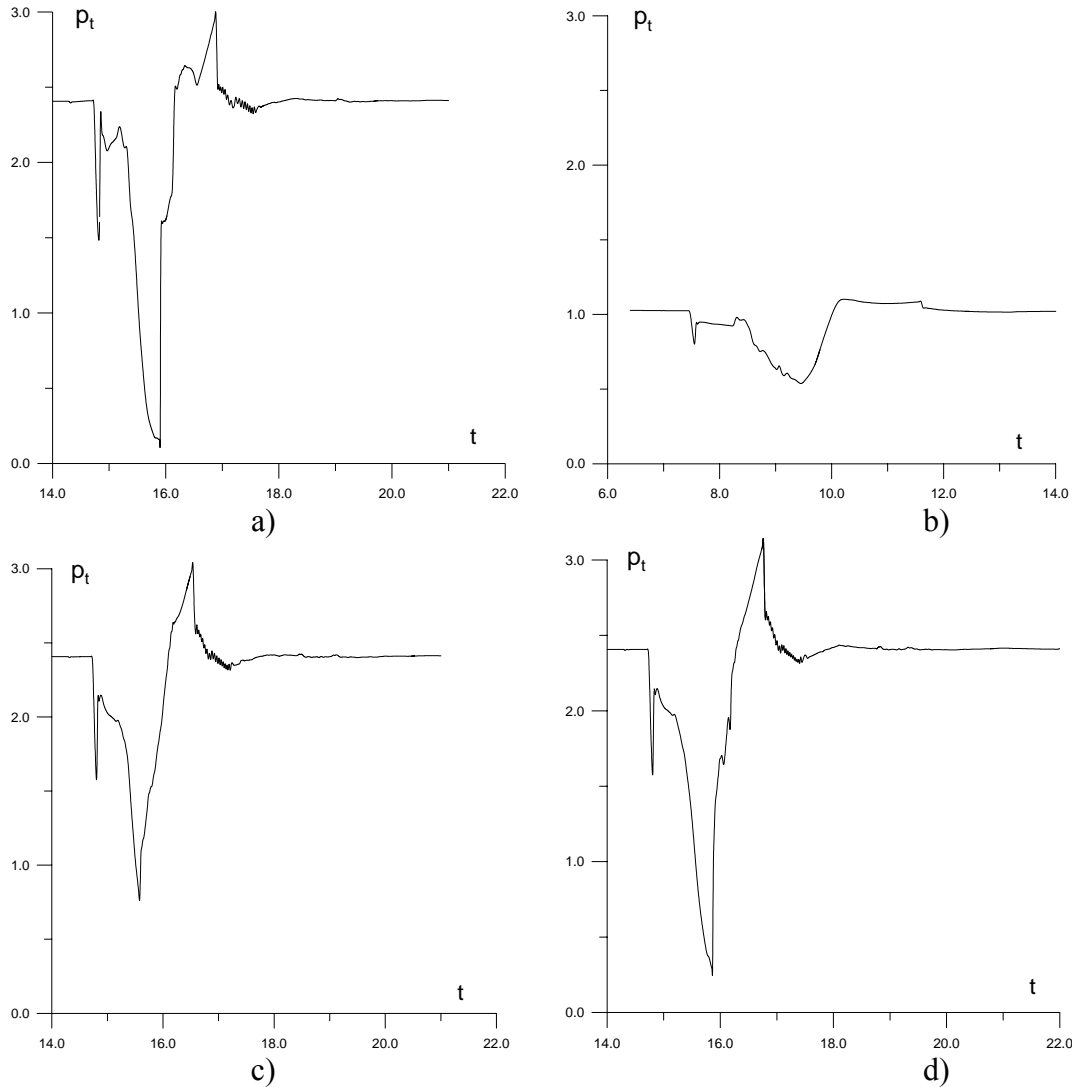


Fig.3.3.7. Dynamics of the stagnation pressure, plane flow symmetry; a) $\alpha_p=0.2$, $\Delta l=1.27$, b) results [2] for $M_\infty=1.89$, $\alpha_p=0.4$, $\Delta l=0.8$; c) $\alpha_p=0.4$, $\Delta l=0.8$; d) $\alpha_p=0.4$, $\Delta l=1.27$.

between the bow shock wave and the body in these calculations. The base features of the process for $M_\infty=1.89$ [3] have been obtained, too. Vortex flow and additional shock waves generate at the beginning stage of the interaction process (Fig.3.3.6a). Generation of the additional shock wave normal to the axes is accompanied by the contact discontinuity arising (Fig.3.3.6b, 6c). The additional shock wave and contact discontinuity move towards the body. Additional shock wave reflects from the front surface of the body (Fig.3.3.6d), “went through” the contact discontinuity (Fig.3.3.6e, 6f)

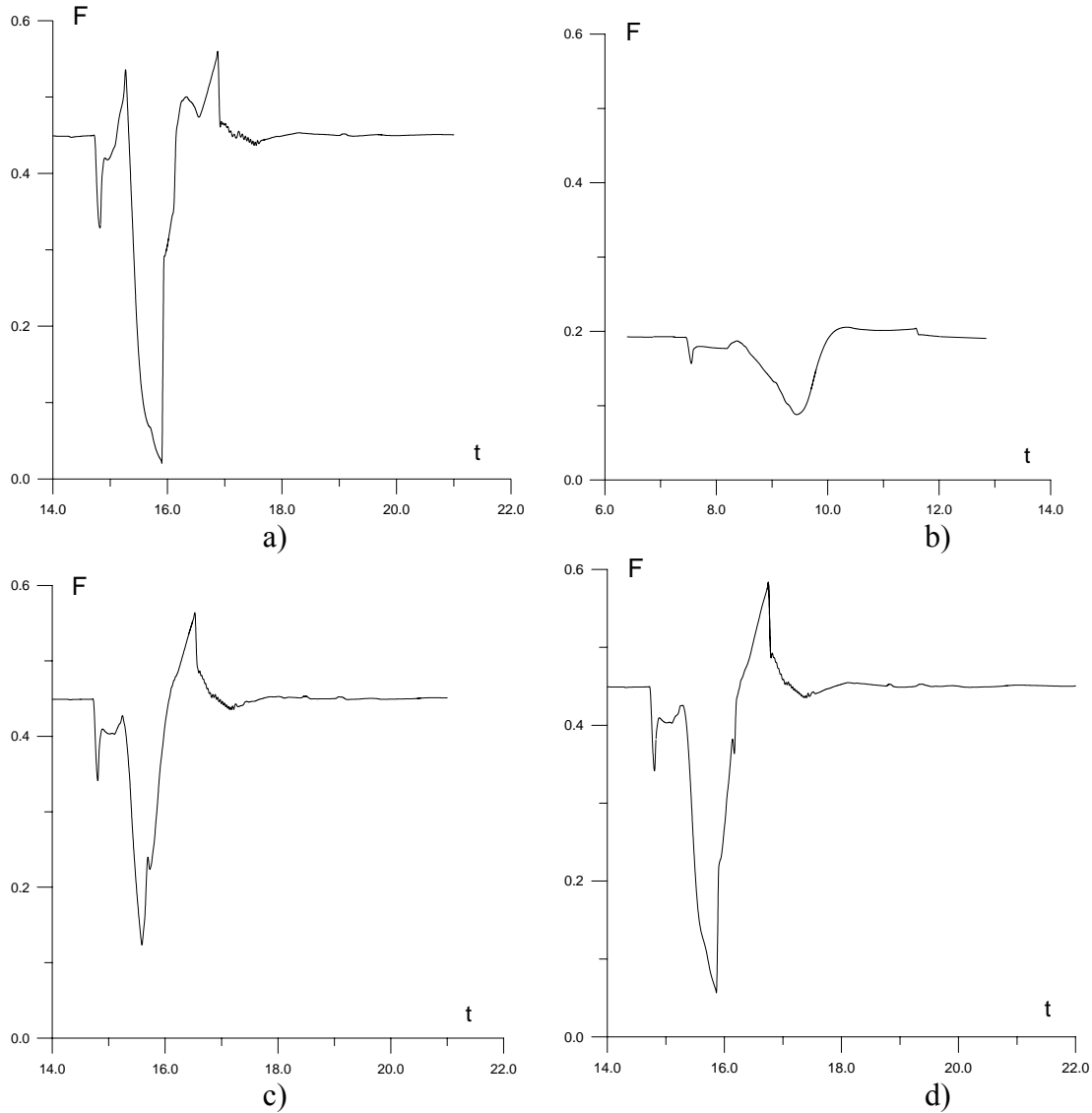


Fig.3.3.8. Dynamics of the front drag force, plane flow symmetry; a) $\alpha_p=0.2$, $\Delta l=1.27$, b) results [2] for $M_\infty=1.89$, $\alpha_p=0.4$, $\Delta l=0.8$; c) $\alpha_p=0.4$, $\Delta l=0.8$; d) $\alpha_p=0.4$, $\Delta l=1.27$

and subsequently confluent with the bow shock wave (Fig.3.3.6g). The confluence is accompanied by the generation of strong contact discontinuity moving towards the body and for some time interval two contact discontinuities are moving inside the shock layer (Fig.3.3.6g, 6h).

Dynamics of the stagnation pressure is presented in Fig.3.3.7a ($\alpha_p=0.2$, $\Delta l=1.27$). The results for $M_\infty=1.89$ and $\alpha_p=0.4$, $\Delta l=0.8$ [3] are presented in Fig.3.3.7b. For comparison the stagnation pressure dynamics for the same parameters ($\alpha_p=0.4$, $\Delta l=0.8$) is presented in Fig.3.3.7c.

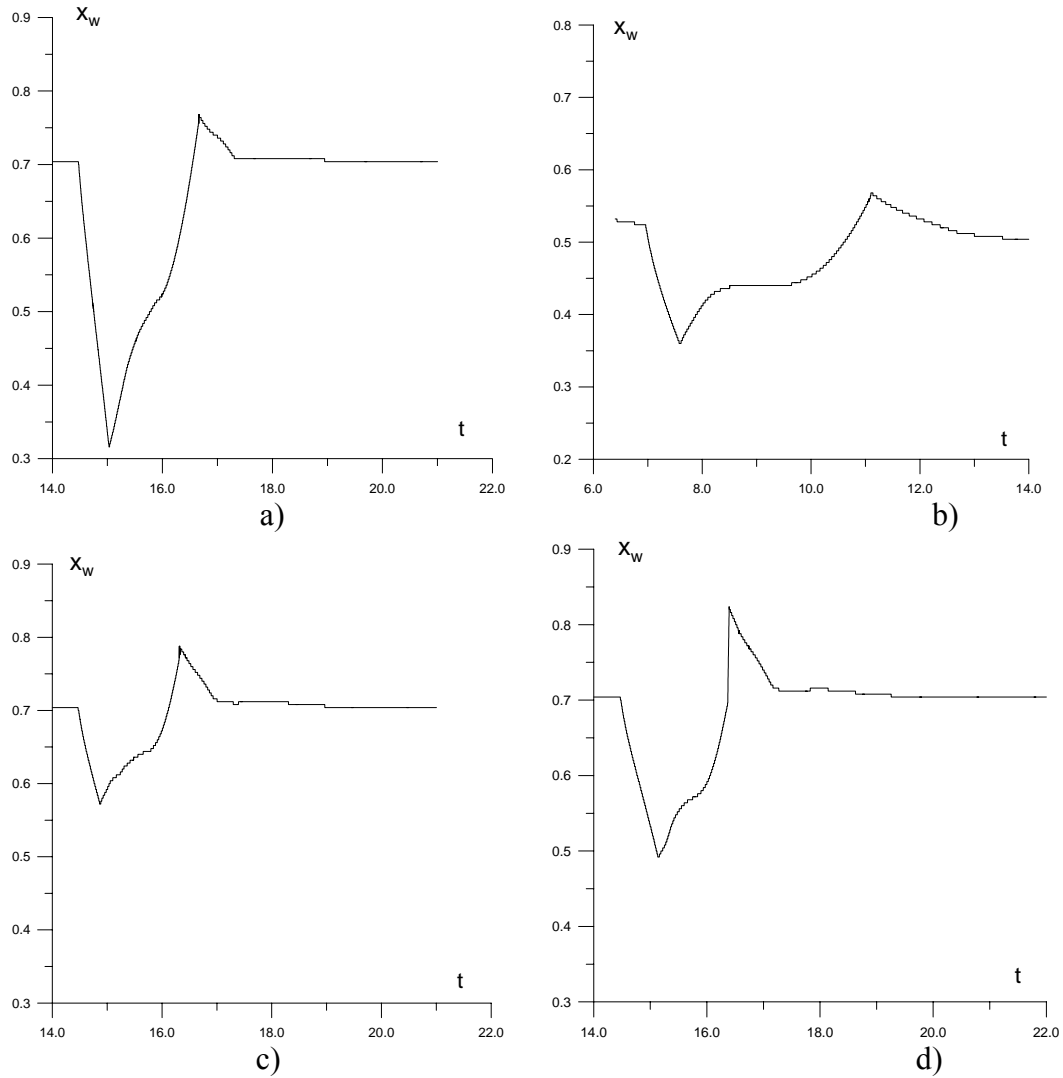


Fig.3.3.9. Dynamics of the bow shock wave coordinate, plane flow symmetry; a) $\alpha_p=0.2$, $\Delta l=1.27$, b) results [2] for $M_\infty=1.89$, $\alpha_p=0.4$, $\Delta l=0.8$; c) $\alpha_p=0.4$, $\Delta l=0.8$; d) $\alpha_p=0.4$, $\Delta l=1.27$

It is seen that the pressure fall down is greater in these calculations. Stagnation pressure dynamics for more longitudinal channel ($\alpha_p=0.4$, $\Delta l=1.27$) is presented in Fig.3.3.7d.

Dynamics of the front drag force F and bow shock wave coordinate is presented in Fig.3.3.8, 9. Here

$$F = \int_0^{y_b} p \times dy$$

The parameters are the same as in Fig.3.3.7. In the opposite to the previous results the stagnation pressure increase is connected with the pressure growth behind the reflected additional shock wave. The same behavior is obtained for the front drag force (Fig.3.3.7a, 8a).

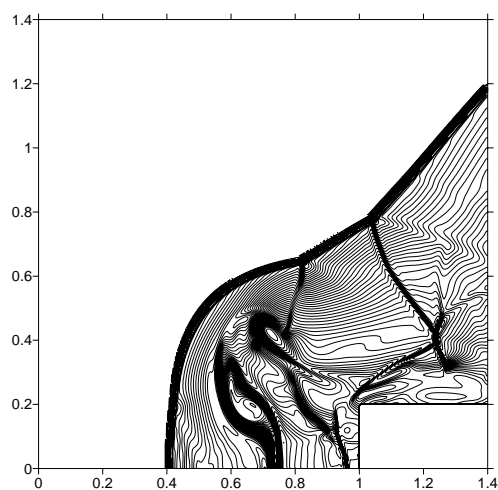
In Table2 the relative changing of the considered parameters Δf is presented.

Table 2. Results for $M_\infty=3$ (plane case).

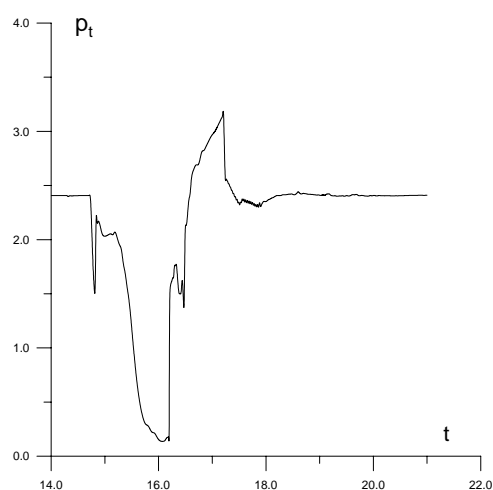
Parameters Functions	$\alpha_p=0.2, \Delta l=1.27$	$M_\infty=1.89, \alpha_p=0.4, \Delta l=0.8$	$\alpha_p=0.4, \Delta l=0.8$	$\alpha_p=0.4, \Delta l=1.27$
Δp_t	0.958	0.474	0.684	0.897
ΔF	0.954	0.544	0.726	0.875
Δx_w	1.31	0.33	0.45	0.72
V	0.70	0.25	0.33	0.33

It is seen that like as in cylinder case stagnation pressure relative fall down is greater for greater M_∞ and smaller α_p . The same conclusions follow from the Table 2 for the values of relative fall down of the front drag force, bow shock wave coordinate and the absolute value of velocity of its variation (see 1, 2 and 4 columns). Δx_w is greater for longer channels (values in columns 3, 4). The value of the velocity is defined by the decision of the Riemann problem and depends on the value of rarefaction degree (and the Mach number of incoming flow) and doesn't depend on the flow symmetry [1] (compare the values from Table 1).

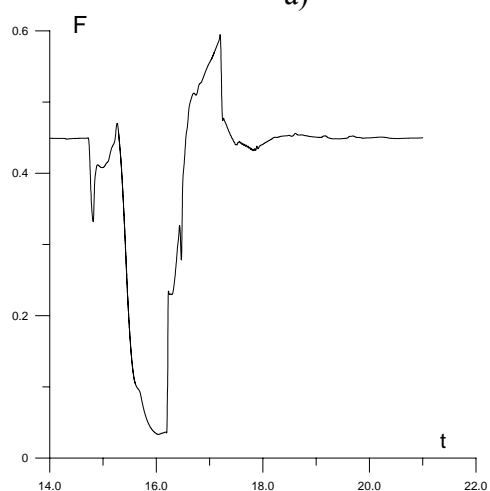
In Fig.3.3.10 the results for the long channel are presented ($\alpha_p=0.3, \Delta l=2.0$). Isochors for the density field in the time moment before the reflection of the additional shock wave from the front surface are presented in Fig.3.3.10a. In Fig.3.3.10b-10d the stagnation pressure, front drag force and bow shock wave coordinate dynamics is presented accordingly. It is seen that the stagnation pressure and drag force growth is defined by the pressure increase behind the reflected additional shock wave. For considered channel parameters ($\alpha_p=0.2\div 0.4, \Delta l=0.8\div 2.5$) Mach reflection of the additional shock wave doesn't observed. However, the generation of the simple wave of compression normal to the front surface has been obtained (Fig.3.3.10e). It suggests that Mach reflection might be possible to take place for more rarefied and longer channels and/or greater Mach numbers of the oncoming flow.



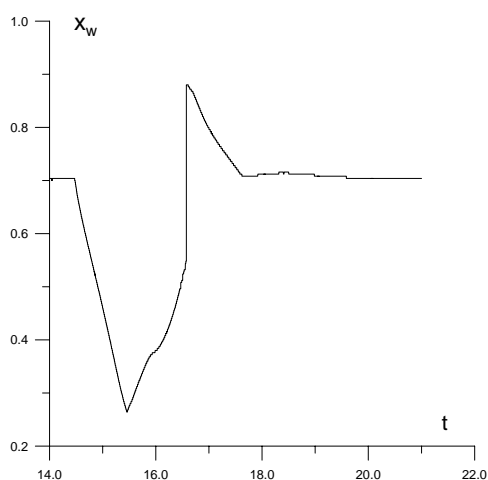
a)



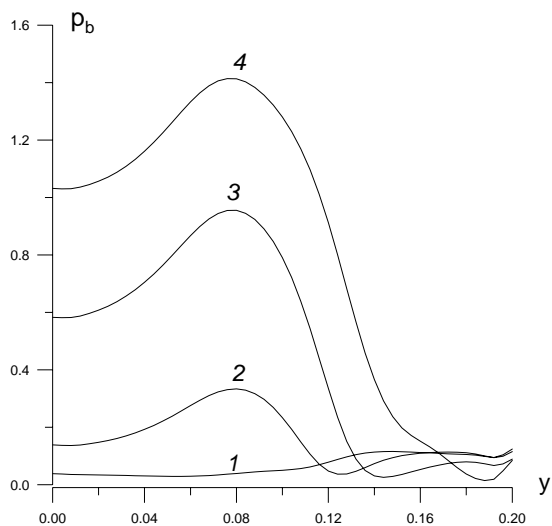
b)



c)



d)



e)

Fig.3.3.10. Calculation results for $\alpha_p=0.3$, $\Delta l=2.0$; a) density field, $t=16.16$; dynamics of b) stagnation pressure, c) front drag force, d) bow shock wave coordinate; e) pressure on the front surface, curve 1 - $t=16.0$, curve 2 - $t=16.005$, curve 3 - $t=16.01$, curve 4 - $t=16.015$

Note, that in the plane case this fact doesn't cause the peaks in the stagnation pressure dynamics because the process of shock wave cumulating on the axis of symmetry doesn't occur in the plane case.

Conclusions

Numerical modeling on a basis of Euler equations of a thin low-density channel – shock layer interaction for Mach number of oncoming flow $M_\infty=3$ has been conducted. Flow structure effects established are:

- arising additional shock waves and contact discontinuities both in cylinder and plane cases in comparison with the previous results for $M_\infty=1.89$ [3];
- generation of additional shock wave normal to the front surface as the result of eddy - front surface interaction;
- arising additional shock waves and contact discontinuities in plane case similar to those for cylinder case;
- peaks generation in the dynamics of the stagnation pressure (cylinder case) as the result of Mach reflection of the additional shock wave;
- simple compression wave normal to the front surface generation as the result of eddy - front surface interaction (plane case);
- stagnation pressure growth after its fall down is caused by additional shock wave reflection from the front surface of the body (for the rarefaction degree $\alpha_p=0.2\div 0.3$);
- stagnation pressure relative fall down is greater for greater M_∞ and smaller α_p ;
- the same is taken place for the front drag force, bow shock wave coordinate and the velocity of its variation;
- relative bow shock wave coordinate variation is greater for longer channels;
- velocity of bow shock wave coordinate variation at the beginning stage depends on the value of rarefaction degree (and the Mach number of oncoming flow) and doesn't depend on flow symmetry;
- it is possible to compensate insufficient channel rarefaction by greater value of the channel length for obtaining the same value of the front drag force;

Some of the conclusions confirm our previous results.

References to Section 3.3

1. Physics and Chemistry of MW Laser-Induced Discharge in Gas Flows and Plasma Jets, 2005, Annual Report, Partner Project 3058p.
2. O.A. Azarova, V.G. Grudnitsky, Yu. F. Kolesnichenko. Some Gas Dynamic Aspects of Flow Control by MW Energy Deposition // Proc. of the 6th Int. Workshop on Magnetoplasma Aerodynamics, Moscow, May 24-27. 2005. V.1. P. 152-163.
3. Yu. F. Kolesnichenko, O.A. Azarova, V.G. Brovkin et al. Microwave Energy Release Regimes for Drag Reduction in Supersonic Flows // 40th AIAA Aerospace Meeting and Exhibit, Paper AIAA-2002-0353. P.1-13.
4. V.I. Artem'ev, V.I. Bergel'son, I.V. Nemchinov, T.I. Orlova, V.A. Rybakov, B.A. Smirnov, V.M. Hasins. Generation of New Flow Structures Caused by Density Perturbation in Thin Longitudinal Channels in front of Shock Waves // Mathematical Modeling. 1989. V.1. №8. P.1-11
5. O.A. Azarova, V.G. Grudnitsky, Yu. F. Kolesnichenko. Numerical Analysis of a Thin Low Density Channel Effect on Supersonic Flow past Bodies with Wedge-Shaped Ledges // Mathematical Modeling. 2005. V.18. №10. P.104-112
6. O.A. Azarova, V.G. Grudnitsky, Yu. F. Kolesnichenko. Stationary Streamlining Bodies by Supersonic Flow with an Infinite Thin Low Density Channel // Mathematical Modeling. 2006. T.18. №1. C.79-87
7. Yu. F. Kolesnichenko, O.A. Azarova, V.G. Brovkin, D.V. Khmara et al. Basics in Beamed MW Energy Deposition for Flow/Flight Control // 42nd AIAA Aerospace Meeting and Exhibit, Paper AIAA-2004-0669, p.1-14
8. O.A. Azarova. Difference Scheme with Shock Extracting for Calculation of Explosion Flows in Liquids and Gases // Acoustics of Inhomogeneous Media. Dynamics of Solid Medium. 105, Novosibirsk, 1992, p. 8-14
9. V.G. Grudnitsky, Yu. A. Prohorchuk. One Approach to Constructing Difference Schemes with Arbitrary Order of Approximation of Differential Equations in Partial Derivatives // Dokl. AN SSSR, 1977, v. 234, №6, p.1249-1252
10. V.A. Lashkov, I.Ch. Mashek, Yu.I. Anisimov, V.I. Ivanov, Yu. F. Kolesnichenko, O.A. Azarova. Method of Vortex Flow Intensification under MW Filament Interaction with Shock Layer on Supersonic Body // 44th AIAA Aerospace Meeting and Exhibit, Paper AIAA-2006-404, p.1-13

Section 4. Plasmadynamic experiments

In the frame of the project activity of the grope from SPbSU was carrying out in the two main directions:

- investigation of interaction of MW discharge with gasdynamic structures near bodies;
- improvement of experimental facility.

4.1. Experimental investigation of influence of MW discharge on aerodynamic drag of different bodies

Experiments have proved that the main reason leading to a substantial reduction of the blunted bodies' aerodynamic drag at their interaction with the microwave discharge is the formation of gas vortex motion in the shock layer. Therefore, it is obvious that to obtain a more significant effect (regarding the body's drag reduction) it is necessary to increase life span and intensity of the vortex. Special experimental models were created for this purpose. Vortex characteristics can be controlled, for instance, by means of gas injection in the shock layer on the body. Models, the front surface of which is formed to support gas vortex motion, have been analyzed as well.

4.1.1. Intensification of gas vortex motion in the shock layer on the body

4.1.1.1. Models design

Experimental models to study the ways of intensification of gas vortex motion are demonstrated in Fig. 1.

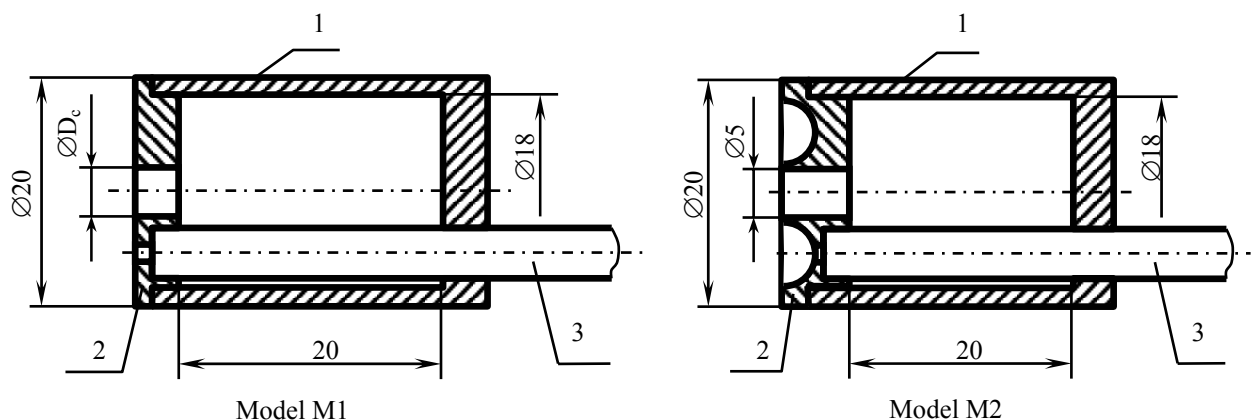


Fig. 1. Experimental models

M1 model represents a blunt cylinder (body 1) with a hollow inside, which is connected to the external atmosphere by means of hole D_c on the front surface. In the course of the experiment, the air accumulates in the hollow under the stagnation pressure of the working flow. When the plasmoid interacts with the shock layer on the model, drop of a pressure on the front surface makes the air to flow out of the hollow. Flowing-out of the hollow the air favors gas vortex motion in the shock layer.

The hollow volume was calculated in the way that the pressure in it should not change for more than 10-15% during the interaction of the microwave discharge with the shock layer. Actual changes of pressure on the model's front surface obtained from the experiments were used for calculations. The model has replaceable washers 2 with different hole diameters, which allows to examine the influence of the gas injection intensity it exerts upon the vortex parameters. Models with a hole diameter $D_c = 2.5$ and 5 mm have been made. The model is mounted on support 3, inside which a pressure transducer is placed. Model M2 looks similar to model M1 but its front surface has a toroidal recess.

4.1.1.2. Results of experimental research of models with gas injection

Experiments were fulfilled with using X polarization of MW energy. Impulse MW power was 200 kW. Impulse time duration was 1.5 mcs.

Since a hole to inject gas is located on the model axis (models M1 and M2), the pressure gauge is shifted by 6 mm from the axis. In order to check if readings of the shifted gauge and that on the model axis differ from each other, a special experiment has been conducted. The trials have shown that for M1 model the pressure measurement results on the model axis coincide with the readings of the shifted gauge within the limits of accuracy of the experiment.

Fig. 2 shows relative pressure behavior inside the model (in the hollow) under interaction of plasmoid with bow shock wave. The pressure in the hollow is practically equal to that in the stagnation point on the model (blunt cylinder). The pressure does not change very much during plasma-model interaction. Oscillation of the pressure can be seen on the Fig. 2. Oscillation frequency is about 5 kHz. Amplitude of the oscillation in the hollow with $D_c=5$ mm is above that in the model with $D_c=2,5$ mm. Interaction of microwave discharge with shock layer on the model disturbs the pressure in the hollow but not very much. Practically the pressure does not change.

Thus it is possible to say that the pressure gauge mounted on the model with a shift measures the stagnation pressure in the critical point on the body.

Results of experimental research of models M1 and M2 are given in Fig. 3. The Y-axis represents a relative pressure (stagnation pressure-to- static pressure relation), while the X-axis represents a time delay after-microwave pulse.

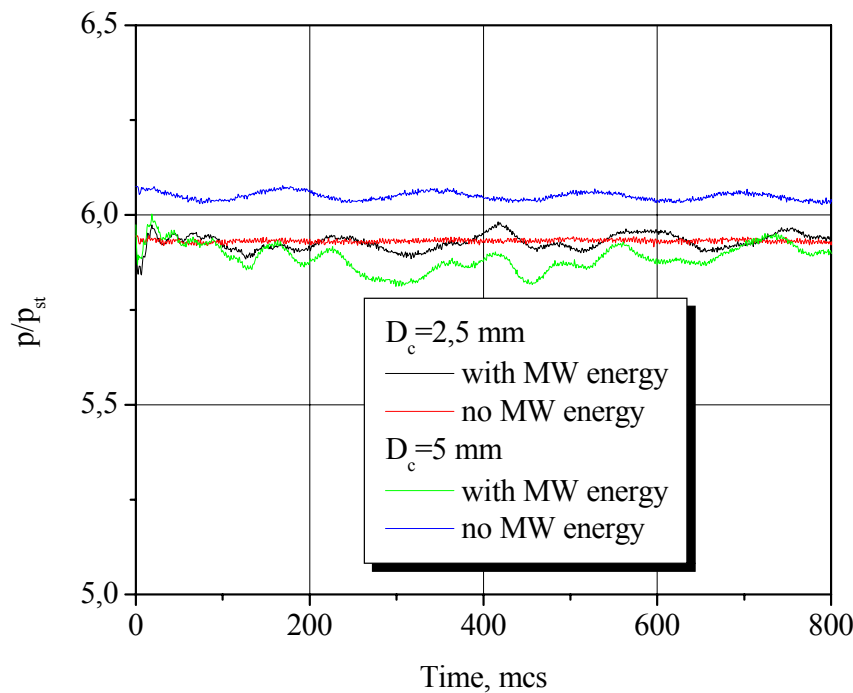


Fig. 2. Pressure behavior in the hollow

It is notable that the initial phase of the process of plasmoid-to-shock layer interaction evolves in the same way both on a blunted cylinder and on models M1 and M2 with a hole. Obviously, one should expect a significant gas injection for models M1 and M2 after a substantial pressure drop on the model's front surface. Therefore, all differences in the pressure gauge readings start after the pressure passes its minimum.

Whereas for the blunt cylinder the restoration of normal airflow is accompanied by a significant pressure surge, for model M1 with a hole of 2.5 mm this pressure increase is smoothed and for model M2 one can observe that the restoration of pressure to its normal value is delayed to 400 mcs. The pressure is restored with oscillations in model M2, it is in average lower than for model M1 with a hole of 5 mm, and this process finishes by the 600th mcs.

In this way, gas injection opposite to the working flow and a specially formed front surface of the body increase the life span and intensity of vortex motion in the shock layer, caused by the interaction of the excited heated gas area after the microwave discharge with the shock wave on the body.

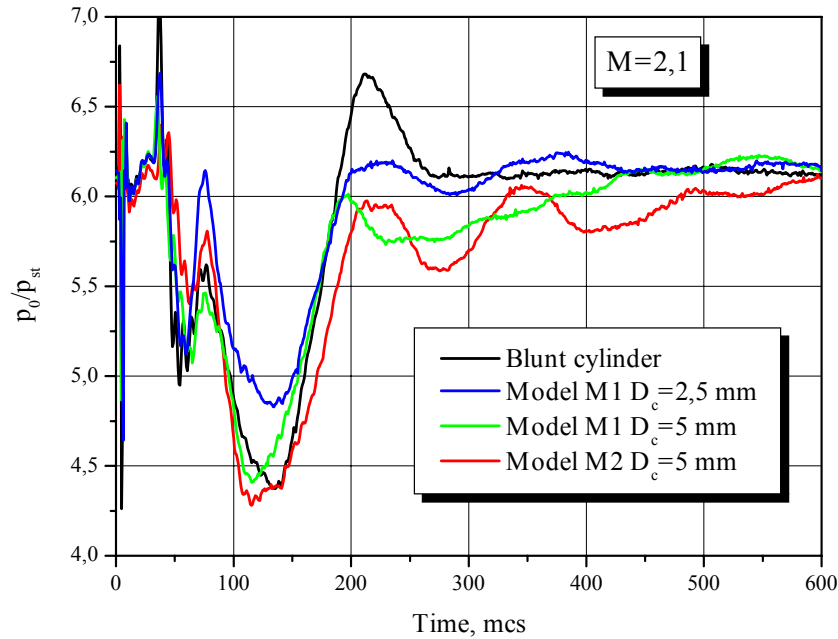


Fig. 3. Results of investigation of M1 and M2 models

Impulse received by the model during its interaction with the microwave discharge has been calculated,

$$I = \int_t \left(\frac{P_0 - P}{P_{st}} \right) dt,$$

where P_0 – stagnation pressure on the model at normal stationary airflow,

P_{st} – static pressure in the flow,

P - stagnation pressure during interaction with the microwave discharge.

Measurements have demonstrated that an impulse received by the blunt cylinder in the process of interaction with the microwave discharge is about 150 mcs. The pulse grows linearly with the increase of a diameter of hole D_c through which gas is injected towards the flow. When a hole diameter is 5 mm, the impulse on the model increases by 1.5 times as compared to the

impulse on the blunt cylinder. Use of the toroidal recess and gas injection causes the pulse to increase even more. The pulse on model M2 is 1.8 times more than that on the blunt cylinder.

4.1.2. Experimental investigation of drag of sphere with gas injection

Influence of gas injection (counter flow) under MW discharge condition was studied. Experimental model was a sphere of 25 mm diameter which had an orifice of 1 mm diameter for gas injection upstream the working flow (see Fig. 4). The model consisted of a body 1 with a cavity inside it. The cavity was used as a fore-chamber for injected gas. It was connected with air feeding tube 3 and pressure measuring tube 4. The model was placed on a sting 2 with pressure transducer allocated inside it.

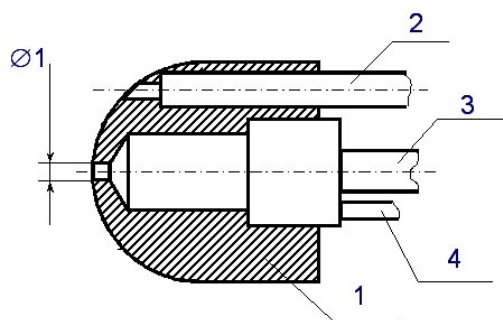


Fig. 4. The model M3 for investigation of drag under condition of counter flow

The transducer measured pressure in the oncoming working flow. The inlet of pressure transducer was placed on the distance of 4 mm from the axis of the model.

The experiments were conducted in the working flow which had static pressure about 40 Torr and Mach number 2.1.

Shadow pictures of streamlining of the model without gas injection can be seen on Fig. 5.

On about 70 mcs heated after MW discharge domain of air begins to interact with shock layer on the body. Discontinuity decay can be seen on the picture. An arisen shock wave moves along the heated channel. A vortex originates from shear layers and extends. Disturbed area in the shock layer becomes broader.

Shadow pictures of streamlining of sphere under condition of both MW discharge and air injection upstream the working flow are presented on Fig. 6.

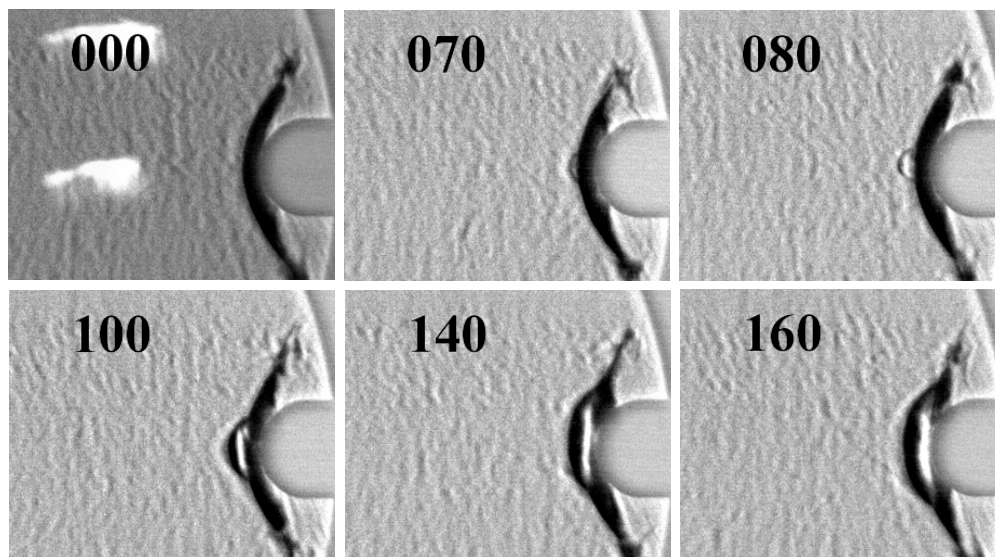


Fig. 5. Streamlining of the sphere without air injection

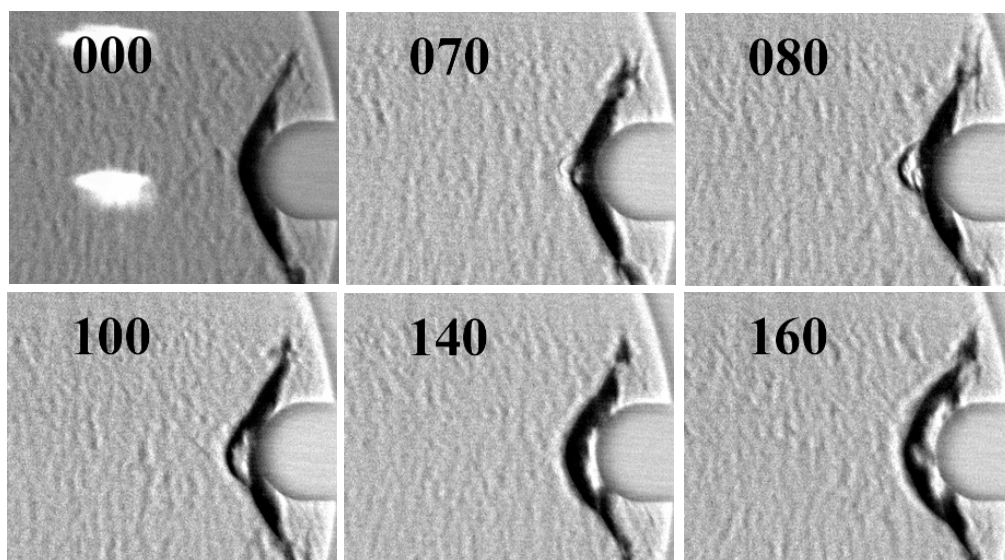


Fig. 6. Streamlining of sphere under condition of MW discharge and counter flow

The same phases of the interaction of MW discharge with shock layer on the model can be seen as in the case of streamlining of the sphere without counter flow. But it should be noted that standoff of the bow shock wave in the last experiments is bigger then in the tests of sphere under condition without counter flow. So the last experiments showed that joint action of MW discharge and counter flow reinforces drag reduction of the model. This result is presented on Fig. 7, where time evolution of pressure on the sphere is shown for different gas flow through the model's orifice.

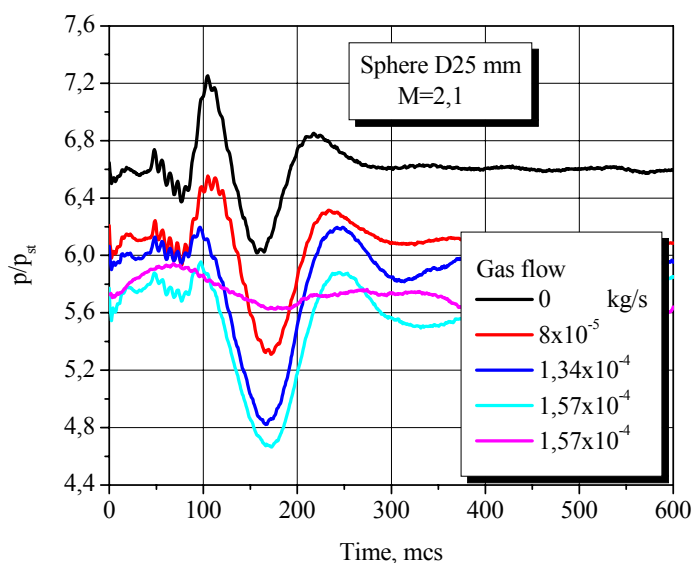


Fig. 7. Time evolution of pressure on the model under condition of MW discharge and counter flow

It is seen that increasing of air flow leads uniformly to decreasing of the pressure on sphere's surface. Magenta line shows pressure behavior on the model under gas flow 1.57×10^{-4} kg/s without MW discharge.

While gas flow is increasing from zero to 1.57×10^{-4} kg/s, value of relative pressure is falling from 6.6 to 5.7. This result can be seen on Fig. 8.

Microwave discharge leads to a headlong fall of pressure during 50-70 mcs. Then the pressure is restoring its usual level. Impulse which the sphere obtained during plasma-body

interaction was calculated using formula $I = \int_t \left(\frac{P_0 - P}{P_{st}} \right) dt$, where P_0 – usual stagnation pressure on the model with neither MW discharge nor counter flow. Results of calculation are shown on Fig. 9.

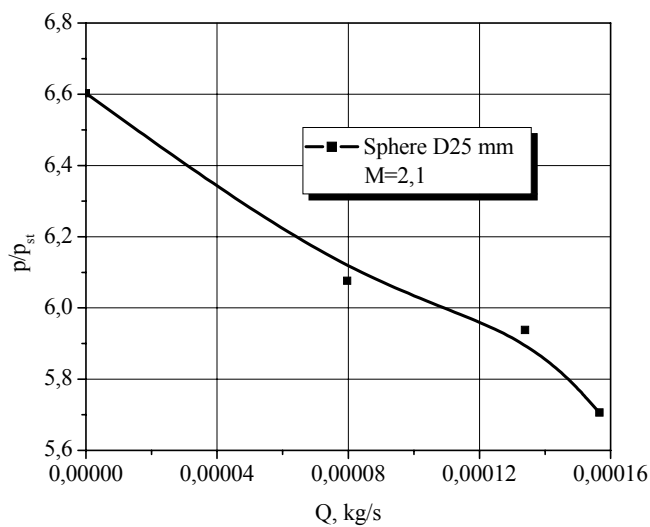


Fig. 8. Influence of gas injection.

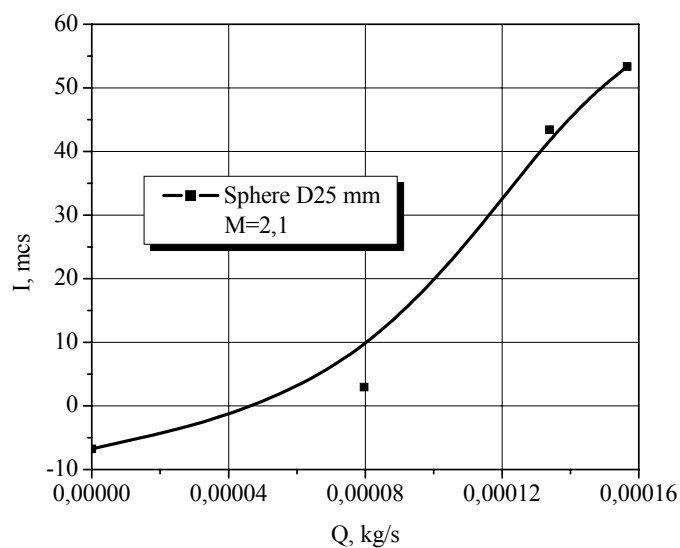


Fig. 9. Impulse which sphere gets during MW discharge to bow shock wave impact

Results of investigations showed that the impulse was growing uniformly with increasing of gas injection.

4.1.3. Investigation MW discharge influence on streamlining of a sphere with a spike

Influence of joint action of MW discharge and gas injection through a spike was investigated on the model M4. The model is shown on Fig. 10. Experimental model M4 was similar to the model M3 (see the Fig. 4) but it had a spike 25 mm long. The spike presented a tube with internal channel of 0.5 mm diameter (external diameter was 1 mm).

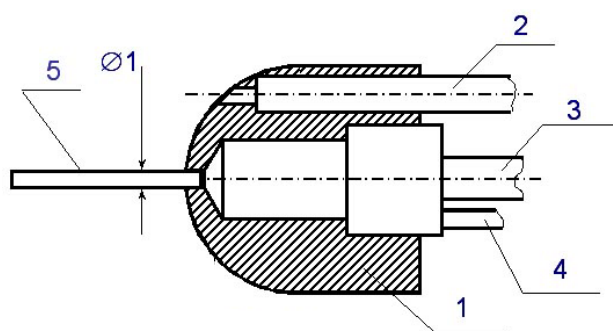


Fig. 10. Experimental model M4

The model M4 was placed on the support 2 inside which pressure transducer was installed. The model was supplied with compressed air by means of feeding tube 3. The tube 4 served for pressure measurements in the model's fore-chamber. Air was injected in the working flow through the tube-spike 5.

Schlieren images of plasma - model interaction without gas injection through the spike is presented on Fig. 11a and Fig. 11b.

It is seen that MW discharge destroys gas moving in the circulating zone on the front surface of the model. Streamlining of the sphere with a spike becomes similar to that near the simple sphere (without a spike). Pay attention to the shadow image equal to time delay 150 mcs of the process.

Situation is changed cardinally when air is injected through the spike upstream the working flow. Influence of gas injection on streamlining of sphere with a spike is presented on Fig. 12a and Fig. 12b.

Injected gas does not allow destroying circulating flow near the sphere. We can see only disturbances moving downstream.

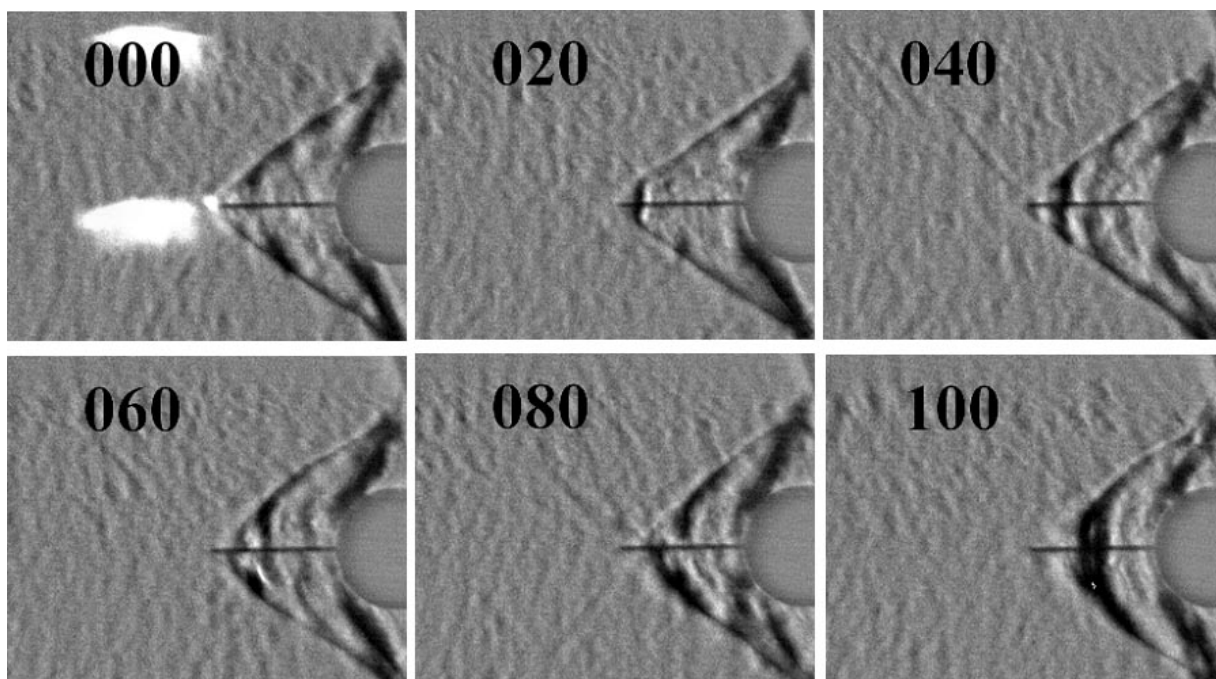


Fig. 11a. Streamlining of sphere with spike

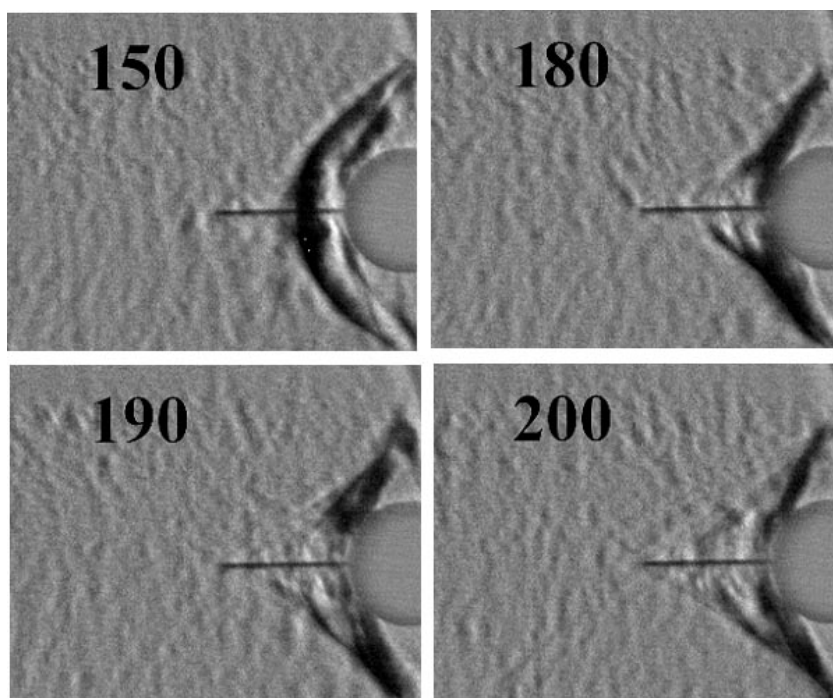


Fig. 11b. Streamlining of sphere with a spike

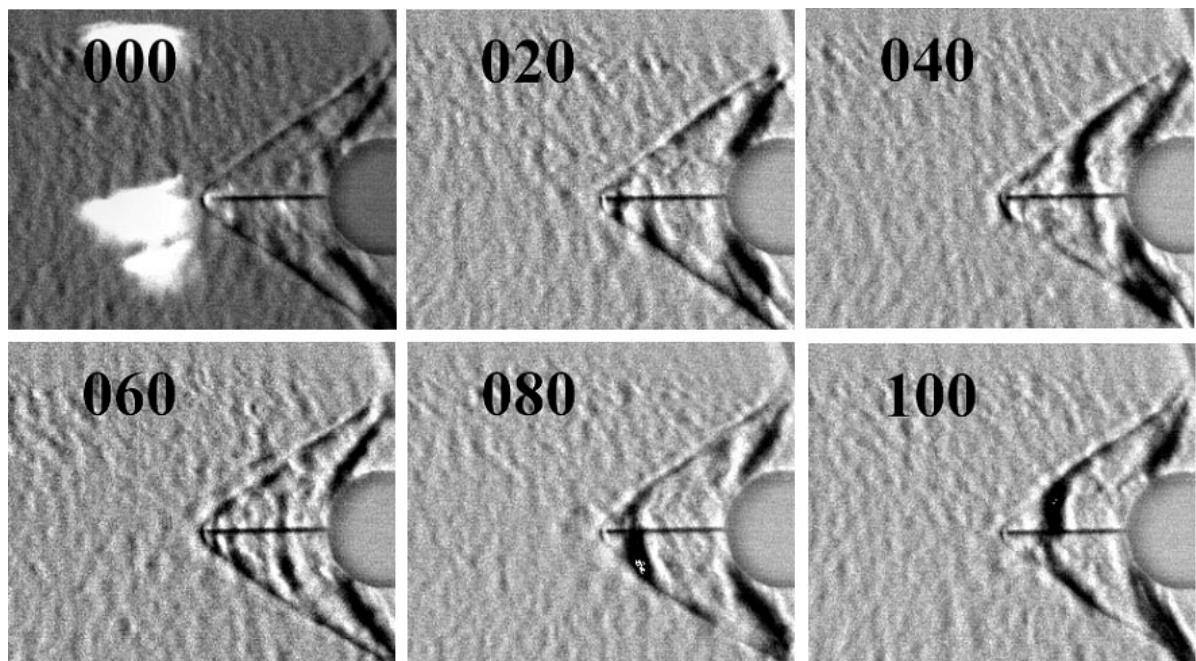


Fig. 12a. Gas injection through the spike

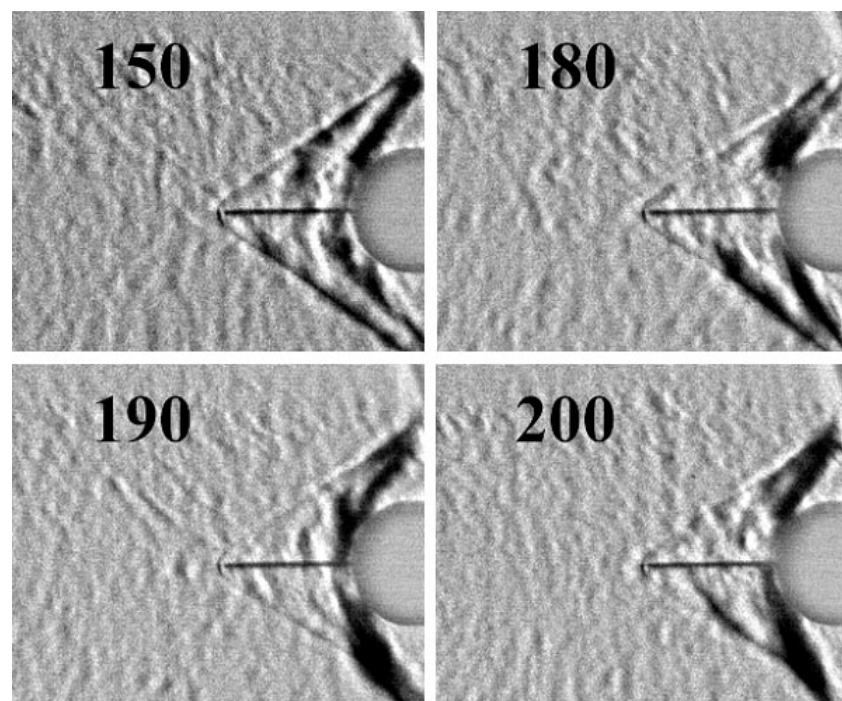


Fig. 12b. Gas injection through the spike

Pressure evolution on the sphere depending on gas flow through the spike under condition of MW discharge is shown on Fig. 13. Black line – there is no gas injection. A great splash of pressure can be seen. The relative pressure is increasing from 2 to 4.

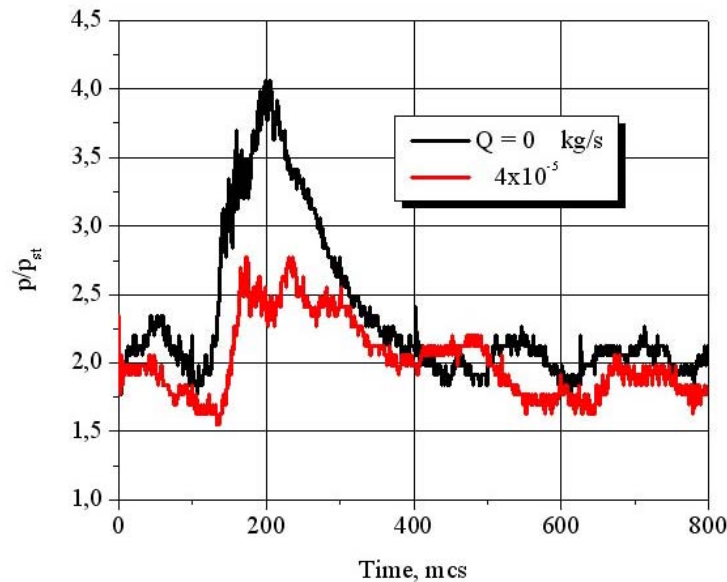


Fig. 13. Pressure evolution on the sphere with a spike depending on injected gas flow

Red line presents the case when gas rate through the spike was 4×10^{-5} kg/s. A pressure splash can be seen too. But it is smaller than in the first case. The pressure jumps to 2.5 only. So gas injection smoothes the influence of MW discharge on streamlining of sphere with a spike.

Pressure on the front surface of the models M3 and M4 is changing smoothly. So the readings of the shifted gauge on the sphere do not coincide with stagnation pressure in the critical point. Thus the readings of this gauge would be considered as a value, which characterizes the drag changing of the model only qualitatively.

4.2. Development of experimental facility

Development of experimental facility has been done with aim of broadening of Mach number range in the tests and attainment of MW discharge at higher static pressure in the test section of wind tunnel.

4.2.1. Substantiation of necessity of conducting of gasdynamic investigations at higher Mach number

Theoretical simplified analysis of gas motion at a decay of discontinuity during discharge-to-body's shock layer interaction has been done [1].

The Mach number of the shock wave moving along the heated channel at a D speed is an implicit function of two independent parameters – Mach number of flow M_1 and heating degree α (the function deduction is given in the appendix)

$$f(M_D, M_1, \alpha) = 0.$$

The interaction character is determined by such dimensionless parameters as the Mach number and flow nonuniformity degree.

Calculated values D/v_1

$$\frac{D}{v_1} = 1 - \frac{M_D}{M_1 \sqrt{\alpha}}$$

and U/v_1 ,

$$\frac{U}{v_1} = 1 - \frac{2 \left(M_D - \frac{1}{M_D} \right)}{(k+1) M_1 \sqrt{\alpha}}$$

obtained at the Riemann problem solution, are given in Fig. 14 and Fig. 15. Here v_1 – velocity of oncoming gas flow, U – velocity of gas in the wake of the shock wave in the heated domain.

Relative velocity D of the shock wave grows with the increase of heating degree (decrease of parameter α) and lowers with the increase of the flow Mach number.

Relative gas velocity shock wave decreases with the increase of the flow Mach number and drop of density in the gas heated area (decrease of parameter α).

It should be noted that under certain conditions gas velocity may change its sign to negative. This means that gas motion in the wake of the shock wave will be directed opposite to the main flow. In any case, conditions under which gas velocity behind the bow shock wave differs from gas velocity in the wake of the shock wave in the heated area, lead to shear layers, which, in turn, may be a source of vortex gas motion in the shock layer on the body.

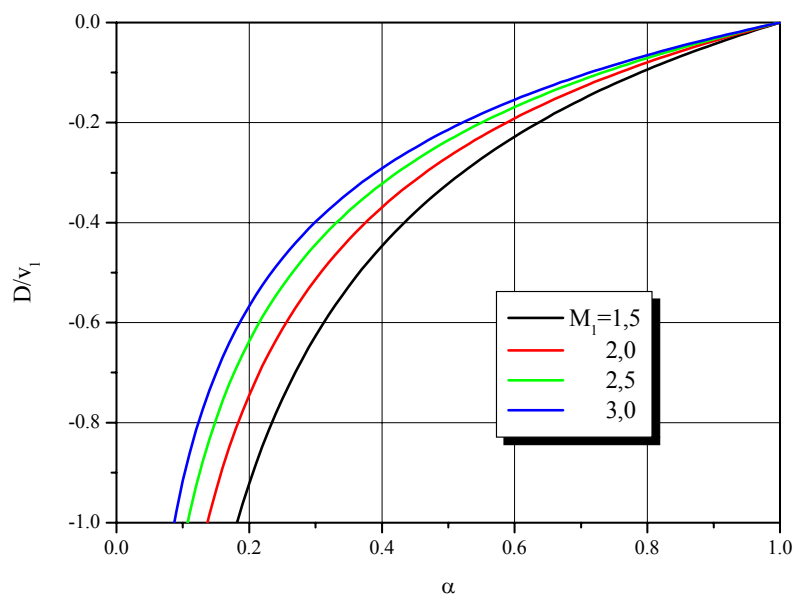


Fig. 14. Relative velocity of the shock wave

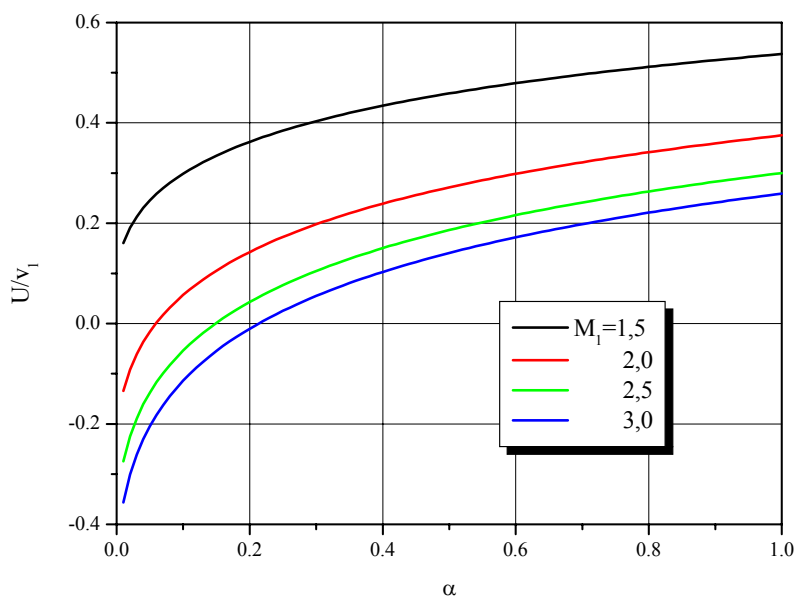


Fig. 15. Relative gas velocity in the wake of the shock wave

In this way, the vortex generation efficiency grows as the Mach number increases and parameter α decreases.

4.2.2. Improvement of wind tunnel TBS

4.2.2.1. Working flow with Mach number $M=2$

Investigation of working parameters of wind tunnel showed that there are significant oscillations of static pressure under working regime (Mach number $M=2$) in the test section. Obviously it is connected with that working jet has a long free length in the test section. It is 1.25 m from output section of the nozzle to ejector. Diameter of the output section of the nozzle is 60 mm. Diameter of diffuser is 135 mm.

A new supersonic diffuser was planed and manufactured in order to diminish length of the free jet. The diffuser represents a cylindrical tube, which has inner diameter 73 mm and length 640 mm. A conical channel connects the supersonic diffuser and input section of the ejector (diameter 135 mm).

Length of the free jet in the test section is about 140 mm now. Test runs of the wind tunnel with the supersonic diffuser have been done. Investigation shows that intensity of the static pressure oscillation in the test section is decreased in about 3 times.

The wind tunnel with the new diffuser allows getting lower static pressure. It makes possibility of the wind tunnel wider. Working flow with Mach number $M=2.1$ has been obtained at static pressure 25 Torr.

The next milestone of our work was realization of microwave discharge in supersonic working flow in the new conditions. Fig. 16 presents Schlieren picture of a model streamlining at the moment of microwave discharge origin. The model was a sphere with diameter 16 mm.

It is seen that microwave discharge exists in the flow but it has diffusive pattern. In the halo of the discharge there is no filament. Evidently this fact explains absence of bow shock wave structure changes on the model when heated domain of the discharge is interacting with shock layer.

It is obvious that needed electric field intensity is not reached in the domain of focus when metallic nozzle and diffuser are arranged inside the focusing system. Apparently it is required either enlarging of power of microwave system (but it is not possible with microwave generator which we have) or modernization of the focusing system.

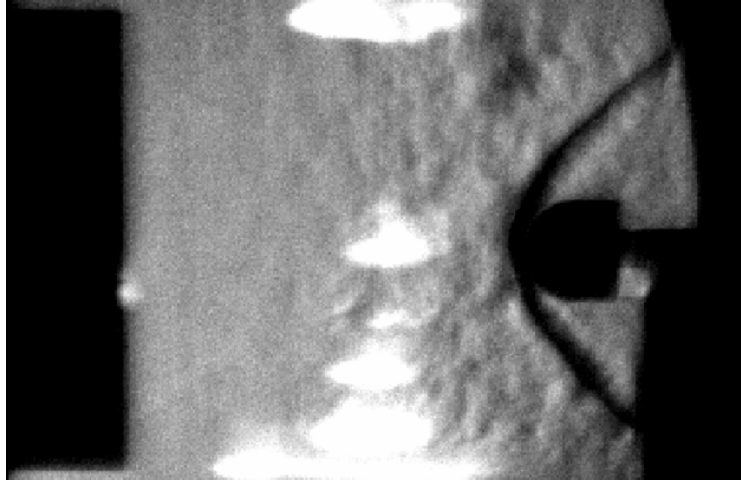


Fig. 16. Working flow with Mach number $M=2.1$ and microwave discharge

Evidently in order to realize a microwave discharge, which has a filament in it, the static pressure should be increased in the test section. So it is very important that microwave facility can create a discharge at higher pressure.

4.2.2.2. Working flow with Mach number $M=3$

A wide volume of works on creating of supersonic flow with Mach number $M=3$ was put into practice. Supersonic profiled nozzle was used for producing of working flow. Diameter of the output section of the nozzle is 35 mm. Supersonic diffuser was designed and manufactured. Its scheme is presented on Fig. 17. The reference [2] was used during diffuser designing.

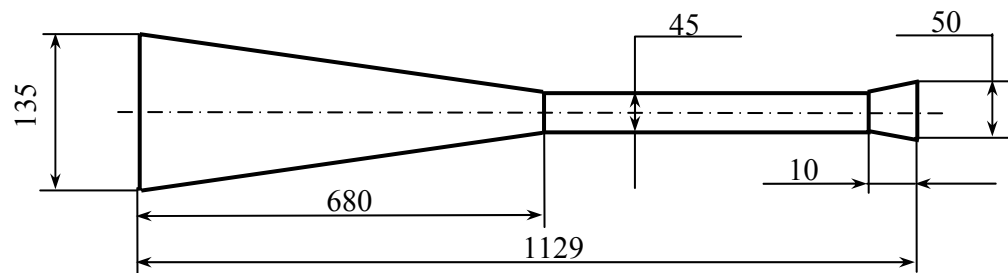


Fig. 17. Supersonic diffuser for working flow with Mach number $M=3$

The supersonic diffuser consists of cylindrical tube and conical channel. The internal diameter of the tube is 45 mm, its length is 449 mm. The conical channel connects the cylindrical section of the diffuser with inlet orifice of ejector, which has diameter 135 mm.

Sight of test section with the nozzle and the diffuser for working flow $M=3$ is shown on Fig. 18. Length of the free stream comes to 150 mm.

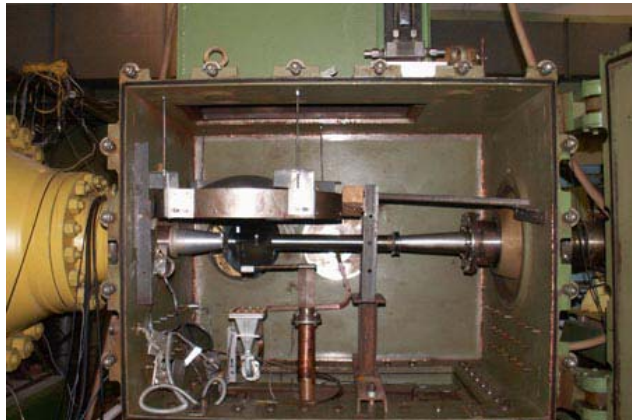


Fig. 18. The test section with nozzle and diffuser for Mach number $M=3$

Runs of the wind tunnel on the working regime with Mach number $M=3$ were tested. A Schlieren photo of working flow is presented on Fig. 19. The working regime of the wind tunnel has the next parameters: Mach number $M=3$, diameter of the flow is 35 mm, static pressure is 20-22 Torr, static temperature in the flow is about 100 K.

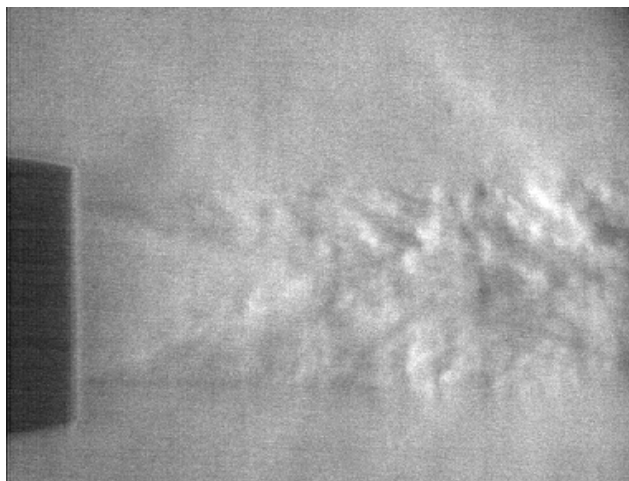


Fig. 19. A shadow picture of the working flow with Mach number $M=3$

Engineering development of the microwave focusing system, which allows obtaining reliable required discharge in the working flow under mentioned conditions with Mach number $M=2.1$ and $M=3$, has been worked out.

4.2.3. Building of a new focusing MW system

The purpose of the work was to increase intensity of the electric field in the area of focus of the system and to enlarge static pressure in the supersonic flow where microwave discharge would be realized. Computation of the new focusing system showed that intensity of the electric field in the focus can be increased in several times in comparison with initial focusing system. The new focusing system was also oriented for creating microwave discharge in the supersonic flow with Mach number $M=3$. It is known that temperature of gas in the flow is diminishing with Mach number increasing. So gas density in the flow is increasing with Mach number growth at constant static pressure. It makes worst conditions for microwave discharge creation in the flow. The more intensity of the electric field is needed for microwave discharge realization.

General view of the new focusing system is presented on Fig. 20.

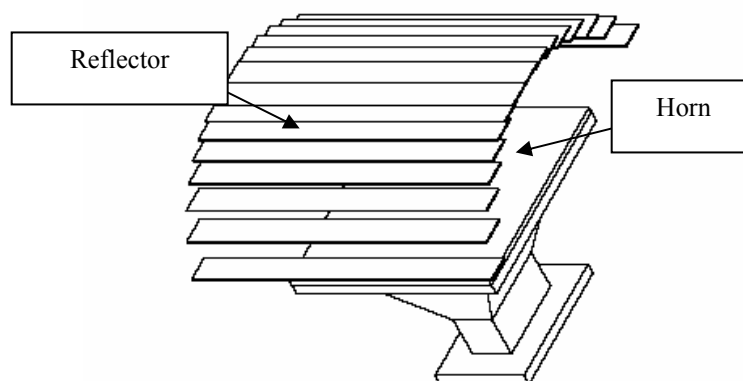


Fig. 20. Scheme of the focusing microwave system

The new focusing system consists of the microwave horn and the reflector. The reflector is produced from separate metallic straps. Position of the straps was determined by computation. Plane of the straps coincides with direction of the Schlieren measuring system. So the straps do not interfere with the work of the Schlieren device.

Installation of the new focusing system in the test section of the wind tunnel is presented in Fig. 21. The focusing system is attached to the nozzle of aerodynamic wind tunnel. The working flow running from the nozzle goes between the reflector and the microwave horn. The model support is seen on the opposite side of the focusing system.

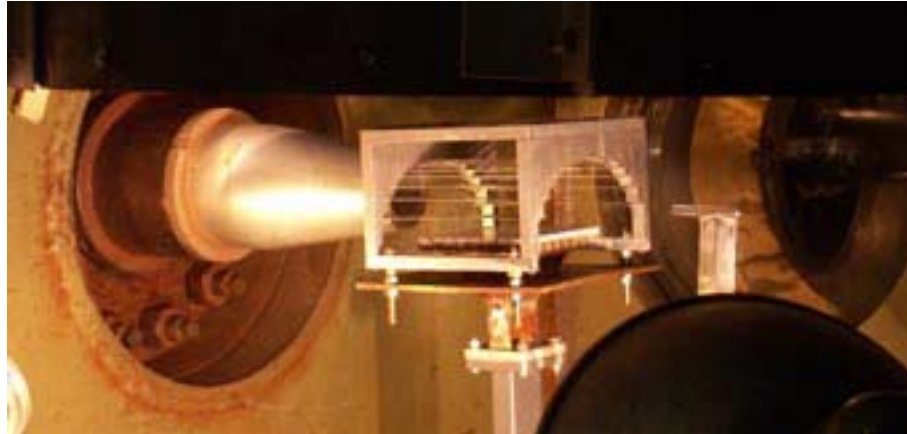


Fig. 21. Allocation of the focusing system in the test section of the wind tunnel

Investigation of behavior of the produced focusing system has been done. The maximum pressure in the test section was measured when microwave discharge was realized in the field of the focus. Air was pumped out slowly from the test section with help of ejector. The working flow was not created. The pressure of microwave discharge appearing was measured. The investigations showed that in the case of the new focusing system microwave discharge was realized at pressures being less then 227 Torr. The initial focusing system created microwave discharge at pressures smaller then 65 Torr. So effectiveness of the new focusing system is higher then initial one in about 3 times.

Investigation of operation of the new focusing system in the supersonic flow with Mach number $M=3$ has been done. The tests showed that microwave discharge did not appear on the working regime of the wind tunnel. The discharge was creating outside the working flow. The discharge attended on the microwave horn constantly. Increasing of pressure in the test section from 21 to 60 Torr did not bring about microwave discharge creation in the working flow. Fig. 22 shows disposition of microwave discharges in the focusing system when wind tunnel creates supersonic flow with Mach number $M=3$.



Fig. 22. Operation of the focusing system in the supersonic flow with Mach number $M=3$

Streamlining of the blunt cylinder with diameter 8 mm in the supersonic flow $M=3$ can be seen on Schlieren image (Fig. 22). Horizontal straps on the image are shadows from the plates of the reflector of the focusing system.

Obviously the difference in gas density inside and outside the flow is considerable. The gas density in the working flow is about 3 times higher than gas density in the test section. So first of all microwave discharge is realized outside the working flow.

In order to examine this supposition investigations of operation of the new focusing system in the working flow with Mach number 1.3 has been carried out. In this case the difference in gas density inside and outside the flow is not so considerable (about 1.5). Supersonic profiled nozzle for Mach number 1.3 made of Teflon was used in these experiments. Diameter of output section of the nozzle was 37 mm. Tests have shown that in this case microwave discharge appears in the working area of the flow. The static pressure in the working flow was 43 Torr. The microwave discharge begins to appear at power of microwave generator more than 90 kW. Microwave generator used in the experiments has maximum output power about 180 kW. So the new focusing system gives opportunity to investigate interaction of microwave discharge with gas dynamic structures in the wide range of output power of generator from 90 to 180 kW. Types of microwave discharge with power of the generator of 180 kW (left) and 90 kW (right) are shown on Fig. 23.

It is seen that intensity of luminescence on the microwave horn is changing considerable. The shape of microwave discharge in the working flow practically does not alter.

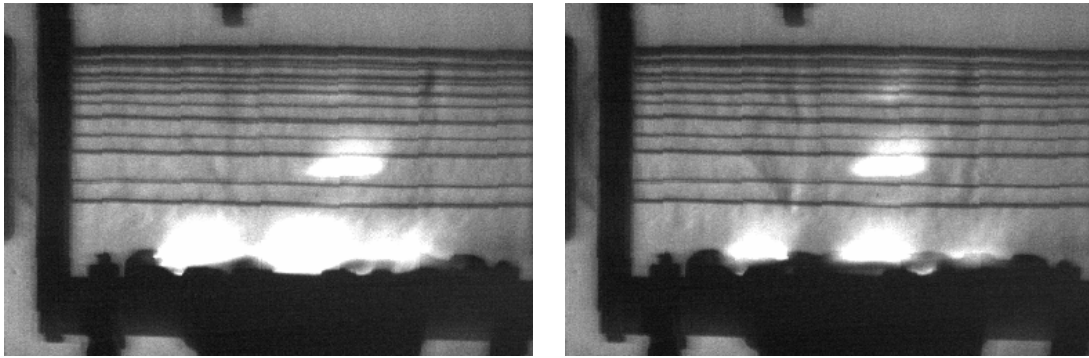


Fig. 23. Influence of the power of microwave generator on type of discharge

Investigations of interaction of microwave discharge with shock layer on the experimental model at Mach number $M=1.3$ have been done. The model was a blunt cylinder with diameter 12 mm. The output power of microwave generator was 90 kW. Schlieren images of interaction of the discharge with the shock layer are presented on Fig. 24, where streamlining of the model in the moment of discharge creation in the working flow (left) and variation of the streamlining of the model on the 60th mcs after discharge (right) are shown.

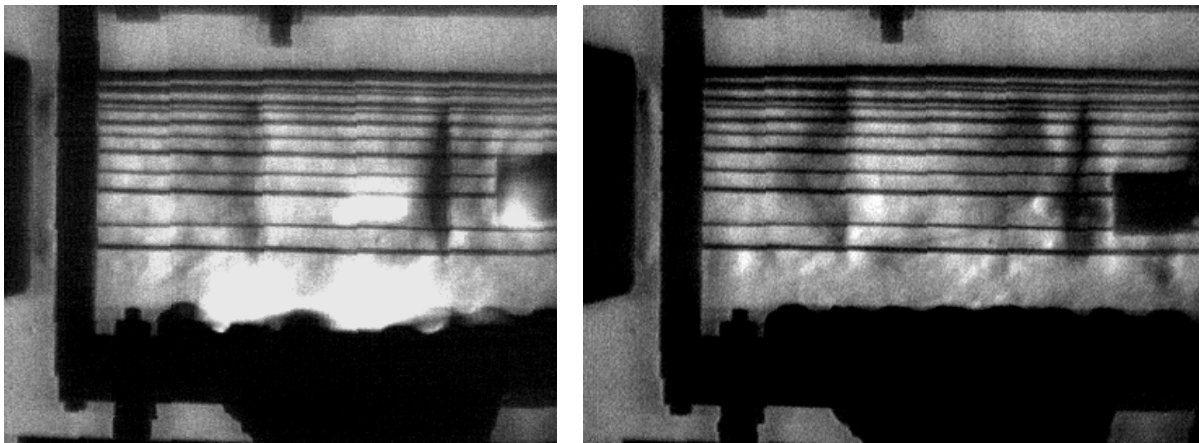


Fig. 24. Investigation of operation of the new focusing system in supersonic flow with Mach number $M=1.3$

It is seen that the shock wave changes its shape after microwave discharge interacts with shock layer.

Investigation of blunt cylinder with diameter 16 mm in Mach number $M=1.35$ working flow has been carried out. Schlieren images of streamlining of the model are shown on Fig. 25.

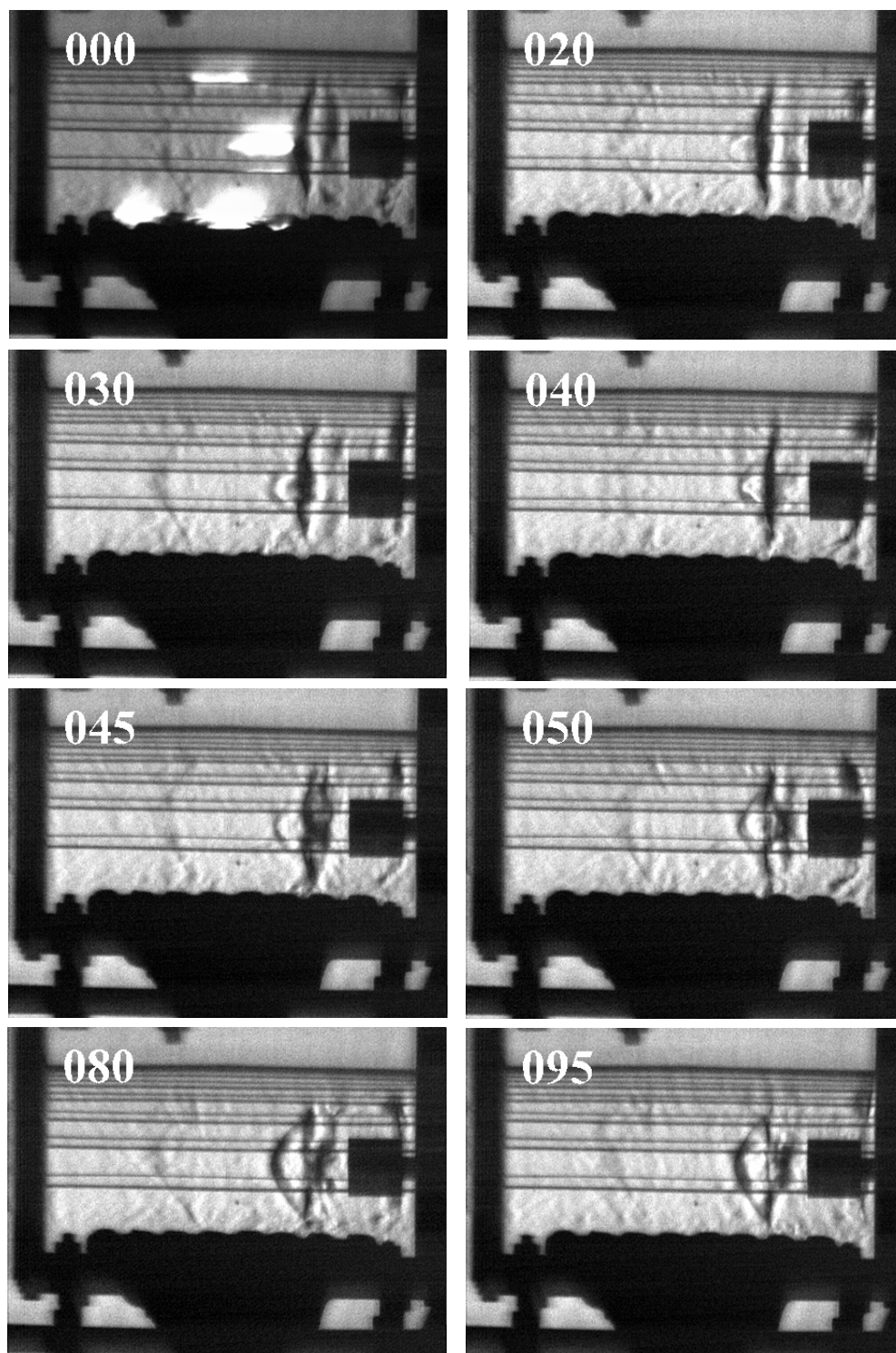


Fig. 25. Blunt cylinder in working flow $M=1.35$

Shock wave moves along the heated channel (images for 20, 30 mcs after discharge). Vortex starts its formation from 40 to 80 mcs. Bubble on the bow shock wave becomes wider (80, 95 mcs of the process). Bow shock wave stands off from the front surface approximately 1.5 times farther then in usual conditions.

Relative stagnation pressure evolution on the model is shown on Fig. 26.

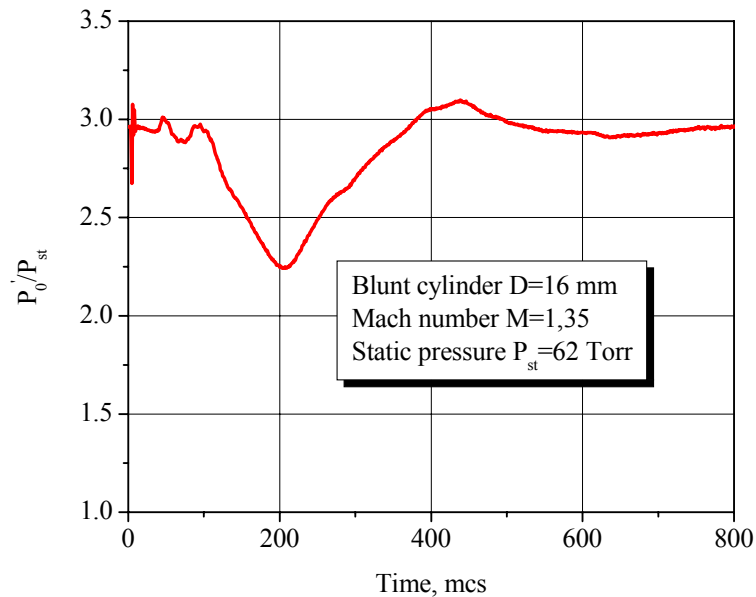


Fig. 26. Stagnation pressure on the model during discharge to shock layer interaction

The curve of stagnation pressure has an usual shape. At the beginning of the interaction dramatic change takes place in the gas flow in the shock layer. It lasts about 100 mcs. Gas vortex in the shock layer leads to stagnation pressure fall. Minimum of stagnation pressure can be seen on the 200th mcs of the interaction. Then the pressure restores its initial value. The experiment has been done at static pressure 62 Torr in the test section.

Thereby the new focusing system has shown its high effectiveness. It allows creating microwave discharge in the working flow at low level of output power of microwave generator. Experiment showed that microwave discharge can be realized in the working flow with Mach number 1.35 (static temperature in the flow 210 K). Microwave discharge did not appear in the working flow with Mach number $M=3$ (static temperature in the flow 100 K). So it is necessary to decrease the difference in the gas density inside the flow and in the test section in order to use its resources. It can be reached by heating gas in the entrance of the nozzle. Evaluation shows

that heating of the gas on 300-400 C will be enough to get microwave discharge in the working flow with Mach number $M=3$.

4.2.4. Construction of gas heater

In order to diminish the difference in density between the working gas flow and gas in the test section a gas heater of ohm type has been worked out and manufactured. It has electric power about 15 kW. The power is enough to rise temperature of working gas up to 300-350 degrees. Gas flow was about 40 g/s.

Gas heater is presented on Fig. 27.

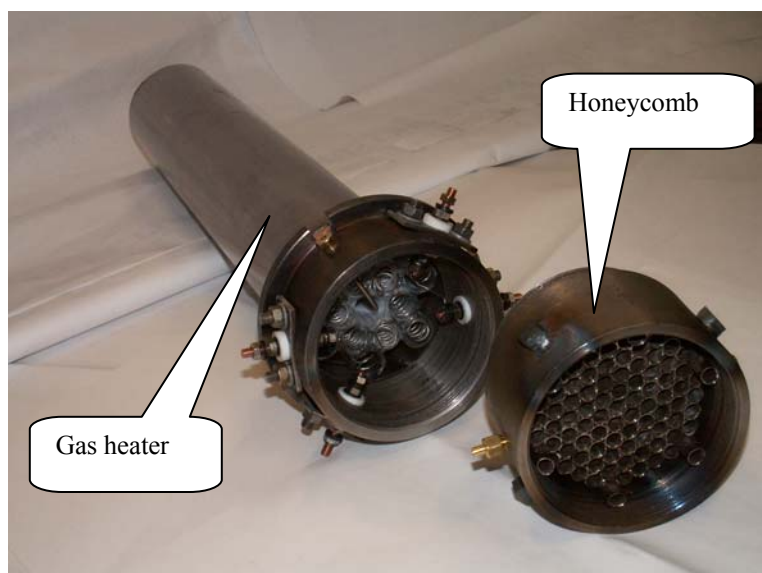


Fig. 27. The gas heater

The gas heater has a body made of stainless steel. There are twelve quartz tubes inside the body. Electric wire spiral made of tungsten is laid in the tubes. The gas moves along the tubes, flows around the spiral and gets warmer. To diminish the turbulence of the gas flow passing the heater there is a honeycomb attached to the outlet section of the heater. The honeycomb consists of thin tubes which are directed along the flow and attach to each other. There are several electrodes on the body of the heater. To measure temperature and pressure of the gas after the heater there are connecting pipes installed on the body.

A view of the wind tunnel with the heater and the new focusing system is presented on Fig. 28.

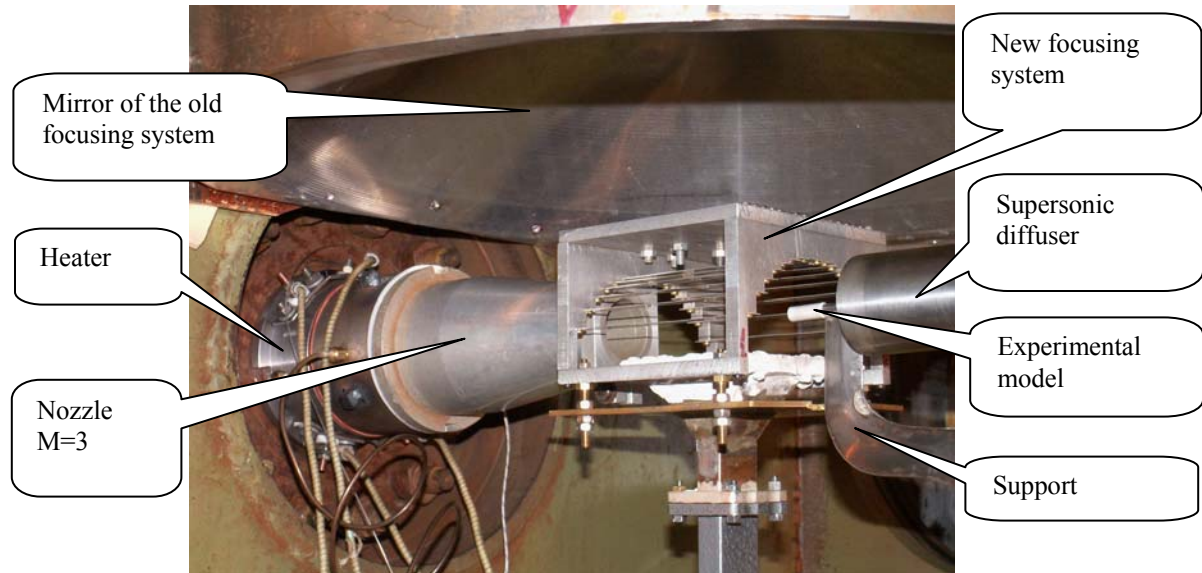


Fig. 28. Test section of the wind tunnel

Power control system of the heater is shown on Fig. 29.



Fig. 29. Power control system

Testing of the wind tunnel with Mach number of the working flow $M=3$ has been carried out. Stagnation temperature of working gas was 598 K. Pressure in the test section was 63 Torr. A blunt cylinder with diameter 6 mm was used as an aerodynamic model. Microwave discharge was realized in the working flow under such conditions. Schlieren images of model streamlining can be seen on Fig. 30.

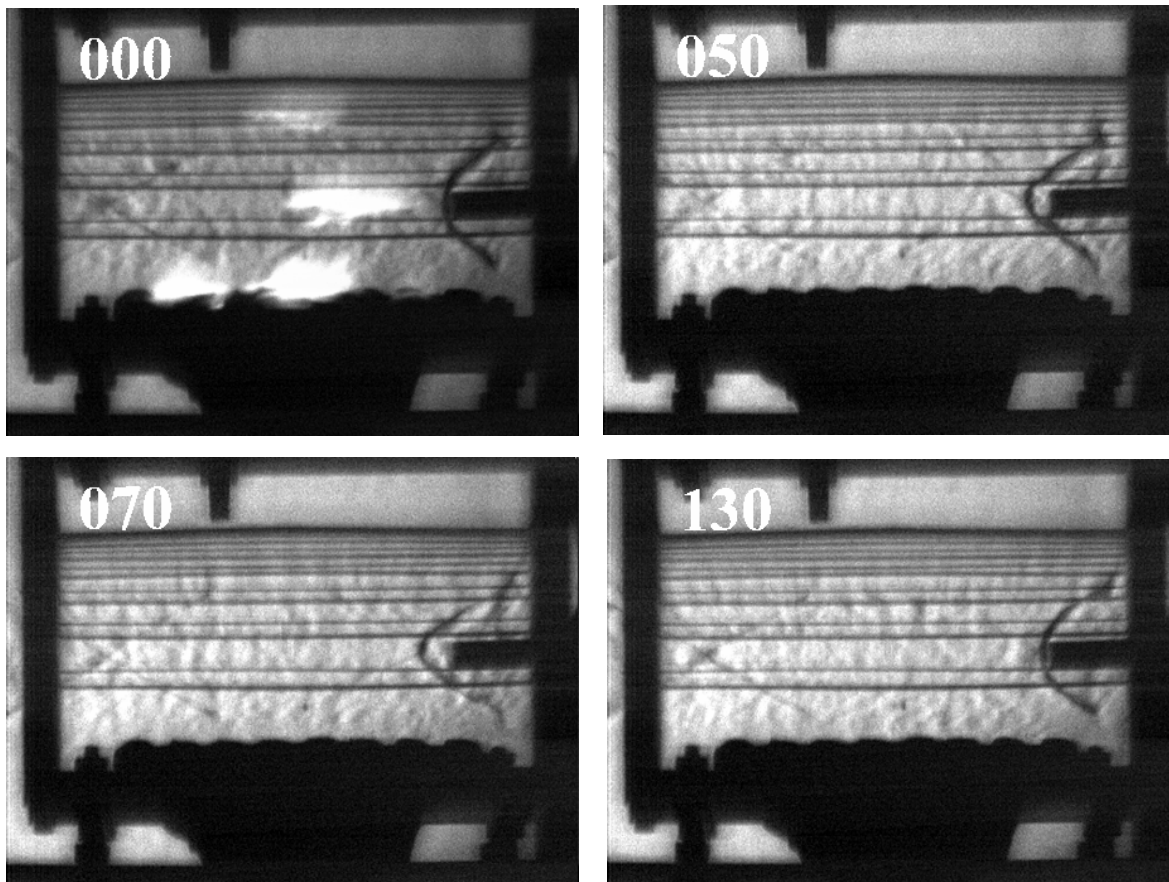


Fig. 30. Interaction of microwave discharge with shock layer under Mach number $M=3$

The microwave discharge has a remarkable length – about 20-25 mm. On the 70th mcs bow shock wave stands four times farther off the front surface of the model than under usual streamlining.

So, modernization of wind tunnel has been carried out. Using the new microwave focusing system and heating of the working gas gives opportunity to investigate interaction of

heated after microwave discharge domain of gas with shock layer on the body in the wide range of Mach number, microwave power and static pressure.

Conclusions

Experimental investigation of microwave discharge to aerodynamic body interaction has been carried out. The microwave discharge is an interesting object, making possible a substantial change of the bodies' aerodynamic drag. Moreover, the microwave discharge permits both to rise and to lower the body's drag. The principal mechanism, leading to the body's aerodynamic characteristics change is gas vortex motion caused by the interaction of the gas area excited by the discharge and the shock layer on the body.

Experimental research has been conducted to study the pressure behavior on the blunt cylinder's front surface in the circumstances of the microwave discharge, using a model with a hollow inside. The experiments have proved that the injection of gas into the shock layer synchronized with the microwave discharge boosts the vortex flow, which leads to a significant reduction of the body's drag (by 1.5 - 1.8 times). Microwave discharge and counter flow reinforced the influence of each other on drag reduction.

Gas injection through the spike on the sphere does not allow MW discharge to upset gas moving in the circulating zone. It diminishes influence of the discharge on drag increase of the sphere.

A deep modernization of wind tunnel has been carried out. Two supersonic diffusers were designed and manufactured for creating working flow with Mach number 2 and 3. A new microwave focusing system was worked out and investigated. It showed its high efficiency. Microwave discharge can be realized at higher pressure. A gas heater was built, which can rise stagnation temperature in the working flow up to 600-650 K.

New experimental results of discharge to shock layer interaction under Mach number $M=3$ were obtained. Tests showed that bow shock wave stands four times farther off the front surface of the blunt cylinder than under usual streamlining.

Using the new microwave focusing system and heating of the working gas gives opportunity to investigate interaction of heated after microwave discharge domain of gas with shock layer on the body in the wide range of Mach number, microwave power and static pressure.

References for section 4

1. Lashkov V.A., Mashek I.Ch., Anisimov Yu.I., Ivanov V.I., Kolesnichenko Yu.F., Azarova O.A. Method of Vortex Flow Intensification under MW Filament Interaction with Shock Layer on Supersonic Body. AIAA 2006-404. 44th AIAA Aerospace Sciences Meeting and Exhibit. 9-12 January 2006, Reno, Nevada.
2. Panichkin I.A., Lyakhov A.B. Basics of gasdynamics and their application to calculations of supersonic wind tunnels. Kiev, 1965 (in Russian).

Section 5. Laser-induced MW discharge

The laser-initiated MW discharges in quiescent gas (air) under the atmospheric pressure for Y-polarization of MW radiation were investigated. Our previous studies of this problem were performing on experimental setup with X-polarized MW field. For this type of MW field – supersonic flow interaction the direction of vector E in MW beam is coincides with flow velocity vector. In this case the MW plasmoid, arising in focal area of focusing system has elongated shape and its interaction with aerodynamic bow shocks is very effective. Unfortunately in this type of polarization the field distribution in focal area of MW focusing system is very sensitive. Therefore it was not possible to introduce the short-focal converging lens into the focal area of MW focusing system without distortion of maximum MW field position. In the case of Y-polarized MW field using, the MW beam is going towards the laser beam, and exact coincidence of laser spark and maximum in MW field distribution is achievable.

The scheme of experimental facility is presented on the Fig.5.1. Gas-dynamic chamber ($1 \times 1 \times 1 \text{ m}^3$) operates both under atmospheric pressure, and in vacuum regime (minimal pressure less than 25 Torr). It contains the MW radiating and focusing system and impulse Q-switched Ruby laser with optical system for laser beam focusing.

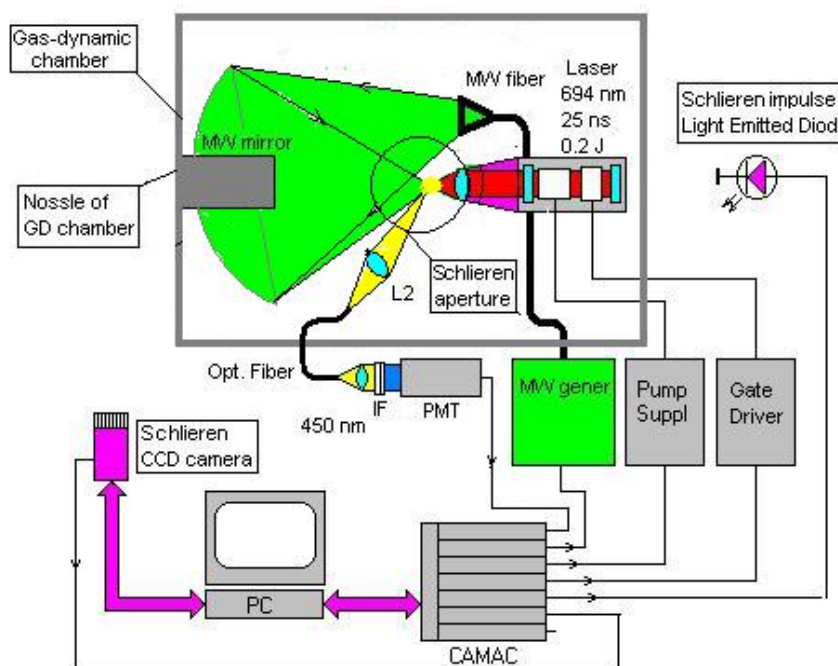


Fig.5.1. Scheme of experimental setup for Laser-Induced Y-polarization MW Discharge investigation

Impulse of 10GHz MW generator with output power 180 kW and pulse duration 1,5 mcs, via radiating system illuminates the parabolic mirror M1. It has the diameter 0,6 m and focal length about 0,3 m. In the focal area of this mirror the complex periodic structure of MW field is arising. This distribution has several maximums, one of these (with a greatest value of electric field) is used as working (main maximum). On this area, placed in the vicinity of main MW maximum, the Ruby laser beam is focused. The photo of experimental setup is shown on Fig.5.2.

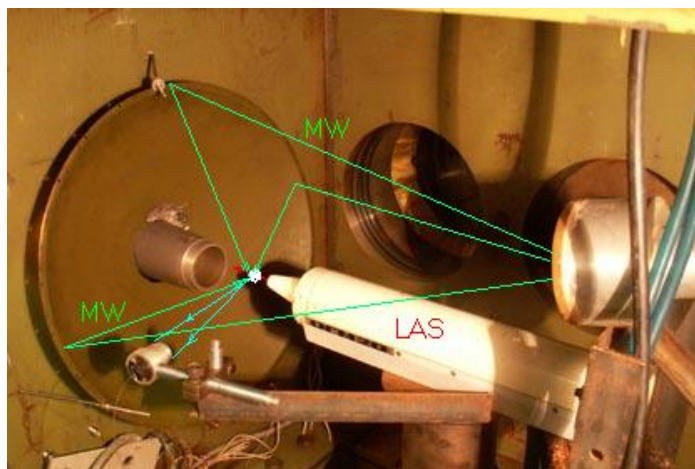


Fig.5.2. Photo of experimental installation

Laser is placed inside the chamber and can operate there only at the atmospheric pressure. For determination of the main MW maximum coordinates in the chamber, it is pumping to pressure 30-40 Torr and under these conditions the position of self-maintaining MW discharge is recording. On Fig.5.3 the structure and dimensions of the working area are presented.

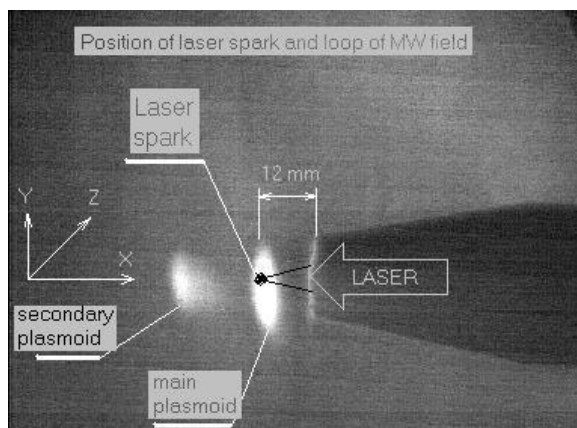


Fig. 5.3. Position of laser spark and loop of Y-polarization MW field

For eliminating the influence of laser body at MW field distribution, laser beam is introduced into this area via the comparatively long tube (lens holder). The focusing quartz lens has a focal length 12 mm. Fortunately, in the case of Y-polarized MW field, the position of laser spark may be precisely coincided with the center of the main MW plasmoid.

Ruby laser operates in Q-switched regime and generates the light impulse with 25 ns duration and output energy about 0.3-0.4 J.

Digital synchronous Schlieren system is used for visualization of shock wave structures arising in working area and recording spatial distribution of emitted discharge light. It has the focal length 2 m for the both telescopes, high-output power impulse LED as a source of light (visible range, 0,5 μ s pulse duration) and computer-managed synchronous CCD camera for image recording. The minimal open gate state for this camera is 12 μ s, but the time resolution of the presented Schlieren system is determined by parameter of LED (0,5 mcs).

The time delays between laser impulse, MW impulse and impulse of Schlieren registration are completely managing by the CAMAC system.

Time behavior of discharges luminosity in working area is measured by PMT. Time resolution of this channel is better than 30 ns. Spectral range of this channel is defined by interference filter (IF) with wavelength for transmission maximum 450 nm and bandpass 10 nm. Output signal of this channel is recorded in the Flash-ADC in CAMAC system. Fig.5.4 shows the typical time diagram on the output of PMT registration channel.

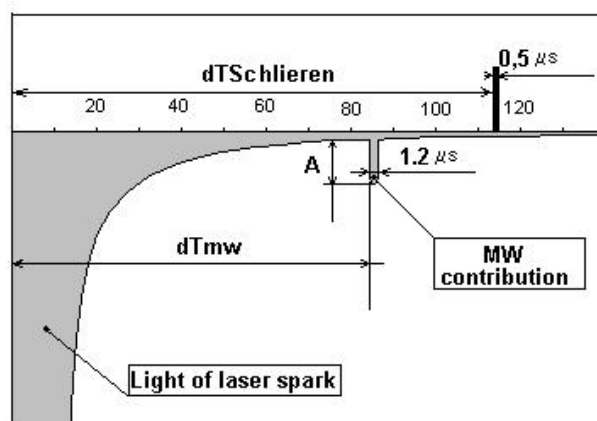


Fig.5.4. Time diagram for PMT signals

Signal from laser induced plasma has a wide “tail”. The impulse of MW contribution in decaying plasma luminosity is stand out against a background for delays more than 15-20 mcs. The small positive pulse in the end of diagram is impulse to Schlieren LED.

On Fig.5.5 the Shock-Wave structures of the combined Laser-MW discharge are presented.

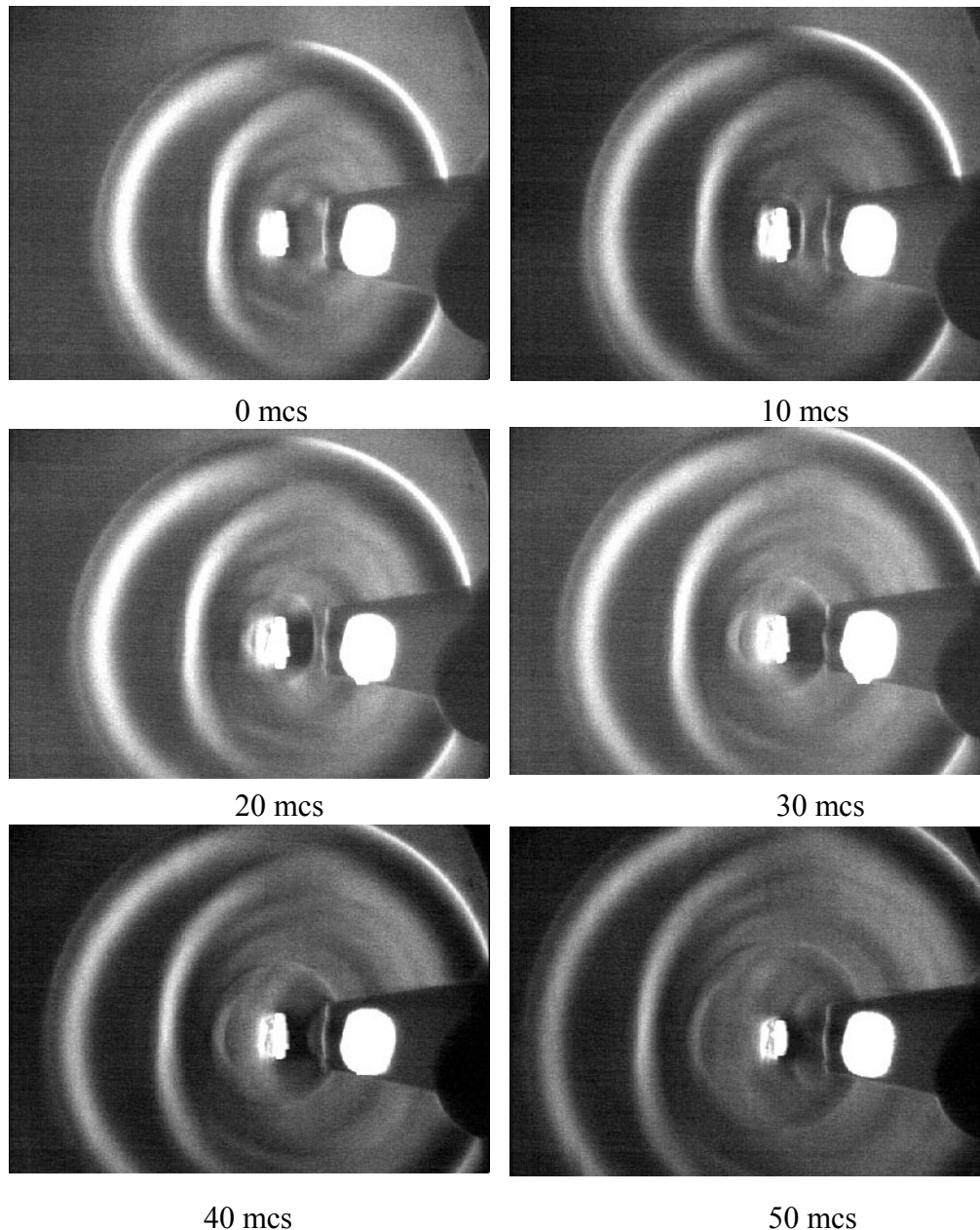


Fig.5.5. Shock-Wave structures of combined Laser-MW discharge. Beginning of the MW shock propagation (the first's 50 μ s after MW pulse). Time-delay between Laser spark and MW impulse is 120 μ s (fixed). Quiescent gas (air), room temperature, atmospheric pressure

Time delay between Laser spark and MW pulse is 120 mcs and fixed. In this case only beginning of the MW shock propagation (first 50 mcs after MW pulse) is studied. Time interval between frames is 10 mcs. In the second and third frames (10 and 20 mcs) is clearly seen that the shape of MW shock is not spherical. At Fig.5.6 the shock structures for different delays Laser-MW are presented. In this experiment the time position of Schlieren pulse is fixed (340 mcs), while time interval Las-MW is varied. For 340 μ s Laser-Schlieren delay the corresponding laser shock radius is more than 100 mm and it is out of the frame. Practically, in these pictures we see the process of MW discharge shock propagation in undisturbed gas under the atmospheric pressure.

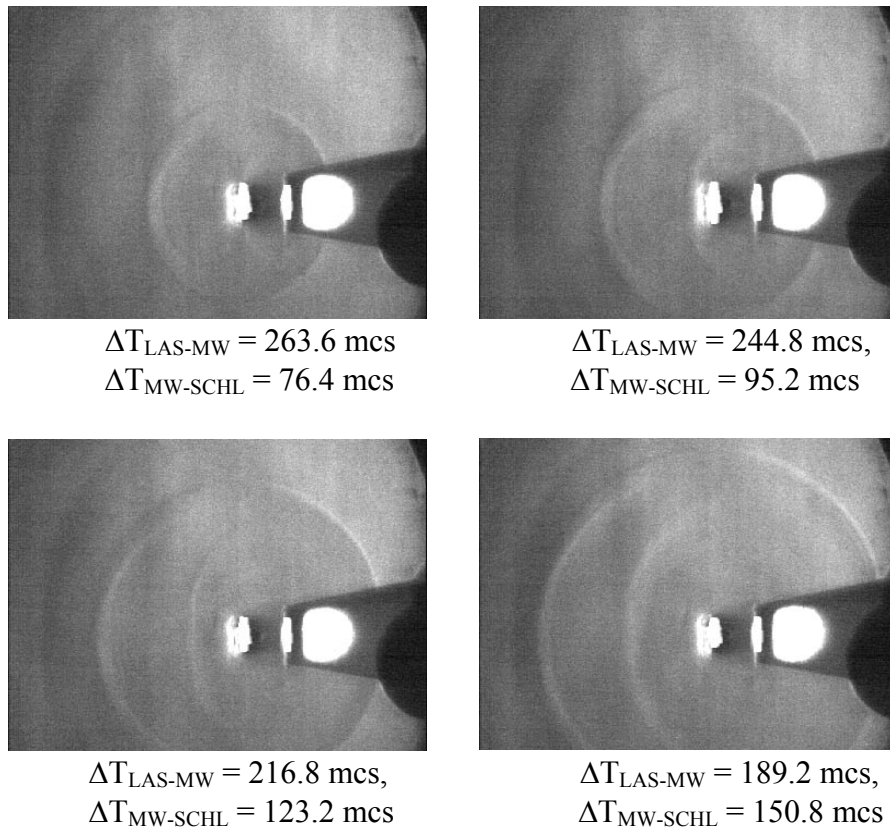
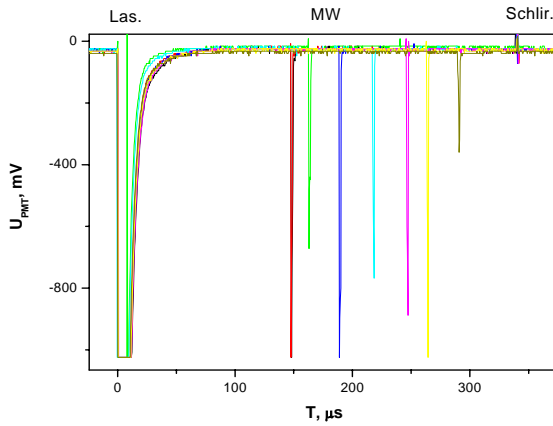
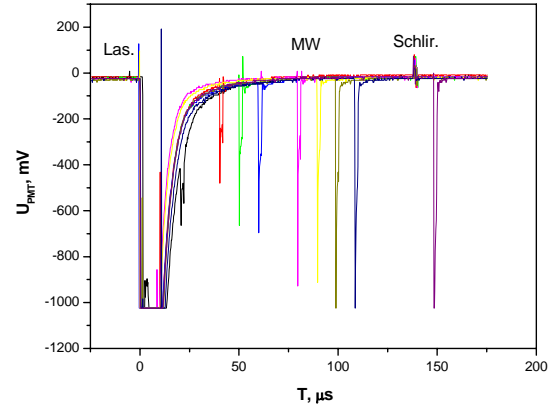


Fig. 5.6. Shock wave structures of combined Laser-MW discharge for different time-delays between laser spark and MW pulse. Laser-Schlieren delay is 340 mcs, the corresponding laser shock radius is more than 100 mm and it is out of the frame. Quiescent gas (air), room temperature, atmospheric pressure

On Fig.5.7a and 5.7b the PMT signals for different delays between laser spark and MW pulse are presented.



(a)



(b)

Fig.5.7.(a) PMT signals for different delays between laser spark and MW pulse. The area of large delays (150-300 mcs). Fig.5.7(b). PMT signals for different delays between laser spark and MW pulse. The area of small delays (20-100 mcs)

On Fig.5.7(b) signals were recording with small Laser Spark – MW delays (20 – 100 mcs), in Fig 5.7(a) - with comparatively large delays (150 – 300 mcs). It is clearly seen, that intensity of MW discharge light has a distinct maximum at the area of delays about 200 mcs. On Fig. 8 the intensity of light, emitted in laser-ignited Y-polarized MW discharge depends upon delays between ignited spark and MW pulse is presented. These data was approximated by the following “peak function”:

$$U = A \exp \left\{ \left[-\exp \left(-\frac{t - t_0}{\omega} \right) \right] - \frac{t - t_0}{\omega} + 1 \right\}$$

were: $A = 628$ mV, $t_0 = 182$ mcs (maximum of effect), $\omega = 112$ mcs.

According this equation, the probability of the effective MW energy deposition for delays 300 – 500 mcs is very high. The physical processes in this type of combined discharge are very interesting and their future investigations are important for the aims of applied aerodynamics and plasmadynamics.

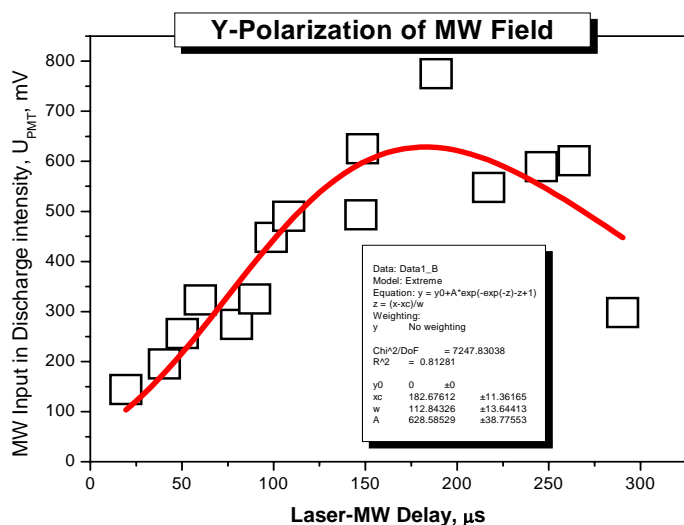


Fig.5.8. The intensity of light, emitted by laser-ignited Y-polarized MW discharge for different Laser-MW delays. The approximation curve is:

Two ways are possible for achieving of breakdown threshold in gas by means of impulse laser. The first is in increasing of the output impulse power for lasers with standard pulse duration (8-20 ns). The second – is the use of laser with comparatively low output energy (0.5 - 10 mJ), but with short pulse duration (picoseconds lasers). It is evident, that the second way is very perspective. With a kind permission of “MULTITECH Limited Co”, Saint Petersburg, Russia, we used in our investigations their solid state Nd:YAG laser with compressor on Stimulated Raman Scattering. The photo of this laser is presented on Fig.5.9.



Fig.5.9. General view of laser used (MULTITECH Limited Co”, Saint Petersburg, Russia)

Laser consists of active head (1), output mirror (2), passive saturation gate (LiF), resonator mirror, several turning mirrors and compressor on Stimulated Raman Scattering (3). Without compression the laser generates impulse with time duration 8 ns. If compressor is turned on, the output impulse has duration less than 400 ps. Laser operates either on the first harmonic (1064 nm), or on the second harmonic (532 nm). The output beam diameter is about 5 mm, beam divergence is less than 1 mrad. Repetition frequency of pulses is 1-10 Hz (internal start generator). Laser is launched in a single - pulse operation mode from an external signal. The output energy of each impulse is measured by means of piezoelectric power-meter with accuracy better than 5%.

For obtaining of laser breakdown in air at the atmospheric pressure the quartz lens with focus 12.5 mm was used. The main arrangements in the area of laser spark are shown on Fig.5.10. The picture is recorded by the synchronous CCD camera (MINOLTA Z3), which also launches the laser. Behind the lens focus area, at a distance of 1 m, the white scattering screen is placed. On this screen the diffraction pictures were fixed, arising in a process of laser breakdown development in gas.

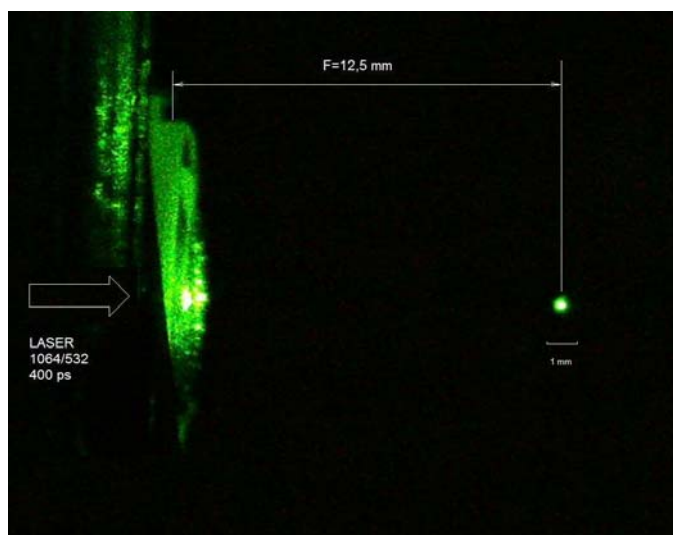


Fig.5.10. Experimental arrangements and main sizes of investigating laser spark

On the Fig.5.11 and Fig.5.12 the photos of laser spark at different wavelengths and impulse powers are shown. All pictures were recorded under the same conditions and, thus, can be compared. It is clearly seen, that laser sparks arise at comparatively low impulse energies – less than 1 mJ for 532 nm radiation and about 3 mJ for 1064 nm radiation. These levels of

breakdown electric field in the focus area correspond to the case of 8 ns laser pulse with energy of 60-80 mJ.

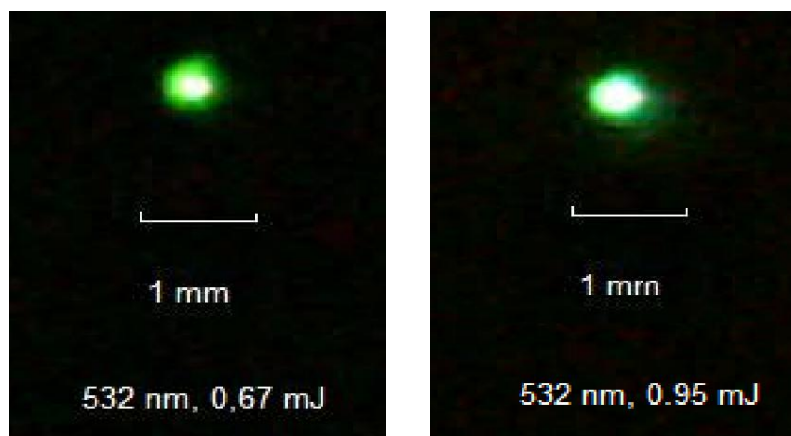


Fig.5.11. Laser sparks at 532 nm, 400 ps, and different input energy

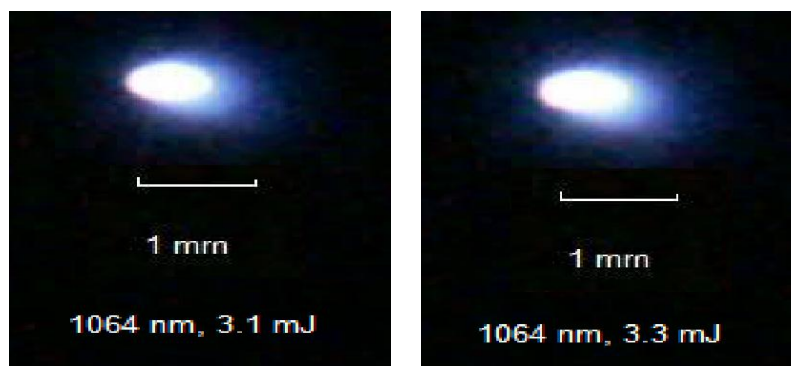


Fig.5.12. Laser sparks at 1064 nm, 400 ps, and different input energy

On Fig.5.13 self-diffraction of laser impulse on the breakdown domain is shown.

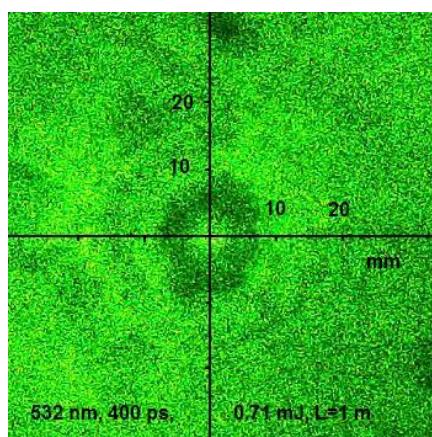


Fig.5.13. Self-diffraction picture of laser impulse on the laser spark

Preliminary estimations are giving the value of about 100-120 microns for the most probable diameter of the breakdown area.

The main task of this step was the getting of more probable estimations of transformation effectiveness of picoseconds laser pulse energy in thermal energy, inputted in gas under the normal conditions. Investigating laser has comparatively low energy (3.2 mJ at 1064 nm and 0.75 mJ at 532 nm) and creates comparatively weak shock waves structures. For measurements of these shock waves parameters with high precision we had have to perform the modernization of the Schlieren optical scheme (increasing this sensitivity and accuracy).

New experimental setup includes the ps-Nd:YAG laser, autocollimator Schlieren system and synchronization circuits.

The schematic diagram of picosecond range laser application is presented at Fig.5.14.

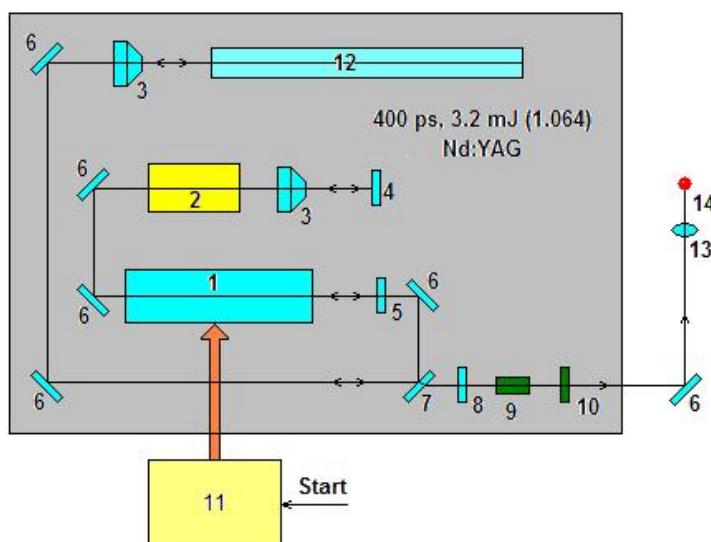


Fig.5.14. Optical scheme of Nd:YAG laser with compressor on Stimulating Raman Scattering. 1 - Nd:YAG, 2- nonlinear passive optical gate, 3 – telescopes, 4,5 – mirrors of laser resonator, 6 - deflecting mirrors, 7 – dichroic mirror, 8 - $\lambda/4$ plate, 9 – crystal-doubler, 10 – green filter, 11 – power supply, 12 – compressor on the Stimulated Raman Scattering, 13 – focusing lens, 14 – laser breakdown area

It contains the standard Nd:YAG laser with passive saturation gate (LiF) and system for compressing its output impulse, using the compressor on the Stimulated Raman Scattering. Nd:YAG laser generates the standard 8 ns output impulse on the wavelength 1064 nm. In Raman compressor this impulse is shortened to 400 ps. It has the energy about 3.2 ± 0.2 mJ. Laser output impulse is focused by the lens 13 (focal length 12.5 mm) in the point 14, where the laser spark is

arising. The shock – wave structure, producing by laser spark is analyzing by modernized Schlieren system with high space and time resolution. This resolution has to be better than 0.1-0.2 mm for shock wave radius and 0.2 mcs in time. Unfortunately, in the used laser, the output impulse arise with delay 150 ± 3 mcs after the beginning of the pumping process (supported by power supply 11). The time dispersion of the output impulse relatively the starting impulse is connected with the use of passive type of intracavity laser optical gate. Strong requirements to resolution for creating measuring system demanded from us to use the output laser light for synchronization.

Optical scheme of the modernized Schlieren system and the main parts of synchronization circuits are shown at Fig.5.15.

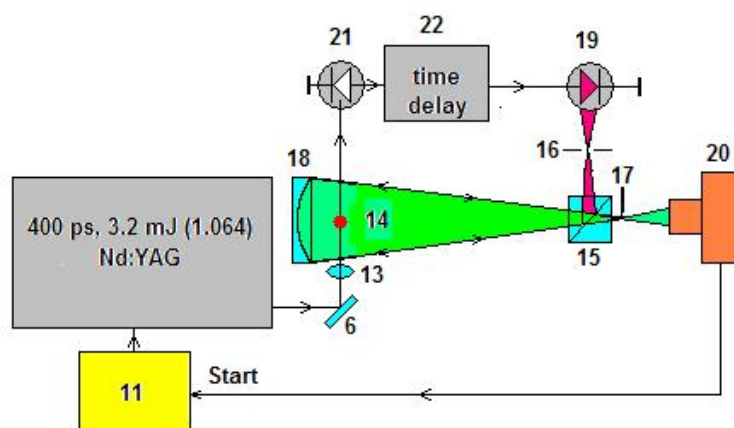


Fig.5.15. Optical scheme of modernized autocollimation Schlieren system for investigation of weak shock waves, arising after low power laser breakdown. 18 – spherical mirror ($F=0,7$ m), 15 – beam splitter, 17- Schlieren knife, 16 – input slit, 17 – output optical knife, 19 – power impulse LED, 20 – CCD camera, launching the Nd:YAG laser, 21 – photo sensor, launching the microprocessor time delay generator for LED after arising of laser generation

Schlieren system consists of a spherical mirror 18 (focal length 0,7 m), beam splitter 15, input slit 16, output optical knife 17, impulse light sours 19 (powerful visible range LED), CCD color camera 20, photo sensor for detecting of laser generation beginning 21 (fast photodiode) and time delay generator 22, based on micro-processor time delay generator (averaged errors for time delays less than 0,2 mcs, interval of delays (0-100) mcs, output impulse 0.5 mcs). The using of this type of Schlieren scheme allowed us to eliminate the double structure of recording picture

and important, because it allows to operate under conditions closely approach to strong explosion model (small time delay after laser breakdown and small shock wave radius).

The modernized Schlieren scheme also was very useful for confirmation of subsonic character of shock wave propagation under large time delays.

On Fig.5.16 the typical shock waves, arising after ps-laser breakdown in air under the normal conditions, are presented.

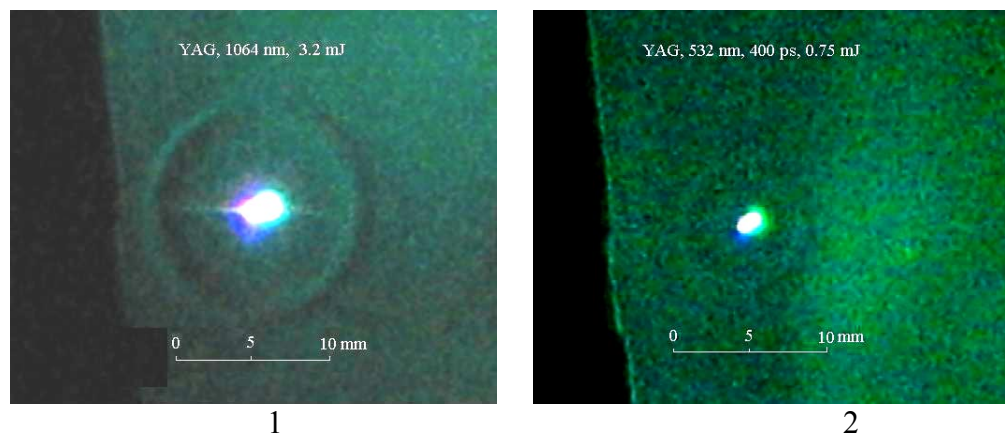


Fig.5.16. The view of low power laser spark shock structures, arising after ps-laser breakdown in air at the normal conditions Fig.16.1 1064 nm, 3.2 mJ, Fig. 16.2 – 532 nm, 0.75 mJ

Space diagram of shock wave structure radius, produced by the spark of ps-laser is shown at Fig.5.17.

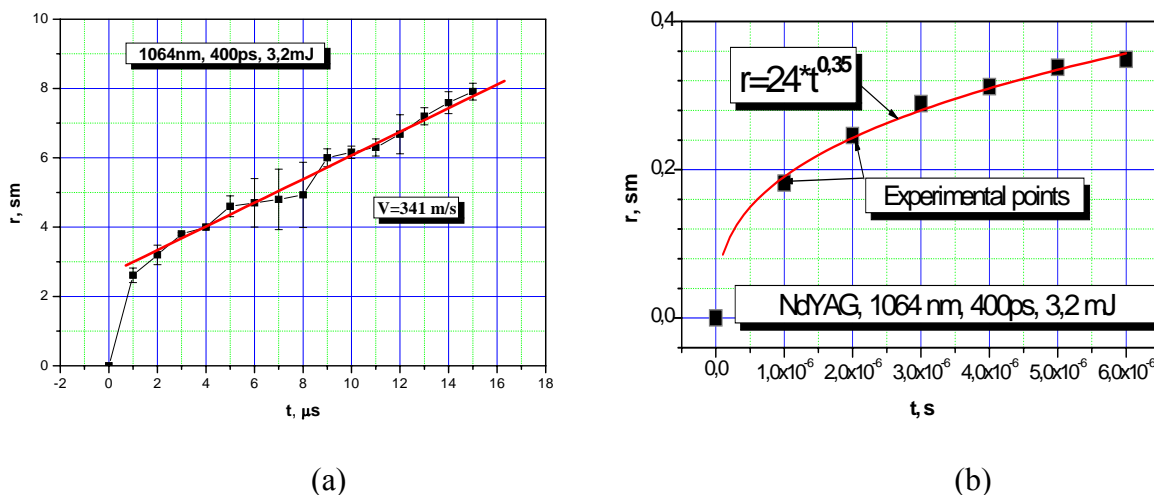


Fig.5.17. Space diagram for radius of shock wave structure, initiated by the low energy ps-laser spark. (a) -The velocity of shock wave propagation is corresponding to sub-sonic regime. (b)-Characteristics of weak laser spark shock wave at the small time delays

The dispersion of experimental points is connected both with the differences in impulse power for each breakdown realization, and as inevitable mistakes in shock wave radius measuring.

For estimating of energy enclosure in gas for our laser type, we calculated the non-dimensional length L and time T according with the theory of “point explosion”

$$L := r_d \cdot \left(\frac{p_1}{E_0} \right)^{\frac{1}{3}} \quad T := \frac{\left(t_d \cdot p_1^{\frac{5}{6}} \right)}{E_0^{\frac{1}{3}} \cdot \sqrt{\rho}}$$

Here p_1 and ρ – are the initial gas pressure and density in spark region, r_d –radius of shock wave at the time t_d , and E_0 – the entire energy, inputted in gas.

For several experimental points, which coordinates are:

$$t_d := \begin{pmatrix} 2 \cdot 10^{-6} \\ 4 \cdot 10^{-6} \\ 6 \cdot 10^{-6} \\ 8 \cdot 10^{-6} \\ 10 \cdot 10^{-6} \end{pmatrix} \quad r_d := \begin{pmatrix} 1.4 \cdot 10^{-3} \\ 2.2 \cdot 10^{-3} \\ 3.2 \cdot 10^{-3} \\ 4.0 \cdot 10^{-3} \\ 4.8 \cdot 10^{-3} \end{pmatrix}$$

the comparison of the experimental couples (L, T) and theoretical couples (l, t) was done for the most probable level of E_0 . The results of this comparison are presented at Fig.5.18.

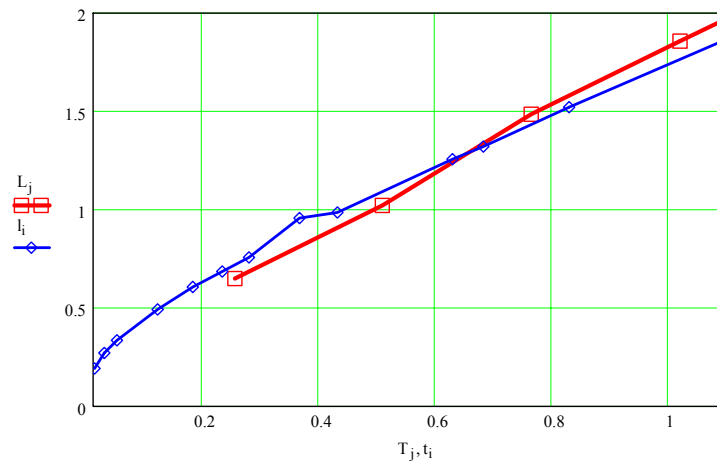


Fig.5.18. The results of comparing of numerical and experimental data. Blue line is a theoretical curve, obtained for $E_0=0.9\text{mJ}$, the red is experimental data. The output laser energy is $3.2\pm0.2\text{mJ}$, the effectiveness of transformation of laser pulse energy in energy, inputted in the gas is estimated as 0.3 ± 0.1

On this diagram the blue line – is a theoretical curve, the red is the experimental data, obtained for $E_0=0.9$ mJ. If to take in mind, that the output laser energy is 3.2 ± 0.2 mJ, the effectiveness of transformation of laser pulse energy in an energy, inputted in the gas can be estimated as 0.3 ± 0.1 .

The obtained value of effectiveness is comparatively high, and it confirms our suggestions about perspectives of using the picosecond range laser in applied aerodynamics. Nevertheless, the accuracy of this result is evidently unacceptable and has to be improved in future measurements.

The previous results, devoted to Laser-Ignited MW discharges show, that this type of discharges is very perspective for MW energy deposition in high-density supersonic and hypersonic flows [1,6,7]. At the same time, the single laser spark in supersonic gas flows and its influence on the wave structures in these flows is a very interesting and perspective direction too [2,5]. The next wide area of using laser systems in plasmadynamic is diagnostics [8]. Therefore the main tasks, resolved by the creating system could note as:

- The creation of initiated laser sparks for MW discharges in supersonic flows with M range 2-3, static pressures and temperatures 20-100 Torr and 150-200 K. These sparks have to arise in necessary points of flow placed upstream from desirable point of MW energy deposition. The lasers for these purposes may be as nanoseconds ranges (Q-switched YAG, Nd^+ , Ruby) as to picoseconds range (compressed YAG^{9,10}, Mode Locked Ruby⁴). The initiating area in the flow may be created by another way – with using of resonant laser radiation (N_2 laser, or Excimer laser [1]);
- The creation of erosion laser plum on the surface of AD body. This plum may be used as to independent tool for modification of wave structures around AD body and as ignited factor for MW discharge (Q-switched or free generating Nd^+ , ruby);
- Diagnostic applications. Such are the Thomson Scattering (Q-switched ruby [8]), Schlieren visualization with nanosecond resolution (Q-switched ruby or second harmonic YAG) and Interferometry (Q-switched ruby).

The general view of multi-target laser system is presented on Fig.5.20. Its scheme is shown on Fig.5.21. It contains the Q-switched Ruby laser (block 1 on Fig.5.21), Q-switched Nd^+ laser (block 1 on Fig.5.21) and the Excimer or N_2 laser (block 2 on Fig.5.21). Laser system, including Ruby and Nd^+ lasers, stays on the common optical base, placed outside the test chamber.



Fig. 5.20. General view of multi-target new laser system

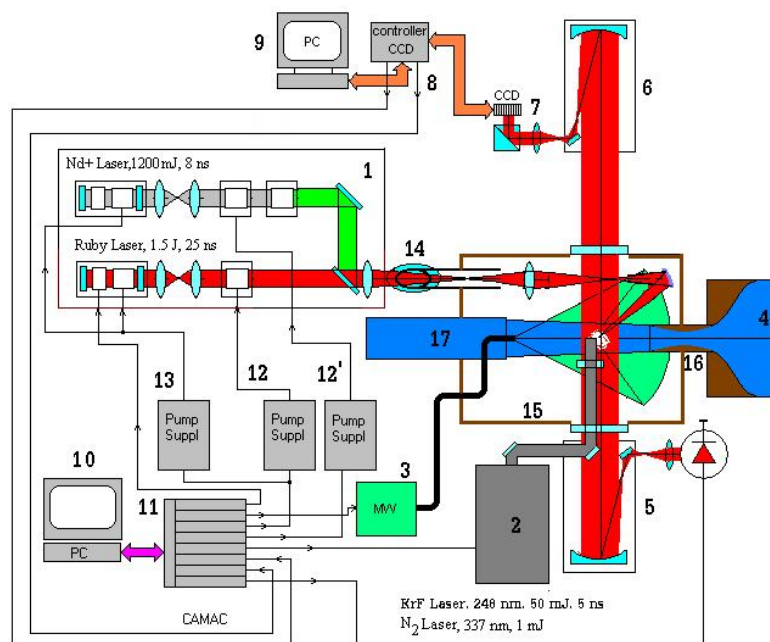


Fig.5.21. Experimental setup for investigation of MW-Laser combined Discharges in supersonic flows

Excimer or N_2 lasers are placed at another side of the test chamber. All lasers are managed by synchronization systems based on the CAMAC.

The main parameters of the created two-stage ruby laser were described earlier [5]. Unfortunately, the dimensions and construction of new MW focusing system (see Fig.5.3) do not allow the using of the short-focus lenses for collimating of laser beam. The minimal lens focus length for this construction is about 80 mm. That was the reason, because the ruby laser with it comparatively long pulse (25 ns) becomes unusable with using flows. Nevertheless, as we note above, this laser part may effectively operate in diagnostically applications.

The next desirable step in the development of this part is operation on the second harmonic of the main wavelength, generating by ruby lasers, – 347 nm. This regime may be very interesting for investigation of multi-photon processes in laser spark.

The main efforts at the present work were directed on the development of two-stage Nd^{+} Q-switched laser. Its first stage was modernized, and now it operates with active gate, checking by the CAMAC system. It generates the laser impulse with wavelength 1064 nm and output energy 200-300 mJ and 8 ns duration. The diameter of the laser beam is about 2.5 mm, its divergence is about 3 mrad. The laser amplifier (pos.6.) is based on the Nd^{+} -glass core with 20 mm in diameter and 240 mm long. It is pumped by the same impulse 5 kJ Xe lamp. The estimated output energy for this two-stage laser is 900-1000 mJ at 1064 nm wavelength and, accordingly, 180-200 mJ on the second harmonic of the main generation – 532 nm.

If the first stage of this laser generates in free regime, its output energy achieves the level 20-25 J. This regime may be used for organizing of erosion plum from AD body. On Fig 5.22 the picture of erosion crater on the surface of Al target is presented. This crater was got with using of 12.8 cm converging lens.

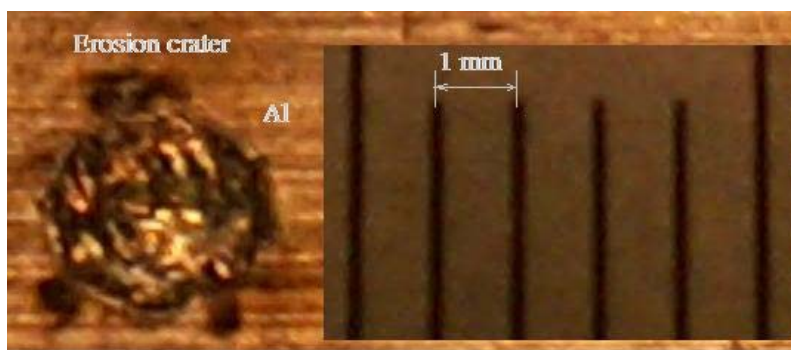


Fig.5.22. Photo of erosion crater on the surface of Al target. Energy of laser pulse 25 J, duration 0,8 ms, converging lens 12,8 mm

In our previous reports we considered the possible variants of vacuum-UV lasers application to MW discharge ignition in SS-flows. In experiments we could operate with three main types of UV lasers, with parameters, presented in Table 1, and with the impulse N₂- laser with output energy 1 mJ and wavelength 337 nm.

Table 1

	XeCl	KrF	ArF
		For these mixtures, the life time of the working medium is comparatively low	
λ , nm	308	248	193
W, mJ/pulse	10-50	60-70	3-5
τ , impulse duration, ns	5-7	5-7	5-7

The considered type of laser could be very useful in our experimental investigations, but unfortunately, the laser with the most interesting spectral diapason (193 nm, ArF) has very small output energy. The N₂ laser has the insufficient energetic characteristics too. That is the reason, why we plan investigations with this laser on the latest steps of our work.

Conclusions

The laser-initiated MW discharges in quiescent gas (air) under the atmospheric pressure for Y-polarization of MW radiation were investigated. Results of our experiments with Q-switched Ruby laser (694 nm, 0,25-0,3 J, 25 ns) confirm that effective MW energy deposition under the mentioned above conditions is realized after the essential time-delays between initiated laser spark and MW pulse (80 – 120 mcs). The mechanism of this effect is connected with two main reasons - arising of thermal (density) well at the place of laser discharge and changing of chemical composition of the heated volume, including production of long-lived states of atoms and molecules.

The multi-targets laser system for investigations of laser-induced MW discharges in supersonic flows with Mach number 1.-3.0 and static pressures 20-100 Torr was created. It contains the Q-switched two-stage Ruby laser (1 J, 25 ns, 694 nm) and Nd⁺ laser (1 J, 8 ns, 1064 nm), the optical translation system for laser spark creation in the Gas-Dynamic Test Chamber, synchronization system with MW generator and diagnostic scheme. The efficiency of this system was demonstrated on the erosion plum arrangement on the test aerodynamic body.

The high perceptiveness of lasers of picoseconds diapason for laser sparks arrangement was demonstrated. It was shown, that Q-switched YAG laser with one-stage Raman compressor (400 ps, 3.2 mJ at 1064 nm and 0.75 mJ at 532 nm) permits to create the laser sparks under the atmospheric pressure with comparatively high effectiveness of energy deposition in shock wave structures (effectiveness 0.3 ± 0.1 for 1064 nm, 3.2 mJ, 400 ps).

References for section 5

1. Mashek I. et al. Microwave Discharge Initiated By Laser Spark in Air AIAA2004-0358
2. Yu. F. Kolesnichenko, A. A. Gorynya, V.G. Brovkin, et. al. "Investigation of AD-Body Interaction with Microwave Discharge Region in Supersonic Flows", 39th AIAA Aerospace Sciences Meeting & Exhibit, 8-11 January 2001 / Reno, Nevada, AIAA 2001-0345
3. Yu. F. Kolesnichenko, V.G. Brovkin, O.A.Azarova, V.G.Grudnitsky, V.A.Lashkov and I.Ch. Mashek "MW energy deposition for aerodynamic application", 41th AIAA Aerospace Sciences Meeting & Exhibit, 6-9 January 2003 / Reno, Nevada, AIAA 2003-0361
4. V. G. Brovkin, D. F. Bykov, I. A. Kossy, et. al. "Gas discharge, exciting by MW radiation and CO₂ laser radiation" Journal of Technical Physics, Vol. 61, N 2, 1991, p.153
5. R.B. Miles "Flow control by energy addition in to high-speed air". AIAA 2000-2324
6. Yu. P. Raizer. Laser spark and discharge propagation, Moscow, Nauka, 1974
7. P. X. Tran, C. M. "Optical characterization of laser-induced spark in air" AIAA 2002-0568
8. Y. L. Chen, J. W. L. Lewis and C. Parigger "Spatial and temporal profiles of pulsed laser-induced air plasma emissions", Journal of Quantitative spectroscopy and radiative transfer, **67**, 91-103 (2000)
9. C. Parigger, J.W.L. Lewis, D. Plemmons "Electron number density and temperature measurement in a laser-induced hydrogen plasma", Journal of Quantitative spectroscopy and radiative transfer, **53**, 249-255, 1995
10. C. Parigger, D. Plemmons, J.O.Hornkohl, J.W.L. Lewis "Spectroscopic temperature measurements in a decaying laser-induced plasma using the C₂ Swan system" Journal of Quantitative spectroscopy and radiative transfer, **52**, 707-711, 1994

11. J. O. Hornkohl, C. Parigger, J.W.L. Lewis “Temperature measurements from CN spectra in a laser-induced plasma” Journal of Quantitative spectroscopy and radiative transfer, **46**, 405-411, 1991
12. R. Kandala, G. V. Candler “Computation modeling of localized laser energy deposition in quiescent air” AIAA 2002-2160
13. H.Yan, R.Adelgren,G.Elliott, D.Knight, M.Bogushko “Laser-energy deposition in quiescent air” AIAA 2003-1051.

Section 6. Plasmadynamic applications of Magneto-Plasma Compressors

6.1. Magneto-Plasma Compressor in Vacuum Regime

The principles of creating of new generation these quasi-stationary accelerators of

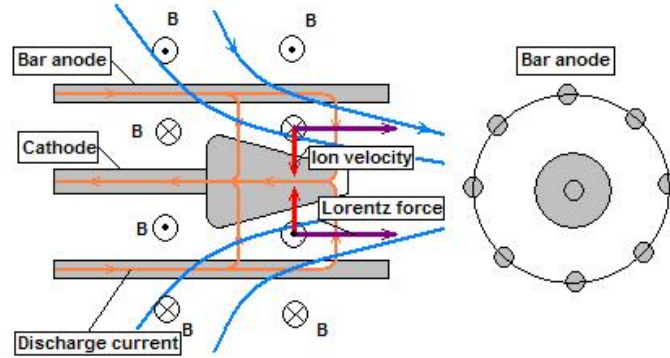


Fig.6.1. The physical foundations of Magneto – Plasma Compressor operation compact geometry were described in [1, 2]. Principal scheme of this MPC is presented in Fig.6.1.

It has two coaxial electrodes - central cone cathode and cylindrical bar anode. When discharge current flows through this system from anode to cathode, it creates strong azimuthal magnetic field between electrodes. Electrons and Ions, moving between electrodes of coaxial system, are accelerating by this magnetic field in the internal area of MPC and compressed on the output in the vicinity of axis. So, this type of MPC operates in the ion current transfer mode and performs both plasma acceleration in the discharge device and plasma compression due to interaction between the longitudinal components of the “swept-away” current and its azimuthal magnetic field.

According with [2] the parameters of MPC can be defined as:

$$U = \left(\frac{I}{c}\right)^2 \left(\frac{dm}{dt}\right)^{-1} \frac{32}{27}$$

the output plasma velocity

$$V_m = \sqrt{2} C_{A0} = \left(\frac{I}{c}\right)^3 \left(\frac{dm}{dt}\right)^{-1} \frac{8}{3\sqrt{3}} \frac{f}{r_0} \approx 0,01 \left(\frac{dm}{dt}\right)^{-1} (I_A)^3$$

the discharge voltage where: C_{A0} - the Alfven velocity, I - discharge current (SGS units), dm/dt - gas mass flux (g/s), f - the width of discharge channel in the critical section (cm), r_a - the average radius of the discharge channel in the critical section (cm), I_A - discharge current (A).

Two main operational modes of Magneto - Plasma Compressor (MPC) exist. The first – (it is named “Vacuum Regime”) is described in detail in [1-3]. In this regime, the compressor is pumped out to the initial pressure less than 10^{-5} - 10^{-6} Torr and then the working gas (He, Ar, N₂, Air) is coming through the fast gas-valve into the internal volume of MPC. The most part of this gas is ionizing and accelerating in discharge processing. For this regime the plasma gun generates the plasma jets of different gases³ (H₂, He, N₂, Ar) with comparatively high density in compression area (up to $(10^{16}$ - $10^{17})$ cm⁻³), temperatures about 3 eV, gas velocity in jets focus up to 70 km/sec for He and 38 km/sec for N₂. The typical duration of current impulse in these type of accelerators is 100-200 μ s, its amplitude - 50-100kA.

More interesting MPC operational mode for applying to aero - and plasma – dynamic is the second one (it is named Residual-Gas-Regime). In this regime the vacuum chamber with MPC is evacuated to the initial pressure 1 - 100 Torr (if MPC operates with Air) or, is pre - evacuated to high vacuum and after this, is filled with working gas ((He, Ar, N₂) at the desirable pressure (1-100 Torr). This regime allows to get the compressed plasma flows with large density and velocities 5-20 km/s (for Air).

At Saint-Petersburg State University the first experimental setup with MPC operated in Vacuum Regime has been built in 1994-1997 years. On this setup the first investigations of the processes of plasmadynamic accelerations of disperse particles were made.

The general scheme of MPC, operated in “Vacuum regime” is presented in Fig.6.2.

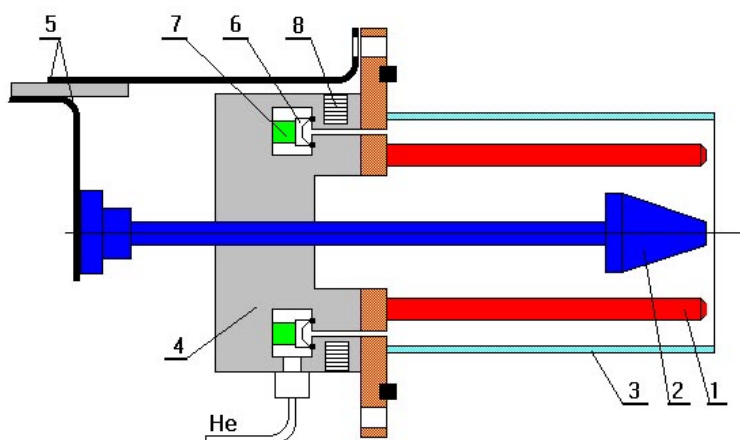


Fig.6.2. The construction of Magneto Plasma Compressor

Accelerator consists of cone cathode 2, bar cylindrical anode 1, quartz tube 3, Teflon body 4 and fast electromagnet valve for gas injection in MPC. Accelerator is connected with

capacity bank by the copper conductors 4. The fast valve contains the elastic ring 7, Al ring 6 and electromagnet coil 8. If the current impulse passes through the coil 8, the 12 channels, connecting high-pressure value with working gas (He, N, Ar) are opened and the gas goes into the quartz tube. The initial pressure in this area is less than 10^{-5} Torr. When the front of gas bow-shock achieves the end of the tube, the main discharge circuit is switches on. Diameter of pivots anode block is 5 cm, the length of the tube is 12 cm. The time-delay between the moment of the fast valve opening and the beginning of the main discharge for this MPC type is 350 mcs. General view of MPC is presented in Fig. 6.3 and Fig .6.4, where 1 – anode holder, 2 – anode bars, 3 – cathode, 4- Teflon's body, 5 – the bandage of the fast valve impulse coil, 6 – quartz tube, 7 – input socket for working gas, 8 – wires of valve coil.

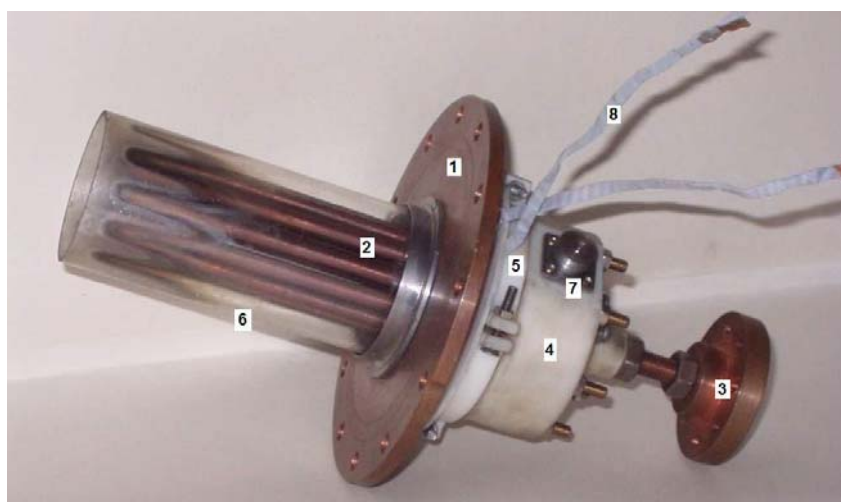


Fig.6.3. The view of Magneto Plasma Compressor

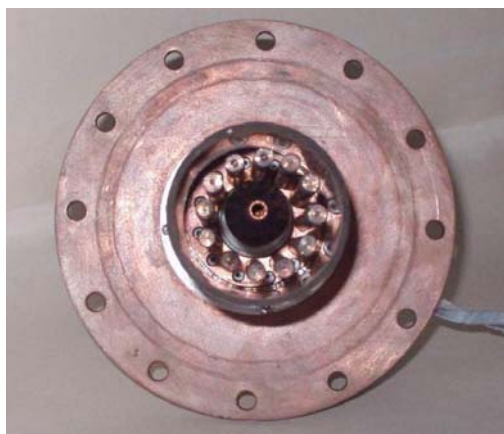


Fig.6.4. Construction of bar anode of Magneto Plasma Compressor

The electrical scheme of MPC using is presented in Fig.6.5. The circuit of the fast valve contains the capacity battery C1 (800 mcF, U_{\max} 2000V), Hg commutator 1 (10 kV, 100 kA) and electromagnet coil. Amplitudes of current impulses in valve circuit are about 20 – 25 kA, the duration of open state – 50-100 mcs, the average mass flux (for He) is about 0,5-5 g/sec. The main discharge circuit contains the main capacity battery (3000 mcF, U_{\max} 5000 V), Hg commutator 2 (200 kA, 15 kV), low-inductive circuit for connecting battery, commutator and MPC, and measuring circuits for discharge current and voltage.

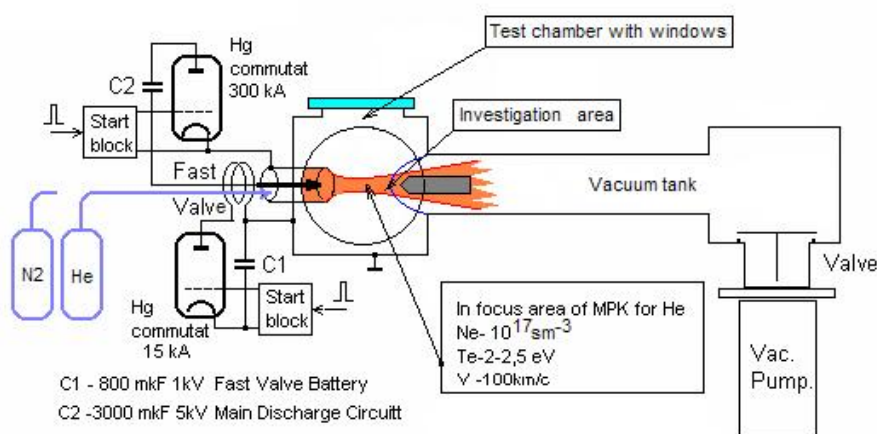


Fig.6.5. The electrical scheme of MPC operated in Vacuum regime

General view of MPC test chamber is shown in Fig. 6.6. In this photo: 1 – MPC, 2 is a

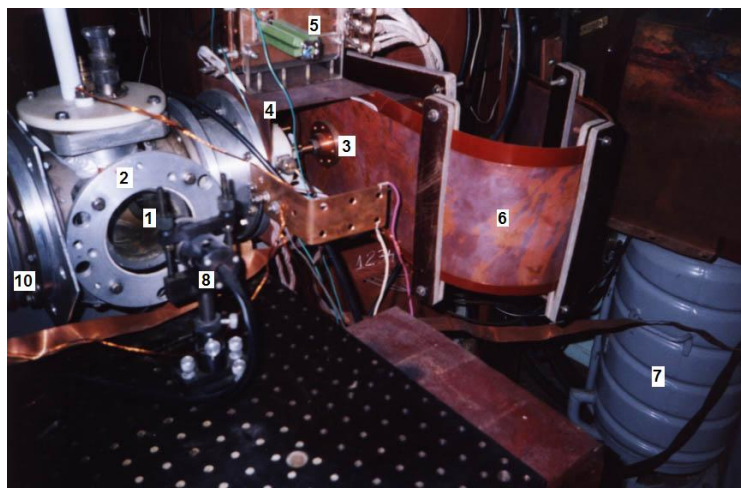


Fig.6.6. The view of the experimental installation for Magneto Plasma Compressor investigations

test chamber, 3 – cathode connectors, 4 – anode connectors (ground), 5 – connectors of fast valve circuit, 6 – low-inductive circuit, connecting main battery and MPC, 7 – Hg – commutator, 8 – diagnostic fiber optic, 10 – vacuum chamber (0.065 m^3).

The diagnostic scheme for investigations MPC plasma jets parameters and interaction processes between plasma jets and AD bodies is shown in Fig. 6.7. It contains three groups of measuring channels.

The first group is used for registration of electrical parameters MPC – discharge current of main and valve batteries (1 mOhm low inductive measuring loop circuit), discharge voltage on MPC and valve coil. The typical discharge voltage and current diagrams for MPC, operating with working gas He, are presented in Fig. 6.8. It shows, that discharge regime for creating MPC is practically aperiodic, duration of existing of acceleration regime in this type MPC is about 150 mcs, amplitude of discharge current is about 90 kA, maximum discharge voltage – 400V. Mass flux of the He, corresponding to these diagrams, is about 3 g/s. According with the mentioned above equations for plasma velocity on the MPC output its value can be estimated as 70 km/s.

The second group of measuring channels is used for spectral measurements in MPC plasma jets. It contains three spectrometers. Spectrometers 1 and 2 are used for measuring of time behavior of single spectral lines, emitting in the focus area of plasma gun. Usually, for working gas N_2 , or Air, the ion line of NII 566,7 nm, 594.0 nm, and 594.2 nm are used. The ratio of these signals permits to measure the gas temperature in plasma focus at the different time of discharge [3]. The third spectrometer is used for getting of review emission spectra of plasma jets (the first operation mode) and for measuring of electron density by the Stark broadening for several single spectral lines (566.7 nm, 571.1 nm, and 594.2 nm) [1-3] (the second operational mode). All these spectrometers have fiber optics connectors with investigation area common collecting lens and common investigating area in plasma focus. As preliminary estimations show, the electron concentration n_e in the plasma focus can be about 10^{17} - 10^{18} cm^{-3} , electron temperatures T_e are about 2-3 eV.

The third group of devices is used for visualization and measuring with high spatial and time resolution of plasma jet parameters and processes of its interactions with AD bodies. It contains the Schlieren system, based on 0,7 m telescope, impulse high – power LED, and two channel systems for image registration.

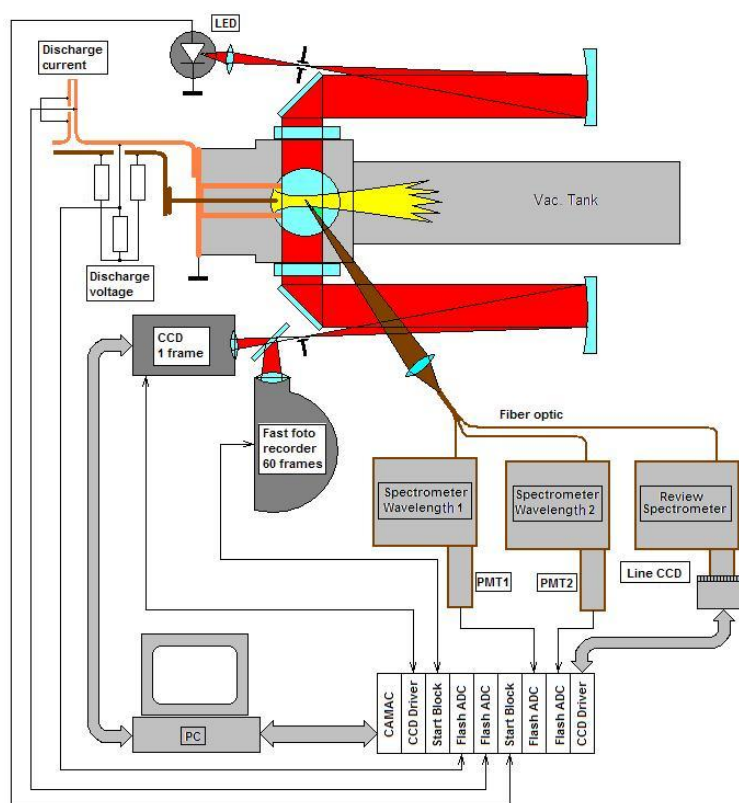


Fig.6.7. Scheme of diagnostics tools for Magneto Plasma Compressor investigations

The main part of this system is Fast Photo Recorder (FPR), operating in two regimes. The first allows to get more than 60 single frames of investigating processes per 150 – 200 mcs (2.5-3 mcs per frame) with comparatively low space resolution (about 200×200 pixels). The second regime (continuously spreading of slit image) is used for measuring of plasma streamers velocity in MPC jet and their spatial and temporal distribution. For getting the pictures with higher resolution and lower exposition time (1 mcs, 600×600 pixels) the measuring system is used in combination with the gating CCD camera.

Diagnostic system has sensors for measuring pressure in the vacuum tank, as well as the pressure sensors for measuring of instantaneous processes in the gas medium, arising after shutting.

In Fig. 6.8.a the typical view of free compression plasma jet is presented. Plasma accelerator with parameters mentioned above allows to create the quasi-state (100-150 mcs) plasma jets with gas velocity in the focus area up to 60-70 km/s (for He) and plasma density

more than 10^{16}cm^{-3} . The dimensions of the focus area are about 5 mm in diameter and 15 mm length.

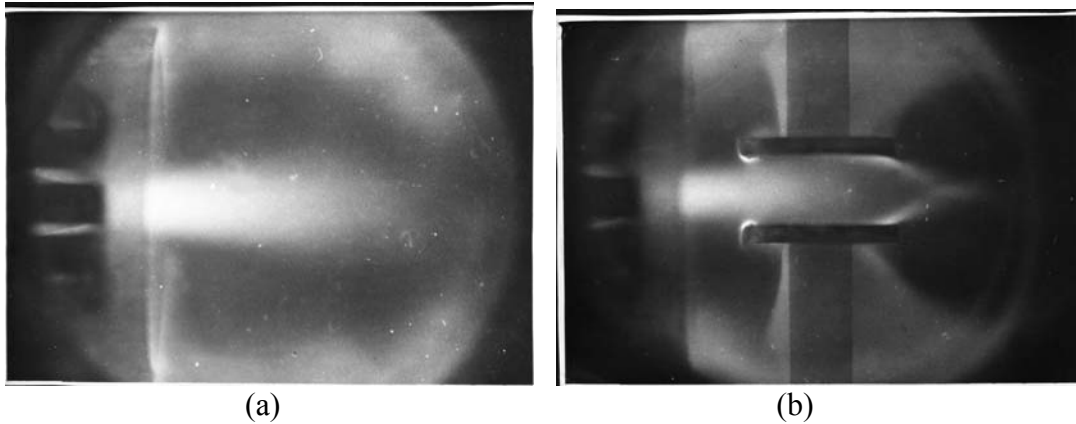


Fig.6.8. General view of free compression plasma jet on the output of Magneto Plasma Compressor

One of the possible applications of the MPC in plasmadynamic may be it using for injection of disperse fuel particles in supersonic flows. It may be interesting for investigations of solid particle fuel combustion processes in supersonic engines.

For demonstrating of these possibilities the experiments of small particles acceleration in MPC plasma jet was performed. For these experiments we used the MPC operated in Vacuum Regime and the disperse target based on the Electro-Dynamics Disperse System (EDDS).

EDDS is the stationary disperse cloud, arising between two electrodes in strong electric field (more than 10-15 kV/cm) when metallic particles put between them (see Fig.6.9). This pseudo-liquid electrodynamics system operates both in vacuum and in atmospheric conditions.



Fig.6.9. Electro-Dynamics Disperse System (EDDS).

The interaction between plasma jet and disperse particles leads to particles accelerating. In Fig.6.8.b the process of interaction of MPC in VR generated jet and EDDS is presented. For

example, the W particles with middle diameter 5 mcm in a result of such accelerating have a velocity about 2.0-2.6 km/c. The fluence of this disperse flow near the target, placed at the distance 1,6 m is about 10-50 particles/cm². Results of our experiments clearly show that the particles with these velocities may be successfully injected in supersonic gas flows with comparable velocities.

6.2. Magneto-Plasma Compressor in Residual Gas-Regime

As we mentioned above, the second variant of MPC using – the Residual Gas Regime of MPC may be more interesting for applying it to aero - and plasma – dynamic.

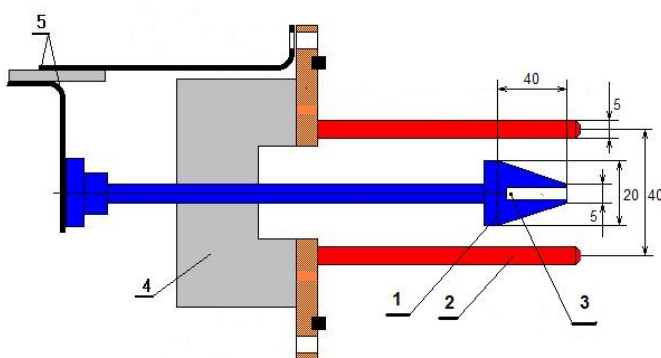


Fig.6.10. Scheme of investigated MPC in RGR. Dimensions are given in mm

The principal scheme of using MPC, operating in R-G regime is presented in Fig.6.9.

It has traditional scheme, but the part, connected with fast gas-valve is withdrawn. Compressor has two coaxial electrodes, - central cone cathode (1) and cylindrical bar anode (2). Cathode has the axial hole, named “Cathode Divertor” [1-4]. MPC is connected with the main discharge capacity bank by means of low –inductive circuit (5).

In Fig.6.11 the general view of experimental installation for investigations of MPC in RGR is presented.

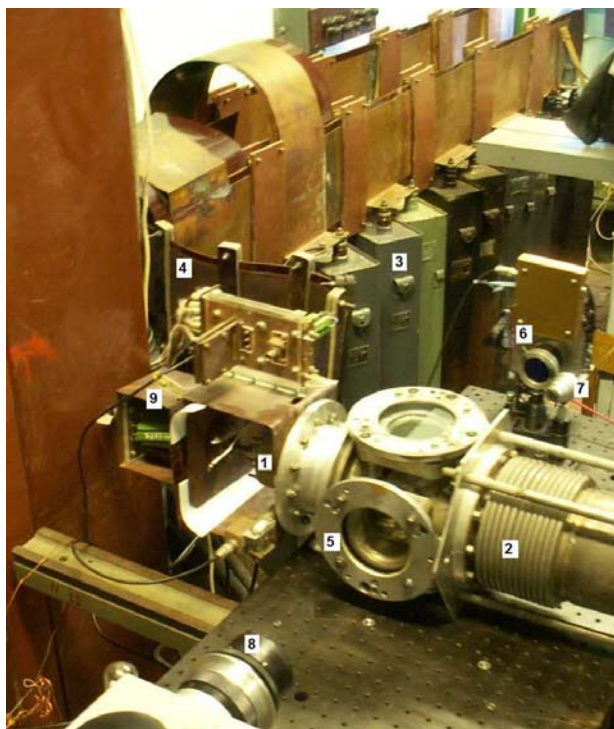


Fig. 6.11. General view of experimental installation for investigations of MPC in Residual-Gas Regime

In the photo, (1)- investigating MPC, (2)- vacuum chamber, (3) – capacity bank (2850 mcF, 1.5-4 kV), (4) – low-impedance circuit, connecting the bank and the MPC through the Hg-switchboard, (5) – windows of testing chamber, (6) – synchronous color CCD camera MINOLTA Dimage Z3 with interference filters, (7)- optical head with fiber output for spectral investigations, (8) – fast photo-recorder, (9) –discharge voltage measuring circuit.

As the first step investigation MPC was used in R-G-regime with working gas Air at the single pressure 0.6 Torr and single capacity voltage 1.6 kV for streamlining of simple AD shapes.

The area of plasma focus was fixed by synchronous CCD camera through several interference filters (IF). The IF used have different transmitted wavelengths (407, 510, 630 and 682 nm) and approximately identical transmission (0.25-0.3) and bandwidth (10-12 nm).

For each wavelength, the free plasma jet picture and picture of interaction of plasma jet with a wedge (material – Teflon FT-4, angle 40°) was recorded. The distance between output plate of MPC and a wedge was 40 mm. In Fig. 6.12. the pictures of free MPC jet and jet with wedge recorded with IF 407 and 630 nm are presented.

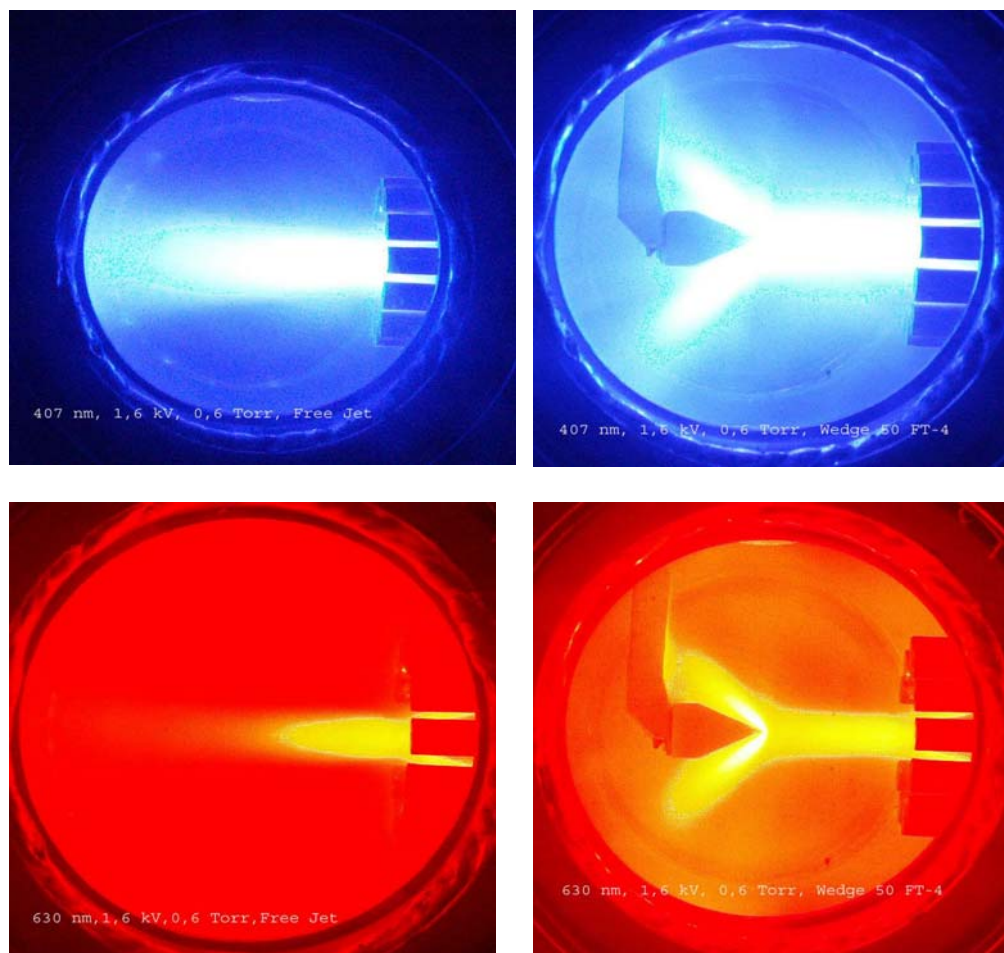


Fig.6.12. MPC in R-G regime, 1,6 kV, 0.6 Torr, 407 nm
MPC in R-G regime, 1,6 kV, 0.6 Torr, 630 nm

The pictures clearly show, that the existing MPC allows to create comparatively homogeneous hypersonic air-plasma jets. The differences in geometrical sizes of free jets and differences in streamline pictures, obtained for different recorded wavelengths, show hypersonic character of investigated jets and their complicated structure.

Results of these first experiments confirm the possibilities of using R-G regime of MPC for experimental modeling of interaction processes of hypersonic plasma flows with different materials and bodies. Existing parameters of MPC jets permit us to realize the investigations of bow shock formation processes for very interesting and very important diapason of plasma velocity, density and temperatures ($5\text{-}20\text{ km/s}$, $10^{17}\text{-}10^{18}\text{ cm}^{-3}$, $1\text{-}3\text{ eV}$).

The next very important experiment, which was made in this work, was the measuring of MPC jet acceleration effect for a small (5 mm in diameter), steel sphere ($M = 0.5$ g). This small aerodynamic model was placed on the axis of MPC on a distance about 20 mm from the exhaust nozzle exit on a thin (0.1 mm) copper thread. This thread is evaporated during the first 50 – 80 mcs of a sphere accelerating process. Its influence on the sphere dynamics is negligible. The fast photo record of these processes was made and it is presented in Fig.6.13.

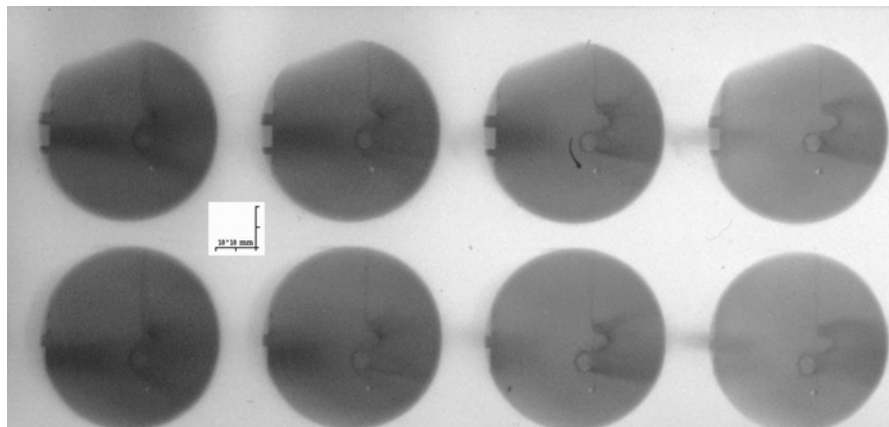


Fig.6.13. Fast-Photo records of MPC jet with steel spherical model. Sphere diameter is 5 mm, it mass is 0,5 g. Model is placed on the jet axis (20 mm from the MPC exhaust nozzle exit). Initial air pressure is 0.75 Torr, capacity voltage – 2 kV. Record begins approximately on the 50 mcs after jet origination. Time delay between frames is 10 mcs, exposition time for each frame – 10 mcs. Position of MPC is clearly seen in the left end of each frame.

Results of these measurements are presented in Fig.6.14.

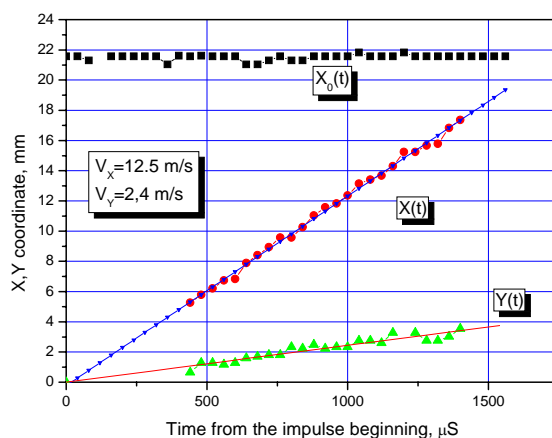


Fig.6.14. Space diagrams for steel spherical model in the MPC plasma Jet. Initial air pressure is 0.75 Torr, capacity voltage – 2 kV.

In this space diagram $X_0(t)$ is the initial position of a sphere (obtained by the exposition without discharge), $X(t)$, $Y(t)$ - horizontal and vertical coordinates of sphere center after discharge ignition. The linear approximations for the both groups of experimental points show that our test aerodynamic body (sphere) moves after accelerating processes with velocity about 12.6 m/s.

For getting the estimations of stagnation pressure level in MPC jets we use the simplest model of accelerating processes, based on the next admissions:

- Drag coefficient of using sphere has not changes during the acceleration processes, and its averaging level is about 0.6;
- Cross-section of plasma jet has not sufficient changes during the acceleration processes, and its diameter is about 5 mm.

The process of sphere acceleration under force action may be described as:

$$m_B \cdot \frac{dV_B}{dt} = F(t)$$

where $F(t)$, - is the force, acting on the body, m_B - body mass, and V_B - is the body velocity.

The acceleration force, acting on the sphere in jet may be presented as:

$$F(t) = C_x \cdot \frac{\rho(t) \cdot V_J^2(t)}{2} \cdot S_B$$

where C_x - drag coefficient for sphere, $\rho(t)$ - density of jet, $V_J(t)$ - jet velocity, S_B - cross-section of body.

In MPC jet the density in focal area depends on mass flow \dot{m}_J , cross section of jet S_J and jet velocity $V_J(t)$ as:

$$\rho(t) = \frac{\dot{m}_J}{S_J \cdot V_J(t)}$$

As shown in [1,2], mass flow in focal area of MPC under compressing conditions may be presented as:

$$\dot{m}_J = 1,18 \cdot 10^{-11} \frac{I_A^3(t)}{U_D}$$

where $I_A(t)$ - discharge current in MPC, U_D - discharge voltage.

According with [2] the jet velocity under compressing regime of MPC may be presented as:

$$V_J(t) \approx 10^{-2} \cdot \dot{m}_J \cdot I_A^2(t)$$

Calculations, based on this model, show that the ram action of plasma jet for MPC in RGR can reach 100-150 Bar. So, high level of MPC jet penetrating ability makes the investigations of mixing MPC plasma jets with supersonic neutral flows very important.

Nevertheless, the practical using of MPC in applied aerodynamic and plasma dynamic demands to operate with it under the static pressure more than 20-100 Torr (altitudes less than 30 km).

6.3. Magneto-Plasma Compressor in High-Pressure Residual Gas regime

The main task of next step of work was the investigations of Magneto – Plasma Compressor under the High Static Pressures and the creation of new experimental setup for investigation of the mentioned above mixing processes, demonstration of their efficiency and obtaining the preliminary results.

The created new experimental installation consists of two main parts. The first permits to create hypersonic plasma jets in the comparatively dense gas media (up to 100 Torr) and is based on the new type of Magneto – Plasma Compressor, operated under the High-Pressure RGR (HPRGR). The second (essentially new part) allows to generate supersonic gas flows with Mach number 1.5-2.5 and is based on the Impulse Wind Tunnel, using the Ludwig scheme.

The final schematic diagram of the created installation is presented in Fig. 6.15, the general view of this installation is shown in Fig. 6.16. Essential parts distinguishing this installation from the preliminary project are the electromagnet Launching Valve (it permits to open the orifice in 30 mm diameter in to vacuum in a time less than 16 ms), new places (more efficient) for pressure sensors (P1 and P2) and constructional element named connection pipe. New installation contains the MPC-jet part, based on the vacuum chamber V_3 taken from the previous experimental setup and impulse neutral supersonic jet part, based on two additional vacuum chambers V_1 and V_0 . The supersonic gas jet organized on the Ludwig scheme has the diapason of Mach numbers from 1.5 to 2.5. For chosen nozzle with $M=2$, the critical diameter of nozzle is 30 mm and the exhaust nozzle diameter is 39 mm. Chamber V_1 has the volume

10.6 dm^3 , the tank V_0 has the volume 280 dm^3 . Internal diaphragm of the launching electromagnet valve determines flow parameters and its lifetime. The test experiments show that Mach number 2.0 is achieving when the diameter for this diaphragm is 16.4 mm and the initial pressure in V_0 - V_3 28 Torr.

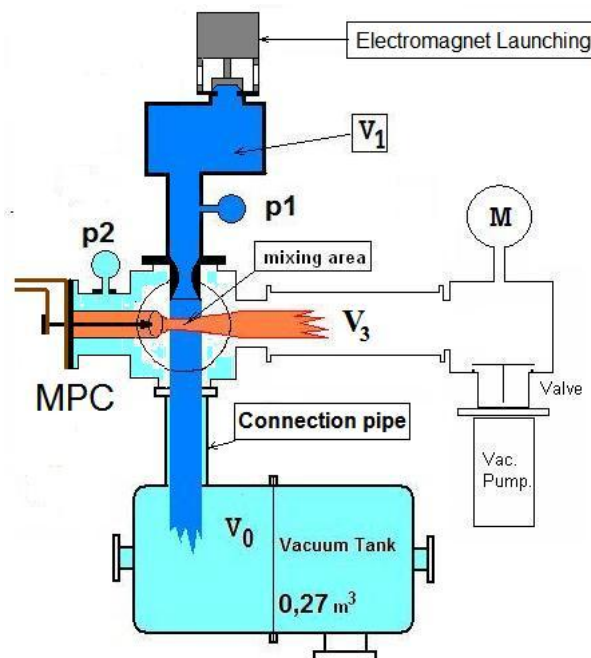


Fig. 6.15. Scheme of new experimental installation for jets mixing investigation

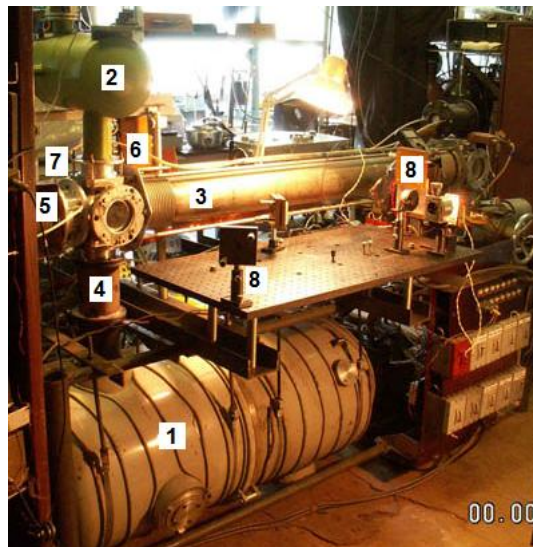


Fig. 6.16. View of the new experimental installation for Jet Mixing Investigation

The pressure sensors P1 and P2 (24PC type Honeywell) are used for measurements of the instantaneous pressure in V_1 and V_3 after the tube launching. Time resolution for the both pressure sensors is about 1 ms. Sensor P1 is placed close to the end of the driver tube (see pos. 6 in Fig.6.16), sensor P2 is placed close to the nozzle outlet and really checks the pressure in tank V_3 (pos.7). The ratio of these pressures defines the Mach number of the flow, arising in the nozzle. The working regime of this impulse aerodynamic tube begins when the ratio p_1/p_2 achieves the necessary level ($P1/P2=P/P0=7.82$ for Mach number 2.0).

The results of the pressure recording are presented in Fig.6.17. The initial pressure in the system ($P0$) is 28 Torr and before the start moment the pressure in the drive chamber P (sensor P1) and the pressure $P0$ (sensor P2) are equal. The ratio $P/P0$ is about 1.

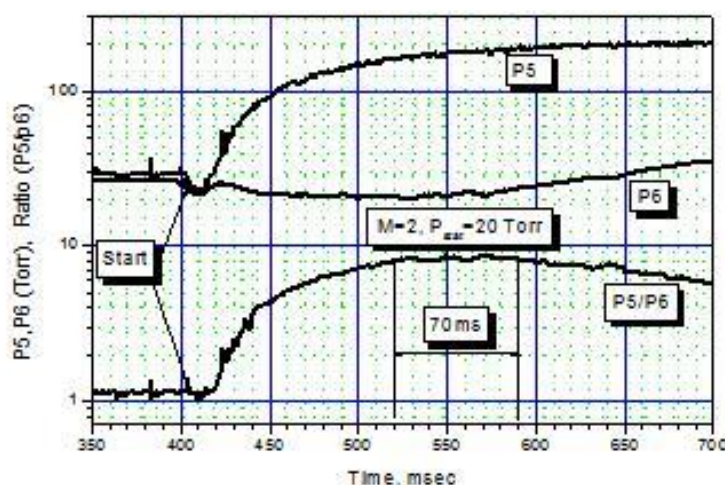


Fig.6.17. Parameters of impulse supersonic gas jet

After the tube launching, EM valve is opening and the arising supersonic jet begins to interact with the “connection pipe” of the installation and the static pressure $P0$ in tank $V3$ slightly goes down. Under the mentioned above experimentally found conditions, the necessary ratio level for $P/P0$ is achieved only after 155 ms after the tube launching. At this moment the MPC plasma jet starts. During the time interval with duration about 70 ms the quasi-stationary wind tunnel generates supersonics flow with $M=2.0$ and static pressure approximately 20 Torr.

The results of first experiments with MPC in RGR created according the simplest scheme (Fig.6.10.) show, that under the initial pressure more than 5-10 Torr the processes of discharge initiation in the simplest kind of MPC become very unstable.

For eliminating of this effect we created the new construction of MPC. This construction is shown in Fig.6.18.

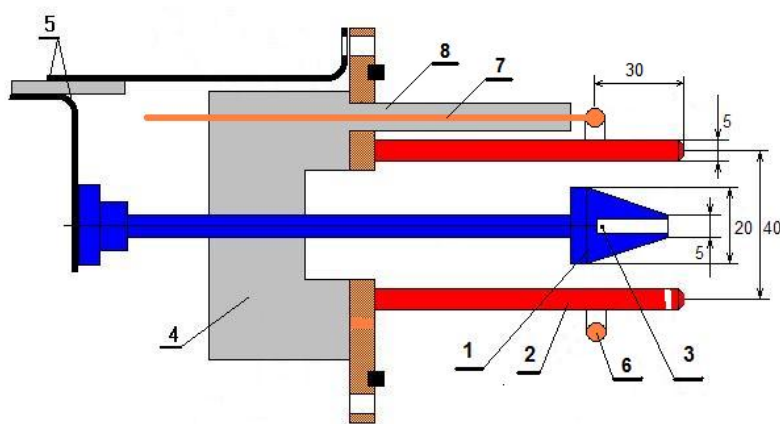


Fig.6.18. Scheme of MPC for High-Pressure Residual Gas regime

Essential new part in this construction is the ring electrode for auxiliary discharge, pos. 6, 7 and 8. This electrode, after applying to it a comparatively high voltage (we use the power supply with output voltage 3.5 kV) permits to create the small auxiliary discharge placed near the critical section of the MPC nozzle. The test experiments show that this discharge (with using the voltage of electrical source) exists in our MPC under the pressure up to 120-150 Torr.

The new construction of MPC permits to get the hypersonic plasma jets under the high static pressure [4,5]. In this report we demonstrate the possibility of MPC operating under the static pressure more than 90 Torr.

The results of our first experiments show that investigation of internal structures in MPC plasma jets is very complicated problem. The high level of MPC jet brightness makes the ordinary methods of Schlieren visualization inapplicable. The scheme of new diagnostic displacement, created for Schlieren visualization of plasma jets with high luminosity is shown in Fig.6.19.

This scheme is based on application of the following main constituents:

- High-power CW diode laser (25 mW, 640 nm.);
- Two telescopes – illuminating (focal length 750 mm) and receiving (focal length 900 mm);
- Interference filter 640 ± 10 nm;

- Space filter for Jet spontaneous radiation including the telescope L2 (900 mm) and pinhole (1 mm) with the Schlieren knife;
- Fast CCD camera with minimal frame time exposition 500 ns.

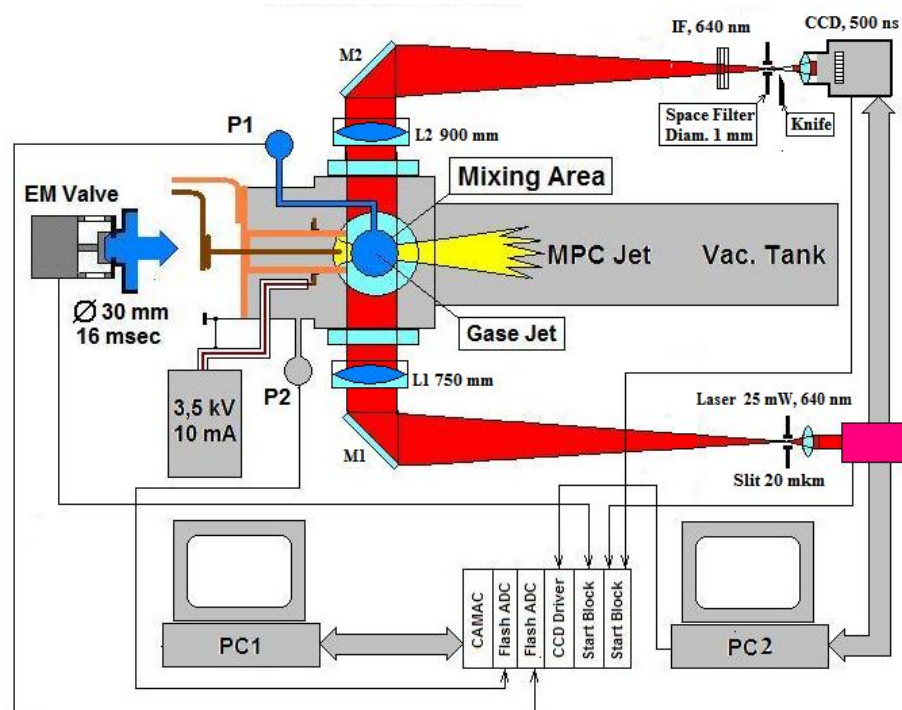


Fig. 6.19. New diagnostic scheme created for investigation MPC plasma jet and SS flow mixing and of spatial-temporal dynamics of jets, generated MPC in RGR

Electrical parameters of the discharges in MPC are managed by the data acquisition system based on the CAMAC. This system checks the discharge current and discharge voltage with time resolution 50 ns, the time behavior of pressures in Ludwig Tube and synchronizes the CCD camera with the launching moments of the Ludwig Tube and MPC. In Fig.6.20 the typical Ampere-Volt characteristics of discharges in MPC HPRGR are presented. Pictures 1 and 2 – low pressure of residual gas (close to the “Vacuum regime” of MPC), 3, 4 – high pressure (21 Torr). Point 1 and 2 corresponds to the beginning and ending of quasi-stationary state of plasma jet in MPC. Pictures 2 and 4 are the “Dynamic” characteristics.

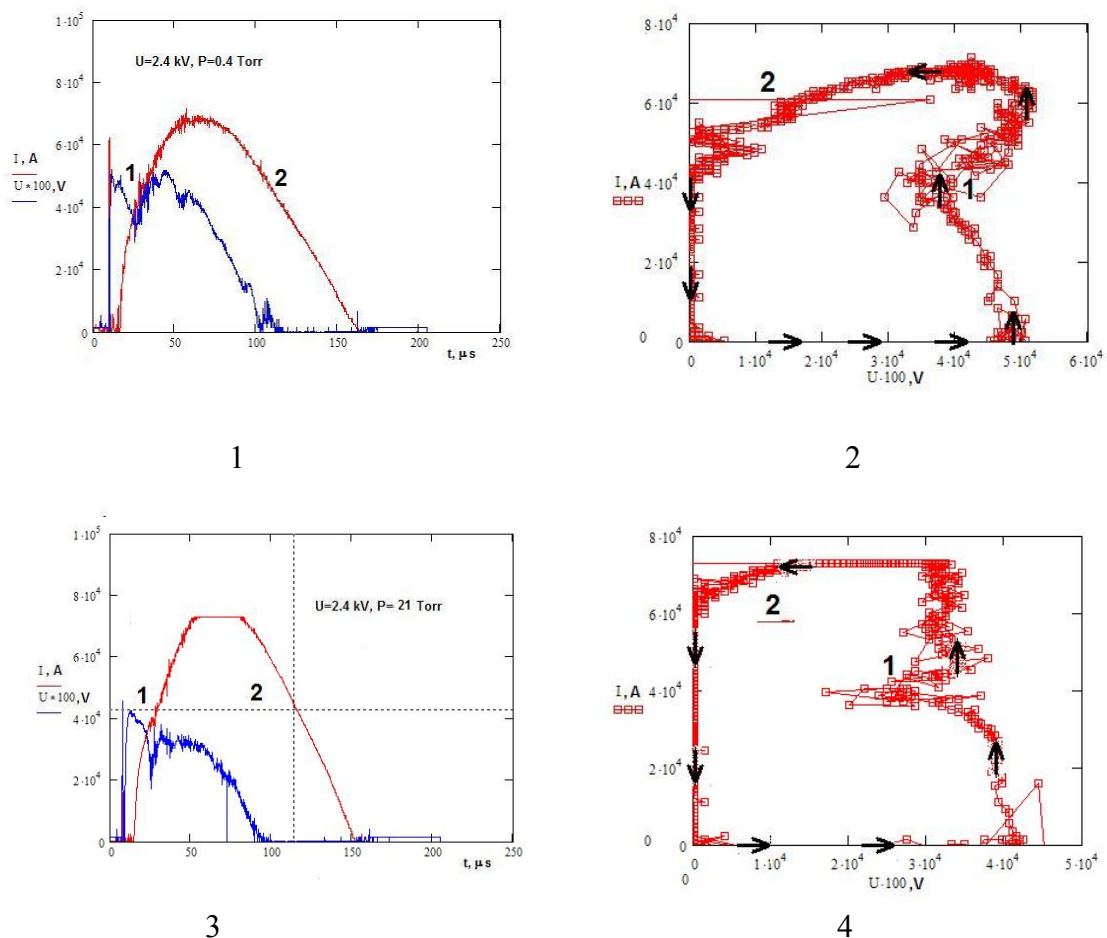


Fig. 6.20. Ampere-Volt characteristics of HP RGR MPC for the different residual gas pressure

Fig.6.21 demonstrates the Ampere-Volt Characteristics of discharge in MPC under the pressure 22 Torr for different discharge voltage (1) and the capacity bank voltage dependence of the whole energy inputs in the discharge for different pressures (2).

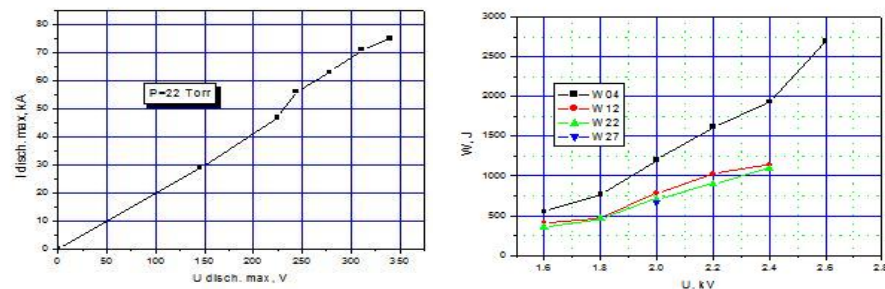


Fig. 6.21. A-V Characteristics of MPC under the 22 Torr and different discharge voltage (1) and the whole energy inputs via bank voltage for different pressures (2)

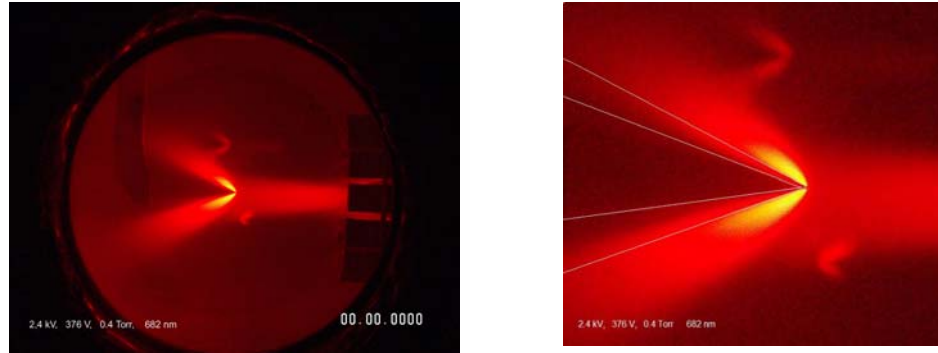


Fig. 6.22. Interaction of a wedge model (Teflon) with MPC jet under 21 Torr static pressure. Photos were obtained through the interference filter (694 ± 10)nm with frame exposition 1000mcs

The streamline of wedge model (Teflon) in MPC jet under the 21 Torr static pressure is shown in Fig.6.22. Photos were obtained through the interference filter (694 ± 10) nm with frame exposition 1000 mcs. This kind of pictures allows to make the approximate estimates of Mach number in MPC plasma jet. The results of these estimations are presented at Fig.6.23.

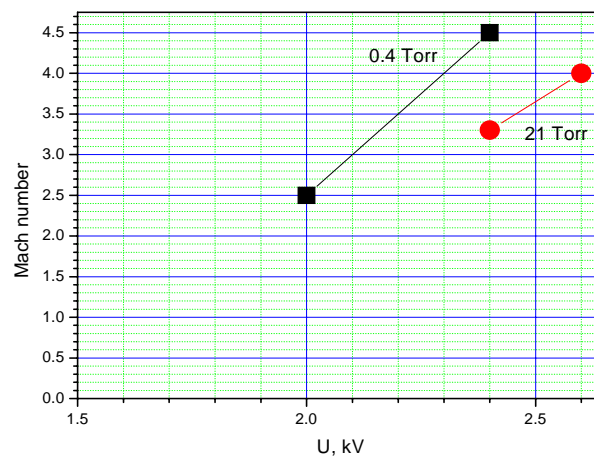


Fig. 6.23. Estimations of the maximal Mach number of MPC plasma jet, getting from analyses of wedge streamline pictures

In Fig.6.24 the processes of propagation of shock wave, created by MPC jet in residual gas with static pressure 30 Torr are presented. Picture 1 – 15 mcs after discharge starting, picture 2 - 20.5 mcs, frame exposition is 1000 ns), picture 3 - 23 mcs (frame exposition 2 mcs), picture 4 – 24,5 mcs. Each picture was received with the frame exposition time – 500 ns (except the

frame 2.14.2 and 2.14.3) and with using interference filter 640 nm and orifice diameter in spatial filter 1 mm.

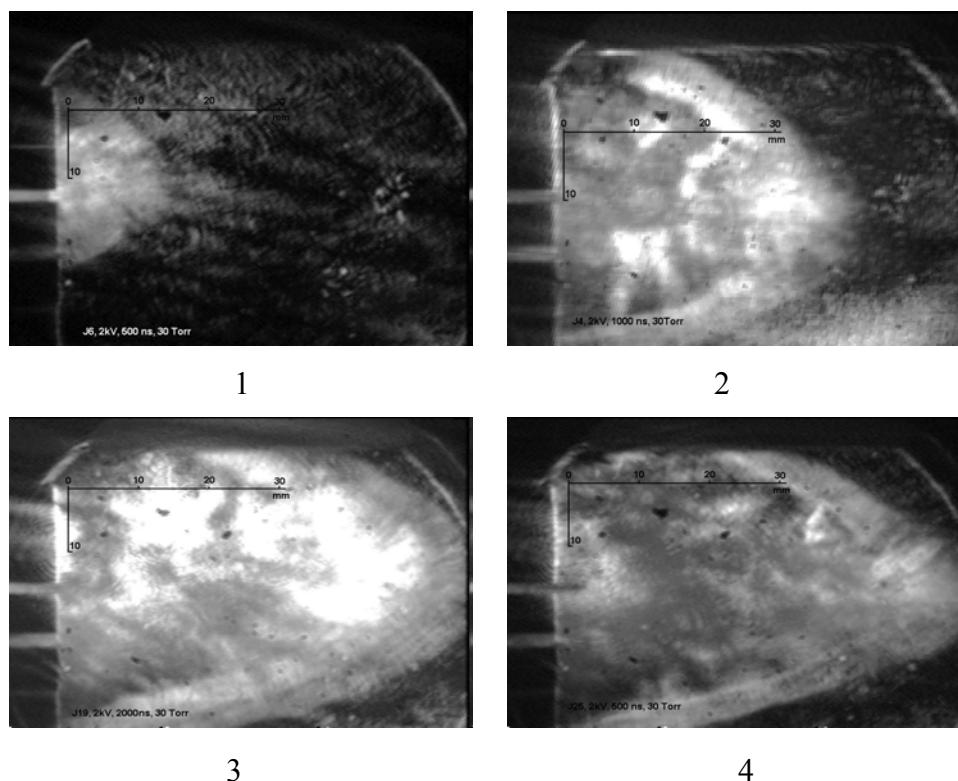


Fig .6.24. Propagation of the shock wave, created by MPC jet in residual gas with static pressure 30 Torr. Picture 1 – 15 mcs from discharge starting, picture 2 – 20.5 mcs (frame exposition 1 mcs), picture 3 – 23 mcs (frame exposition 2 mcs), picture 4 – 24.5 mcs. All frames were made under the exposition time – 500 ns (except the frame 2.14.2, 2.14.3), interference filter 640 nm, and orifice diameter in space filter 1 mm.

The estimation of velocity of MPC jet propagation in residual gas under the pressure 30 Torr and bank voltage 2 kV gives the value about $(4,4 \pm 0,2)$ km/s.

Fig.6.25 demonstrates the possibility of using the created MPC under the static pressure 50 Torr (frame 1) and 90 Torr (frame 2), the exposition time is 500 ns, interference filter 640 nm, and orifice diameter in space filter 1 mm. The comparison of plasma jet shapes obtained under the comparatively low pressure 7.8 Torr and pressure 90 Torr shows, that formation of elongated plasma gets demands higher energy (higher voltage of capacity).

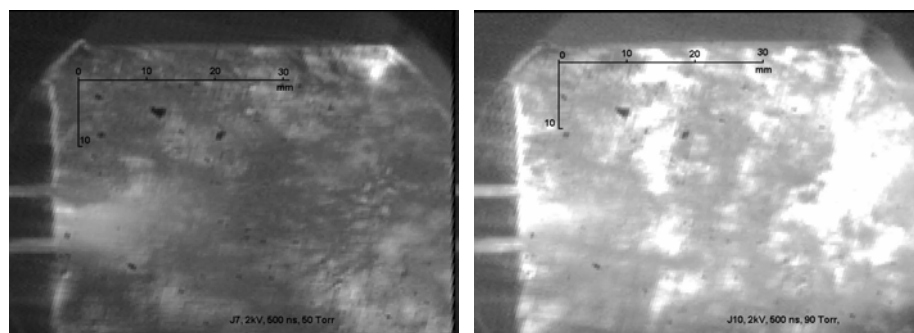


Fig. 6.25. Pictures of MPC plasma Jets under the high pressure of residual gas. Picture 1 – 50 Torr, picture 2- 90 Torr. Frame exposition time – 500 ns, interference filter 640 nm, and orifice diameter in space filter 1 mm.

The results of mixing processes diagnostics are presented in Fig.6.26.

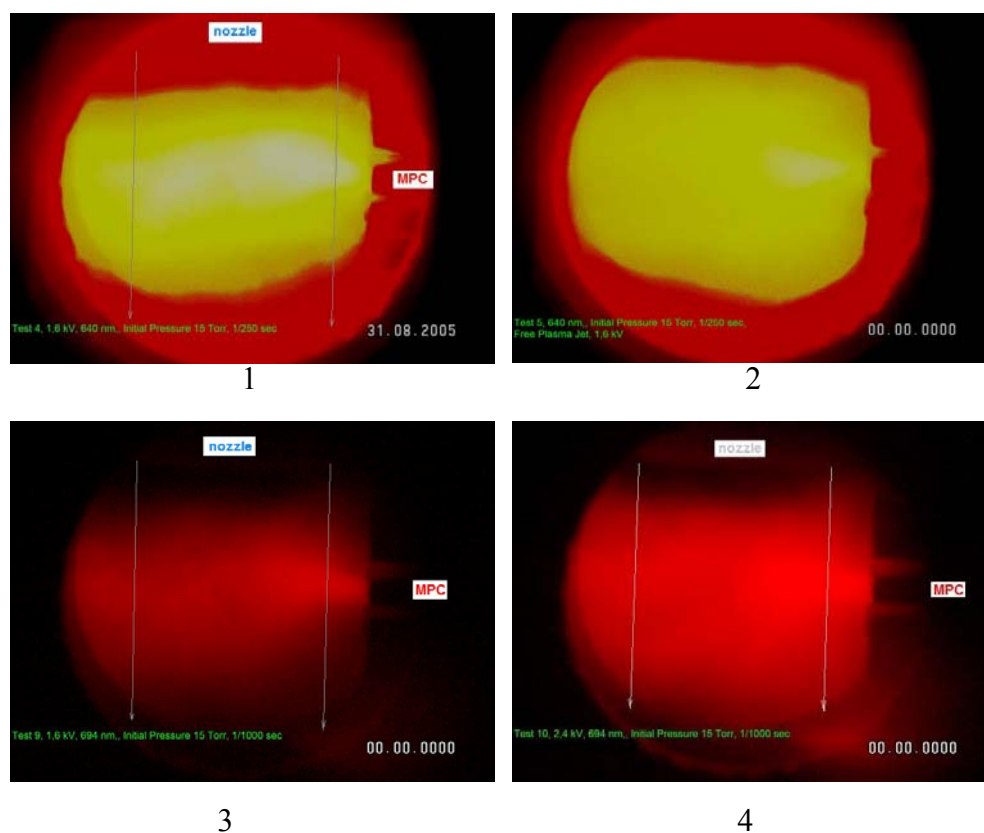


Fig. 6.26. MPC plasma jet and SS flow mixing

In Fig. 6.26.1 and 6.26.2 the pictures of plasma jets of MPC with and without supersonic gas flow ($M=2,0$) crossing are shown. Both frames were made under the exposition time $1/250$ sec and through the interference filter 640 ± 10 nm. For the both tests the voltage of MPC capacity was 1.6 kV. The frame (2) corresponds to the free plasma jet under the static pressure 15 Torr. The frame “Test 4” (1) is the photo of interaction of plasma jet with supersonic gas flow. The comparison of the shapes of two jets shows that under the mixing condition used the plasma jet has an essential deflection, asymmetric and inhomogeneous structure. Two additional tests were made under the exposition time $1/1000$ sec and through the interference filter 690 ± 10 nm (Fig.6.26, 3 and 4). Test 9 (3) corresponds to the plasma jet produced by MPC with initial capacity voltage 1.6 kV, Test10 (4) – 2.4 kV. Both photos show the slightly asymmetrical and inhomogeneous character of plasma jets, interacting with supersonic flow.

The results of our investigations show that Magneto-Plasma Compressor (MPC), operated in Residual Gas Regime (RGR) could generate comparatively long-live hypersonic plasma jets with high density, temperature and penetration ability in neutral supersonic flows [1-3]. Also we had demonstrated the possibilities of MPC to generate the jets under the high static pressures of residual gas (HPRGR) – upper level of this pressure is about 100 Torr [4,5]. The properties of these jets are so unique that carefully investigations of their spatial and temporal behavior became very important and necessary.

The important task of presented work were the carefully investigations of mechanisms of jet arising in MPC operated in RGR, the measuring of their temperatures and estimation of value of jet charge efflux in external space.

For estimations of MPC current efflux value the steel cone model was used. Cone placed on the axis of MPC at the distance 27 mm from the MPC outlet. The measuring resistor has the value 0.1 Ohm.

For spectrometric investigations the optical radiation collected from the point of plasma focus (it placed at the distance about 10 mm from the MPC outlet on it axis) directed in to the spectrometer by the quartz-polymer fiber guide with numerical aperture 0.5 and pass bandwidth 0.2-0.9 mcm.

The results of jet dynamics visualization presented in the Fig. 6.27 and 6.28. In general, the Plasma generated jet has the two main temporal phases. Phase I (fast phase) corresponds to the interval about (0-10) mcs from the beginning of the discharge in MPC. At this phase MPC

generate unfocused plasma jet with very high velocity and comparatively low density. Nevertheless, the shock wave, arising in residual gas, when this jet propagates in it, clearly monitored. The pictures corresponded to the fast phase are presented in the Fig.6.26. The estimation of propagation velocity for this fast jet gives the value about 6 ± 0.5 km/s. Phase II (slow phase)

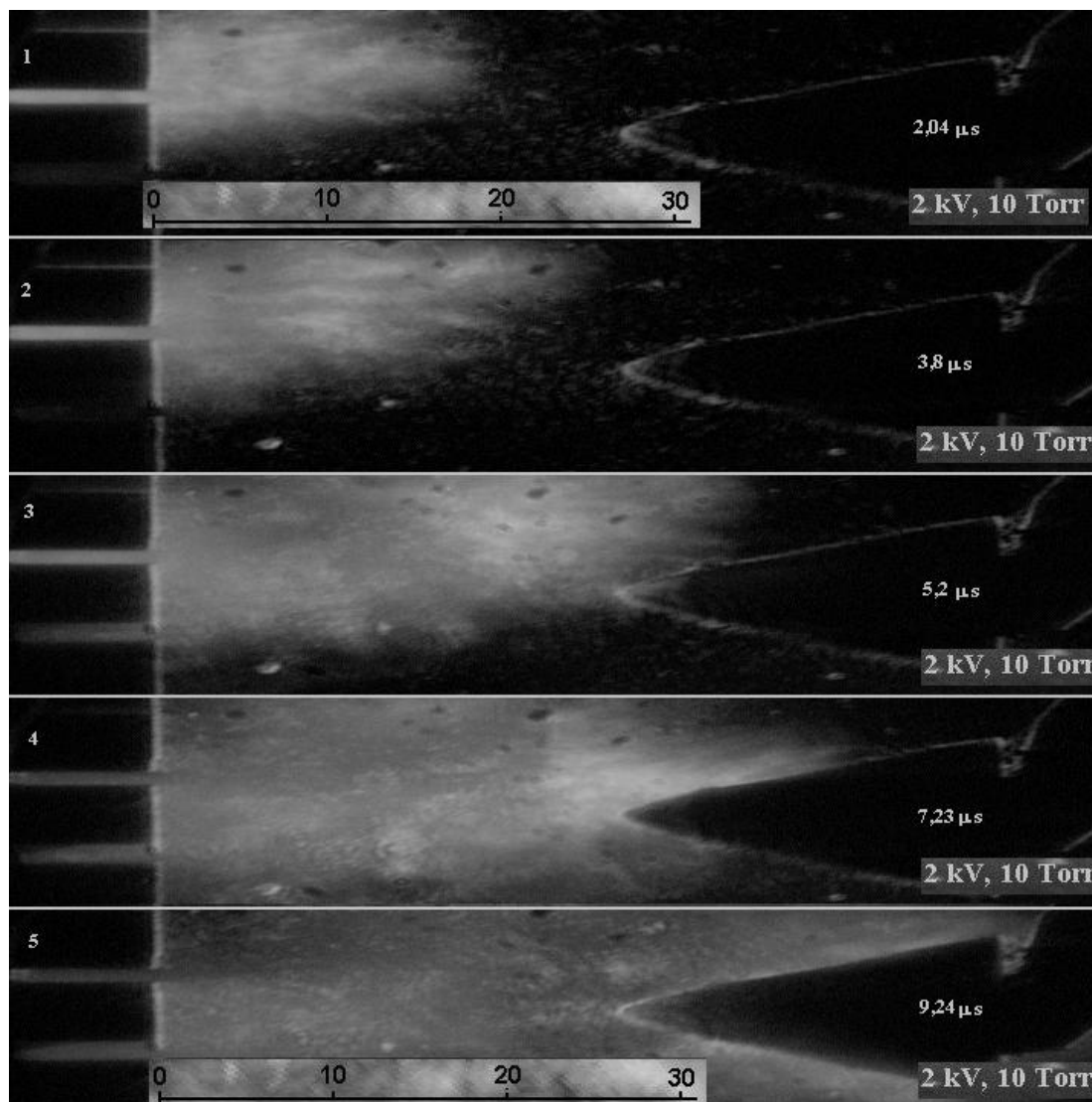


Fig. 6.26. Dynamics of jet arising in MPC in RGR under the 10 Torr static pressure.

Phase I (fast phase)

begins at the 10-12 mcs later than fast phase. At this phase MPC forms the quasi-stationary compressed jet with high density and temperature. The dynamics of slow phase arising and it

evaluation are shown in the Fig. 2.3. All experiments presented in the Fig.6.26 and 6.27 were performed under the static pressure (air) 10 Torr and capacity voltage 2 kV.

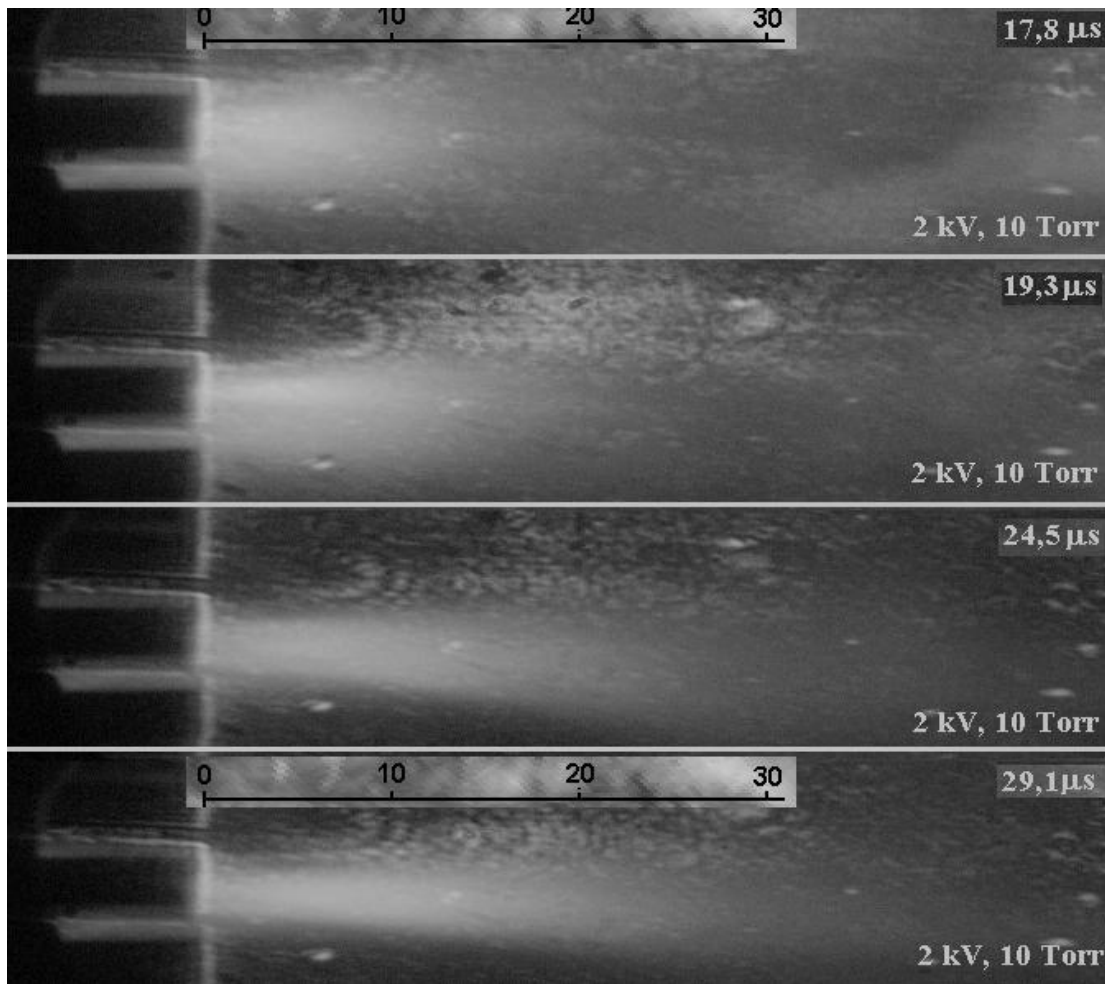


Fig.6.27. Dynamics of Phase II (slow phase) arising and evaluation for MPC in RGR under the pressure 10 Torr and capacity bank voltage 2 kV

The capability of jets, generated by MPC to produce the plasma media with high conductivity at the external area of the accelerator may be very important for its possible application in hypersonic plasmadynamic as a device for MHD applications and flow control techniques. The experiments for estimations of efflux effect (efflux current, efflux charge) in MPC in RGR were performed on the mentioned above setup. The time diagram for MPC discharge current and efflux current to the AD model placed at the 27 mm from the MPC outlet is shown in Fig. 6.28.

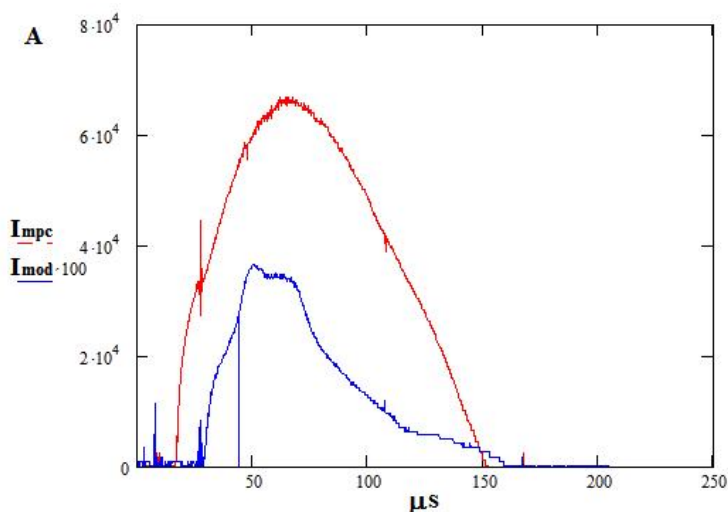


Fig.6.28. Discharge current (I_{mpc}) and efflux current ($I_{mod} \times 100$) for the MPC generated jet in RGR under the pressure 10 Torr

This typical diagram shows that efflux current corresponded to the Phase I is comparatively low, and main efflux effects are beginning after the arising of quasi-stationary phase (Phase II) in MPC discharge. The typical amplitude of efflux current is about 300-350 A, the general charge flows through the MPC during all phases of discharge processes is about 5.5 Coulomb, the general efflux discharge through the model – is about 0.017 Coulomb. The curve of efflux current has an interval, when the current value is practically constant. This temporal interval corresponds to more stationary stage of MPC generated jet.

In Fig.6.29 the typical review spectrum for the plasma jet, generated by MPC in RGR under the pressure 30 Torr and capacity voltage 2.4 kV is presented.

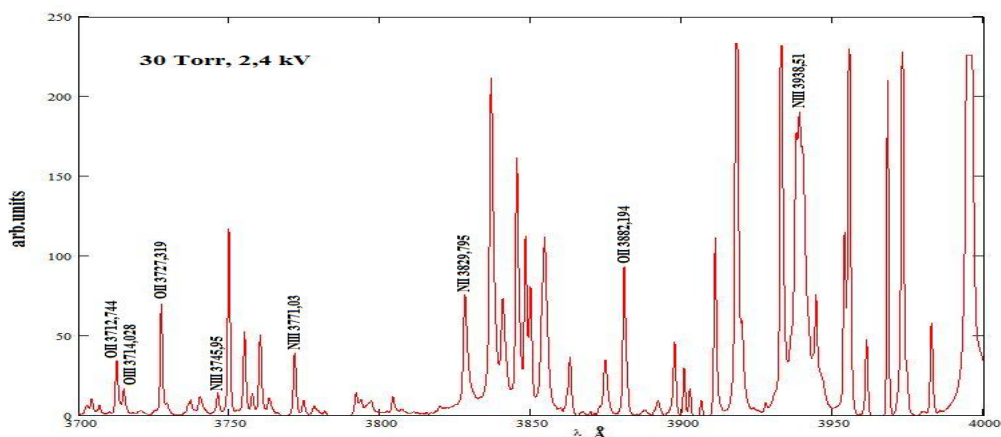


Fig.6.29. The review spectrum of jet, generated by MPC in RGR under the pressure 30 Torr and capacity voltage 2.4 kV

The spectral lines of monoatomic Oxygen and Nitrogen in different degree of ionisation practically create the presented spectrum. The calculation of atomic temperatures performed with using “two-line ratio” technique gives it value about 34000 ± 5000 K, and the electron concentration about $3 \times 10^{15} \text{ cm}^{-3}$.

In Fig.6.30 the short wave range spectrum for different levels of input energy is presented. Data was getting under the static pressure 100 Torr. In this spectrum the most important lines are noted – NII 361.57 nm and NII 366.38 nm.

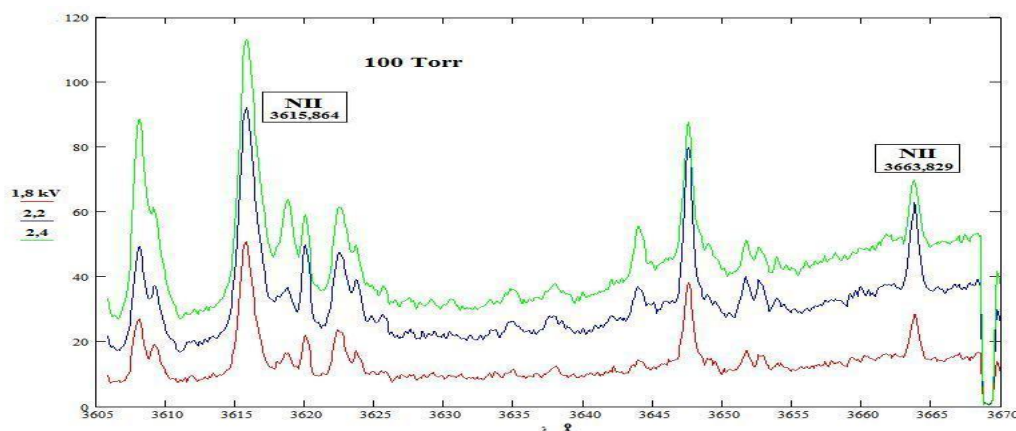


Fig. 6.30. The spectrum of MPC generated jets under the pressure 100 Torr and for different input energy (voltage of capacity 1.8-2.4 kV)

Fig. 6.31 presents the same spectrum for different static pressures of residual gas – 30, 50, 70, 90 and 100 Torr and for constant input energy – voltage of capacity bank is 1.8 kV

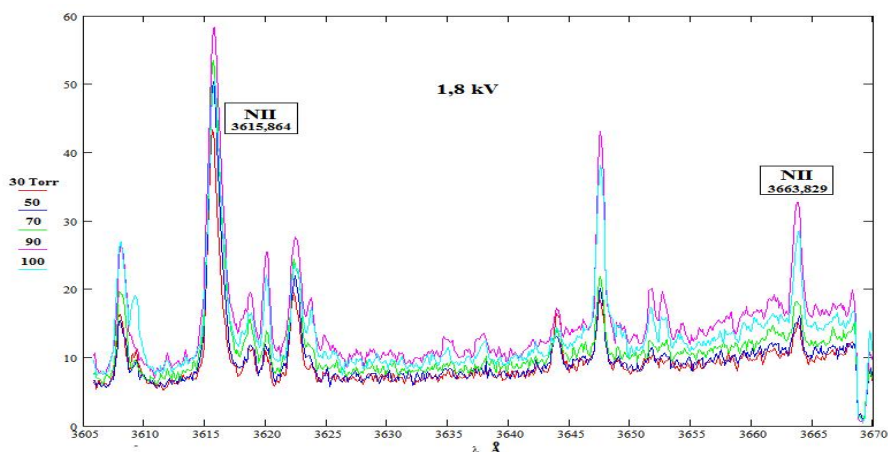


Fig. 6.31. The spectrum of MPC generated jets under the different static pressure and energy voltage of capacity 1.8 kV

It is very interesting, that spectral distribution in these spectra is not dramatically changed with pressure variances. The last fact allows to hope, that the properties MPC generated jets has the similar character for different pressures.

On the next steps of the work it is necessary to carry out more careful measurements of the efflux effects in far external area of MPC and perform the attempt of spectral measuring of plasma properties in this area.

6.4. Miniature Magneto-Plasma compressor in HPRGR

The jets generated MPC in HPRGR have unique properties and could be useful in applied plasmadynamics for development of a new type of plasma actuator for injection of high-enthalpy plasma jets both into quiescent gas and in supersonic flows with static pressure up to 100 Torr. Unfortunately, the specific energetically parameters of the tested large-scale MPC (outlet diameter 40 mm) are comparatively low [3-5]. It was the reason for creation and investigations of low-dimensional, Miniature MPC (MMPC) [6]. This type of MPC with comparatively low input energy may be very important for problem of flow control problems in supersonic engines and MHD applications.

The simplest model of Miniature MPC (MMPC) is shown in Fig.6.32. Compressor has six bar anode with 2 mm diameter and 40 mm length. These anodes are placed along the circle of 12 mm diameter and are gathered round the cone cathode. The effective outlet diameter for this MMPC is about 14 mm. Usually MMPC has an additional electrode for auxiliary discharge. This low-power DC discharge is placed near the critical section of MPC quasi-Laval nozzle and stabilizes operation regimes under the high pressures.

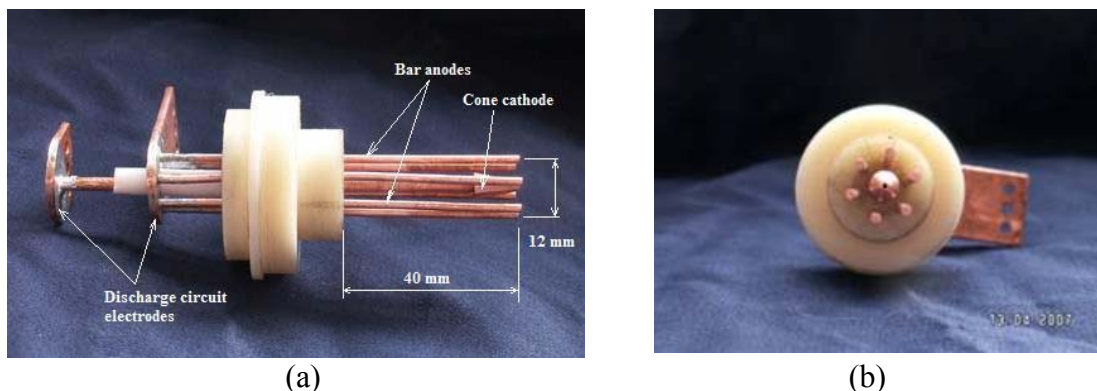


Fig 6.32. Design of the simplest model of Miniature MPC

This miniature MMPC places in the glass test pumped chamber (Fig. 6.33.a). It has the place holder for MMPC, high-voltage bushing for auxiliary discharge electrode, pressure sensor and tube for pumping. The glass walls of test camera permit to view and record all space phases of generating plasma jet. In Fig.6.33.b the auxiliary discharge electrode and the view of auxiliary discharge under the static pressure 30 Torr are presented.

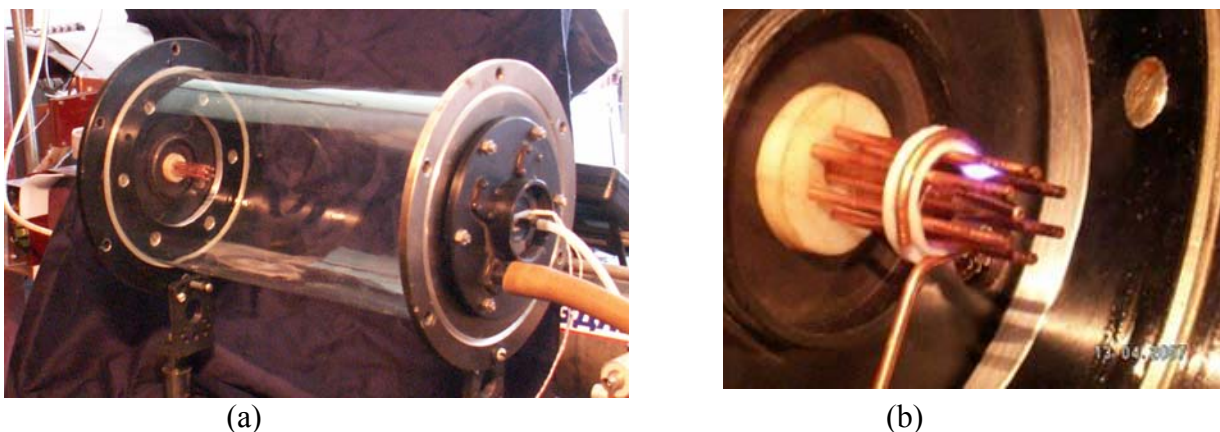


Fig.6.33. The MMPC in the test chamber and auxiliary discharge arrangement

The electrical circuit for MMPC energy supply has a standard scheme and consists of capacity bank (800 mcF, 2000 V), Hg-switchboard (100 kA, 5 kV) and circuits for measuring and recording of discharge current and voltage.

The first results of experimental investigation of MMPC in HPRGR demonstrate, that MPC in micro-size variant has the similar specific parameters as it large-scale analog, but with dramatically decreased input energetic characteristics.

In Fig.6.34 the general view of MMPC plasma jet under the residual gas pressure 35 Torr is shown. This photo was made through interference filter 393 ± 10 nm with exposition time 1 ms. It includes the images of all spatial and temporal phases of jet life. In the presented photo clearly seen that plasma jet generated by investigated MMPC has a typical plasma focus (compression area corresponds to places of high brightness) and elongation more than 6-8 outlet diameters of used MMPC.

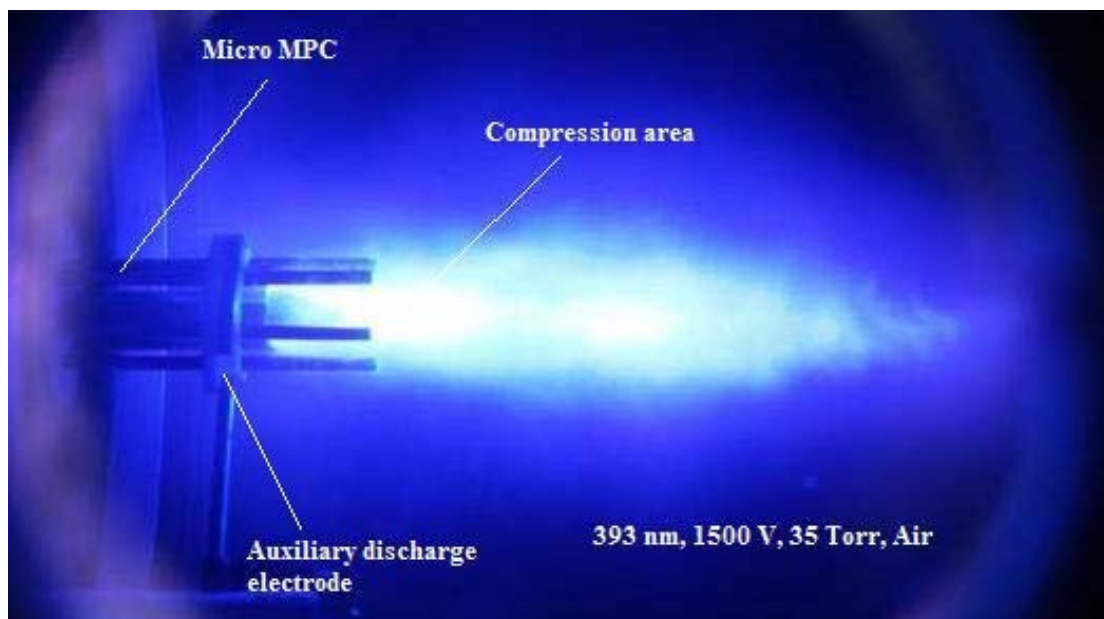


Fig.6.34. General view of plasma jet generated by Miniature MPC

The shape of generated jet has a strongly dependence from input energy. The view of MMPC generated jets for two different capacity voltages is presented in Fig.6.35.

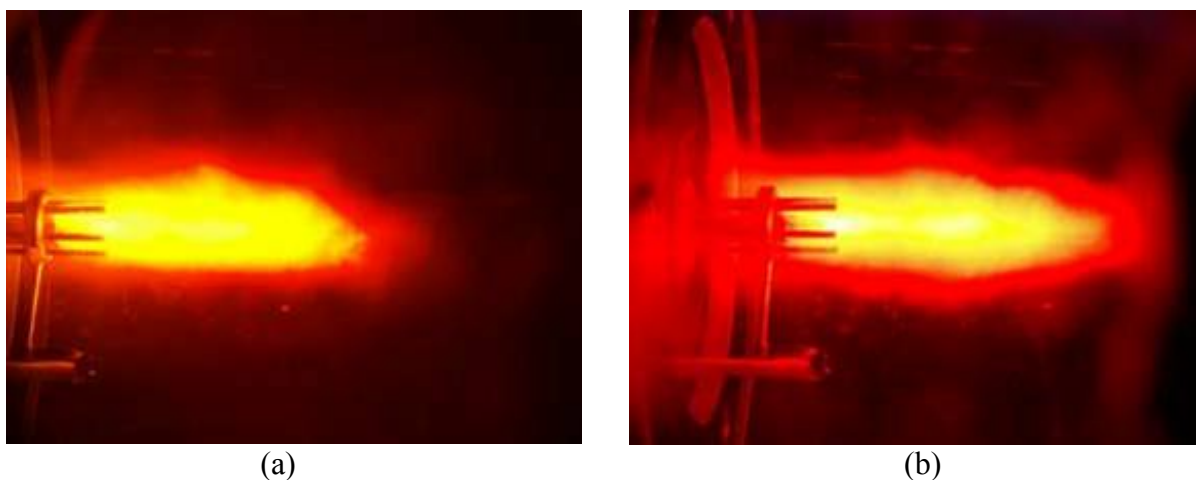


Fig.6.35. The view of MMPC generated jet for different input energy. (a) – Voltage of capacity bank 1250 V, (b) – 150 V. Interference filter 596 ± 10 nm was used. Pressure for both frames is about 35 Torr.

Typical Volt-Ampere characteristics for investigated type of MPC are presented in Fig.6.36a and b. Fig.6.36a is the time-dependence of discharge current (maximal discharge current for this jet is about 20 kA, typical duration 60 mcs) and Fig.6.36b is a “dynamic” characteristic. It shows that impedance of discharge for using type of MMPC is a sufficiently nonlinear.

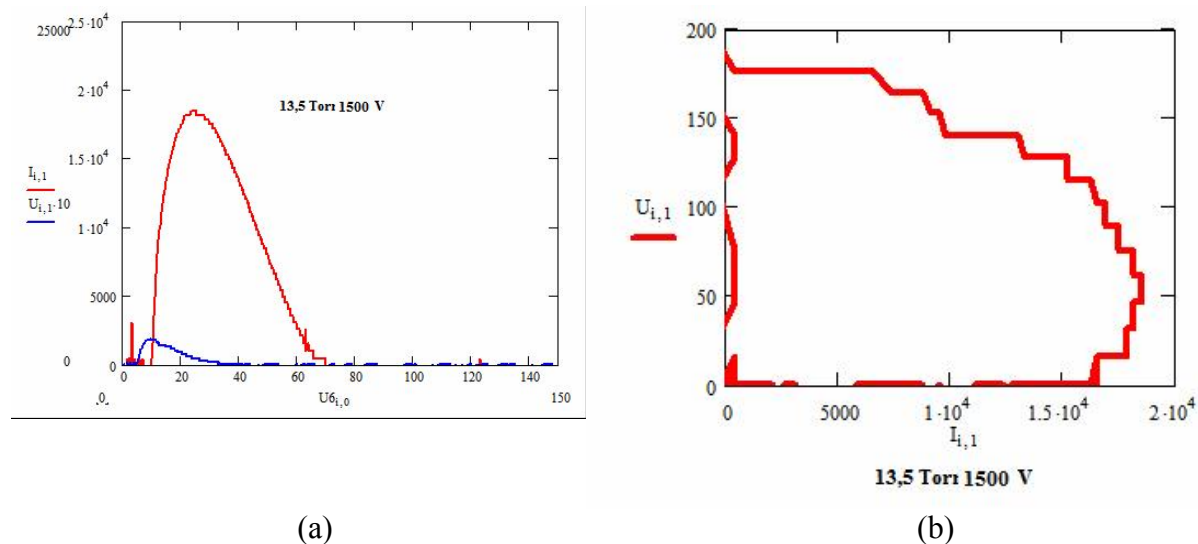


Fig.6.36. Typical Volt-Ampere characteristics of investigated MMPC

Energies and total charge, inputted in the MMPC discharge for different gas pressures are presented in Fig. 6.37.

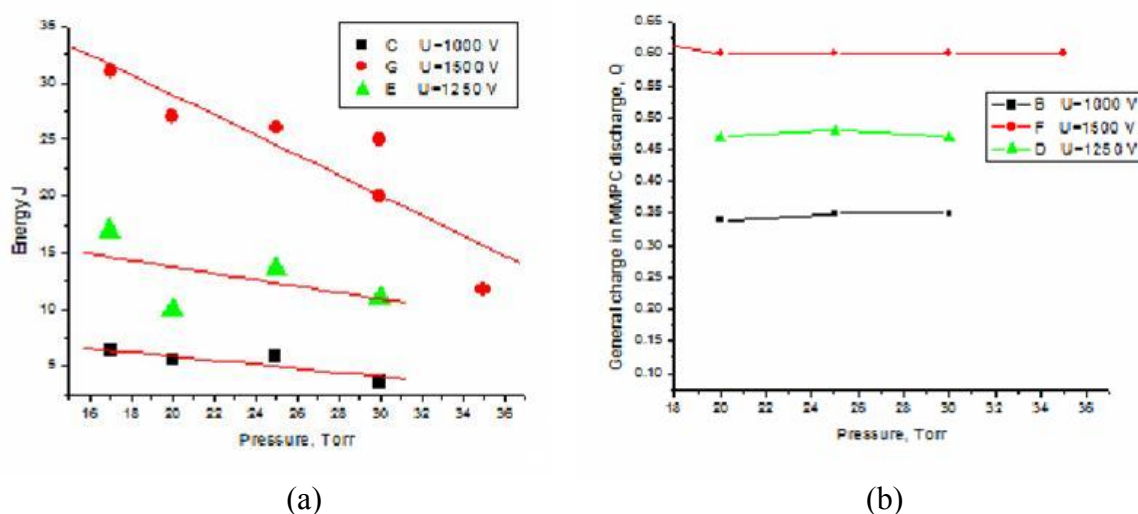
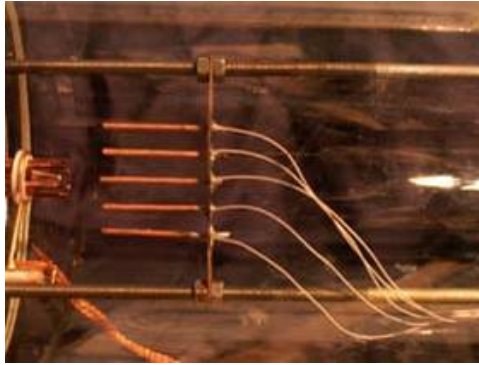


Fig.6.37. Energy and total charge inputted in MMPC discharge for different pressures of residual gas

The efflux current for MMPC generated jets was measured by array of Langmuir probes, placed at the different position from the outlet of MMPC. The view of location of probe array in the test chamber is shown in Fig.6.38a. In Fig.6.38b the photo of process of interaction of plasma jet is presented. Actually, the probe array makes sufficient flow disturbance in investigated jet, but for the first steps of efflux effects investigation this method can be accepted as admissible.

(a)



(b)

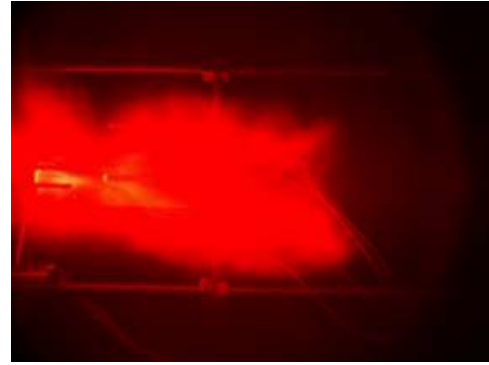
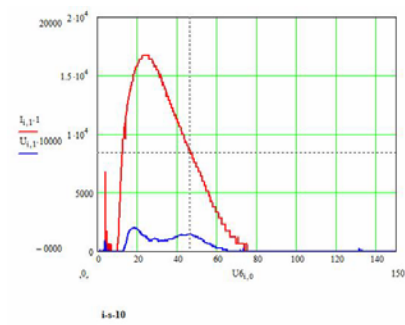
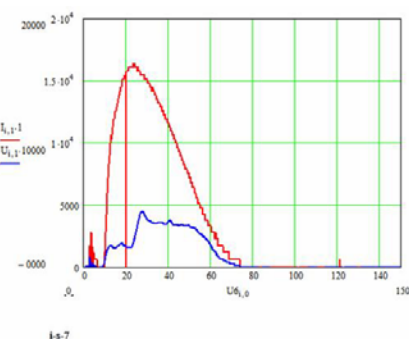


Fig.6.38. The view of Langmuir probe array arrangement and photo of Jet-Probe array interaction

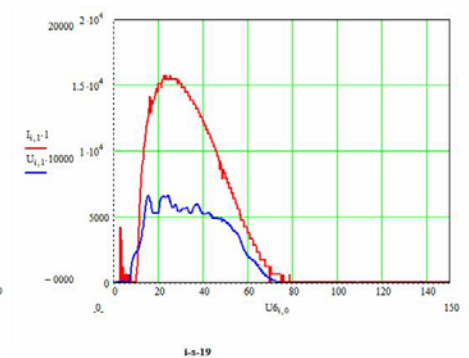
The typical Langmuir probe characteristics for different input energy (battery Voltage 1000, 1250 and 1500 V) are presented in the Fig.6.39a (1000 V), b (1250 V) and c (1500 V).



(a)



(b)



(c)

Fig.6.39. Signals for axis Langmuir probe at the different MMPC input energy

The sensor was placed on the axis of jet at the distance 12 mm from MMPC outlet. Simultaneously, on these pictures the discharge MMPC current is presented.

Values of efflux current density for different distance (100 mm maximal) from MMPC are presented in the Fig.6.40. The results of measurements of efflux current for investigated type of MMPC show, that the actual length of MPC generated jet exceeds 100 mm.

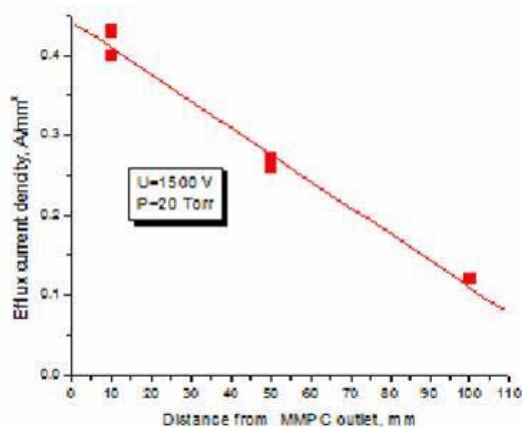


Fig.6.40. The efflux current density at the different distances from MMPC outlet

The analysis of efflux effects for investigated MMPC shows that created miniature plasma compressor has the same mechanism of jet arising as its “large-scale” analog. Actually, it has the “Fast phase” (Phase I) and “Slow phase” (Phase II). The main efflux effects are beginning after the arising of quasi-stationary phase (Phase II) in MPC discharge. The typical amplitude of efflux current density for MMPC is about 0.2-0.3 A/mm². The curve of efflux current has an interval, when the current value is practically constant. This temporal interval corresponds to more stationary stage of MPC generated jet.

The brief results of the first steps of MMPC investigations can be presented as:

- High –Pressure Residual gas regime of MMPC is investigated for pressure diapason 15-30 Torr;
- MMPC generated plasma jets have the parameters similar to it “Large Scale” analog (two main phase of jet forming, compression area arising);
- Energy characteristics of MMPC essentially lower than , L-S MPC (15-20 J/pulse, and 0.6-1.5 kJ/pulse);
- .Efflux current density for MMPC is about 0.1 A/mm² at the distances 80-100 mm from outlet;

- The results of the present experiments show that creation of MMPC with exhaust diameter 8, 6 and 4 mm is undoubtedly real;
- Miniature MMPC permits to arrange the array of MMPC-based plasma injectors. The possible construction of this device presented in Fig.6.41, where (a) is a project of “single” plasma ejector, the (b) – the project array of MMPC.

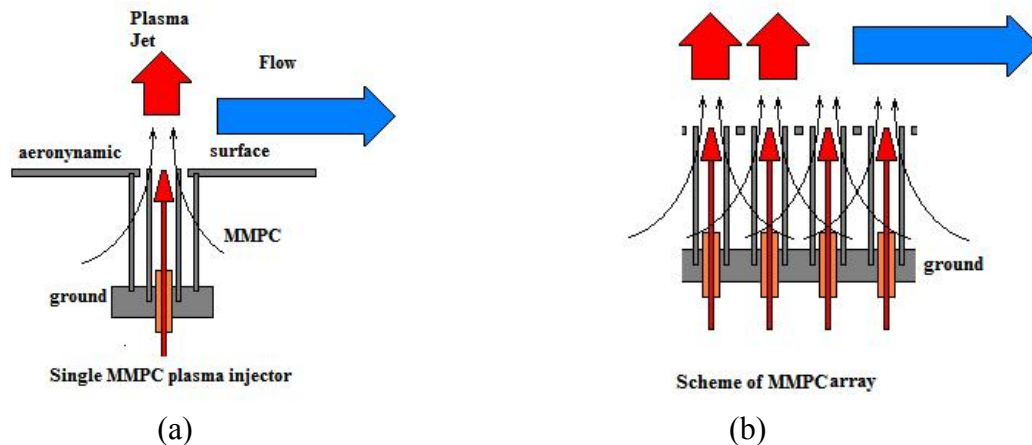


Fig.6.41. Possible construction of MMPC-based actuator array (project)

References for Section 6

1. Astashinsky B., Bakanovich G., Minko L. Investigations of dynamic of plasma arising and forming processes of compression area in gas magneto-plasma compressor. Journal of Applied Spectroscopy, Vol. 33, 1980, p.629-633.
2. Morozov A. The principles of coaxial quasi stationary plasma accelerators. Physics of Plasma, vol.16, 1990, p.131-146.
3. Mashek I.Ch., Lashkov V.A., Anisimov Yu.I., Kolesnichenko Yu.F. Quasi-Stationary Magneto-Plasma Compressor For Investigation of Plasma Jets in Aerodynamic, 44th AIAA Aerospace Meeting and Exhibit, January 2006, Reno, NV, paper AIAA 2006-1458.
4. Mashek I.Ch., Lashkov V.A., Anisimov Yu.I., Kolesnichenko Yu.F. Hypersonic Plasma Jets Generated by Quasy-Stationary Magneto – Plasma Compressor and their Applications for

Applied Plasma Dynamics. The materials of 5th Workshop Thermochemical and Plasma processes in Aerodynamics, Saint-Petersburg, 19-21 June, 2006, paper No 21.

5. Mashek I.Ch., Lashkov V.A., Anisimov Yu.I., Kolesnichenko Yu.F. Investigation of Plasma Jets Generated by Quasi-Stationary Magneto-Plasma Compressor under the High Static Pressure, 45th AIAA Aerospace Meeting and Exhibit, January 2006, Reno, NV, paper AIAA 2007-0221.
6. Mashek I.Ch., Lashkov V.A., Anisimov Yu.I., Kolesnichenko Yu.F. Investigations of Miniature magneto-Plasma Compressor. The materials of 7th Workshop on Magnetoplasma Aerodynamics, Moscow, April 2007.

Summary

Sufficient progress has been achieved in experimental, theoretical and numerical investigation of the basic processes in MW discharge, its interaction with Laser and DC plasmas and plasma jets. These investigations are aimed at creation of thin filaments at low energy expense at the desirable spatial position, as well as eliminating of plasma effects in its interaction with shock waves. The Project tasks were implementing hand by hand with deep modernization of installations, improvement of diagnostics and developing of new codes. Below brief description of the main investigation trends and obtained results are given.

Interaction of MW radiation with Laser spark and plasma stimulators

Flexible MW – Laser stand with wide range of MW parameters control and gas pressure variation, 3 wavelengths of Nd:YAG laser operation in nanosecond generation regime with ability of mutual position of MW – laser beams variation was created in IHT RAS.

For the first time the stable electrodeless MW discharge initiated by laser spark different orientation relatively electric field of MW wave in wide range of air pressure is realized. Experiments are carried out under all principle geometries of interaction of MW and laser beams. Laser spark effectively initiates MW discharge, as well as laser beam without spark production. The MW breakdown threshold under the presence of laser beam is visibly less that for self-ignition and in some cases even less that for its extinction. Sufficient decrease of MW breakdown level is observed under the laser spark origination.

MW discharge structures development along the laser beam and across MW beam is revealed (directional effect). The ability of igniting of MW discharge during the long period between initiating pulses (up to 100 ms) but under the elevated MW power is fixed. It is shown that interaction of MW radiation with laser plasma is most effective under the small delays of MW pulse relative laser one; as a result amplification of pressure and sound from the discharge region is detected.

In the mode of transversal beams the stable initiation of MW discharge by focused UV laser radiation is obtained. In experiments sufficient decrease of MW discharge initiation threshold was detected in the case of UV laser beam irradiation of the MW focal area.

For the first time the effect of very strong interaction of free microwaves with an external plasma channel, created by pulse air spark is revealed. The ability of HV spark triggering by

stimulated MW discharge is shown. Experiment has demonstrated efficiency of DC channel initiation and directing by laser spark

Numeric modeling of kinetic effects arising under interaction of MW radiation with laser-created domains

Kinetic modeling of MW interaction with nanosecond decaying laser spark answered in the affirmative on the principal question about the transparency “time window” existence, when combination of electron concentration and spark density allows of MW penetration into spark domain. Moreover, kinetic modeling has shown that such effect is possible for wide range of ambient medium pressures (100-750 Torr) and at that local amplification of reduced field E/N takes place, when the relation of E/N inside of laser spark occurs bigger than the same relation in ambient medium. Mentioned effect is obtained during isobaric decay of laser spark, when electron concentration becomes so much small that depolarization reduction turns out a negligible one, but spark domain keeps a still hot, i.e. its density N is less than ambient one.

Three regimes of MW field interaction with decaying laser plasma under the atmospheric air pressure were revealed. After 60 mcs delay the medium became not only a transparent one, but its composition becomes a “friendly” one for MW breakdown. At early delays (≈ 100 mcs) filament growth conditions are enhanced due to the absence of molecular oxygen (and as a result the absence of electron losses during their dissociative attachment to O_2) and the decreasing of partial content of N_2 in isobaric medium composition. Enhancement of breakdown conditions at late delays (≈ 300 mcs) is connected with visible production of NO. This specie has low threshold of ionization, what decreases total threshold of the medium. In general these results correlate with experimental ones.

For ambient pressure of 100 Torr the value of E/N amplification is about 40 times and for 750 Torr – about 8 times. This dependence exhibit the common tendency to increasing of amplification with the drop of pressure. Moreover, the pressure value influences on energy spectra of electrons: under low pressures spark domain is predominantly atomic one (N, O, traces of N_2) while species composition under high pressures is N_2 , O_2 , O. In the first case energy spectra contains more high energy electrons than in the second one, i.e. the processes of excitation and direct ionization are much more intensive under low pressures than at high ones.

Maximal amplification approach time during LS decay varies from about 200 mcs under 100 Torr down to 110 mcs under the atmospheric pressure. Minimal MW power density necessary for ionization avalanche start varies from about 1 kW/cm² under 100 Torr up to 10 kW/cm² under the atmospheric pressure. Laser spark elongated in the direction of electric field of EM wave is somewhat more efficient for initiation of MW discharge than LS of spherical shape.

Kinetic modeling of MW pulse interaction with low temperature and strongly conductive long thin spark created by femto-, pico-second laser pulse has shown the possibility of MW discharge origination on this object. At that MW incident field energy deposition for ionization avalanche start decreases from 1.5 eV/particle at 85 Td down to 0.8 eV/particle at 120 Td. The time of avalanche start decreases from ~ 1 mcs down to ~ 10 ns. Avalanche process is over when the rate of medium expansion becomes approximately equal to the rate of electrons production in the medium. Temperature growth amounts to ≈ 5000 K at avalanche end.

Code preparation, debugging and testing for numeric investigation of MW filament origination, including gas dynamic effects, which is implemented in collaboration with Prof. Doyle Knight (Rutgers University), was carried out. First results are obtained, which are to be presented at 46th AIAA Aerospace Sciences Meeting & Exhibit, Reno, NV, 7-10 January, 2008.

Numeric modeling of gas dynamic effects arising under interaction of MW discharge channel with AD body

Numeric modeling of gas dynamic effect of a thin longitudinal heated low-density channel on supersonic flow around AD bodies of different shapes was carried out. Such kind of heated channel can be obtained via MW energy injection into a supersonic flow. Situation of an infinite channel is investigated, too. The computed data are in agreement with the experimental ones for the dynamics of the bow shock wave standoff and the stagnation pressure in the experimental investigations of MW energy interaction with supersonic models.

New results on behavior of front drag force and total drag force during an interaction of a thin limited length low-density channel – cylinder shock layer have been obtained. AD body with complicated cavity has been considered. It is established that the presence of the cavity in the cylinder body amplifies the effects of drag force reduction in the process of thin low density channel – shock layer interaction and it is possible the presence of two or three minimums in the

front drag force dependence on time. Arising two or three minimums in the dependence of front drag force on time is obtained to connect with eddies generation inside the cylinder shock layer. The special features of flow dynamics for the cases of short and long cavities have been analyzed. The effects established are stronger for smaller values of gas rarefaction in the channel. It is pointed out that there exists the time interval in which the effects established do not practically depend on the radius of the release channel and are defined only by the value of the channel length and the value of gas rarefaction degree in the channel (and the Mach number of oncoming flow).

The results of numerical modeling of an infinite rarefied heated channel of constant density cross-section – cylinder shock layer interaction are presented. Details of flow structure have been analyzed on the most representative grids. Stochastic pulsation flow mode has been observed. Mechanism of pulsations based on relationship between circulation flow and reversal flow is revealed. New flow structure effects concerning generation of contact discontinuities instabilities like Richtmayer-Meshkov instability and shear layer instability have been obtained. Main flow areas forming inside the shock layer has been researched including the flow separation area.

Investigation of details of flow structure for a very thin heated rarefied channel was conducted. The channel radius was equal to one tenth of the body's radius. The vortices generated via shear layer instabilities were established to be stronger than in the case of less thin channels. Formation of the heated channel inside the shock layer is established. The reversal eddies generated were found to be strong sufficiently for the achievement of turbulent mixing of the hot gas in the formed channel and cold surrounding gas inside the separation area. It is obtained that the turbulent mixing is taken place cyclically in dependence with increasing the amount of the reversal eddies in the separation area. It is shown that in the case of thin channel the small scaled stochastic process dominates with the large scaled flow pulsations.

The results of numerical modeling of a thin low-density heated channel of limited length – shock layer interaction for the Mach number of the oncoming flow $M_\infty=3$ are presented. New flow structure effects for plane and cylinder cases in comparison with the previous results for $M_\infty=1.89$ have been established. Arising additional shock waves and contact discontinuities both in cylinder and plane cases in comparison with the previous results for $M_\infty=1.89$ was established. In cylinder case the peaks generation in the dynamics of the stagnation pressure as the result of

Mach reflection of the additional shock wave was characterized. Stagnation pressure growth after its fall down was shown to cause by additional shock wave reflection from the front surface of the body (for the rarefaction degree $\alpha_p=0.2\div 0.3$). Relative bow shock wave coordinate variation is obtained to be greater for longer channels. The possibility of compensation of insufficient channel rarefaction by greater value of the channel length for obtaining the same value of the front drag force has been established.

Stochastic pulsation flow mode has been analyzed for the value of the relation a release channel radius to body's radius equal to 0.1 and 0.25. The Mach number of the oncoming flow was equal to 1.89 and 3; the degree of the gas rarefaction in the heated release channel was supplied to be 0.3-0.5. Generation of Richtmayer-Meshkov instability, dynamics of shear layer instability and dynamics of flow defining parameters were investigated. For particular set of the flow parameters a tendency to instability suppressing is shown to take place. These results have been obtained in Rutgers University (USA, New Jersey) in the Laboratory of Computing Design headed by Professor Doyle Knight.

Plasma-aerodynamic experiments

Experimental investigation of microwave discharge interaction with supersonic aerodynamic body has been carried out. The microwave discharge is an interesting object, making possible a substantial change of the bodies' aerodynamic drag. Moreover, the microwave discharge permits both to rise and to lower the body's drag. The principal mechanism, leading to the body's aerodynamic characteristics change is gas vortex motion caused by the interaction of the gas area excited by the discharge and the shock layer on the body. Experiments on gas dynamic stand of SRIMM were aimed at increasing a lifetime and intensity of a vortex in a shock layer during MW filament interaction with supersonic AD body.

Experimental research has been conducted to study the pressure behavior on the blunt cylinder's front surface in the circumstances of the microwave discharge, using a model with a hollow inside. The experiments have proved that the injection of gas into the shock layer synchronized with the microwave discharge boosts the vortex flow, which leads to a significant reduction of the body's drag (by 1.5 – 1.8 times). Microwave discharge and counter flow reinforced the influence of each other on drag reduction.

Gas injection through the spike on the sphere does not allow MW discharge to upset gas moving in the circulating zone. It diminishes influence of the discharge on drag increase of the sphere.

A deep modernization of wind tunnel has been carried out. Two supersonic diffusers were designed and manufactured for creating working flow with Mach number 2 and 3. A new microwave focusing system was worked out and investigated. It showed its high efficiency. Microwave discharge can be realized at higher pressure. A gas heater was built, which can rise stagnation temperature in the working flow up to 600-650K.

New experimental results of discharge to shock layer interaction under Mach number $M=3$ were obtained. Tests showed that bow shock wave stands four times farther off the front surface of the blunt cylinder than under usual streamlining.

Using the new microwave focusing system and heating of the working gas gives opportunity to investigate interaction of heated after microwave discharge domain of gas with shock layer on the body in the wide range of Mach number, microwave power and static pressure.

Combined Laser-MW discharges in supersonic flows

The laser-initiated MW discharges in quiescent gas (air) under the atmospheric pressure for Y-polarization of MW radiation were investigated. Results of our experiments with Q-switched Ruby laser (694 nm, 0,25-0,3 J, 25 ns) confirm that effective MW energy deposition under the mentioned above conditions is realized after the essential time-delays between initiated laser spark and MW pulse (80 – 120 μ s). The mechanism of this effect is connected with two main reasons - arising of thermal (density) well at the place of laser discharge and changing of chemical composition of the heated volume, including production of long-lived states of atoms and molecules.

The multi-targets laser system for investigations of laser-induced MW discharges in supersonic flows with Mach number 1,3-3,0 and static pressures 20-100 Torr was created. It contains the Q-switched two-stage Ruby laser (1 J, 25 ns, 694 nm) and Nd^+ laser (1 J, 8 ns, 1064 nm), the optical translation system for laser spark creation in the Gas-Dynamic Test Chamber, synchronization system with MW generator and diagnostic scheme. The efficiency of this system was demonstrated on the erosion plum arrangement on the test aerodynamic body.

The high perceptiveness of lasers of picoseconds diapason for laser sparks arrangement was demonstrated. It was shown, that Q-switched YAG laser with one-stage Raman compressor (400 ps, 3.2 mJ at 1064 nm and 0.75 mJ at 532 nm) permits to create the laser sparks under the atmospheric pressure with comparatively high effectiveness of energy deposition in shock wave structures (effectiveness $0,3 \pm 0,1$ for 1064 nm, 3.2 mJ, 400 ps).

Plasmadynamic applications of Magneto-Plasma Compressors

The unique properties of plasma jets, generated by the Magneto-Plasma Compressors (MPC), operated in High-Pressure Residual Gas Regime (HPRGR) were demonstrated. For these purposes the new type of MPC with internal auxiliary discharge was constructed. This new compressor operates under the static pressure diapason 0.5-100 Torr and creates the impulse plasma jets with lifetime 50-80 μ s, velocities 5-20 km/s (static pressure 80-1 Torr), temperature 34000 ± 5000 K, electron concentration about $3 \cdot 10^{15} \text{ cm}^{-3}$ (static pressure 30 Torr) and high value of stagnation pressure – 150-200 bar. The Mach number for these jets was estimated as 4,0-5,5. The mechanisms of jets arising in MPC operated in HPRGR were investigated. It was shown, that plasma generated jet has two main temporal phases. At the phase I (fast phase) MPC generates unfocused plasma jet with very high velocity ($6 \pm 0,5$ km/s, RGR with static pressure 10 Torr) and comparatively low density. At the phase II (slow phase) MPC forms the quasi-stationary compressed jet with mentioned above high density and temperature.

The high level of stagnation pressure, arising in MPC jets made these jets very perspective both for plasma injection in supersonic flows and in plasmadynamic acceleration of disperse particles and their seeding in SS flows. The both of these possibilities had been demonstrated. For these experiments the new Ludwig wind tunnel ($M=2.0$, static pressure 20-100 Torr, stream lifetime 60-70 ms) has been constructed. The experiments with mixing of MPC plasma jet and Supersonic Ludwig wind tunnel flows had shown that penetration ability of MPC plasma jets is very high. The experiments with disperse particle acceleration by MPC plasma jet had demonstrated that 10 micron W-particles are accelerating in MPC plasma focus up to 2.0-2.6 km/s (MPC in Vacuum Regime) and can be successfully injected in gas flows with comparable velocities.

The practical realization of MPC plasma injection in supersonic flow demands creation of MPC with comparatively low input energy. The possibilities of construction Miniature Plasma

Compressor (MMPC), operating in HPRGR were demonstrated too. The MMPC with outlet diameter 12 mm was successfully created. Its tests show that MMPC generated plasma jets have the parameters similar to its “Large Scale” analog (two main phase of jet forming, compression area arising). Energy characteristics of MMPC are essentially lower than its large-scale analog (15-20 J/pulse, and 0,6-1,5 kJ/pulse). The results of experiments show that creation of MMPC with exhaust diameter 8, 6 and 4 mm is undoubtedly real. It was shown, that the miniature MPC may become the base unit for creation of MMPC arrays in new generation of plasma actuators in applied plasmadynamics.

Our technical paper AIAA Paper No. 2007-1228, “Optimization of Laser-Pulse-Controlled MW Energy Deposition” has been named as AIAA Best Paper by the AIAA Plasmadynamics and Lasers Technical Committee.

Acknowledgments

We are sincerely grateful to Dr. John Schmisseur (AFOSR) and Prof. Doyle Knight (Rutgers University) for their support of our activity.

Our deep gratitude is also addressed to the European Office of Aerospace Research and Development (EOARD) and personally to Dr. Surya Surampudi.